Development of High-throughput Microscope Imaging Mass Spectrometry

A thesis submitted for the degree of Doctor of Philosophy

Physical and Theoretical Chemistry



Robert J. Burleigh

Jesus College, University of Oxford

Trinity 2019

Abstract

Mass specific surface images with micron and sub-micron spatial resolution can be recorded with a mass spectrometer. Ion microscope mass spectrometry imaging uses a defocused laser or ion beam to simultaneously analyse large sample areas. The ions are subsequently separated by their time-of-flight (ToF) and their spatial location is electrostatically transferred onto a two-dimensional position-sensitive detector. The detected ions are converted to light and recorded by either, a charged coupled device (CCD) camera and a photo multiplier tube (PMT), or an event-triggered complementary metal-oxide semiconductor (CMOS) sensor. CMOS sensors such as the Timepix3 cam and a PImMS camera are capable of multi-mass ion imaging. The result is a series of images corresponding to each recorded m/z, further demonstrating the high-throughput capability of the instrument.

An ion microscope has three drawbacks when compared to microprobe MSI: low mass resolution, a small mass range and poor spatial resolution. For each of these limitations, this thesis presents a solution that can be applied simultaneously to improve the performance and applicability.

An ion microscope, incorporating a reflectron, was used to simultaneously image mass-resolved ions generated from a 0.3 mm diameter surface. Mass and spatial resolutions of $8100 \pm 700\, m/\Delta m$ and $14\,\mu$m were obtained by using post extraction differential acceleration (PEDA) ion optical focusing to create a pseudo-source plane for a single-stage gridless reflectron. The obtainable mass resolution was limited only by the response time of the position-sensitive detector, and could potentially reach $30\,200 \pm 2900\, m/\Delta m$.

Single-field PEDA has a mass-resolved window that is approximately 19% of the spatially-resolved mass window. A time-dependent pulse applied after ions have exited the extraction region facilitates an increase in the mass resolution over the entire spatially resolved mass range. The potential energy surface of the time-dependent pulse is chosen so that it approximates the dependency between the ion ToF and molecular weight. Mass resolution between 2500 - 8100 $m/\Delta m$ has been achieved for ions between 300 - 625 Da, whilst preserving approximately $14\,\mu$m spatial resolution.

The spatial resolution has been improved *in silico* with the introduction of a four-plate ion optic. The electrode arrangement and potentials have been optimised

using minimisation routines. An 800 nm spatial resolution has been achieved with the optimised ion optics.

The Timepix3 cam has recorded time resolved ion images from a reflectron ion microscope. The camera has been operated in continuous readout mode and the individual experiments have been separated using optical fibre that directs part of the laser pulse onto the sensor. This provides an alternative to the expensive readout systems that are typically used. The resolutions achieved with this technique are comparable to those obtained using a CCD/PMT combination.

Future publications

1. **Microscope Imaging Mass Spectrometry with a Reflectron (Submitted)**
   R. J. Burleigh, A. Guo, A. Green, S. Thompson, M. Burt and M. Brouard

2. **High-resolution ion microscope imaging over wide mass ranges using electrodynamic post-extraction differential acceleration**
   R. J. Burleigh, A. Guo, N. Smith, M. Burt and M. Brouard

3. **Imaging Mass Spectrometry with a Timepix3 cam using a Novel Readout System**
   R. J. Burleigh, D. Wood, F. Allum, R. Mason, M. Burt, R. Plackett, A. Nomerotski, I. Shipsey and M. Brouard

Acknowledgements

I would like to express my sincere gratitude to Prof Mark Brouard. I owe a great debt for his mentoring, constant encouragement and unwavering support. It has been an immense privilege to be his student.

As part of the spatial imaging sub-group I have had the fortune of working with very talented scientists. I am very grateful for insight and guidance throughout my DPhil from Dr.Micheal Burt. His attention to detail is second to none. Dr.Ang Guo laid the ground work for the reflectron presented in this thesis. His ability to see through a problem was an inspiration. Technical discussions and cold refreshments with Dr.Steve Thompson were incredibly useful. I am indebted to Dr.Daniel Wood for his tireless work with the Tpx3Cam and for the countless hours spent in the laboratory. The final six months have been filled with many highs and lows, but thankfully the challenges were never to tall for Dan. In addition, I am incredibly grateful to Dr.Cornelia Heid for giving numerous helpful suggestions when proofreading this thesis. She has been a lovely person to be around. I wish Natasha Smith good luck with the continued development of the reflectron. I hope that she gets the same level of enjoyment that I have had.

I would like to express my gratitude to the mechanical and electrical workshops team, in particular to Andrew Green, Philip Hurst and Kevin Valentine, for their relentless efforts in fixing the reflectron.

I have had a fantastic time in Oxford thanks to Garreth, Sean, Hansjochen, Henry, and all of the great friends that I have made. Robbie and Felix: thank you for continuously suggesting help and making the office an interesting place with your unique behaviour - it always has, and always will be a scream. With a special mention to Lewis for the entertaining nights and great friendship.

This thesis would not have been possible without the support of my family. To my Mam, Dad, Gran and Grandpa, you have been a constant source of motivation, laughter and good times. To my best friend and brother: thank you for always finding a challenge for us to overcome, and always knowing how to celebrate afterwards. And, finally, I would like to thank my partner Kate for her love, tireless support and ability to turn everything into a success. You make everyday better.

Contents

1 Introduction **2**

1.1 Charged particles . . . 3
1.2 Time-of-Flight . . . 5
1.3 Ionisation methods . . . 11
1.4 Ion imaging . . . 17
1.5 Ion detection . . . 26
1.6 Thesis overview . . . 30

2 Experimental methods **32**

2.1 Reflectron ToF mass spectrometer . . . 32
2.1.1 Ion optics . . . 34
2.2 Sample preparation . . . 35
2.2.1 Electrosprayer . . . 36
2.2.2 TM sprayer . . . 38
2.3 Laser . . . 39
2.4 Oscilloscope and triggering . . . 42
2.5 Detector assembly . . . 43
2.6 Camera . . . 46
2.6.1 CCD . . . 47
2.6.2 PImMS sensor . . . 47
2.6.3 Tpx3Cam . . . 49
2.6.4 Focusing the Camera . . . 51
2.7 Mass spectrometer calibration . . . 53
2.8 Summary . . . 55

3 Ion trajectory simulations **56**

3.1 Introduction . . . 56
3.2 Ion optics work bench . . . 57
3.3 Instrument geometry . . . 57
3.4 Defining Ions . . . 59
3.5 Analysis of simulation results . . . 64
3.6 Minimisation algorithms . . . 67

3.6.1 Genetic algorithm 67
3.6.2 Nelder–Mead minimisation algorithm 69
3.7 Summary 71

4 Characterisation of a reflectron ion microscope 73
4.1 Introduction 73
4.2 Principles of a reflectron 74
4.3 Simulation 81
4.4 Spatial resolution 83
4.4.1 Correcting distortions 85
4.4.2 Ion focusing 93
4.4.3 Image magnification 95
4.4.4 Fourier transformation 96
4.5 Mass Resolution 101
4.5.1 Pseudo-source 105
4.6 Fast imaging sensors 108
4.7 Conclusion 110

5 Time-dependent velocity correction 112
5.1 Introduction 112
5.2 Theory and simulation 114
5.2.1 Linear time-dependent PEDA 116
5.2.2 Quadratic time-dependent PEDA 122
5.2.3 Comparison of pulsed variants 125
5.3 Experimental methods 126
5.3.1 Mass resolution 127
5.3.2 Spatial resolution 129
5.4 Conclusion 131

6 High resolution ion optics 133
6.1 Introduction 133
6.2 Improving spatial resolution 135
6.2.1 Spherical and Chromatic aberrations 135
6.2.2 Modelling ion trajectories with transfer matrices 137
6.2.2.1 Derivation of transfer matrices 140
6.2.2.2 Uniform electric field 140
6.2.2.3 Emission surface 144
6.2.2.4 Aperture 145
6.2.2.5 Field free region 149
6.2.2.6 Trajectory calculation 150

6.2.3 Modelling ion optic trajectories with SIMION 151
6.2.4 Comparison of ion trajectory calculation methods 152
6.2.5 Electrostatic analysers 153
6.2.6 Simulation 156
6.2.7 Results from the minimisation algorithms 158
6.3 Improving mass resolution 160
6.3.1 Post Extraction Differential Acceleration 163
6.4 Summary 166

7 Ion imaging with a Tpx3Cam **168**
7.1 Introduction 168
7.2 Experimental setup 171
7.2.1 Timepix3 chip 171
7.2.2 Methods 173
7.3 Data processing 175
7.3.1 Data conversion 175
7.3.2 Clustering 177
7.4 Experiments with the Tpx3Cam 178
7.4.1 Results 179
7.5 Exploring the time spread 181
7.5.1 Laser shot variation 182
7.5.2 Centroiding 183
7.6 Future improvements to the time resolution 187
7.6.1 Pixel calibration 187
7.6.2 Time-walk correction 188
7.7 Summary 189

8 Conclusions and future work **191**
8.1 Conclusions 191
8.2 The future 193

References **196**

Appendices

A Appendix 1 **206**
A Genetic algorithm parameter values 206

List of abbreviations

ESA Electrostatic analyser

FWHM Full width half maximum

LDI Laser desorption ionisation

MALDI Matrix assisted laser desorption ionisation

MCP Micro-channel plate

MSI Mass spectrometry imaging

m/z mass to charge ratio

m/Δm Mass resolution

PEDA Post extraction differential acceleration

PImMS Pixel imaging mass spectrometry

PMT Photomultiplier tube

SIMS Secondary ionisation mass spectrometry

SPIDR Speedy pixel detector readout

Tpx Timepix

ToF-MS Time of flight mass spectrometry

VMI Velocity map ion imaging

1 Introduction

Mass spectrometry is an analytical tool that can quantify the atomic composition of complex molecular environments and provide diagnostic information on biological events such as diseased tissue. Imaging mass spectrometry (MSI) retains the chemical specificity of MS, and provides spatial information of the molecular composition.

There are two techniques for MSI analysis: ion microprobe which uses a focused ionisation source, and a ion microscope which uses defocused ionisation source. The resolving power recorded with a microprobe technique is decoupled as a result of an ionisation source being rasterted over a surface, and the acquired mass spectra being attributed to a particular raster position (or pixel). This allows delayed extraction or ion traps to improve the mass resolution in imaging mass spectrometry.

In contrast, an ion microscope simultaneously ablates a large surface area. This technique is a mechanism for high-throughput MSI analysis: an entire sample surface can be simultaneously imaged. However, an ion microscope precludes ion trapping; the spatial information is no longer acquired on a pixel-by-pixel basis. The spatial information from the surface must be retained to generate an ion image. Typically, ion images generated with an ion microscope are less resolved compared with the microprobe technique. This thesis develops the high-throughput

capability of an ion microscope by improving the resolution of the instrument. First, the mass resolution is improved by the incorporation of a reflectron. Second, the mass range over which the instrument has an improved mass resolving power is increased with time-dependent pulsed extraction variants. This is followed by an ion optic configuration that uses specific electric fields to improve the spatial resolution. Finally, a Tpx3 cam is combined with the instrument to record ion events with high timing precision.

This chapter will present fundamental concepts of mass spectrometry, focusing on those most relevant to MSI. Ionisation methodology and detector technology used throughout this thesis will be discussed. The last section of this chapter will give an outline of the thesis.

1.1 Charged particles

Michael Faraday discovered charge carriers in solution and coined the name *ion* (greek: wander) in 1834 [1]. The first gas phase ion was observed in 1858 by Julius Plucker whilst investigating the action of a magnet on the electric discharge of rarefied gases [2]. Plucker observed the first evidence of cathode rays: a cathode-induced green fluorescence on the glass walls of a discharge tube. The next major development in charged particles was in 1886 from Eugen Goldstein. Goldstein noticed that if a perforated cathode was used, two rays were emitted that moved in opposite directions. If the cathode was relatively thick, they would appear as a parallel beam. These rays became known as canal rays [3]. Using a magnet, Goldstein was able to affect the direction of canal rays, but observed no change in the path of the cathode rays.

J.J Thomson, the founder of mass spectrometry, carried out a series of experiments to measure the mass to charge ratio (m/z) of cathode rays. Thomson concluded that the cathode rays were much lighter than the canal rays and negatively charged, later to be called electrons. Thomson further developed his research,

focusing on the composition of canal rays using a stream of ionised neon. The neon ions (the canal rays) were directed through a magnetic and electric field and their deflection was measured by placing a photographic plate in their path. This instrument was the first mass spectrometer (parabola spectrograph). Thomson observed two patches of light on the photographic plate, shown in Fig. 1.1, which suggested two different deflections [4]. Thomson concluded that the neon gas was composed of atoms of two different atomic masses (^{20}Ne and ^{22}Ne).

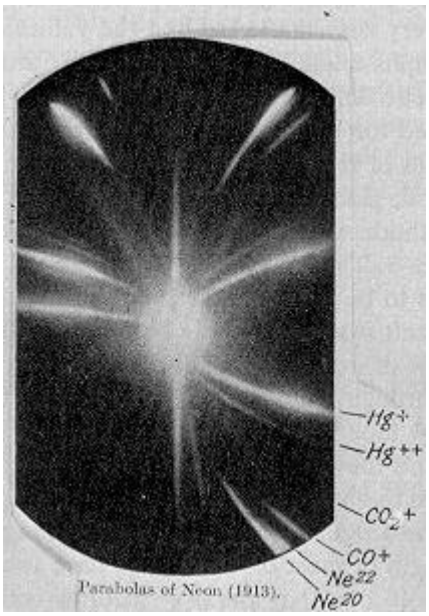


Figure 1.1: Image of light emitted from photographic plate as a result of recording the isotopes of ^{20}Ne and ^{22}Ne. The photographic plate consists of different parabolas that correspond to trajectories of ions with different masses [4].

Francis Aston (Thomson's student) built a fully functional mass spectrometer in 1919. Aston identified isotopes of chlorine, bromine, and krypton, proving that these natural occurring elements are composed of a combination of isotopes [5].

During the 1930s, the parabola spectrograph was applied to organic compounds. Conrad was able to investigate simple hydrocarbons including cyclohexane and benzene using electrical discharge [6]. The positive rays created by the discharge tubes created parabolas on photographic plates which were used to determine the molecular compound, these parabolas are shown in Fig. 1.2.

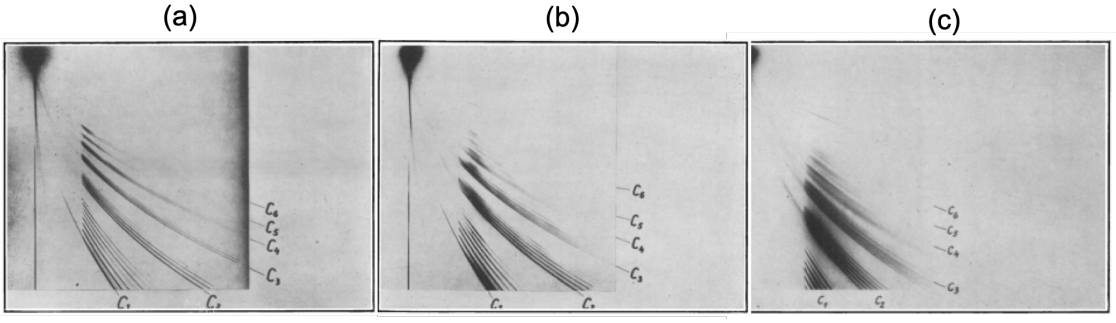


Figure 1.2: Image of photographic plates after the analysis by electric discharge of positive rays: (a) benzene, (b) cyclohexane and (c) hexane. The figure has been adapted from [6].

1.2 Time-of-Flight

A Time-of-flight mass spectrometer (ToF-MS) records the time taken for an ion to travel from a source region to a detection device. The ToF-MS was pioneered by Cameron and Eggers, and the first mass spectra from this instrument was recorded in 1948 [7]. The ToF-MS was able to record multiple ion events within a single experiment. The masses of C^+, H_2O^+, OH^+, CF_2Cl^+ and many other species were recorded. This instrument was further developed with the incorporation of multiple stages by Wiley and McLaren in 1955 [8]. The Wiley-McLaren ToF-MS comprised three regions: the ionisation, acceleration and drift region. At the end of the drift region there was an ion collector connected to an oscilloscope. The ToF-MS was able to record an entire mass spectrum every two microseconds. This instrument achieved unit mass resolution up to 300 Da. The design is shown in Fig. 1.3.

A ToF-MS analyser separates ions in a field free region according to their respective velocities. Fig. 1.4 illustrates a ToF-MS, and is used in the following derivation. Before entering a ToF analyser, ions are ejected from the sample surface (or molecular beam) by a non-continuous ion source. This creates packets of ions with defined start times. The ions are then accelerated by the electric field along the ToF axis towards the flight tube. All ions gain the same kinetic energy, therefore heavier ions have a smaller velocity and vice versa. After the

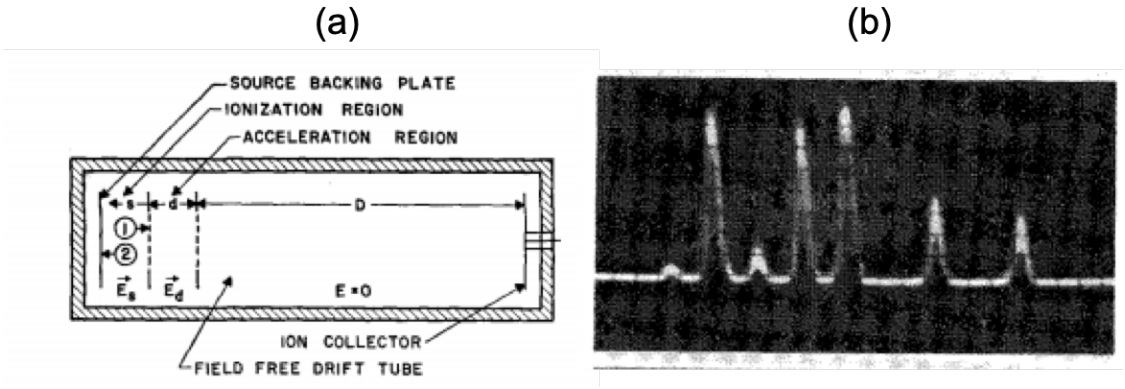


Figure 1.3: (a) Wiley-McLaren ToF-MS design. (b) ToF-MS spectrum on an oscilloscope from the Wiley - McLaren instrument. The peaks correspond to the different isotopes of Xenon.

ions have exited the acceleration region, they enter a field-free region within the ToF analyser and separate as a result of their velocity difference, before their trajectories terminate at the detector.

Mass to charge ratios are determined by measuring the time taken for an ion to travel from the sample surface to the detector. The flight time can be determined from the fundamental equations of motion [9]. An ion with mass m, has a charge number $ze = q$ (where q is total charge) after ionisation. The ion is accelerated by a potential V_s. The potential of the ion is therefore $E = qV_s$. This can be equated to the kinetic energy of the ion at the exit of the acceleration region to determine the velocity in the field free region:

$$v = \sqrt{\frac{2qV_s}{m}} \, . \tag{1.1}$$

The ion's velocity in the field-free region is constant. If the length of the flight tube L is known, the flight time of the ion t, before it impacts on the detector is therefore:

$$t = \frac{L}{v} \, . \tag{1.2}$$

Substituting equation (1.1) into equation (1.2) gives the ToF-MS as a function of instrument variables and mass to charge:

$$t = \sqrt{\frac{m}{z}\left(\frac{L^2}{2eV_s}\right)} \, . \tag{1.3}$$

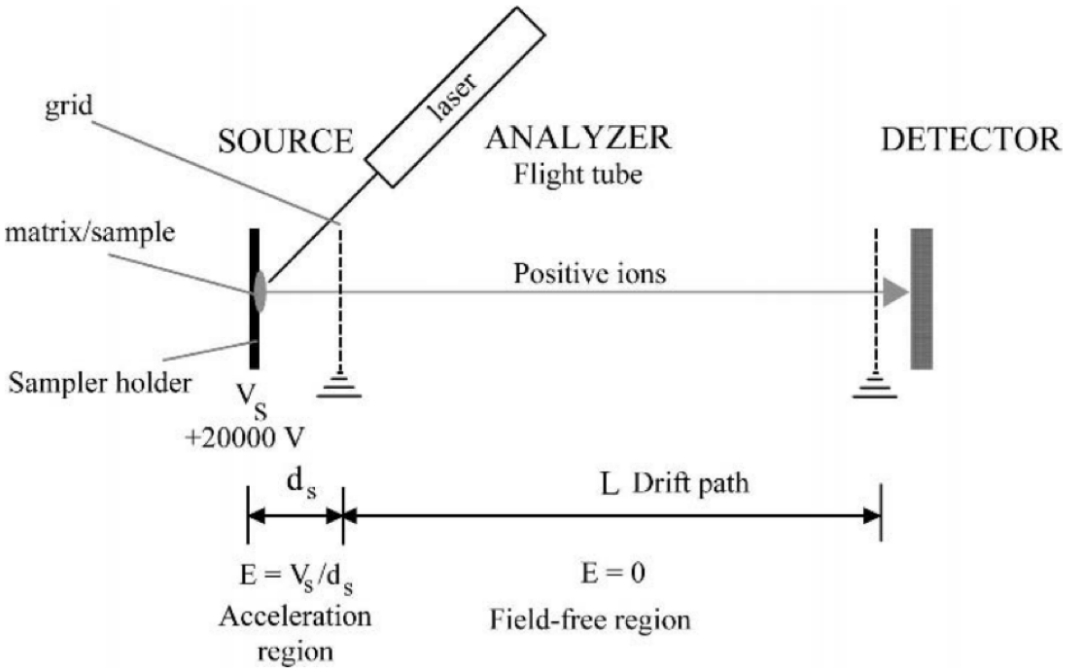


Figure 1.4: Schematic of a mass spectrometer explaining the principle of a ToF-MS tuned to analyse positive ions. After their formation, ions are subject to the applied electric field. The ions are continuously accelerated until they enter a free-field region. Ions travel through this region with a velocity that depends on their m/z ratios. The arrival time at the detector therefore depends on m/z.

Equation (1.3) shows the ion ToF is dependent on $\sqrt{m/z}$. Furthermore, this equation demonstrates that ToF-MS do not have an upper limit for recording the mass. However, practical limits such as physical size of the instrument, collisions of ions with gas molecules, and angular dispersion of the ion beam, limit a linear ToF-MS to only measure ions smaller than 300 kDa [10].

Ions are created with a distribution of initial velocities. The range of velocities is a result of the energy distribution of the ionisation method. For example, a laser pulse typically has a Gaussian intensity profile. As a result, different locations receive different amounts of energy. Therefore, a peak in a mass spectrum is a result of a distribution of arrival times, Δt for a given m/z. The size of the distribution of arrival times determines the resolution. The resolution is quantified by differentiating equation (1.3):

$$\frac{\mathrm{d}m}{z} = \left(\frac{L^2}{2eV_s}\right)2\,\mathrm{d}t\ . \tag{1.4}$$

The ability to resolve different m/z is given by dividing equation (1.3) by equation (1.4):

$$\frac{m}{\mathrm{d}m} = \frac{t}{2\,\mathrm{d}t}\ . \tag{1.5}$$

If the gradient defined by this equation does not change over a small range, which is the case in the region of the ToF-MS spectrum where the full width half maximum (FWHM) is measured, the change d, can be replaced with Δ, giving:

$$R = \frac{m}{\Delta m_{50\%}} = \frac{t}{2\Delta t}\ , \tag{1.6}$$

where R is the mass resolution, m is the centre (or weighted average), and $\Delta m_{50\%}$ is the FWHM of the peak. For the remainder of this thesis $\Delta m_{50\%}$ will be referred to as Δm.

Mass resolution is affected by the flight time t, and factors that create a distribution in flight times Δt, for ions with the same m/z. The factors influencing Δt include: the length of the ion formation pulse, the volume in which the ions are created (space distribution), the variation of the initial kinetic energy of the ions (kinetic energy distribution), space charge effects (caused by ion formation occurring in close proximity to one another), the stability of power supplies, and mechanical precision of the instrument. A number of techniques to improve mass resolution will be discussed extensively in the remainder of this thesis.

In addition to mass resolution, it is necessary to consider mass accuracy, which is a metric describing the difference between the measured m/z of an ion, γ, and the exact m/z of the ion, β. The measured m/z is calculated based on the recorded time of flight and the input mass calibration. Mass accuracy A, is measured in parts per million (ppm) using:

Year	$m/\Delta m$	Author
1913	13	Thomson (Positive ray analysis)
1918	100	Dempster (Positive ray analysis)
1919	130	Aston (Positive ray analysis)
1937	2000	Aston (Mass spectrograph)
1998	8,000,000	Marshall (FTICR)

Table 1.1: Mass resolution improvement since the inception of mass spectrometry [4, 5, 19–21] .

$$A = \frac{\gamma - \beta}{\beta} 10^6 \, . \tag{1.7}$$

A high mass accuracy is crucial to distinguish a particular ion using mass spectrometry. If the mass accuracy is not sufficient, a given ion can have multiple potential chemical formulae. This reduces the efficacy of a mass spectrometer.

During the 1950s the applicability of mass spectrometry to the analysis of unknown compounds was realised. Beynon showed the efficiency in combining a Wiley-McLaren ToF-MS with gas chromatography [11]. This allowed complex mixtures to be deconvoluted into the individual spectra of each compound. This instigated developments in resolving power to expand the scope of mass spectrometry. Improvements of mass resolution were achieved using a number of other novel instruments and instrument combinations such as a quadrupole mass filter (later double and triple quads), tandem mass spectrometers, ion mobility mass spectrometers, HPLC-ToF-MS, FTICR and Orbitraps. These improvements cemented the mass spectrometer as a powerful tool for chemical analysis [12–18]. Since the inception of mass spectrometry, the resolving power of mass spectrometers increased more than 4000% [19]. Table. 1.1 presents some of the highlights.

A particular development discussed in this thesis is the reflectron time-of-flight mass spectrometer. This instrument uses an electric field to reflect the ion trajectories, correcting the initial velocity distribution. For a given m/z, an ion with high kinetic energy travels a greater distance into the reflecting field than

an ion with low kinetic energy. This reduces the temporal spread at the detector, improving the mass resolution.

A cartoon that depicts the energy correction is shown in Fig. 1.5.

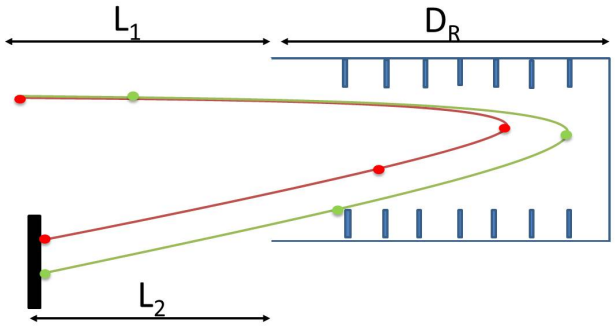


Figure 1.5: Cartoon showing two ions with the same m/z but different kinetic energies: red (low) and green (high). The reflectron corrects this difference so that when ions reach the detector their temporal spread has been reduced, improving the mass resolving capabilities of the instrument.

Reflectrons were first developed in 1973. The initial design used fine gridded electrodes to achieve the electric field required for temporal focusing [22]. However, the typical transmission for a reflectron that uses gridded electrodes is approximately 90% (in a reflectron ions travel through the grid twice) [23, 24]. Grids with a smaller wire diameter have increased transmission, but cause a lens effect on the electric field [25]. This results in divergence of the ion trajectories, which adversely affects the mass resolution. A gridded reflectron can be replaced with open lens electrodes to prevent angular deflections occurring within the reflectron [26]. Reflectrons were combined with a ToF-MS (Wiley-McLaren) to reduce the temporal spread of ions with the same mass, improving the mass resolution [14].

There are different types of reflectrons: single-stage with a linear gradient (V type), single-stage (non-linear gradient), double-stage reflectron (W type) and multi-stage reflectrons (W type). A single-stage reflectron (linear gradient) is equipped with an ion mirror that has a single electric field region as shown in Fig. 1.6(a). Single-stage reflectrons minimise the first derivative of ToF with respect to the ion energy (first order time focusing). With a single-stage reflectron, Mamyrin reported

a mass resolution of HgI_2^+ (454 Da ion) of 3500 $m/\Delta m$ improving the resolution in ToF-MS by an order of magnitude [22]. Further improvements have been achieved with a SIMS ion source combined with a reflectron. This instrument recorded a mass resolution of 10,000 $m/\Delta m$ for a 1348 Da ion [24]. A derivation for the conditions required for first order temporal focusing are given in Chapter 4.

Double-stage reflectrons have two distinct electric field regions, as shown in Fig. 1.6(b). The first stage contains a strong electric field responsible for the rapid deceleration of ions, reducing their kinetic energy by approximately 70%. The electric field in the second stage is smaller and reflects the ions. Double-stage reflectrons can achieve first and second order temporal focusing by using the first electric field as an additional controllable parameter. The variation of this parameter enables the second derivative of flight-time with respect to energy to be reduced. This further reduces the time spread compared with the single-stage. This is especially useful if there is a large energy spread. Multi-stage reflectrons (up to 6 th order) comprise three or more distinct electric field regions [27]. They provide a high degree of focusing compared to single- or double-stage reflectrons and become increasingly more useful as the mass of interest becomes larger [28]. More recent developments of reflectrons include a single-stage (non-linear) electric field. This instrument comprises three electrodes within the reflectron, and facilitates second order focusing without the need for a complex sequence of distinct electric fields [29, 30]. This design can achieve approximately 16,000 $m/\Delta m$ for a 15% kinetic energy variation. This thesis presents work using a single-stage reflectron as the ionisation process results in a relatively small energy spread [31].

1.3 Ionisation methods

As mentioned above, to analyse a compound in a mass spectrometer, an ion must be introduced into the instrument. Since the inception of the mass spectrometer, numerous ionisation processes and sources have been developed.

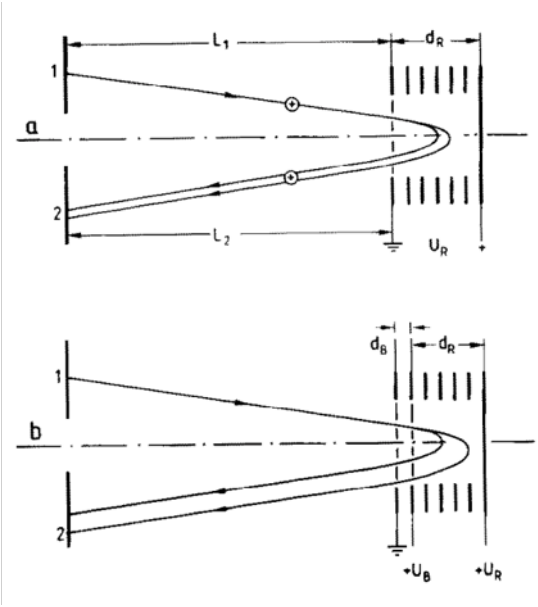


Figure 1.6: (a) Single-stage reflectron. (b) Double stage-reflectron. d_x indicates distances within the reflectron, U_x indicates the potentials of the reflectron, and L_x indicates the distance of the field free regions. Reprint from [22].

Ionisation typically occurs prior to the analyte entering the mass spectrometer. The most important considerations are the internal energy transferred to the analyte during the ionisation process and the physico-chemical properties of the analyte that can be ionised [32–34]. Some ionisation techniques are very energetic and cause extensive molecular fragmentation. Other techniques are softer and only produce ions of the parent molecular species.

Ionisation techniques can be categorised into high energy (hard) and low energy (soft) ionisation methods. Hard ionisation includes: electron ionisation (EI), and secondary ion mass spectrometry (SIMS) using small primary ions such as Cs^+. Soft ionisation includes: SIMS using large primary ions such as C_{60}^+, chemical ionisation (CI), field ionisation (FI), atmospheric-pressure chemical ionisation, electrospray ionisation, laser desorption ionisation (LDI) and matrix-assisted laser desorption ionisation (MALDI). Work presented in this thesis uses LDI and MALDI which will be discussed in more detail in the next section.

EI, CI and FI are best suited for gas-phase ionisation as they are most compatible with compounds that are volatile and thermally stable [35–37]. EI generates electrons

from heating a filament, the electrons are then accelerated towards an anode, where collision with an analyte occurs (liquids and solids can be analysed, but need to be heated to increase their vapour pressure). EI is a harsh ionisation technique, resulting in extensive fragmentation of the analyte. This can result in complex spectra and can prevent the molecular ion from being recorded. This problem increases in severity as the mass of the analyte increases. In comparison, CI is a softer technique, which can allow molecular ion peaks to be determined. Ions are produced from collisions with the analyte and primary ions that are present in the source region. FI is an even softer ionisation technique, ions are generated by using a large electric field (8 - $12\,\mathrm{kVmm^{-1}}$) between the filament and a counter electrode [33]. Electrons are removed from the analyte by quantum tunnelling which generates positive ions. This technique allows the molecular ion to be observed.

A large number of compounds are thermally labile or do not have sufficient vapour pressure to ionise without fragmentation. These analytes can be extracted using liquid-phase ion sources or solid-state ion sources. In liquid-phase ion sources, the analyte is in solution. This solution is introduced by nebulisation of droplets into the source chamber where ions are produced at atmospheric pressure and are focused into the mass spectrometer through vacuum pumping stages. Examples of this ionisation include, electrospray, atmospheric pressure chemical ionisation and atmospheric pressure photoionisation sources [38–40]. In solid-state ion sources, the analytes are non-volatile deposits. Ions can be obtained by various preparation methods which normally involve the introduction of a matrix that can be either a solid or a viscous fluid. This deposit is then irradiated by energetic particles or photons that desorb ions near the surface of the deposit (although the specific mechanism is contentious, and will be discussed later). These ions can be extracted by an electric field and focused towards the analyser. Such methods of ionisation include, LDI, MALDI, SIMS (using large primary ions such as C_{60}^{+},) plasma desorption and field desorption sources [41–45].

Laser desorption ionisation is an efficient method for producing gaseous ions. Generally, laser pulses with an intensity of 10^6 - 10^{10} Wcm^2 are focused on a sample surface with dimensions 10^{-3}-10^{-4} cm^2, which is normally a solid. These laser pulses ablate material from the surface and create a microplasma of ions and neutral molecules which may react among themselves in the dense vapour phase near the sample surface. The laser pulse causes both the vaporisation and the ionisation of the sample, releasing neutral and charged species respectively. This technique is routinely used in the study of surfaces and in the analysis of the local composition of samples. It can allow some control over ionisation by adjusting the laser wavelength. However, in the most conventional infrared or UV laser desorption modes, the laser creates a thermal spike; it is not necessary to match a specific laser wavelength with the sample. The ability to obtain a useful mass spectrum depends on the specific physical proprieties of the analyte, e.g., photoabsorption, volatility, etc. Furthermore, the ions produced are normally fragments of the original molecule if its mass is above approximately 900 Da [46, 47]. In the scope of this thesis, analytes measured using LDI are laser dyes that have molecular weights below 750 Da.

Fragmentation of heavier ions has been addressed with the development of MALDI [48]. MALDI is a versatile ionisation technique that enables a spectrum of non-volatile molecules such as proteins, peptides, synthetic polymers and large inorganic compounds to be ionised into the gas phase without fragmentation. Molecular ions with a mass > 100 kDa are routinely measured [49, 50].

An analyte is co-crystallised within excess of a solid matrix material, typically with a ratio 1:1000 (analyte : matrix). The choice of matrix is crucial for MALDI experiments. Fig. 1.7 gives the structures of commonly used MALDI matrices. Most MALDI experiments are performed using UV lasers. Derivatives of benzoic acid, cinnamic acid, and related aromatic compounds are recognised as good MALDI matrices for proteins [41]. Juhasz *et al.*, introduced HABA as a matrix for peptides, proteins, and glycoproteins up to 250 kDa [52]. Efficient ionisation of oligonucleotides

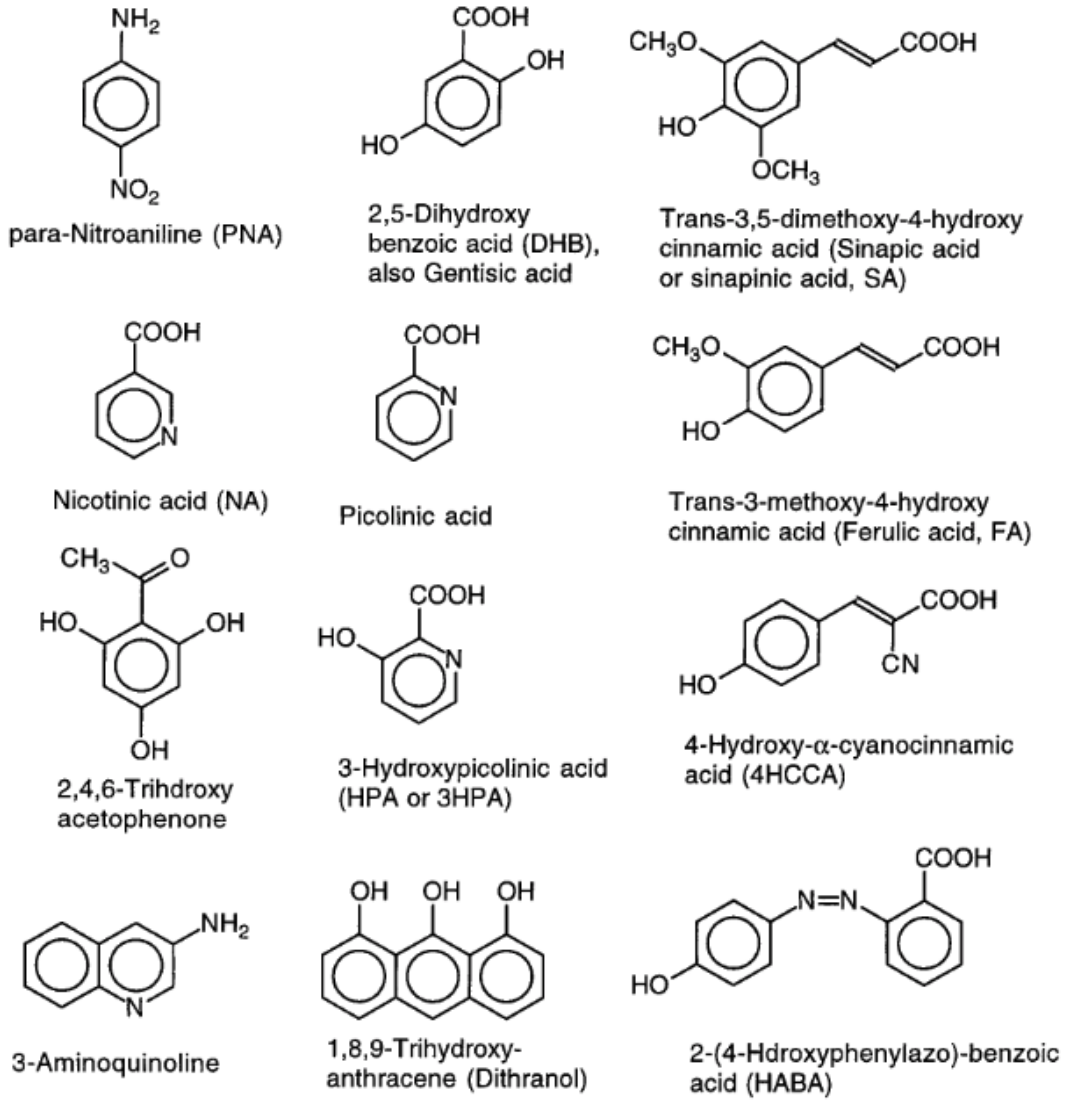


Figure 1.7: List of commonly used MALDI matrices - adapted from [51].

has been achieved with 3-HPA [53]. Glycerol was ionised successfully with an infrared laser [54]. Common UV matrices such as DHB and CHCA, are compatible with infrared lasers, but their ionisation efficiency is reduced [55]. Other matrices that are not carboxylic acids, such as the laser dye, coumarin 120, have been found useful in the analysis of monosulfated oligosaccharides [56].

Despite the applicability to chemical analysis, the MALDI mechanism that produces ions is still a contentious topic. Understanding the mechanism will provide a greater insight into factors that can increase the ion yield. There are many

proposed mechanisms that, under specific conditions, can explain the ionisation process such as: excited state proton transfer, polar fluid model and thermal proton transfer [57–62]. However, the two proposed mechanisms that are widely accepted are energy pooling and the cluster model, a schematic is shown in Fig. 1.8 [63].

The energy pooling mechanism produces ions by combining the energy from multiple matrix molecules that are in an excited state. This pooling mechanism would normally produce a limited number of charged analytes, but in a matrix the excited state can move. Mobile excitons (electron hole pairs) can be thought of as pseudo particles. The moving pseudo particle is facilitated by an efficient orbital overlap with a neighbouring matrix molecule. The time taken for an excited state to move to an adjacent matrix molecule is approximately 50 ps [33]. As a result, large areas can be covered in a few nanoseconds, which approximately corresponds to the width of a laser pulse. Furthermore, analytes are very efficient at trapping pooled excited states. Every time a pooled excited state matrix is adjacent to an analyte, electrons in the analyte are ionised, this process is shown in Fig. 1.8 (a) [64, 65].

The cluster model explains ionisation from MALDI experiments as the result of preformed ions, separated in the preparation solution, and then contained in clusters in the solid material. Some clusters contain a net excess of positive (or negative) charge. Upon laser ablation these cluster fragments evaporate and an analyte is liberated. In other clusters, charge can migrate from its initial location, e.g., on the matrix, to the more favourable location on analyte. Neutralisation by electrons or counter ions does take place, but there is incomplete stochastic recombination. This leaves lucky survivors which can then be detected by the mass spectrometer, as shown in Fig. 1.8 (b) [66, 67].

The laser fluence, laser beam diameter, laser pulse length, laser homogeneity and sample homogeneity all impact the quality of an obtained spectrum [68–70]. Therefore it is necessary that the laser / matrix combination is chosen appropriately, and sample surfaces are as even as possible. Chapter 2 details methods used in

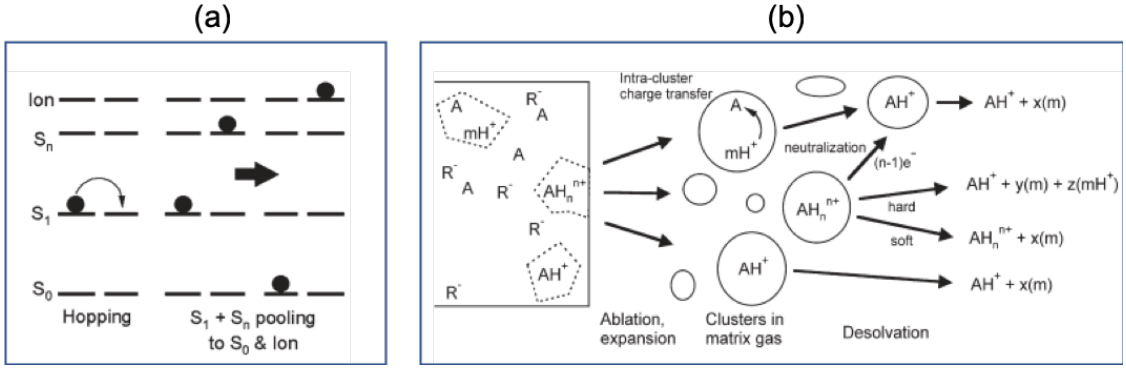


Figure 1.8: A schematic representation of the two widely accepted mechanisms that describe the MALDI ionisation mechanism. (a) Energy pooling mechanism between multiple excited state matrix molecules and an analyte molecule, the pooling reactions of matrix excited states are key steps in energy concentration and subsequent ionisation. (b) Cluster models of MALDI ionisation. m = matrix, A = analyte, R = generic counter ion. This figure is adapted from [41].

this thesis to improve sample homogeneity and reproducability. Development of liquids matrices can mitigate the problems associated with laser ablating solids. Liquid matrices such as 2,5-dihydroxybenzoic acid butylamine (DHBB) and α-cyano-4-hydroxycinnamic acid butylamine (CHCAB), can continuously refresh their surfaces, largely eliminating the hot spot phenomenon that is known for solid matrices [71, 72]. Furthermore, as a result of the homogeneous surfaces there can be even ionisation across the entire laser profile.

1.4 Ion imaging

A focused or defocused ionisation source can be combined with mass spectrometry to produce a chemically specific three dimensional ion image of a sample surface, where the third dimension is m/z [73]. There are two operating modes that are distinct and complementary, they are defined as: ion microprobe, which uses a focused ionisation source; and ion microscope, which uses a defocused ionisation source.

The first laser microprobe mass spectrometry (LMMS) studies were reported by Honig and Woolston [74]. A pulsed ruby laser with a 150 µm diameter beam, irradiated a sample surface at 45°. Microprobe experiments create images pixel-by-

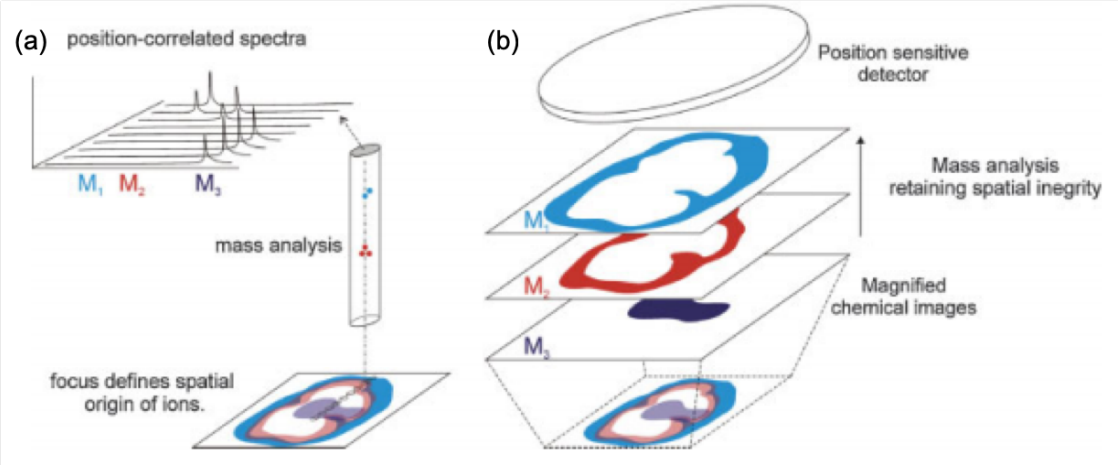


Figure 1.9: A cartoon illustrating two methods of ionisation for imaging mass spectrometry. (a) Ion microprobe - a laser or ion beam is rastered across a sample surface recording mass spectra at each pixel, the spatial resolution is dependent on diameter of the ablating laser (or ion beam). (b) Ion microscope imaging - a defocused laser or ion beam ablate the entire sample surface, the spatial plane is collected simultaneously by controlling electric fields above the surface. The spatial plane is stigmaticly projected onto a position sensitive detector. Figure adapted from [73].

pixel. Individual locations on the sample surface are called pixels. The size of the pixel is determined by the diameter of the ablating laser because this dictates the spatial resolution. The resulting mass spectra are stored, along with the spatial coordinates of the laser spot, defined by the focus of the ionisation beam. The sample stage or laser is then moved, a new region is analysed and another mass spectrum recorded. This process is repeated (a rastering process) until the entire sample area has been examined, and mass spectra associated with each location have been obtained. The molecular images are then reconstructed from the individual mass spectra. This process is illustrated in Fig. 1.9 (a). In a microprobe experiment, all spatial information from within the ionisation area is lost, therefore, origins of specific ions within a pixel cannot be determined. Hillenkamp improved the resolution by reducing the ablation area using a laser focused to 0.5 µm diameter [75]. LMMS was primarily used to scan a surface sample for metal ions [76]. Only metal ions were analysed, as an extended mass range was not available on these instruments; whilst analysis of biological samples was limited to small organic molecules [77].

MALDI provided a method to image compounds with a large molecular weight. To effectively use a MALDI ToF-MS instrument as an imaging device, software was developed to automate the scanning process, correctly assigning each mass spectra to its location from the sample surface [73, 78].

Ion microprobe MS can offer high resolution mass spectra and ion images because the mass and spatial resolution can be decoupled. The location of the ions are determined by the coordinates of the laser. The spatial resolution is determined by the size of the ablating laser: the smaller the laser profile, the higher the spatial resolving power. However, the image acquisition time is inversely correlated to the laser diameter. Using a laser with a smaller diameter reduces the ablation area and gives highly resolved ion images, but the number of rasters increase, resulting in a greater acquisition time. Table. 1.2 provides the spatial resolution and the acquisition time for a state-of-the-art microprobe instrument [79]. Furthermore, commercial mass spectrometry systems such as the Brucker rapiflex can routinely achieve a mass resolution of approximately 1,200 $m/\Delta m$.

As the spatial origin of the ions is known at each raster position, the distribution of kinetic energies can be compensated by using a number of trapping methods which do not preserve spatial information [15, 18]. Ion trapping techniques such as an orbitrap, hold ions in orbit around a central electrode by balancing their electrostatic attraction to the electrode with their inertia. The use of trapping can provide ion images with a mass resolution greater 30,000 $m/\Delta m$ [80]. However, high mass resolution is achieved by a large trapping time, which reduces through-put.

Ion microprobe MS can provide high resolution ion images, but the acquisition rate required can be detrimental for time-sensitive samples, such as food line production testing, and dynamic biopsy analysis during surgical procedures. To circumvent this throughput problem, microscope ion imaging can be used.

Microscope ion imaging is analogous to an optical (light) microscope: ions generated at the sample surface are projected onto a position-sensitive detector,

Pixel size (µm)	Pixel number (10^6)	Acquisition time (h)	Raster rate (p/s)
10	1	2.95	94
20	0.25	1.04	67
50	0.04	0.32	35

Table 1.2: A table showing the inverse correlation between spatial resolution and pixel size (laser diameter). The acquisition time is recorded in hours and the raster rate is number of pixels recorded per second. The mass spectrometer used was constructed by Bednarik *et al.* [79].

as shown in Fig. 1.9 (b).

Spatial characteristics of charged species were first elucidated in the initial mass spectrometer experiments [4]. In 1987, Chandler and Houston imaged ion velocities to give internal energy distributions from a photodissociation experiment. This velocity-map imaging (VMI) technique gave direct information on the dynamics and time scale of the photodissociation event [81]. Ten years later, Parker *et al.* further developed the ion optic and improved the energy resolution [82]. Recent work using VMI has provided an insight into complex molecular reaction dynamics by allowing their three dimensional velocity distributions to be recorded. This information, recorded from the VMI apparatus, can give a detailed mechanistic insight into a wide range of gas-phase physical and chemical processes [83]. VMI uses a two-dimensional position sensitive detector to record ion locations. The velocity focus, which is the point when all ions with the same velocity occupy the same position in space irrespective of starting position, must be positioned on the detector, shown as the red line in Fig. 1.10. Mapping of the velocity focus is achieved using a Wiley-McLaren mass spectrometer with appropriate voltage applied to the repeller and extractor to focus ions [82]. The voltages used in velocity-mapping mode can be re-tuned to focus a spatial plane, where ions from the same starting position are focused to the same position on the detector. The spatial mapping configuration is shown as the green line in Fig. 1.10.

Using an adapted VMI with spatial mapping voltage applied to the electrodes, the spatial information from the sample surface is obtained within the ionisation

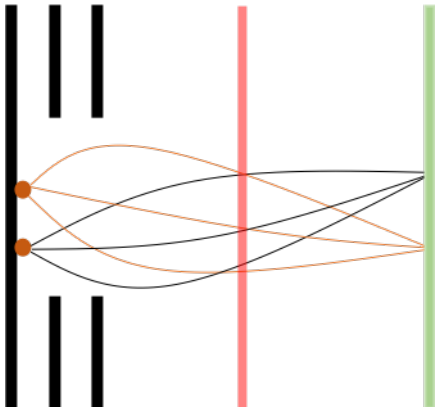


Figure 1.10: Ion trajectories for two ions with the same m/z in a Wiley-McLaren mass spectrometer. Red line indicates the velocity focus and green line indicates the spatial focus.

area, which makes the spatial resolution independent of the spot size of the ionising beam. The spatial resolution is determined experimentally from the following: the initial velocity spread, magnification of the microscope, the quality of the ion optics, and the resolution of the positive ion-sensitive detector. Decoupling the spatial resolution from the laser spot size allows a much larger area to be examined without having to move the sample (or the ionisation beam). Larger areas can in principle be rastered depending on the size of the desired ion image, but the number of positions is greatly reduced compared with microprobe imaging.

The first use of an ion microscope in mass spectrometry was a SIMS instrument, later known as CAMECA. This sector-based stigmatic ion optics obtained 1 µm spatial resolution using a Ar^+ primary ion beam with a 0.5 mm diameter. The achievable spatial resolution with this instrument depends on the primary ion source [84]. Moreover, this instrument could only be used to analyse ions less than 100 Da [85–87].

The CAMECA experiments bombard a sample surface over an extended area (approximately 1 mm) with a beam of primary particles with energies of a few keV. The impact of a primary ion triggers a cascade of atomic collisions that eject multiple atoms belonging to the uppermost layers. During this impact process, some of the particles become ionised. The secondary ions are accelerated by an extracting field

(emission lens). This secondary beam is guided to the entrance of a double focusing magnetic sector mass spectrometer. The ions then enter an electrostatic sector and a magnetic prism coupled with the electrostatic lens. Mass discrimination is provided by the magnetic prism. Ions used for producing the image (same m/z) are chosen by adjusting the electrostatic prism. These ions are directed towards the exit slit of the mass spectrometer in an ion beam that can be guided and enlarged by a projection lens. The ion image is then detected, an illustration of the instrument in shown in Fig. 1.11. A mass resolving power greater than $5000\,m/\Delta m$ can be achieved with this instrument [88–90]. Fig. 1.11 (b) shows ion images of metals and metal oxides taken with the CAMECA with lateral resolution of 1 - 3 µm.

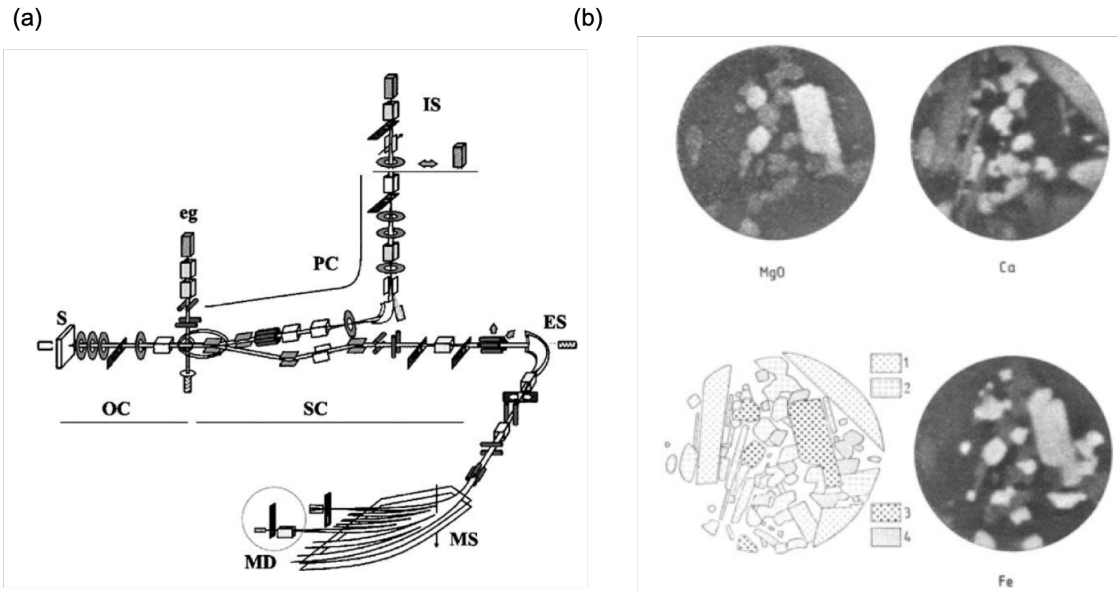


Figure 1.11: (a) Schematics of a CAMECA. IS - Primary ions source (cesium and duoplasmatron primary), S - sample, PC - primary column, OC - objective column, SC - secondary column, ES - electrostatic sector, MS- magnetic sector and MD- multi-detection unit. (b) Ion images of MgO^+, Ca^+ and Fe^+. 60 µm ablation diameter of a basalt. The figures are adapted from [84, 91].

The initial SIMS ion microscope provided high spatial and mass resolutions, but were limited to a small m/z as a result of ion separation occurring with magnetic and electrostatic sectors as increased field strengths are required to separate larger m/z species. To circumvent this problem and increase the magnitude of m/z that

could be analysed, the SIMS ion microscope was combined with a ToF-MS, allowing microscope images to be recorded for all secondary ions [92, 93]. ToF-SIMS is a highly surface-sensitive analysis technique due to its inherent capability to detect all masses simultaneously with high secondary ion transmission. Fig. 1.12 (a) shows the ToF-SIMS set up and a typical ion trajectory. When the primary ion pulse strikes the sample, charged secondary particles of selected polarity (typically positive) are electrostatically extracted using a similar method to the CAMECA, and a magnified image of the secondary ion emission profile is projected from the sample into the spectrometer. Following this, the ions undergo energy filtering using three identical hemispherical 90° electrostatic analysers (ESAs). An aperture is placed at the focal point between each ESA to remove ions with extreme trajectories.

A resistive anode encode (RAE) was used to detect the ions. The RAE had a field view of 300 µm and the image resolution was 1 - 5 µm over a 500 Da mass range. A mass resolution of approximately 15,000 $m/\Delta m$ was obtained for $C_2F_5^+$ secondary ions [93]. Despite the high resolutions, this instrument was limited by an inability to successfully ionise (without fragmentation) larger biomolecules.

Herren *et al.* further developed the ToF-MS SIMS technique. The new instrument was called the triple focusing time-of-flight mass spectrometer (TRIFT) [94]. This instrument was applicable with a MALDI ion source, which allows ion images of high mass molecules such as proteins and peptides, such as single shot mass-resolved images of the spatial distributions of intact peptide and protein ions, for example insulin which has a $m/z = 5537$, over an area of 200 μm diameter with a 4 μm spatial resolution.

The combination of microscope ion imaging with MALDI demonstrates the high throughput and versatile nature of the ToF-MS microscope ion imaging. However, when compared with conventional probe based imaging mass spectrometry the mass resolution is significantly worse.

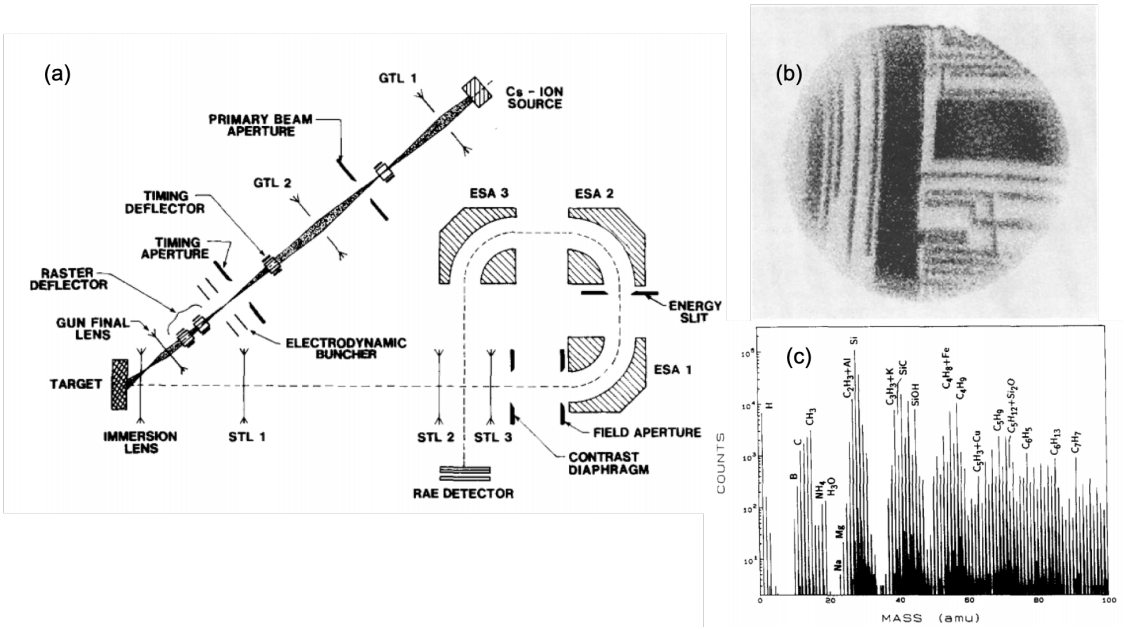


Figure 1.12: (a) ToF-MS SIMS instrument schematic. (b) Ion image of Al^+. (c) Mass spectrum demonstrating the range mass range of the ToF-MS SIMS instrument. Figure adapted from [92].

This problem was addressed by Hazama *et al.*, who developed the MULTUM-IMG as shown in Fig. 1.13 (a). MULTUM-IMG has four sector electrodes that produce a figure - eight ion trajectory. In each sector, toroidal electric fields are produced by a combination of cylindrical electric condensers and a pair of plane electrodes called Matsuda plates. The ions exit the figure of eight when one of the condensers is switched off. This instrument demonstrates a mass resolving power approximately equal to 130,000 $m/\Delta m$ for ions of the peptide angiotensin II (m/z 1046.5), after 500 cycles in the multi-turn ToF-MS. However, this mass resolution is limited to a mass range of approx 6 Da [95]. A spatial resolution of 4 - 5μm can be recorded when the instrument is operated in a linear configuration. This instrument cannot simultaneously achieve high spatial and mass resolution. This is evident from Fig. 1.13 (b), after 10 turns, which corresponds to a mass resolution of 2,000 $m/\Delta m$, the ion image suffers significant distortions.

The MULTUM demonstrates that high mass resolution for large organic molecules is possible with imaging mass spectrometry. The spatial and mass resolutions are

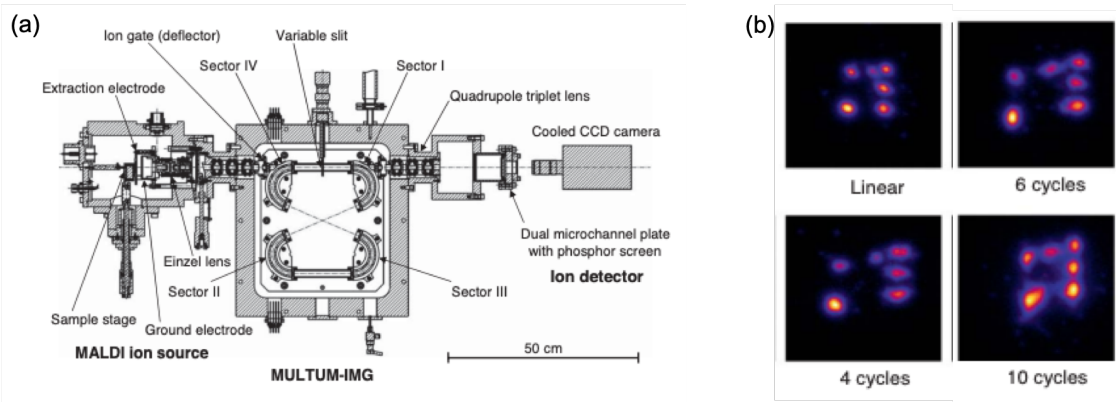


Figure 1.13: (a) Schematic of the MULTUM IMG mass spectrometer. (b) Ion image after an increased number of cycles through the ESA (in the linear configuration the ions do not enter the ESAs). Figure adapted from [96].

coupled within the MULTUM, it can be either in a linear mode resulting in 4 µm spatial resolution and 150 $m/\Delta m$, or achieve 130,000 $m/\Delta m$ mass resolution, over a 6 Da mass range.

To further develop microscope ion imaging Aoki *et al.*, incorporated a pulsed electrode into the ion optic arrangement with the objective of improving mass resolution whilst retaining spatial resolution [97]. Pulsed extraction differential acceleration (PEDA) is a method to reduce the distribution of ion velocities that result from ionisation. The pulse time is chosen so that ions with lower kinetic energies can have an increased potential, causing an increase in velocity. This technique is a variant of delayed extraction which is used in an ion microprobe MS [98]. Delayed extraction pulses the repeller plate, whereas pulsed extraction increases the voltage on the extractor plate to retain the spatial resolution. The pulse time and magnitude are chosen so that ions with different initial velocities have a reduced temporal focus plane at the detector. More detail on this method is given in Chapter 4. This technique improves the mass resolution for a crystal violet molecular ion (379 Da) to 1450 $m/\Delta m$ compared with 60 $m/\Delta m$ for a Wiley-McLaren extraction experimental setup. Moreover, a spatial resolution of 4 µm over a $\approx$ 50 Da mass window was achieved.

To address the limited mass window where spatial and mass resolution are simultaneously well resolved, Guo *et al.*, developed a PEDA variant that used two pulsed electrodes [26, 99]. Using a second pulsed electrode focuses an additional mass range. The two focused masses can be chosen so that the effective mass range (where $m/\Delta m > 1500$) is increased to 165 Da. The spatial resolution for ions within the mass range of interest was approximately 50 μm over a field of view of 5 mm^2.

1.5 Ion detection

There are a number of different methods for the ion detection and they all require amplification of the signal before recording the output [100]. Mass spectrometers can use many different types of ion detectors such as Faraday cups, secondary electron multipliers (SEM), and microchannel plates (MCPs) [101, 102]. The choice of the detector depends on the type of mass spectrometer, the required detection sensitivity and the required detection speed.

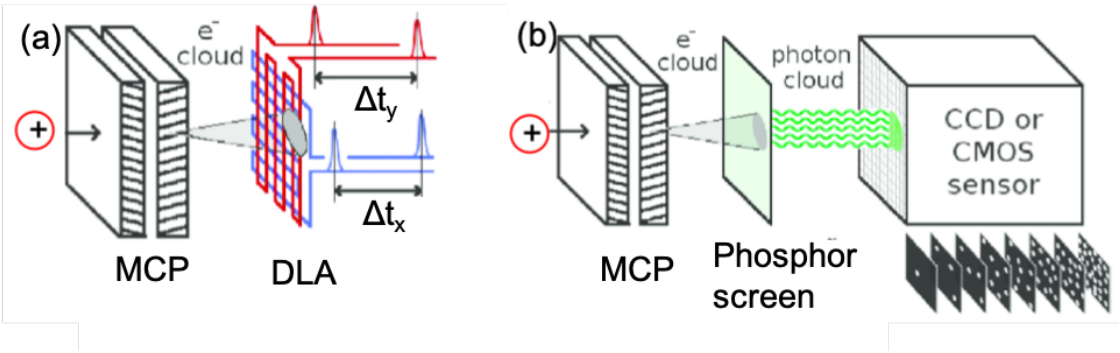


Figure 1.14: Cartoon showing different ion detection technologies used in ion imaging mass spectrometry. (a) Delay line anode (DLA) is attached to the MCP stack, the spatial position of incident electrons, generated from collision between the ions and the MCPs, is determined from the time difference in the electrical signal. In a two-dimensional array, the x-coordinate is determined Δt_x (red) and the y-coordinate is determined Δt_y (blue). (b) Pixel sensor either CCD or CMOS. Photons are generated from electronic excitation and subsequent emission of a phosphor screen. Photons are then recorded by individual pixels within the camera's sensor. Images, corresponding to different experimental cycles or different times within a single experiment are shown below the camera. See the text for more details on each camera type.

When the charged pulse from the MCP is collected by the anode, the charge

divides proportionally between the four corners (or edges) of the anode for two dimensional imaging. Furthermore, the distributed capacity of the anode causes the the rise time of an event to be dependent on the location, shown in Fig. 1.14 (a). A measurement of the fraction of charge or the difference in rise times of the signals arriving at each electrode allows determination of the position at which the photons impact on the detector [103, 104]. Using delay line anodes provides well resolved ion images, but the dead time (the time for the sensor to come back online after it has recorded an event) is relatively long. Modern delay line anodes have dead times larger than 60 ns [102]. Furthermore, delay line detectors reduce applicability as they are only suitable for lower count rates. Typical MALDI ToF-MS experiments produce an order of magnitude more ion events, count rates can be as high as 150,000 per laser shot [105]. This has been partially addressed with a hexanode DLD which can facilitate a higher count rate, but has a dead time of 10 ns. In addition, ions arriving within 1 mm^2 proximity on the detector cannot be resolved [106]. This can be a significant problem for applications requiring high spatial resolution.

Applications of microscope ion imaging, specifically with complicated tissue samples, require a detection method that can record many ions events in each laser shot. To achieve this, MCP plates can be combined with a phosphor screen and a camera, shown in Fig. 1.14 (b) [107]. In this configuration the electrons ejected from the MCPs are accelerated to the phosphor screen. A collision between the electrons and the screen results in the emission of photons. The location of the photon emission is dependent on the ion position. The photon emission is recorded with a camera. Phosphor screens are typically made from organic dyes, different phosphors will scintillate at different wavelengths, and with different response times, typically the more photons that the phosphor emits the slower the response [108]. The lifetime of the exalite screen used in this work is approximately 4 ns, which means that any ion event separated by less than this cannot be distinguished by within the ToF spectrum. Similar to a restive anode encoder (RAE), the dead time

of the phosphor screen can limit the resolving power of imaging mass spectrometers, this will be discussed further in Chapter 4 and 5.

Using a phosphor screen with a reduced emission lifetime would be one method to improve the applicability of microscope ion imaging. Another is to address the inability of charged coupled device (CCD) cameras to record timing information in addition to spatial information [109, 110].

The CCD cameras are pixel arrays, with one column of pixels constituting the output register. When recording photon events, light incidents on a pixel generate electron–hole pairs within the silicon, and the charge is stored by a capacitor within the pixel, as shown in Fig. 1.15 (a). The charge is grouped within the pixel and then transferred between pixels in the array by switching the potentials on a series of gating electrodes positioned at the pixel surface, creating a bias. The image is a two-dimensional array of charge that is detected within each pixel during an experimental cycle. The charge in each pixel, at the end of each experimental cycle, is transferred along the rows of pixels so the entire image is stepped one pixel to the right, placing the charge from the final column of pixels into the output register, see Fig. 1.15 (b). The charge is then transferred pixel-by-pixel along the output register. An amplification stage converts the charge to a voltage which is then read out by external electronics. The process is repeated for each column of pixels until the entire image has been read out from the camera, as shown in Fig. 1.15 (c).

A CCD camera records one image per experiment, this is achieved by gating either the MCPs, or the exposure time of the camera itself. To gate the MCPs, a voltage is applied across one of the plates which reduces the gain, this can be adjusted as a function of time. With a reduced gain, no image is seen, but when the gain is reapplied, the image appears. Therefore to image each constituent ion within a sample, multiple images must be acquired [111]. This becomes a significant problem if the sample is time-dependent or has a low abundance of ions of interest.

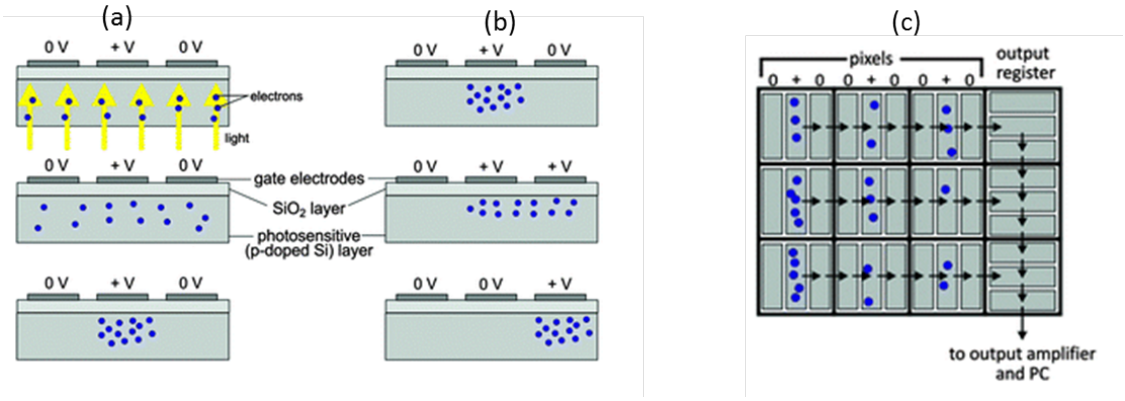


Figure 1.15: Charge transfer process in a CCD sensor. (a) Illustrates the charge accumulation within a pixel during the experimental cycle. (b) Charge transfer across a pixel at the end of an experimental cycle. (c) Pixel array showing charge moving through each pixel within a row towards the output register.

The advent of complementary metal-oxide sensors (CMOS) or active pixel sensors, specifically the Pixel Imaging Mass Spectrometry camera (PImMS) and Timepix sensors, provide an alternative [112, 113]. CMOS sensors, like CCD cameras convert photons to charge, providing spatial information after a predetermined threshold is exceeded (this prevents background radiation from adversely affecting the image). A schematic of the CMOS architecture is shown in Fig. 1.16. However, unlike CCD cameras, CMOS sensors have most of their required circuitry and components integrated into the sensor. Within each pixel there are numerous transistors that are incorporated into CMOS circuitry allowing many individual logic functions within each pixel[1]. Each pixel can effectively act as its own sensor, time stamping events within an experimental cycle. The PImMS camera has four memory registers per pixel, which allows up to four events to be stored in each experimental cycle. At the end of an experimental cycle each pixel reads out the stored information in the form of a three column matrix (x, y, t) where x, y are the pixel location, and t is the arrival time of the event [114]. This is contrast to the readout used by the Timepix 3 sensor, where the pixel information is relative to the external trigger which keeps pixels sensitive at all times [115]. The ability to record

[1]A logic gate is a physical device implementing a Boolean function. It performs a logical operation on one or more binary inputs and produces a single binary output.

and time stamp multiple events in each pixel, within one experimental cycle allows multi-mass imaging of a ToF-MS spectrum as all peaks are recorded simultaneously. This removes the requirement to record multiple ion images for a particular sample as all images can be recorded at once, increasing the instrument throughput. CMOS technology has been used in numerous imaging experiments including, velocity-map imaging, TRIFT ion microscope, Linear ToF-MS ion microscope and neutron detection [116–119]. Specific CMOS sensors technology and their application to imaging mass spectrometry will be discussed in more detail in Chapter 7.

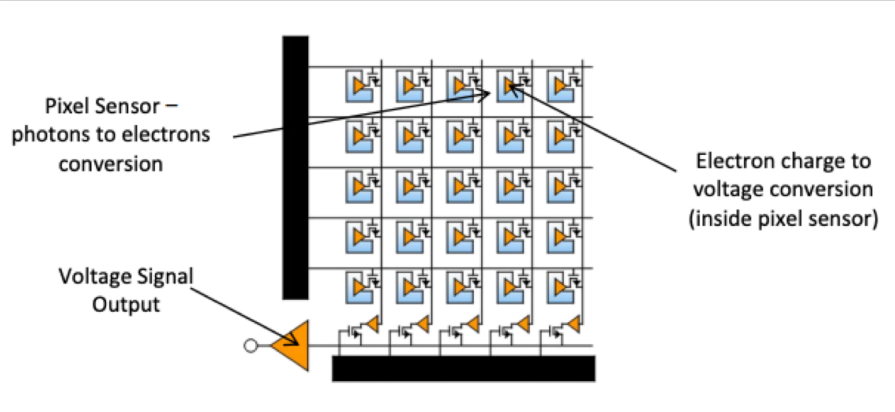


Figure 1.16: Pixel architecture of a CMOS sensor. Each pixel comprises its own transistors and photon to electron conversion device.

The combination of CMOS sensors and high resolution microscope ion imaging is a method to simultaneously measure the spatial distribution of every ion in a mass spectra, within one experimental cycle, leveraging the high throughput capacity of the instrument.

1.6 Thesis overview

The work presented in the following sections of this thesis address the performance of microscope ion imaging. The objective of this research is the simultaneous improvement of instrument resolutions over an increased mass range.

The next chapter presents an overview of the experimental methodology and the instrumentation used to obtain mass-resolved ion images. This is followed by a short

chapter explaining the simulation software used to develop the instrumentation. Experimental data that characterises a reflectron augmented with a microscope ion imaging ToF-MS is then presented. In this chapter, a stigmatic image is retained through the reflectron stack. Combining the reflectron with the linear ToF-MS offers significant increases in mass resolution. Further experiments are presented using the reflectron-ToF-MS ion microscope incorporating a time-dependent PEDA variant, electrodynamic PEDA. Electrodynamic PEDA increases the voltage on the extraction optic as a function of time. This simultaneously reduces the temporal spread of ions in a 500 Da mass range. This is followed by the design of a high spatial resolution ion microscope. This chapter uses optimisation routines, that model the multidimensional topography of a microscope linear ToF-MS, to determine a combination of parameter values to achieve optimal spatial resolution. Finally, a fast imaging CMOS sensor is used in combination with the reflectron ion microscope to demonstrate multi-mass ion imaging with potentially less than 2 ns timing precision.

2
Experimental methods

This chapter details the apparatus used for experiments presented throughout this thesis. First, an ion microscope combined with a reflectron will be detailed. This is followed by sample preparation methods, the laser system, clock synchronisation, and data acquisitions systems.

2.1 Reflectron ToF mass spectrometer

An imaging mass spectrometer developed from a VMI experiment, constructed by the Brouard group provides the foundation for the ion microscope presented in the thesis [120]. This instrument was augmented with a reflectron in Chapter 4, upgraded with pulsed optics in Chapter 5, and was used in the design of the high spatial resolution ion optics discussed in Chapter 6.

The reflectron MSI is illustrated in Fig. 2.1. The instrument achieves a high vacuum with three turbo-molecular pumps (Leybold TMP 600, SL300 and SL80) which are backed by two rotary pumps (Leybold TRIVAC B). The instrument pressure was monitored by an Active Inverted Magnetron gauge (Edwards AIM-X-DN40CF) and held at 1×10^{-7} mbar. The reflectron MSI consists of four regions: a sample loading chamber, an ion source chamber, a reflectron, and a fight tube.

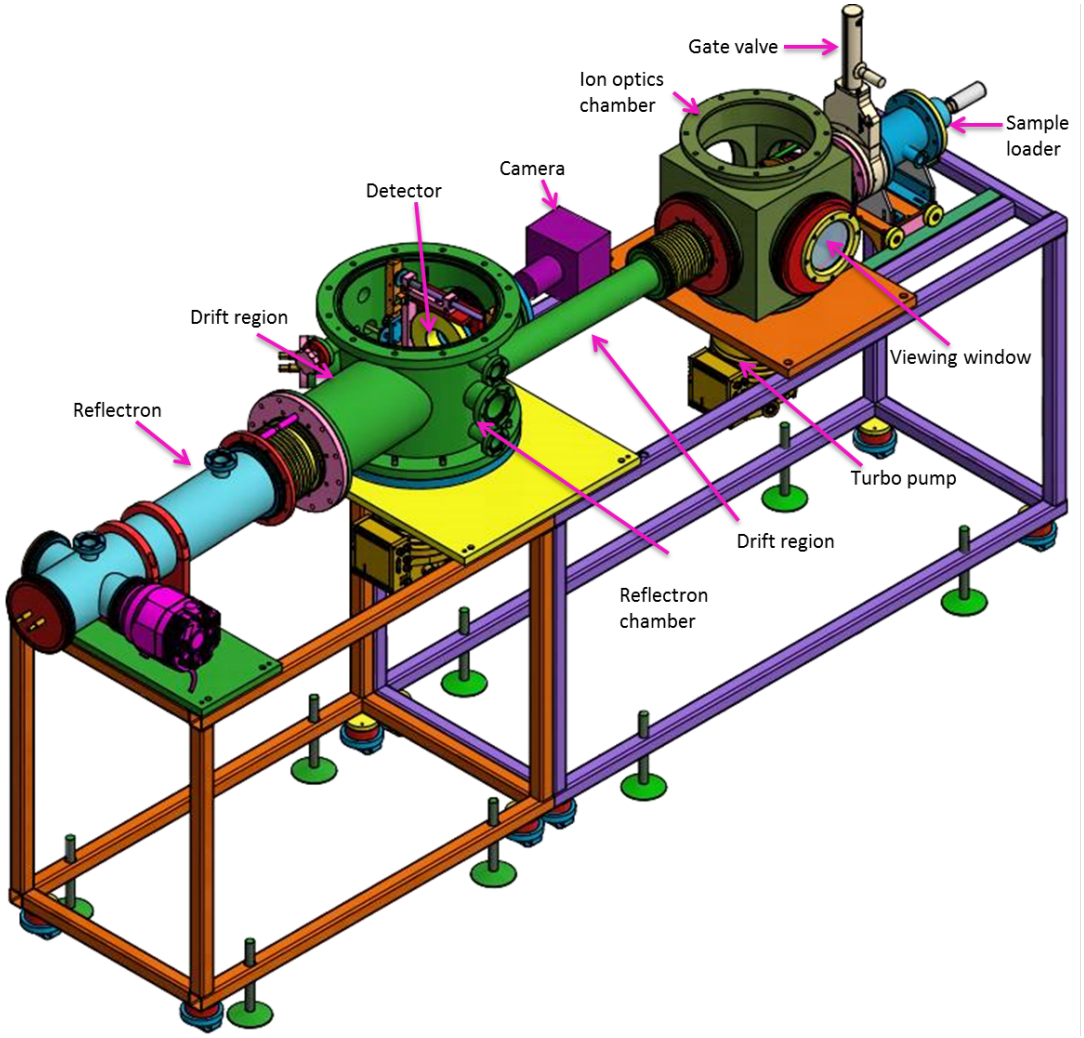
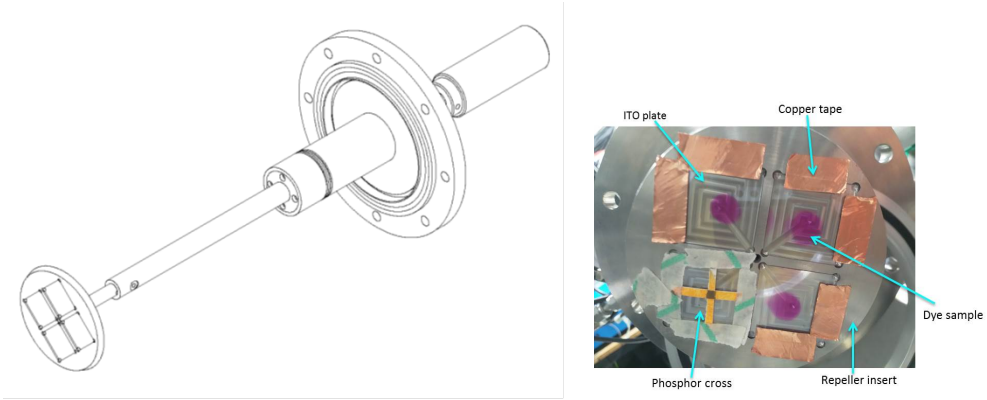


Figure 2.1: Spatial imaging reflectron operating as a ion microscope.

The sample loading chamber is attached to a retractable trolley which allows samples to be replaced easily. A rotary pump reduces the pressure in the sample chamber to 10^{-3} mbar quickly and safely. The sample loader is connected to the ion source chamber through a gate valve. This allows the vacuum within the instrument to be retained when samples are replaced. The samples (deposited on ITO plates) are loaded into four 25 mm × 25 mm × 1 mm depressions in the repeller and secured with copper tape, shown in Fig. 2.2. The copper removes excess surface charge from the ionisation process. Surface charge causes aberrations in the image, and broadening mass peaks [26].

Samples are transferred into the ion source chamber, where they are ionised



(a) (b)

Figure 2.2: (a) Sample loading chamber. (b) Samples embedded into the sample plate. Phosphor cross is used for laser alignment.

with a laser beam and spatially mapped by the ion optics onto a detector assembly at the end of the fight tube. Then ion signals are recorded by a photo multiplier and a camera before being stored in a computer.

2.1.1 Ion optics

The ion optics are located in the ion source chamber and are mounted on four stainless steel rods insulated by ceramic spacers. The ion optics comprise: the repeller (into which the samples are placed), an extractor and a three plate einzel lens. The repeller is separated from the extractor plate by 14.5 mm. The extractor plate has a 19.5 mm aperture in the centre of the plate to allow the ablated ions to pass through. The final component in the ion optic setup is the einzel lens, and is separated from the extractor by 39.5 mm. The einzel lens comprises three plates: a grounded plate, a charged plate and another grounded plate. The first plate in the einzel lens has a 2 mm aperture, the second and third plate have 5 mm apertures. The cubic ion source chamber which encompasses the ion optics has side lengths of 360 mm. The ion optic dimensions are shown in Fig. 2.3 (a).

The ion optic chamber is connected to a cylindrical field free flight tube with a diameter of 150 mm and length of 1436 mm. Two sets of parallel plates 30 mm in length are used to deflect ions. They are located 721 mm from the einzel lens.

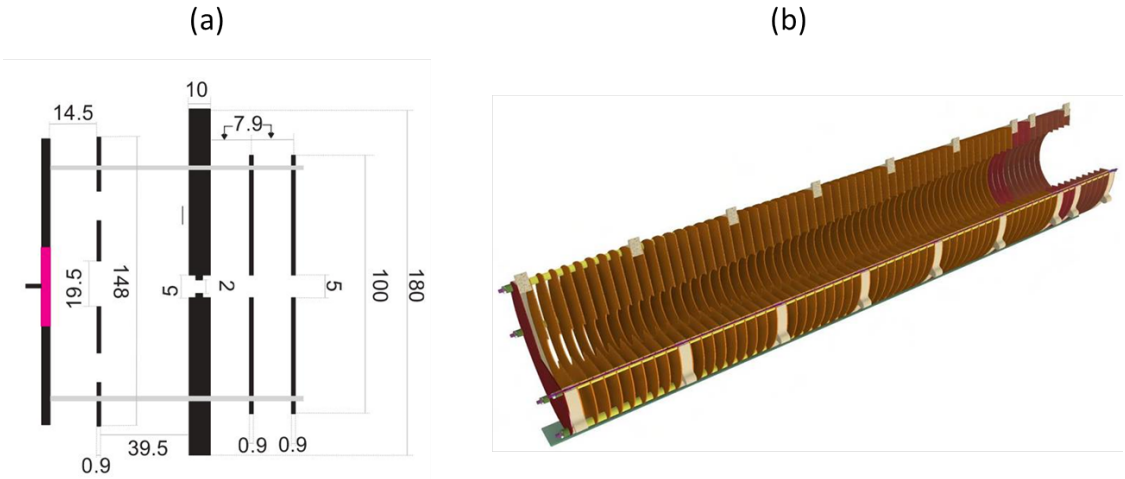


Figure 2.3: (a) Ion optics used in microscope ion imaging mass spectrometer. All dimensions are in millimetres. (b) CAD drawing of the reflectron electrode stack which comprises 63 individual electrodes separated by ceramic spacers. The first 8 (red) are held at 0 V. The remaining 57 electrodes (brown) have decreasing irides to reduce the penetration of unwanted electric fields. The voltage is applied as a linear gradient from the last plate within the reflectron stack.

These plates are used to steer the ion beam into the reflectron. Ions then travel into the reflectron. The first eight plates in the reflectron assembly are grounded, and the remaining electrodes are connected to a printed circuit board containing a resistor chain that creates a linearly decreasing potential gradient. The electrodes in the reflectron have linearly decreasing irides, starting at 90 mm and finishing as a solid plate where the reflectron potential is applied, as shown in Fig. 2.3 (b).

2.2 Sample preparation

Homogeneous matrix deposition in MALDI imaging mass spectrometry is required for reproducible analysis, along with analyte detection and identification. Efficient and accurate sample preparation has a number of requirements including, co-crystallisation of matrix and analyte, crystals with less than 10 µm diameter, and retention of analyte localisation when matrix is applied [121].

Generally, a compromise is made between homogeneity and speed; quicker methods of matrix application result in poor samples. An example of a fast

method for matrix application is to use a pipette to drop pre-made matrix onto the sample. This technique results in irregular crystallisation over the sample surface, a consequence of the uneven deployment of the matrix. This technique has limited application, but is useful for instrument calibration and when high spatial resolutions are not required.

The following sub-sections detail techniques that have been used for data presented in this thesis, the techniques have a reasonable application time, but differ in crystal homogeneity.

2.2.1 Electrosprayer

An electrosprayer is comparable to an oscillation capillary nebulizer [122]. However, it is more cost effective and has been used to increases the evenness of sample deposition, compared with the pipetting technique [102, 118]. The electrosprayer forces analyte or matrix solution through a positively charged needle. The solution forms a Taylor cone and jet, as shown in Fig. 2.4.

The needle is mounted above the sample on a grounded plate, this plate has three dimensional adjustment, allowing the needle to be positioned over the sample at the desired height. The sample plate is grounded to increase the uniformity of the deposition. A grid pattern is formed from the deposition of an analyte (typically a laser dye) through the needle to form a periodic structure. Different pitch size grid patterns ($63\,\mu m - 101\,\mu m$) were used to categorise the magnifications and spatial resolution of the reflectron (see Chapter 4). The sample is sprayed onto the conductive face of an indium tin oxide (ITO) coated plate. Plate conductivity is essential to prevent surface charging in the mass spectrometer [123]. Surface charging has a deleterious effect on spatial and temporal resolution due to the change in velocity of ions leaving the surface of the sample plate. This is caused by electrostatic repulsion of the charged ions. The electrosprayer is able to deposit very even layers of dye molecules onto the ITO plate.

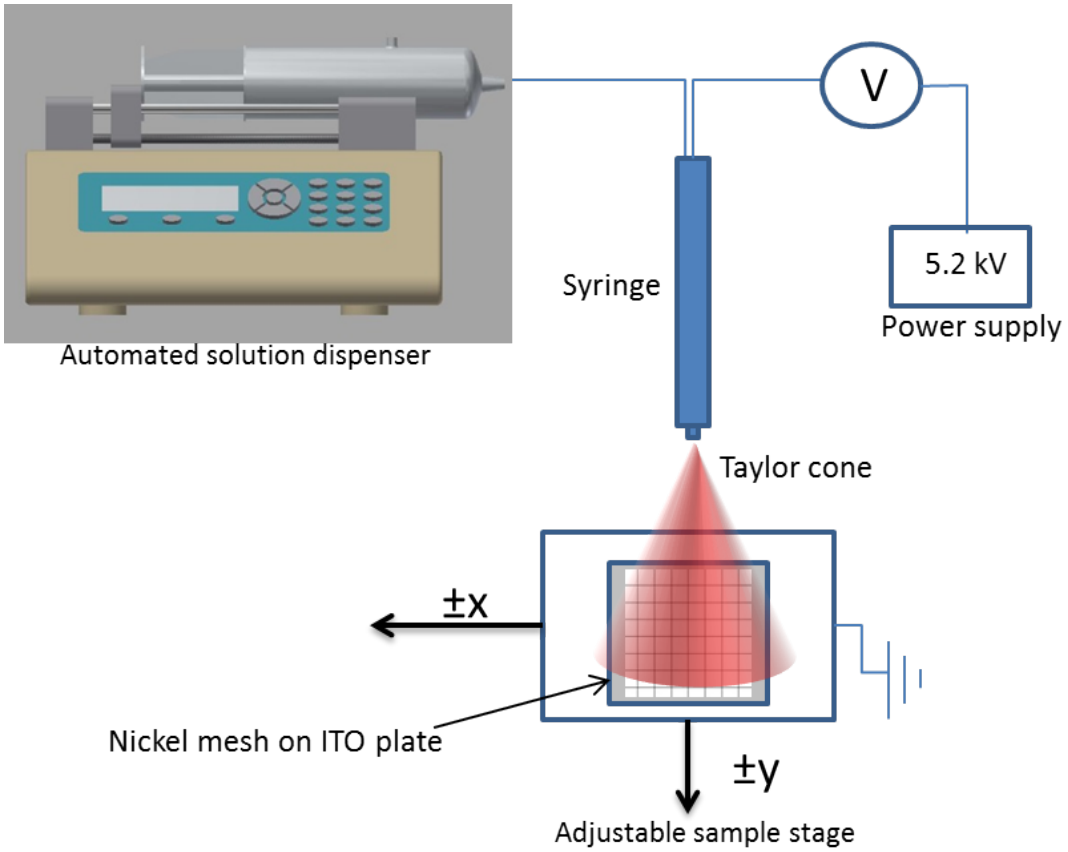


Figure 2.4: Schematic of a home-built electrosprayer used to deposit dye sample onto an ITO plate through a nickel mesh.

The electrosprayer is less useful at creating a homogeneous layer of a matrix solution compared to a dye solution. First, analyte matrix crystals are formed with varying sizes [102]. Second, the electrosprayer causes the ions from the matrix solution to be spluttered onto the ITO plate as the Taylor cone is prone to instability (typically as a result of vibrations from other pieces of equipment).

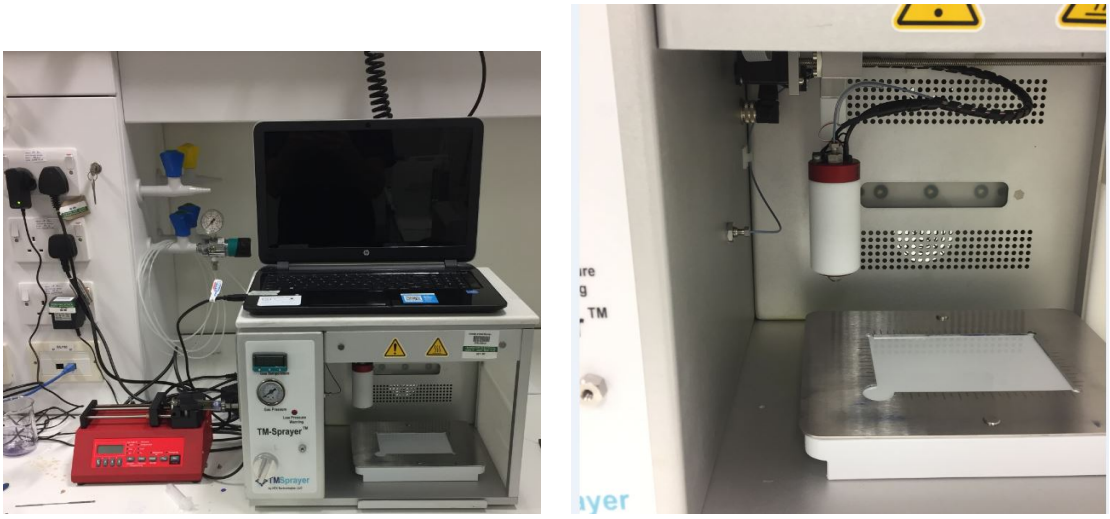
The electrosprayer can also reduce the ability to resolve features on a surface. If the flow rate through the needle is too high, solvent reaches the ITO surface and causes the matrix and analyte to be transported to positions that do not reflect their true origin. Local variations in matrix concentration can also affect the ionisation homogeneity. If a particular region has a significantly reduced matrix volume ionisation from this region may be reduced [124, 125].

2.2.2 TM sprayer

To maximise homogeneity and reproducibility, an automated HTX TM-sprayer was purchased. The TM sprayer shown in Fig. 2.5 (a), is controlled by a laptop and interfaced through a USB. Software provides control over a number of features on the sprayer including: the temperature of the nozzle, the nozzle velocity, spray pattern (horizontal, vertical or criss-crossed) and the nozzle cycle repetition number. These parameters allow exact matrix dispensation replication which facilitates sample comparison.

The controls embedded within the software allow individual customisation and replication of sample preparation procedures. For example, different samples require different concentrations of matrix. The automated sprayer allows a specific quantity of the matrix to be dispensed. Specific quantification has two benefits. First, it allows different volumes of matrix to be tested, therefore determining the optimal volume. Second, once the optimal volume is identified for each sample, the numerical quantity is easily repeated using the software. The matrix solution flow rate is controlled by a (NE-300 Infusion) syringe pump, capable of a variable flow rate (0.1 µL - 9.9 mL). In addition to the syringe pump injecting the matrix, nitrogen gas is discharged through the nozzle and regulated between $2\,\text{bar} - 20\,\text{bar}$. Nitrogen gas prevents crystallisation within the capillaries of the TM sprayer. The nickel mesh is secured onto the ITO plate by pipetting methanol onto the nickel grid. This prevents the pressurised nitrogen gas from dislodging the mesh before the matrix solution is applied.

The TM sprayer produces a homogeneous layer of matrix solution using a heated nozzle, as shown in Fig. 2.5 (b). The nozzle is heated to a temperature predetermined by the software. The matrix solution is vaporised at the nozzle (if the temperature sufficiently high), and the resulting atomised solution is then directed at the sample plate. Matrix ion velocity is controlled by the flow rate of nitrogen gas through the nozzle, the drying time is defined by the time between



(a) (b)

Figure 2.5: (a) TM sprayer connected to an automated pump and interfaced with a usb connection to a laptop. (b) Sample discharge nebuliser.

deposition cycles, and the dispensing rate of the pump. The nozzle moves in a preset two-dimensional pattern (x, y). This is customised by the user so that the whole sample is sprayed. Once the samples have been coated with the matrix solution, copper tape is used to attach electrically conductive wire to the ITO plate and to secure the ITO plate into the recesses on the repeller plate.

The TM sprayer is capable of producing approximately 1 µm crystal assuming that the correct concentration of matrix and pressure of the gas line are used. However, due to the versatility of the TM sprayer, crystal size can be varied. Variation in crystal size is required for tissue analysis, as large crystals inhibit the amount of analyte incorporated into the matrix layer, and therefore reduce the sensitivity and ion yield.

2.3 Laser

The frequency tripled output of a neodymium-doped yttrium aluminium garnet laser (Nd:YAG, continuum Powerlite 8010) was used to produce ions at 355 nm. A schematic of the laser is shown in Fig. 2.6. Solid state lasers commonly use Nd:YAG media for photon generation. A small fraction of yttrium ions ($\approx 1\%$) in the Yttrium

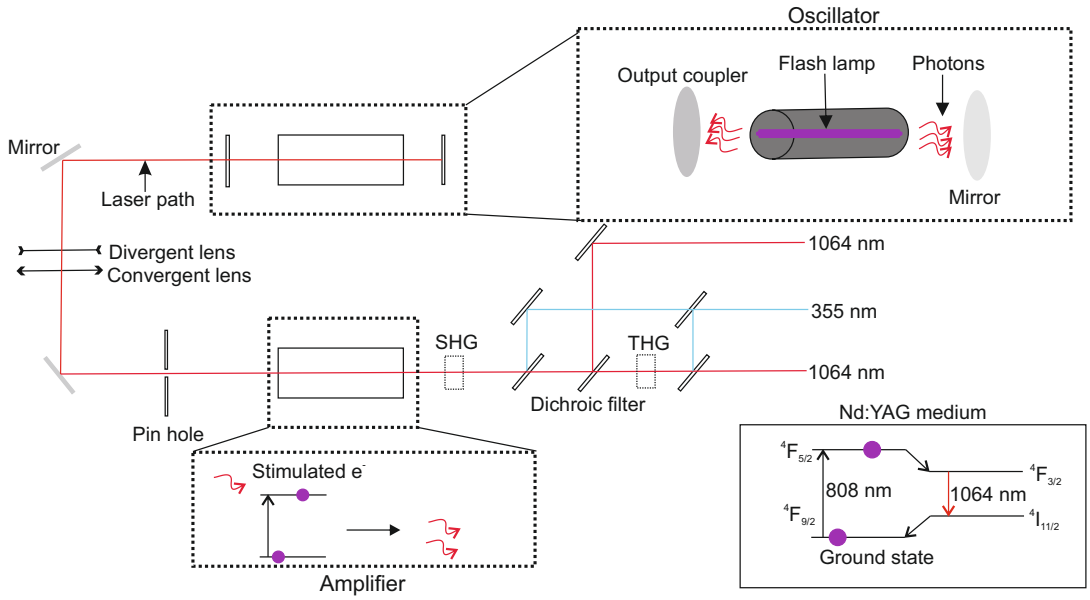


Figure 2.6: Schematic of Nd:YAG continuum powerlite 8000 precision II. The red trace indicates the laser path. At the oscillator, a flash lamp inside the Nd:YAG medium excites electrons with 808 nm light. This excitation results in the release for 1064 nm photon (shown in the Nd:YAG medium inset). The lasers travels through the lens to refocus the beam. An amplifier increases the number of 1064 nm photons by creating a stimulated electron in the medium of the amplifier, which results in increased emission of photons. Photons then travel through a second harmonic generating crystal, doubling the frequency of light and producing 532 nm photons. A dichroic filter is placed in the beam path to filter out 532 nm light. The remaining 1064 nm light enters a frequency tripling the third harmonic crystal, producing 355 nm light. These photons are filtered and are used in the experiments presented in this thesis.

Aluminium Garnet (YAG) crystal are replaced with neodynimum (Nd) ions. In the oscillator, a flash lamp located in the Nd:YAG medium, induces a population inversion with 808 nm light. Electron relaxation emits coherent 1064 nm light.

Q-switching is employed to obtain 3 - 7 ns laser pulses of 1064 nm light, which have much higher peak powers compared to continuous wave lasers. Producing Q-switched pulses involves three steps. The gain medium is pumped and the light is allowed to leave providing a population inversion without any feedback (i.e stimulated emission is suppressed), this corresponds to a low Q factor, where the Q-factor is a measure of light transmission (low Q-factor corresponds to a high transmission). This resets after each pulse. Then, the optical cavity switches to a high Q factor (losses are sharply reduced), the time that the optical cavity has

a high Q-factor dictates the length of the laser pulse. The output pulse is then amplified by a second gain medium resulting in stimulated emission (the amplifier in Fig. 2.6). The laser amplifies the light in the gain medium until its stored energy depletes. The power of the laser is controlled by changing the delay time between the Q-switch in the oscillator and the two flash lamps in the amplifier, using a Quantum Composer 9520 pulse generator. The optimal laser fluence (above the sample ionisation threshold) is sample dependent. Optimal laser power is defined as the minimum fluence such that sufficient ions are produced to acquire an image and a mass spectra. Excess ions result in space charge effects that distort the ion trajectories, reducing the mass and spatial resolutions.

1064 nm light is frequency tripled (355 nm) using Potassium Hydrogen Phosphate to improve ion yield. The experimental repetition rate is limited by the laser, which operates at 10 Hz. The laser flux ablating the sample is significantly attenuated compared to the flux exiting the laser. The power leaving the internal components of the laser is 3 W. It is then reduced by a 20:80 beam splitter, prisms, and mirrors as it propagates through the external optics onto the sample surface. The pulse energy is between 10 - 1000 mJ.

The laser pulse enters the ion optics through a borosilicate window with lambda 5 flatness. This prevents excess inhomogeneity in the laser profile. To irradiate the sample, the laser beam travels through a hole in the extractor plate. The diameter of this hole is maximised to allow the position of the laser beam on the sample surface to be easier manoeuvred. This has two benefits: first, the laser alignment is more practical and second, a larger portion of the sample can be imaged. The laser beam enters the ion optic chamber at a 20 degree angle to the sample surface which causes horizontal divergence of the beam profile. This is discussed further in Chapter 4.

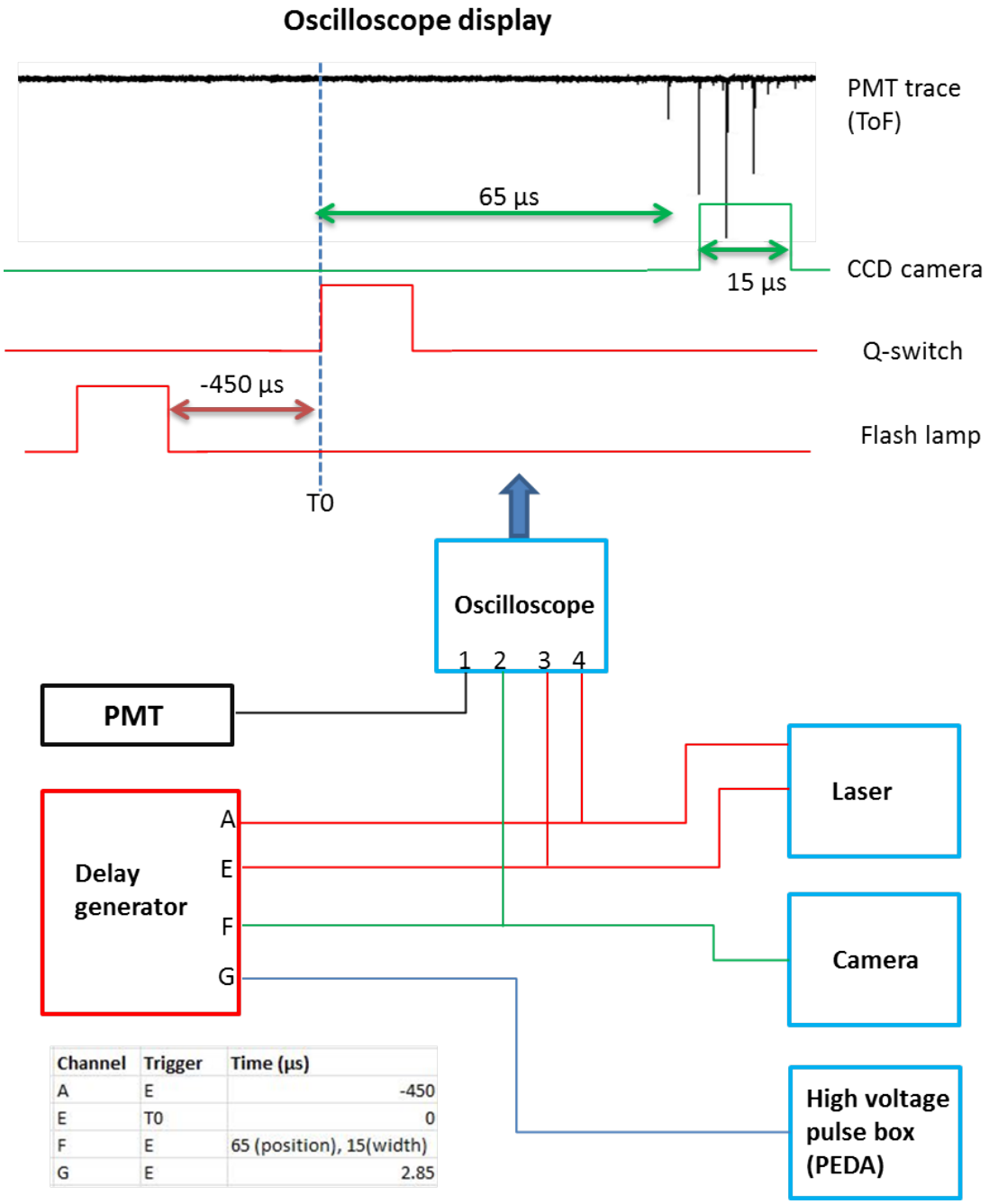


Figure 2.7: Cartoon showing the triggering setup of the reflectron MSI. TTL pulses are used to fire the laser, pulse the electronics and the camera.

2.4 Oscilloscope and triggering

The experimental cycle is 50 µs with a 10 Hz repetition rate. An exact arrival time is crucial for determining mass resolution: it is imperative to have accurate triggering times for the experiment. A pulse generator (Quantum Composer 9520) with 250 ps

time resolution was used to ensure that pulses generated to initiate experimental cycles were precise. Transistor-transistor logic (TTL) 5 V pulses are used in this experimental setup with the exception of the CCD camera and PImMS which require a 3.4 V and 3 V pulse respectively. Typical pulse timings are shown in Fig. 2.7.

The experiment begins with a TTL pulse to turn on the Nd:YAG flash lamp. A second pulse is then sent to the Q-switch. This occurs at 450 µs after the initial pulse. Once this pulse is received, the laser ionises the sample. This is defined as T_0. After an additional 2.85 µs a third pulse is sent to the high voltage switching box. This pulse instructs the pulse box to increase the voltage on the extractor plate. After 65 µs the Q-switch is triggered, a fourth signal from the delay box is sent. This signal provides instructions to the CCD camera to begin recording an image. The camera records for 15 µs. The camera is turned on at a time where the camera gate (shown in green in Fig. 2.7) overlaps with peaks from the PMT spectrum (shown in black). The live time of the camera which is determined by the width of the TTL signal, is chosen so the relevant peak(s) in the spectra are recorded. A trace of each TTL signal is monitored using a LeCroy DDA-260 oscilloscope which has 65 GHz sampling rate.

2.5 Detector assembly

The detector assembly used for experiments in this thesis comprises a dual MCP stack (Baspik) and a home-built fast scintillator screen. The MCPs have a 32.75 mm diameter, 0.4 mm thickness and a 12° chevron bias angle. The scintillator screen was made by sublimating and depositing exalite 404 onto an ITO plate. This process provides even thickness and ensures homogeneous fluorescence across the screen. Previous experiments have used a P47 phosphor screen. This was substituted for a home-built exalite 404 scintillator screen as it has a shorter decay time ($\approx 3.7\,\text{ns} \pm 0.2\,\text{ns}$) in comparison to a P47 (70 ns) as well as a greater fluorescence and increased longevity [108, 126].

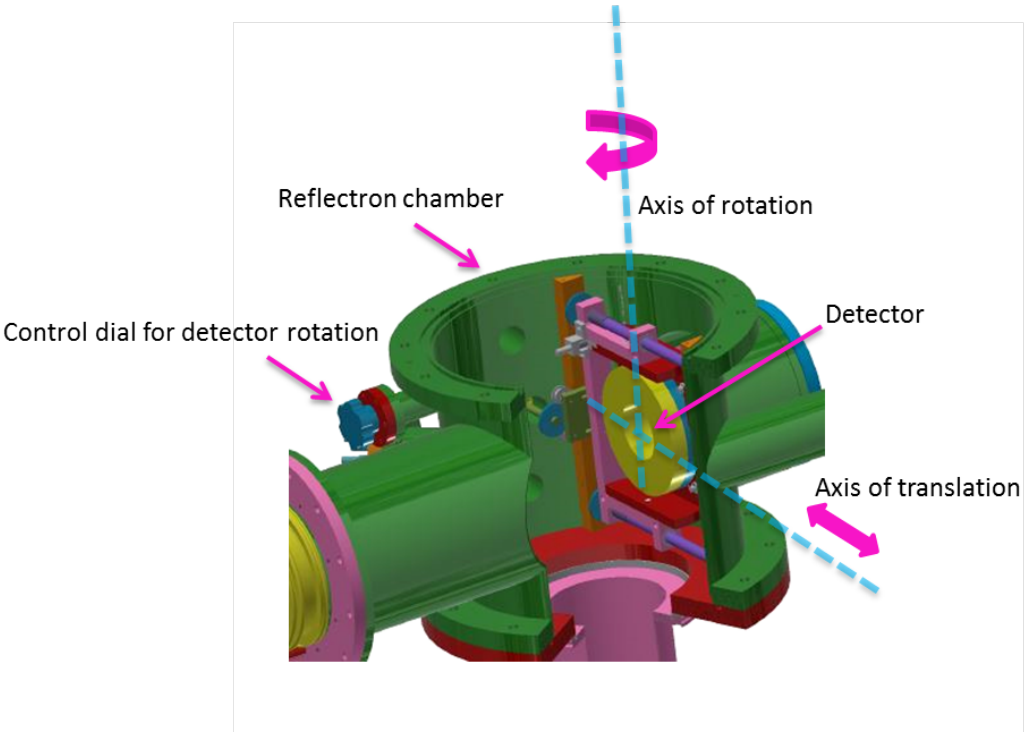


Figure 2.8: CAD image showing the manoeuvrability of the detector within the reflectron chamber.

The mass resolution is inversely proportional to the FWHM of the ion ToF peak. The FWHM for the microscope-mode mass spectrometer is less than 8 ns which corresponds to a mass resolution greater than 10,000 $m/\Delta m$. Therefore, if a P47 phosphor screen is used, the detector assembly becomes a limiting factor to calculating the mass resolution of the experiment, a FWHM of 70 ns limits mass resolution to greater than 200 $m/\Delta m$. It is therefore necessary to have a screen with a short decay lifetime, such as exalite 404, for imaging ToF-MS experiments with high mass resolution.

The detector is mounted on a mobile platform that allows movement in two-dimensions, as shown in Fig. 2.8. The position of the detector is controlled on two dials located outside of the reflectron chamber. This allows the detector position to be adjusted while retaining high vacuum. Manoeuvrability of the detector allows the lateral spread for ions with different masses to be reduced, this is discussed further in Chapter 4.

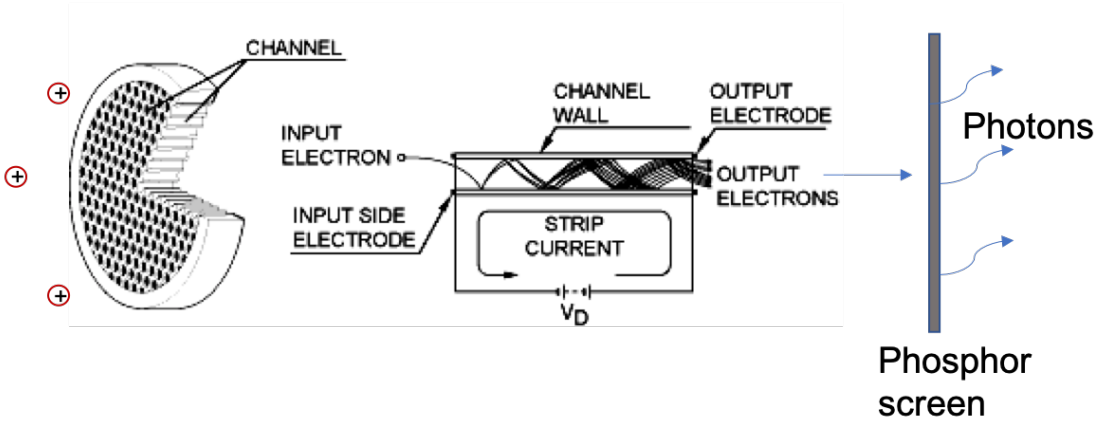


Figure 2.9: Double stack MCP assembly followed by a photon emitting scintillator screen.

Fig. 2.9 depicts the systematic conversion of an ion from the time of flight mass spectrometer to a photon than can then be recorded by a camera. The ions collide with pores on the front face of the MCP which is grounded. Upon collision, an ion produces a cascade of electrons. The chevron geometry maximises collisions and secondary emission, increasing the electron gain. The electrons are accelerated towards the back MCP plate. The voltages are controlled by a single power supply which uses resistors to split the potential across the MCP stack at a ratio of 2:1 (front : back). Ion collisions with the back plate of the MCP result in 1×10^6 electron gain leaving the front face MCP [127]. The potential of the scintillator is 4.6 kV which causes the electrons to be accelerated from the back plate of the MCP toward the screen. The collision between electrons and exalite molecules on the scintillator screen cause excitation and resultant photon emission with a wavelength $\lambda \approx 400\,\text{nm}$. Photons emitted from the scintillator are recorded with two devices, a photo multiplier tube (PMT) and a light detecting camera.

The PMT is required to record mass spectra with high mass resolution, a schematic is shown in Fig. 2.10. It has a high gain, low noise, high frequency, and fast response ($< 2\,\text{ns}$), with a 1 cm diameter collection area. Photon flux from the scintillator is converted to electrons in the PMT by a primary cathode which generate a current. The PMT comprises dynodes, which amplify electron density.

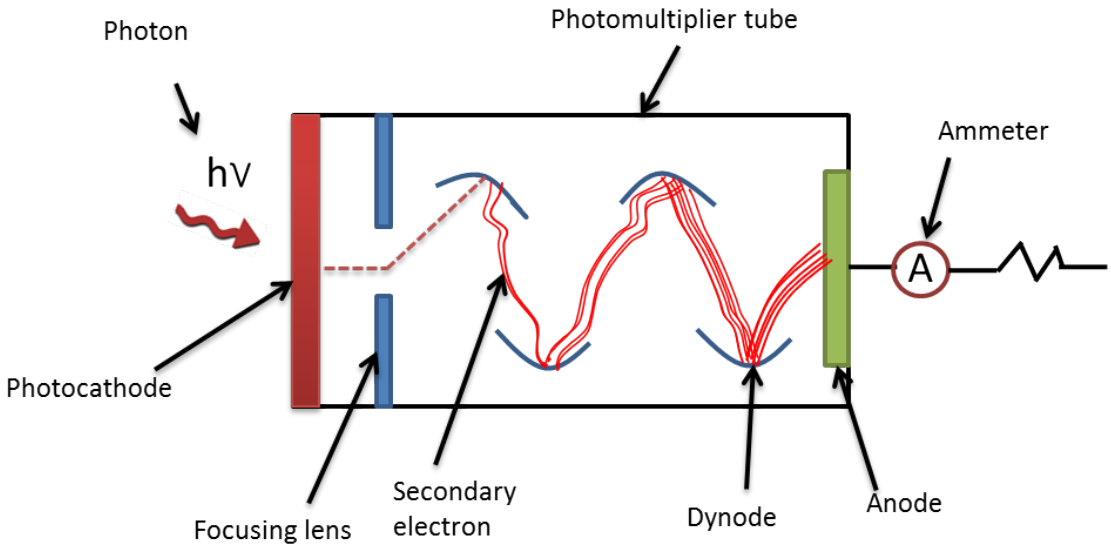


Figure 2.10: PMT schematic.

A low photon count from each laser shot can therefore be recorded. The electron flux causes a sharp increase in current at the anode, and can be detected by an oscilloscope. This information provides a precise record of the time that photons are emitted from the scintillator and, by extension, the time of flight of ions reaching the end of the mass spectrometer. PMTs typically have a temporal resolution of less than 1 ns which is sufficient for these experiments. To minimise background signal, a black shroud is placed over the PMT and detector to reduce the amount of ambient light that is incident on the PMT.

2.6 Camera

Images presented in this thesis were collected with either a Charged Coupled Device (CCD) camera, a Pixel Imaging Mass Spectrometry (PImMS) sensor or a Timepix based camera known as Tpx3Cam. CCD cameras with large pixel arrays and large active areas within each pixel were used to record highly spatial revolved ion images. The CMOS sensors (PImMS and Timepix3) are used for multi-mass ion imaging. However, as a result of the circuitry required to record multiple ions in

each experiment cycle, the pixel arrays are currently smaller than a CCD and have a reduced active area, which results in a worsened spatial resolution.

2.6.1 CCD

A CCD camera converts photons from a scintillator to electrons. A photon incident on a particular pixel is converted into electrons: the charge is stored in capacitors within the pixel until it is transported and converted to a digital signal and a corresponding image, at the end of an experimental cycle. The intensified CCD camera (Photonic Science) used in these experiments comprises a 768×576 pixel array and has a temporal resolution of 50 ns. This CCD camera contains MCPs which further amplify a signal emitted from the phosphor screen.

The CCD camera is positioned in front of the detector using a scissor jack. The scissor jack provides a stable platform and an adequate height range. A 25 mm screen requires the detector to be positioned at 175 mm from the detector for optimal focusing (optimal focusing conditions will be detailed later in the chapter). Like the PMT, the scissor jack, detector housing and camera are covered with a black shroud to reduce the ambient light. This gives a greater contrast between flashes on the detector screen and background noise.

The CCD camera records an image after each laser shot. Pixels are activated when the threshold voltage is surpassed. This threshold voltage is applied to reduce background signal. Each image records (x, y) coordinates of ion events, creating a two dimensional ion image, after each laser pulse. The ion image is further processed through a centroiding program, improving the spatial resolution by reducing clusters to single pixels. The resulting image of each ion is created from the summation of each centroided image.

2.6.2 PImMS sensor

Mass spectra were recorded using the the Pixel Imaging Mass Spectrometry (PImMS) sensor. The PImMS sensor is an event-triggered, time-stamping complementary

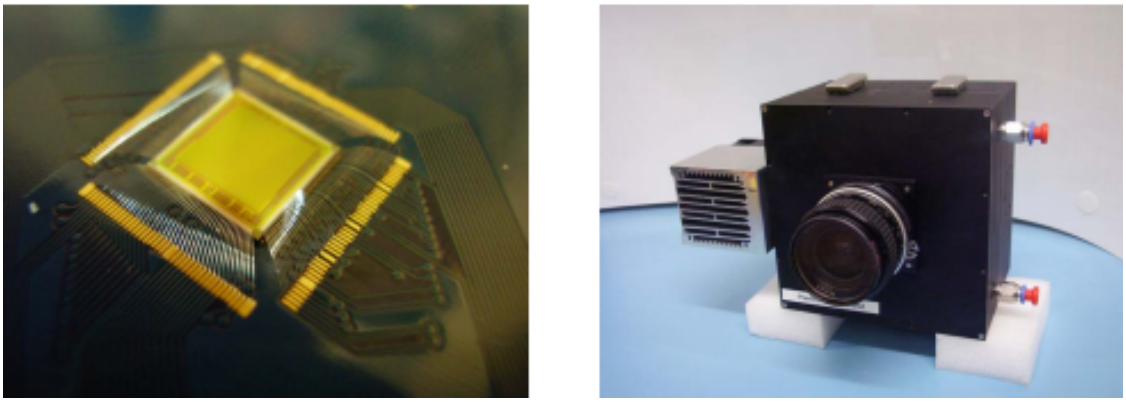


Figure 2.11: PImMS 1 sensor and PImMS camera.

metal–oxide–semiconductor (CMOS) device, that enables the spatial distributions of multiple ToF peaks to be collected in one experimental cycle, and and image of this is shown in Fig. 2.11. This allows microscope MSI to be applied to irreproducible samples, as ion images for every mass peak can be recorded in one experiment. There are currently two cameras, PImMS1 (72×72 pixel array) and PImMS2 (324×324 pixel array) with a maximum clock frequency of 80 MHz, corresponding to a 12.5 ns timing precision (each peak in the mass spectrum can be recorded if they are separated by more than 12.5 ns). Each pixel is 70 µm × 70 µm and comprises four diodes (14.5 µm × 14.5 µm). Ion hits are recorded and time-stamped by one of these four diodes when the signal threshold is surpassed in a pixel. The camera is able to run continuously for 50 µs, ensuring that a typical experimental cycle can be fully analysed. The digital readout of the pixels' timestamp registers are the main method to display experimental information. The data are stored in the following format: $(x, y, t, n$ frame, m register), where x, y are the two-dimensional spatial coordinates of the pixel (ion event,) t is the time bin that the event occurs (relative to an external trigger), f frame is a sequence of numbers for iterated experiments, and n is the register number (1-4). During an experimental cycle, the majority of pixels are not expected to receive a signal. Furthermore, only ion events are stored in contrast to a framing camera, where every pixel records data for a set length of time.

This significantly reduces the size of the stored data sets. After every laser shot, the coordinates of ion impact voxels are transferred to a computer for processing.

The PImMS (1 and 2) sensor is interfaced with a computer through a USB connection to run the PImMS software program. The features include: configuration; calibration; readout of the sensor; and online, or offline visualisation of the data. Additionally, a second software application, the PImMS post-processing software, is used to visualise and process mass spectrometry data, including a display of mass spectrum and, time windowing, noisy pixel filtering and centroiding of clusters. The centroiding process takes each cluster and reduces it to a single pixel and a single time code. The centroiding algorithm identifies clusters through 8-fold connectivity (8 nearest neighbours), and determines the coordinate of the cluster centre through a weighted average of the coordinates of each pixel that belong to the cluster. The weighting factor for each pixel is determined by the time code of the event recorded, with earlier time codes corresponding to a larger weighting factor [118].

The sensor can also read out in analogue mode (displayed adjacent to the digital readouts in the processing software), presenting a shot-by-shot grey-scale image. This image can be used to focus the optical lens of the camera. The PMT is used in conjunction with PImMS to provide precise time of flight information.

2.6.3 Tpx3Cam

Tpx3Cam is a CMOS detector with a 256×256 pixel array ($14\,\text{mm} \times 14\,\text{mm}$), each pixel is $55\,\mu\text{m} \times 55\,\mu\text{m}$ [128, 129], a schematic is shown in Fig. 2.12. Similar to a PImMS sensor, Tpx3Cam can record multiple ion events in each experimental cycle. Tpx3 has a timing precision of 1.5625 ns [130]. The Timepix3 sensor can run continuously with zero dead time if the hit rate is below $40\,\text{Mhits}\,\text{s}^{-1}\,\text{m}^{-2}$.

The Tpx3 cam used for experiments in this thesis was controlled by Pixet pixel acquisition software [131]. Pixet controls the camera functionality, optimisation of detectors and image correction, and records Timepix data. Data are recorded as

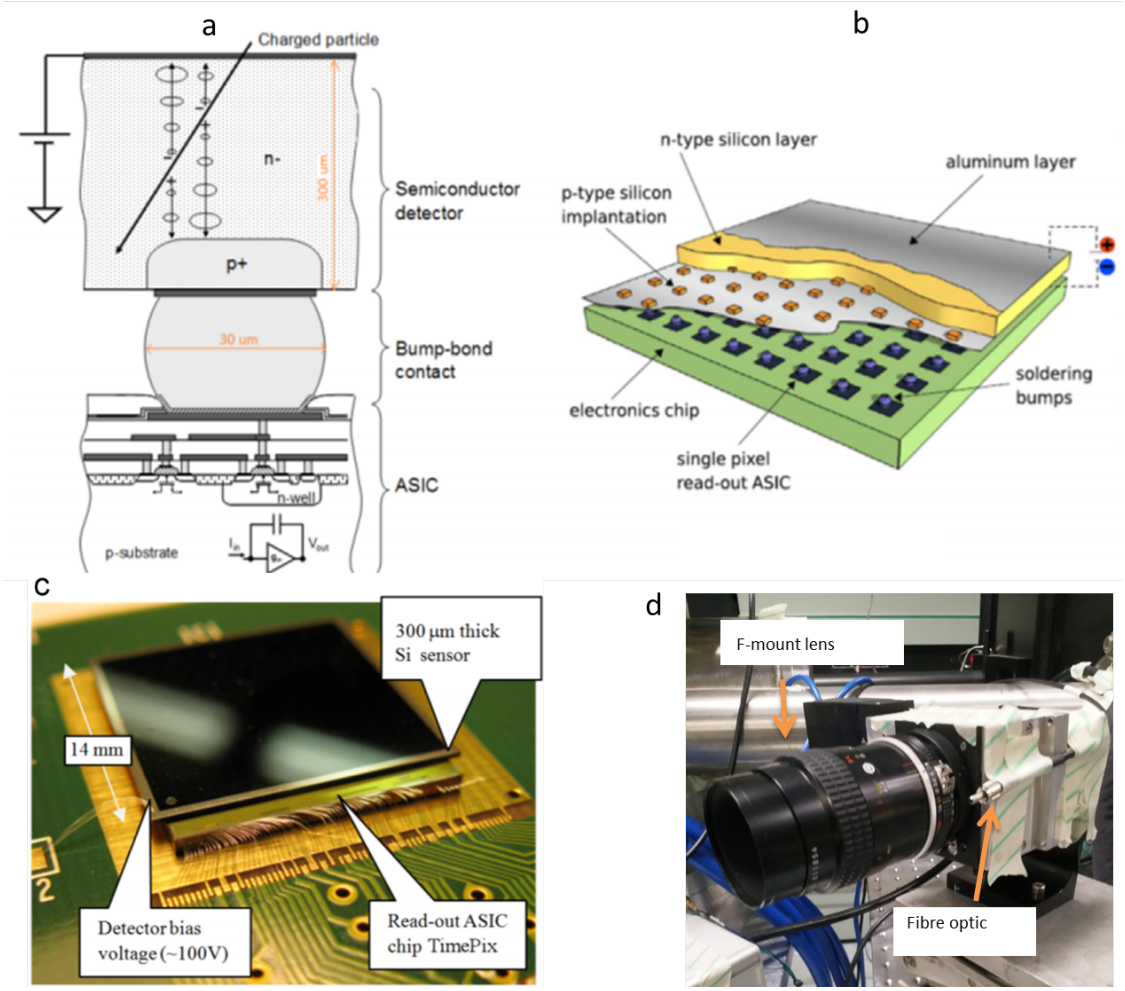


Figure 2.12: (a) Illustration of an individual pixel, showing p-n junction and the bump bond contact to the pixel circuitry. (b) Cartoon of complete pixel array of the CMOS sensor in Timepix (c) Image of sensor. (d) Image of Tpx3 camera and fibre optic used in microscope ion imaging experiments in this thesis.

.t3pa file and comprises 5 columns: Matrix index, Time of Arrival (ToA), Time over Threshold (ToT), fine Time of Arrival (fToA) and overflow. Information recorded using the Timepix sensor is transferred to a computer using a USB connection. In continuous mode, Pixet is set to record five second data files (50 laser shots) which are typically less than 4MB. This is to prevent significant data processing time. Further detail on the camera specifications given in Chapter 7.

The camera is positioned on a scissor jack, placed close to the scintillator. The distance between the lens and scintillator screen was 95 mm. An F-mount Nikon (55 mm f/2.8 AI-s) lens maximises photon flux at each pixel. Pixel threshold is held

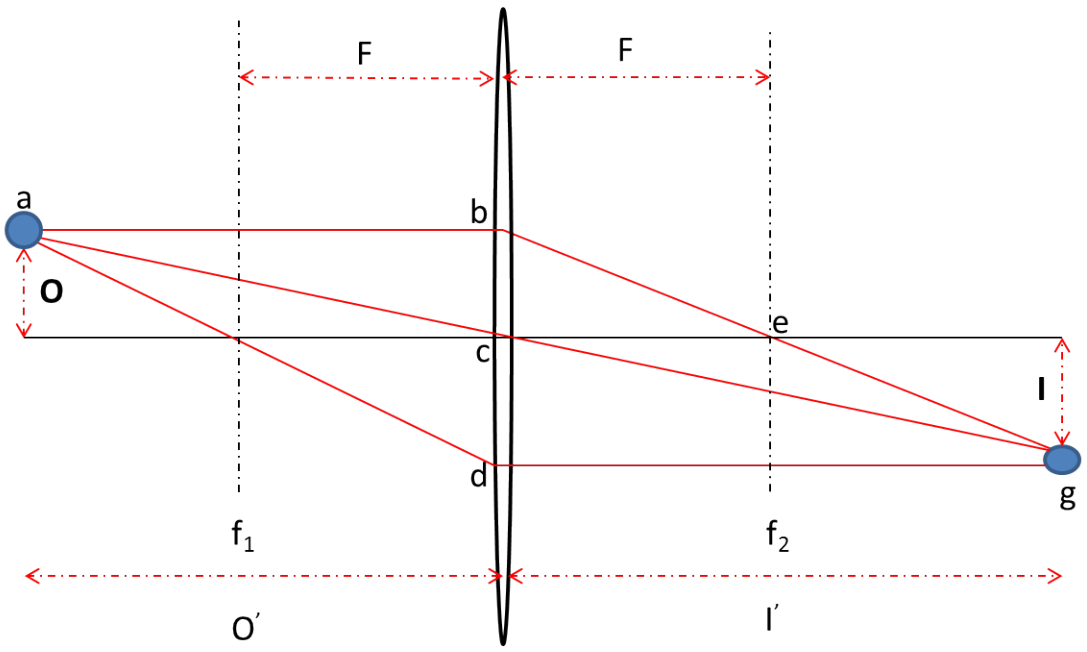


Figure 2.13: Cartoon illustrating a thin convex lens focusing photons as they propagate through the lens.

at 1.39 eV to prevent ambient light and cosmic rays from activating pixels. Ambient light is further reduced by covering the camera with a curtain.

2.6.4 Focusing the Camera

Cameras are employed to capture ion events that cause photons to emit from the scintillator screen. To accurately determine the spatial profile of a sample, an optical convex lens focuses light emitted from the scintillator screen onto the sensor. Fig. 2.13 illustrates a simple convex lens that converges light rays to a focal point and is used in the following derivation to predict minimum focusing distance of a thin lens (thickness of lens $\ll$ distance from the lens to the focal point).

The focal length can be determined using similar triangles:

$$abc = cdg \cdot x \ , \tag{2.1}$$

where x is a ratio to equate vertices of each triangle. Therefore, due to their similarity:

$$\frac{O'}{I'} = \frac{O}{I} \,, \tag{2.2}$$

where O' is the object to lens distance, I' is the image to lens distance, O is the objects displacement from the central axis and I is the displacement of the image from the central axis. Further similar triangles *bdg* and *bce* can be compared to give:

$$\frac{F}{I'} = \frac{O}{O+I} \,, \tag{2.3}$$

where F is the focal length of the lens. Combining equation (2.2) and equation (2.3) yields the Gaussian form of the lens equation:

$$\frac{1}{F} = \frac{1}{O'} + \frac{1}{I'} \,. \tag{2.4}$$

Each lens has an inherent focal length, and has a specific lens - image distance when attached to a camera. Therefore, it is possible to use this equation to predict the distance that the camera must be positioned to be focused on the detector:

$$O' = \frac{IF}{I-F} \,. \tag{2.5}$$

The camera used to record ion images from the reflectron MSI uses a Nikon 800 lens with a focal length of 50 mm, the spacing between the lens and the camera sensor at the minimum focal length is 55 mm. This combination requires the camera to be positioned 550 mm from the detector.

Ambient light increases background signal and therefore decreases resolution. Ambient light is reduced as the camera is moved closer to the detector. To retain the focus as the camera closer to the detector requires the spacers between the lens and sensors. This increases the magnitude of I:

$$O' = \frac{(I+L)F}{I+L-F} \,, \tag{2.6}$$

where L is the width of the spacer. A 5 mm spacer reduces the minimum focusing distance to 200 mm.

2.7 Mass spectrometer calibration

After the mass spectrometer is operational the instrument must be calibrated. Calibration has to be carried out every time the instrument parameters change. A calibration function that provides the transformation from the time domain into m/z, needs to be accurately determined to prevent mischaracterisation of parent ions and their fragments. This is achieved by recording a mass spectrum with well defined m/z peaks. Examples of calibration compounds include: Perfluorotributylamine, Perfluorotripentyl, Polyethylene glycol 400, Red Phosphorous and laser dyes. Initial calibrations with the instrument presented in this thesis were carried out using Rhodamine B as it can be ionised easily. This compound has been extensively characterised, and therefore the mass peaks corresponding to the parent ion and fragment ions are well defined [102, 118].

Once preliminary calibrations have been completed with Rhodamine B, polyethylene glycol 400 (PEG) can provide further improvements to the calibration function due to the fragmentation pattern caused by sequential loss of -CH_2CH_2O-. In addition, once the calibration is known it is possible to predict the mass accuracy of the reflectron.

A first order calibration can be achieved by equating the experimentally determined ToF peak t, to the ion's kinetic energy. The ion flight time t, is proportional to the $\sqrt{m/z}$, and can therefore be modelled as:

$$t = a\sqrt{\frac{m}{z}} + b \,, \tag{2.7}$$

where a is the gradient and b is the y-intercept. The y-intercept accounts for experimental adjustments that may cause the flight time to shift, such as Q-switch timing.

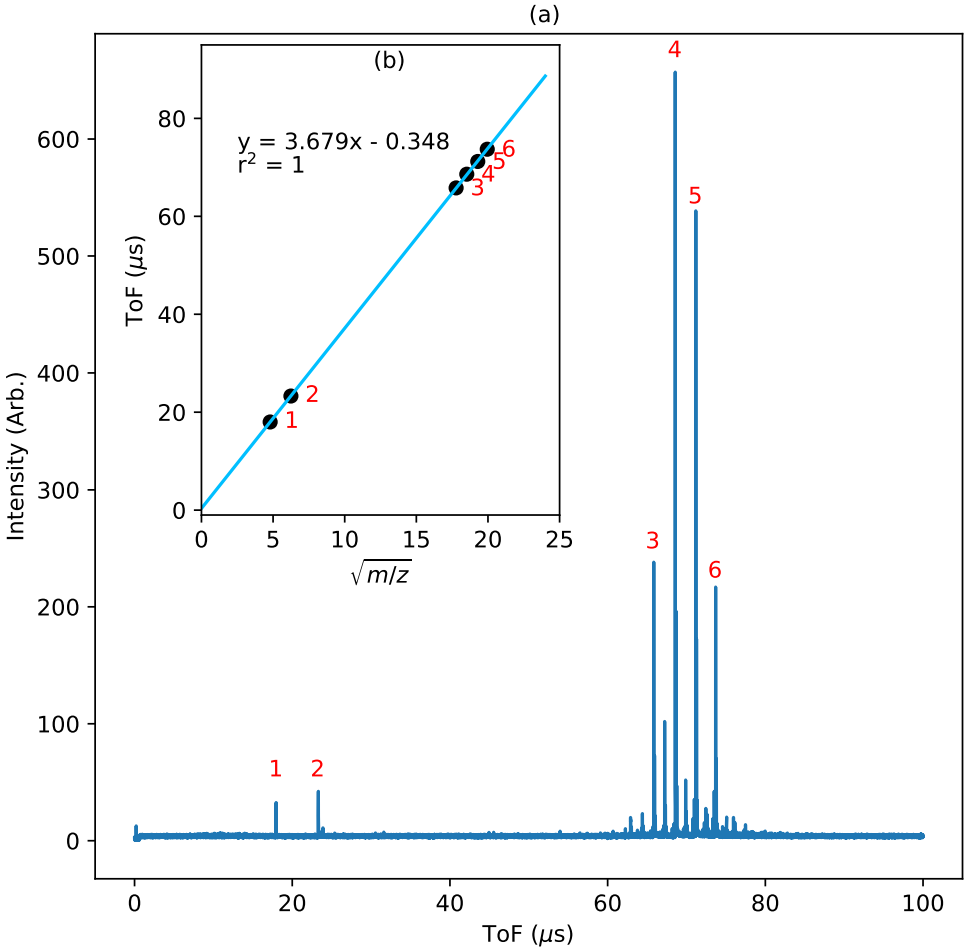


Figure 2.14: (a) Mass spectra of Rhodamine B. (b) Linear regression calibrated using six peaks: 1- Na^+ (23 Da), 2- K^+ (39 Da) and 3-6 are fragment ions of Rhodamine B (316 Da, 343 Da, 372 Da and 398 Da). .

Fig. 2.14 shows the four peaks (315.2 Da, 343.2 Da, 371.2 Da, 399.2 Da) from Rhodamine B and peaks corresponding to Na^+(23) and K^+(39). These peaks are used to determine the linear regression line (equation (2.7)). Once this function is known it is possible to determine the mass of any peak from the ToF.

2.8 Summary

This chapter has outlined the processes by which the data presented in this thesis have been collected. The instrument detailed is a reflectron augmented with an ion microscope time of flight mass spectrometer. Sample preparation methods for the production of gridded laser dye patterns and homogeneous matrix deposition have been described. The triggering system which instructs the various entities of the instrument to operate has been detailed, with a more specific description of the laser system and detector assembly. This was followed by a description of the CCD camera and CMOS sensors used to produce spatially resolved images. The final section explained the calibration methods that transform a ToF spectrum into a mass spectrum.

3
Ion trajectory simulations

3.1 Introduction

Before construction, the performance of the instrument was simulated. As the ion optics have to focus ions both spatially and temporally (i.e. position and mass), any adjustments to the assembly's parameters will affect both of these resolutions. Therefore, it is important to understand the interplay between these specifications so that an optimised design can be determined.

All of the ion optical experiments presented in this thesis were modelled and studied in SIMION before becoming reality in the laboratory. The simulations recorded in this thesis use version 8.1. This chapter will describe the constituent features of the simulation used throughout this thesis.

SIMION is a commercial ion optics simulation package developed by David Dahl, and is now maintained by David Manura [132]. SIMION models ion/electron optics and calculates the corresponding electric and magnetic electric fields. SIMION can then calculate the motion of charged particles (ions or electrons) in these static and/or time-dependent electric and magnetic fields.

Ion trajectories are calculated in an ion optic workbench file (.iob). This file comprises potential array instances (.PA) files which contain solutions to the

Laplacian for a given instrument geometry. The dimensions of the potential are determined by a geometry file (.gem). A user program (script) controls the variables within the ion optic work bench file such as, the electrode potential and the number of experimental repetitions. The final component of the workbench is the .fly2 file which defines initial ion parameters such as velocity and position.

3.2 Ion optics work bench

There are two simulated instruments presented in this thesis: a high resolution ion microscope and a reflectron ion microscope. The reflectron ion microscope is used to describe the simulation tools.

The simulated reflectron is comprised of four potential arrays (PA) representing different regions of the spectrometer: the ion optics chamber, the deflector plates, the reflectron and the detector. The instrument is split into multiple potential arrays so that different symmetries can be used for each array. For example, the ion optics have cylindrical symmetry, and the reflectron chamber has planar symmetry. PAs that are symmetric have significantly reduced computational time. Each PA is individually loaded into an ion optics work bench before the trajectories are determined.

3.3 Instrument geometry

A SIMION geometry file defines the electrode geometries using constructive solid geometry (CSG) primitives. CSG operations define shapes using unions and intersections of other basic shapes e.g a rectangular slab with a cylindrical hole. Electrodes and their positions are defined within ASCII geometry files. An electrode description includes: electrode origin (x, y, z), shape, length, width (or radius), symmetry and axis rotations (elevation, rotation, and azimuth angle). SIMION can then convert a geometry file to a potential array file. Specific designs of the ion optics, reflectron, and flight tube can be found in Chapter 1. Geometry files were constructed to approximate the instrument. Further additions can be made to

improve the simulation, for example, a voltage ripple can be applied to each of the ion optics to model the instability of power supplies (typically the power suppliers used in the experiments presented in this thesis drift by $\pm 1\,V$). However, in the majority of cases it is adequate to neglect these additions to the simulation; the benefit of reducing simulation time outweighs the minor gains in simulation accuracy.

In SIMION, the potential array is a one-dimensional array of double precision points (64 bit). Each array element represents a point within the 2D or 3D array and stores two pieces of information: the potential at the point and whether or not it is an electrode. Electrodes are defined as points having twice the maximum allowable array voltage plus their actual voltage.

The ion trajectories within the simulation are determined from solutions to Laplace's equation. Laplace's equation is solved in the refining process, which determines the electrostatic potential at any point as a function of the potentials at all surrounding points. This is calculated before the charged particle is introduced into the optics using the zero charge density assumption [133, 134]. The form of an electrostatic field, E, can be calculated from the potential field, V. Laplace's equation states that the divergence of the gradient of an electric field is equal to zero:

$$\nabla E = \nabla^2 V = 0\,, \tag{3.1}$$

$$\frac{\delta^2 V}{\delta x^2} + \frac{\delta^2 V}{\delta y^2} + \frac{\delta^2 V}{\delta z^2} = 0\,. \tag{3.2}$$

This equation does not allow solutions to be a maxima or minima. Furthermore, there are two boundary conditions for this function, Dirichlet and Neumann. A boundary condition specifies the domain of the function. The Dirichlet boundaries in SIMION are the electrode voltages. A Neumann boundary is determined from the first derivative of Laplace's equation. In SIMION the Neumann boundary describes the electric flux through electrodes. The Neumann boundary for simulations presented in this thesis are zero.

Once the electric fields have been calculated, the trajectories of charged particles in these fields can be determined. Particle trajectory calculations require three interdependent computations. First, the electrostatic forces at the current position of the ion are calculated. Second, these forces are used to compute the current ion acceleration. Finally, a fourth-order Runge–Kutta method is used to predict the position and velocity of the ion at the next time step. This iterative approach has the additional benefit of accounting for higher-order aberrations, for example, the lens effect (more details can be found in Chapter 6). This is a result of the potential being calculated from the average of four symmetric points. The non-uniformity (at a lens for example) of the electric field is factored into a 4 or 6 (2D or 3D) point moving average of the electric field. Increased accuracy is achieved by reducing the step size in the Runge-Kutta integration. However, increasing the precision of the calculated electric field increases memory use and processing time.

This iteration process continues until an electrostatic equilibrium is reached. That is, there is no change in potential at any point in the PA after successive iterations, the potential array is then refined. To optimise the instrument *in silico*, electrode potentials need to be dynamically changed. It is not necessary to repeat the computationally expensive refining process as long as the geometry does not change. SIMION uses a fast adjust feature which exploits the additive property of the Laplace equation.

3.4 Defining Ions

Ions used in SIMION simulations are created individually from a .fly2 file for a particular experiment. An ion requires a number of predetermined parameters which include charge, mass and initial velocity. The initial velocity is defined by the speed of the ions, the azimuth angle and the elevation angle (there are also other formats for the velocity and direction definitions such as the kinetic energy and momentum,

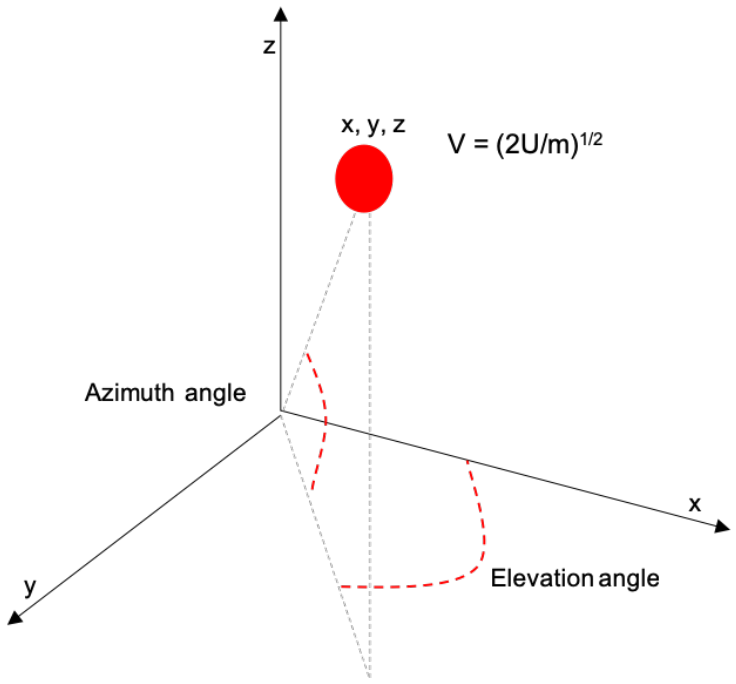


Figure 3.1: Parameter used in SIMION to define an ion position.

a cone distribution etc, but they are not used in this thesis). Fig. 3.1 shows the variables used to define the starting positions of the ions and initial direction.

Ions generated by laser ablation have a spread of non-zero initial speeds, which reduces the mass and spatial resolution of ToF mass spectrometers. The initial velocity distribution was chosen to represent ions created by MALDI/LDI ionisation process [31], allowing the microscope imaging mass spectrometer to be correctly optimised. Beavis *et al.* measured the velocities of singly charged positive polypeptides over a mass range of 200 - 16,000 Da, which were accelerated perpendicular to the sample surface [135]. A mean axial velocity (along the ToF axis) for each ion was 500 $\mathrm{m\,s^{-1}}$ [135]. A second study investigating the change in axial velocity as a function of mass also determined the independence of molecular mass on initial velocity. However, the measured mean axial velocity of this matrix analyte combination was 750 $\mathrm{m\,s^{-1}}$ [31]. It was concluded that in MALDI experiments, mass does not affect the initial ion axial velocity distribution, but the average initial velocity varies with mass. The major factors that define the initial velocity are

Analyte	Matrix	Ion	m/z	v_0
bovine insulin	SINA	$[M+H]+$	5735	332 ± 29
DNA-24mer	3-HPA	$[M+H]+$	3687	619 ± 16
bovine insulin	THAP	$[M+H]+$	5735	306 ± 32
carbonic anhydrase	2,5-DHB	$[M+H]+$	29025	599 ± 119
melittin	2,5-DHB	$[M+H]+$	2848	530 ± 52
maltoheptaose	2,5-DHB	$[M+H]+$	689	187 ± 97
human-milk oligosaccharide 3	2,5-DHB	$[M+Na]+$	2776	545 ± 29

Table 3.1: Initial velocities for different analyte matrix combinations. Further values can be found here: [136].

the matrix, sample preparation process (solvent crystal size etc.), and the laser power. Table. 3.1 is adapted from Karas *et al.* This shows a large variability in initial velocity, v_0, for a range of different matrix-analyte combinations [136].

Further variations in axial speed are caused by changing the laser power. Ens *et al.* showed the laser flux affects the arrival time of ions with the same m/z [137]. The axial speed distribution was measured at the detector for the parent ion of an insulin molecule. The irradiance was increased by four times the threshold value and resulted in an approximately 60% speed increase, as shown in Fig. 3.2.

Simulated ions were given an average initial axial speed, $v_0 = 500\,\mathrm{m\,s^{-1}}$, and a distribution with a FWHM $= 500\,\mathrm{m\,s^{-1}}$. Due to the lack of consensus on what ion definitions should be used, a set of parameters were chosen that would give a conservative estimate for the instrument resolutions.

In addition, the ionising laser has a temporal width 5 - 12 ns, but the actual ionisation time of molecules in the MALDI process has been shown to have a much reduced variance. It has been proposed that this is a result of the energy pooling mechanisms only occurring during the plume expansion (more detail is given in Chapter 1). This results in the ionisation event occurring only when there is a high concentration of multiple excited state molecules, a criterion that is most probable when the laser power within each pulse approaches its maximum power [138].

In addition, ions have an angular distribution on the sample surface. This parameter in the .fly2 file needs to be chosen correctly to optimise the instrument.

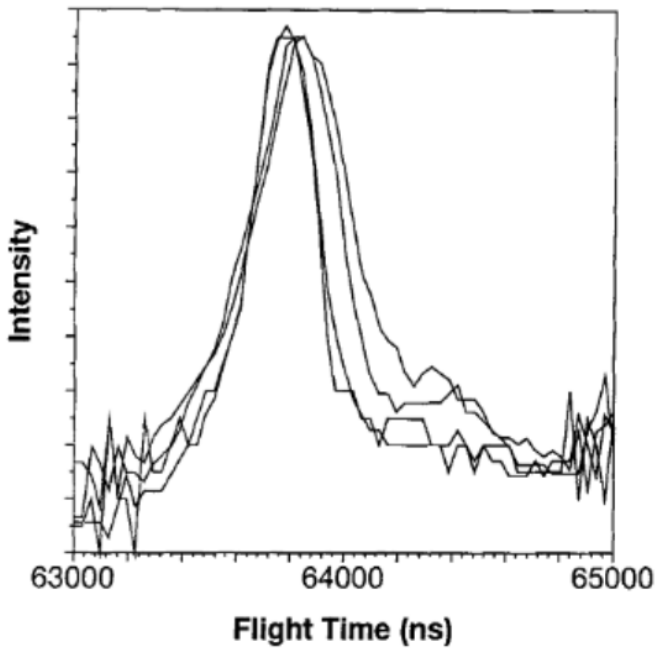


Figure 3.2: ToF spectra adapted from [137]. Broadening of the temporal spread of an insulin molecular ion as a consequence of increased laser power.

The angular spread also contributes to the deterioration of the instrument's resolution. Ions that have identical m/z and kinetic energy, but different starting directions will have different velocities along the ToF axis resulting in a different ToF. The radial velocities (perpendicular to the ToF) do not have a uniform distribution, axial speeds dominate for ions with low m/z, but ions with larger m/z have increased radial speed. Chait *et al.* fit a $\cos^n \theta$ distribution to radial velocity, where n is dependent on mass [136]. For example, the angular distribution of protonated dynorphin 1-13 (1605 Da) can be fitted with a $\cos^{28} \theta$ distribution, which indicates a high preference for a paraxial angular distribution. This is contrast with a protonated CHCA dimer (379 Da) which can be fitted with a $\cos^{12} \theta$ distribution as a result of a larger angle distribution. Chait *et al.*, concluded that lighter peptide species have a preference for a larger angular distribution.

The initial ion directions (azimuth and elevation angle) should therefore be defined using a $\cos^n \theta$ distribution, with an average direction set normal to the sample surface. However an approximation for the angular distribution is required

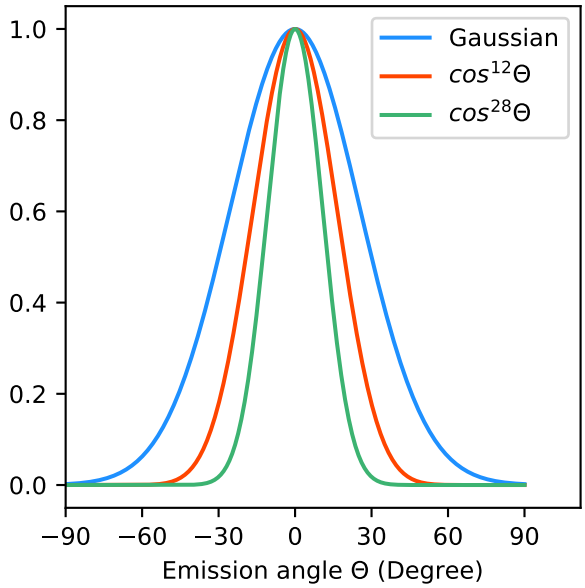


Figure 3.3: Emission angles for three different angular distributions of ions ejected from a sample surface. Red and green $\cos^n \theta$ distributions are an experimental fit of a protonated CHCA dimer (379 Da) and protonated dynorphin 1-13 (1605 Da) respectively. The Gaussian fit has a FWHM = 60° and a modal angle = 0°. The Gaussian function is used as a conservative estimate for the angular distribution of a Rhodamine B 343 Da mass peak.

as SIMION does not have an option for $\cos^n \theta$. Instead, a Gaussian function is used to model the distribution, where the FWHM and modal value are chosen to closely approximate a $\cos^n \theta$ function. In the simulations presented in this thesis a FWHM = 60° and modal direction = 0 have been used. These approximations are taken from previous investigations [26, 102, 136, 139–141]. The Gaussian fit overestimates the emission angles determined experimentally ($\cos^{12} \theta$, for 379 Da), and this is shown in Fig. 3.3. A Gaussian with these parameters was chosen to estimate the resolutions of a Rhodamine B peak (343 Da). As a result, any mass and spatial resolution determined using SIMION are conservative calculations. More accurate simulations could be produced using a Gaussian distribution with a FWHM of 45° and a modal direction of 0°. However, as a number of assumptions have been made for the distribution of the ion's axial speed, a conservative estimate of 60° for the emission angle was also used.

The topography of a sample can impact the obtainable mass and spatial resolution as the ion's focusing condition for different positions will vary. Samples with an uneven surface will have a range of starting positions from which ions can be ablated. Sample surface homogeneity has been addressed with an electrospray device and thermal nebuliser (a description can be found in Chapter 2). Using either of these devices reduces the thickness variance to less that 50 nm [142]. Therefore, the x-position spread of the sample along the ToF axis and the "time-of-birth" distribution of the ions are considered to be negligible.

3.5 Analysis of simulation results

Once the ion optics have been modelled and particle trajectories have been calculated, the results from the simulation have to be interpreted. To maximise efficiency and use SIMION to its full capacity a user programme is combined with the ion optics work bench. The user programme, which is written in lua (but can be written in other languages), can change variables such as the electrode potential, the pulse time, the electrode position (angle and x, y, z coordinate), the m/z, and can initialise defined variables to perform calculations. Minimisation scripts (which are detailed later in this chapter) can optimise the instrument by changing these variables.

To calculate the mass and spatial resolutions, the flight time, t, and position (x, y, z), of the ions when they arrive at the detector are recorded. The initial position of the particles are defined as originating from one of several discrete point sources (typically three, with one centred on the ToF axis). Although, in practice ion images are not developed from a distinct point source, but rather from the surface. If the instrument is spatially mapping, the resulting positions on the detector are also separated into a progression of spots. The average distance between each spot allows the magnification M, of the ions at each position to be calculated, and the spatial resolution of each point source can then be determined. The spatial spread is approximated as a Gaussian distribution, this is expected as

there is a Gaussian distribution of velocities at the sample surface. The standard deviation of the ion positions, σ_y and σ_z (the spread parallel to the detector face) are used to calculate the FWHM of each spot on the detector:

$$\Delta R_{50\%} = 2\sqrt{2\ln(2)}\sqrt{\sigma_y^2 + \sigma_z^2}\ . \tag{3.3}$$

When the instrument is optimised, ion impacts result in a circular distribution where $\sigma = \sigma_y = \sigma_z$. This is a requirement if the geometry is cylindrically symmetric. Experimentally the spatial resolution is characterised with a repeating grid, using 20-80% of the maximum intensity at each feature within the grid and can be defined as follows:

$$\Delta R^i_{20-80\%} \approx 1.683\sigma \approx 0.715\Delta R^i_{50\%}\ . \tag{3.4}$$

This relationship between σ and 20 - 80% rising edge of the feature is valid under the condition that the pitch of the repeated grid pattern is greater than 5 times the resolution [143]. The experimental resolutions determined in this thesis are at the largest contribution to the overall achievable resolution. If the resolution is further improved in subsequent iterations of the instrument, a new scale factor for σ will need to be used.

The magnification and the spatial resolution of the sample are dependent on their displacement from the time-of-flight axis at the detector plane. This means that it can be helpful to consider the standard deviation of these values over all of the point sources as well as the average. A high standard deviation implies that there is some distortion or aberration in the focusing property of the lens system. There are two types of distortion that can cause this, a pincushion distortion and a Petzval distortion [144]. Pincushion distortions in an image are a result of the magnification increasing with greater displacement from the centre. Petzval field curvature distortions are a result of using an electrode with an aperture which causes the electric field to bulge through the iris. The curvature of the electric field

results in an image that is focused across a concave plane, instead of a flat plane. This a consequence of the spherical aberrations from finite width lenses.

SIMION is able to record the time of arrival for an ion at the detector to a precision of 100 ps. The Lua programme records each ion impact at the detector as a hit. If the number of hits is greater than a predetermined threshold, an average arrival time for the ions t, is determined. The FWHM of the distribution of arrival times Δt, is combined with the average arrival time to determine the mass resolution:

$$\frac{m}{\Delta m} = \frac{t}{2\Delta t} \, . \tag{3.5}$$

A major limitation of the mass resolution which will be discussed extensively in Chapter 4, is the response time for the instrument. The instrument response is thought to be approximately 3.7 ns [102]. The main contribution to the instrument response time is from the emission lifetime of exalite 404. Exalite 404 is used as the scintillator in the detector assembly. It is therefore necessary to incorporate both the distribution of ion arrival times $a(t)$, and the instrument response time $b(t)$, when determining the arrival time of ions $c(t)$, in the simulated instrument setup. The flight time is determined from the convolution of the integrals from the two distributions:

$$c(t) = (a \times b)(t) = \int_0^t a(\tau) b(t - \tau) \mathrm{d}\tau \, . \tag{3.6}$$

As mentioned earlier, ions are ejected with a Gaussian distribution of velocities, it can therefore be assumed that the arrival time at the detector will also be Gaussian in nature. Winter *et al.* showed that the response time of an exalite screen also behaves as a Gaussian function [108]. Therefore the standard deviation of the convoluted normal function σ_c, can be determined:

$$\sigma_c = \sqrt{\sigma_a^2 + \sigma_b^2} \, , \tag{3.7}$$

where σ_a is the standard deviation of the arrival time of ions at the detector, and σ_b is a convolution factor indicative of the instrument's response time. The distribution of arrival time can be quantified explicitly:

$$\Delta t_{50\%} = 2\sqrt{2\ln 2}\sigma_c \,. \tag{3.8}$$

To achieve a mass resolution greater that 8,500 $m/\Delta m$ the temporal spread of ions has to be less than 3.7 ns (for a reflectron measuring the mass resolution of a 343 Da ion with a flight time that is approximately 70 µs). Therefore, the instrument response time limits the mass resolution to this value.

3.6 Minimisation algorithms

Minimisation algorithms have been used throughout this thesis to find the optimal values for instrument variables that result in improved performance. These algorithms have been used to optimise spatial and mass resolution in Chapter 6 and Chapter 4, and mass resolution over a mass range in Chapter 5. The following subsections will detail how the algorithms determine the required conditions for a an instrument with multiple variables that need to be simultaneously optimised.

3.6.1 Genetic algorithm

A genetic algorithm (GA) is a method for solving constrained optimisation problems based on a natural selection process that mimics biological evolution [145, 146]. The genetic algorithm assigns values to parameters in a multi-parametric problem, and attempts to minimise a function of interest. In this case, the objective function is to determine the best spatial resolution for a ion microscope mass spectrometer. For example in the high resolution ion microscope (which is detailed in Chapter 6) the parameters that need to be simultaneously optimised include: electrode voltages, electrode position, aperture width, ESA position and ESA voltage.

The genetic algorithm then requires the population size and generation number to be defined. The population size is the number of different parameter sets that are tested by the algorithm in each iteration, where a parameter set is a combinations of values (taken from within the pre-set parameter limits) assigned to the variables (stated above). The generation number is the number of iterations of the population that the algorithm produces to minimise the objective function.

A fitness value is assigned to each individual within each population. Fitness, in this case, is determined by the spatial resolution. The better the resolution; the higher the fitness level. These fitness levels are then used to rank the parameter sets. Individual sets with a better rank are more likely to be selected for breeding. The breeding process involves individual sets winning a tournament. Six individuals are selected from the population. Those with better spatial resolution, higher fitness and better ranks, are more likely to be selected. The fitness of each individual set within the tournament is compared; the best fitness is declared the winner. The tournament selection process is repeated until the number of children are equal to the population in the previous generation. These solutions are then used as the parents for the next generation. Each winner (parent) then undergoes a cross-over with the winner of another tournament. The cross-over process involves assigning each new individual set (child) a value halfway between the value of each variable of the parents. For example, if the extractor voltage of parent one is 6000 V and parent two is 3000 V the child would be assigned 4500 V. Two parents create one child. This results in no change to population size of the new generation. The final input is a mutation rate, which was set at 12%. This ensures that in each successive generation, random values can be assigned to the variables. This helps the algorithm find the global minimum and prevents isolation in a local well. A flowchart that describes this procedure followed by the genetic algorithm, is shown in Fig. 3.4. For these simulations, the population size was 200 and generation number was 80. This results in 16,000 runs for each algorithm.

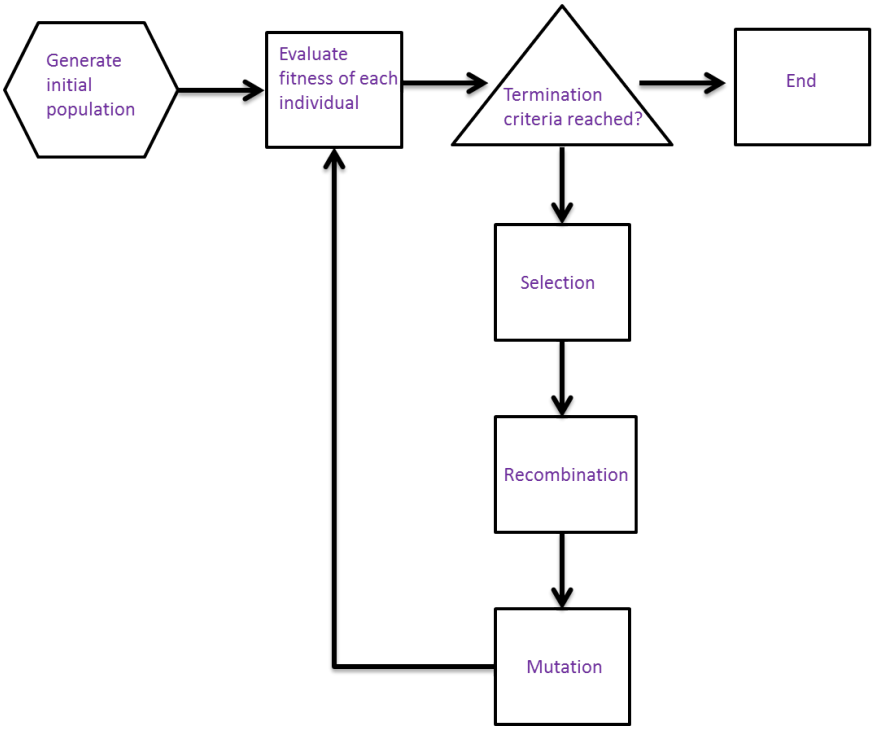


Figure 3.4: Genetic algorithm procedure.

3.6.2 Nelder–Mead minimisation algorithm

The Nelder–Mead numerical method is used to find the minimum or maximum of an objective function in a multi-dimensional space [147]. This direct search method is applied to non-linear optimisation problems for which derivatives may not be known (as this method requires only function evaluations, not derivatives). The Nelder–Mead technique is a heuristic search method that can converge to non-stationary points, but it has sufficient accuracy for this application.

The Nelder–Mead minimisation algorithm was used to assist in the search for the value of the parameters that result in the optimal spatial resolution in two ways. First, the Melder-Mead algorithm was used as a validation tool to ensure the values obtained by the genetic algorithm result in the minimisation of the multi-parametric problem. Second, to further improve spatial resolution. It was used to perform a more refined search of the minimum well that was discovered by the genetic algorithm.

A simplex is the geometrical figure, in N dimensions, consisting of $N+1$ points (or vertices) and all their interconnecting line segments, polygonal faces, etc. A simplex in two dimensions is a triangle. In three dimensions it is a tetrahedron, but not necessarily a regular tetrahedron. If any point of a non-degenerate simplex are taken as the origin, then the N other points define vector directions that span the N-dimensional vector space. The algorithm is given a starting point of an N - vector of independent variables ($N+1$ points, defining an initial simplex). Each vertex in the initial simplex has a spatial resolution assigned to it. The worst point (lowest spatial resolution) on the simplex is replaced with a point reflected through the centroid of the remaining n points. If this point is better than the current point, it is increased along this line. Alternatively, if this new point does not result in improved resolution, then the simplex is contracted, as illustrated in Fig. 3.5. This process is then repeated again for the vertex with the worst spatial resolution (this vertex will be different to the first iteration of the vertex reflection). The algorithm then makes its way downhill through N-dimensional topography until it encounters a minimum. Termination occurs when the vector distance moves in a step that is fractionally smaller in magnitude than a preselected tolerance level. Alternatively, it can be required that the decrease in function value in the terminating step be fractionally smaller than the preselected tolerance level.

The drawback of this technique is the propensity to get trapped in local minima, not the global minima, for this reason the Nelder-Mead downhill simplex could only be applied to the search once the parameter space has been reduced by the GA. The GA will converge close to the global minimum by itself, but it takes significant time and requires many generations to do so. Therefore, a parameter space containing the minimum was defined when the genetic algorithms converge on values for the parameters that were within 10 percent of each other, on three separate occasions.

To avoid the Nelder–Mead minimisation algorithm converging incorrectly, the operating area was set to search a relatively small parameter space. For example,

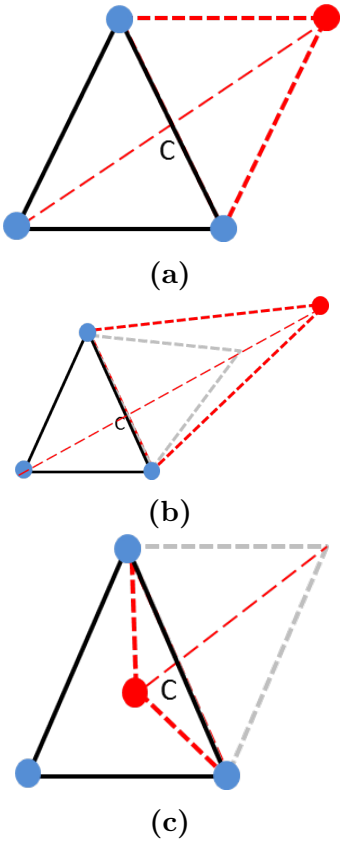


Figure 3.5: Nelder–Mead minimisation algorithm for a two dimensional, three parameter problem (a) initial simplex (b) reflection of the worst solution through the centroid C forming a new simplex (c) contraction in the direction of the minimum and creating another simplex.

if the genetic algorithm concluded that the optimal extractor voltage was 8500 V, the Nelder–Mead minimisation algorithm is set to search from 7 kV - 10 kV.

3.7 Summary

SIMION provides a method for quantitative analysis of ions in an electric field. With this tool an ion microscope can be optimised. SIMION allows precise modelling for every part of the instrument. The ion trajectories can then be specifically characterised to elucidate parameters that have a profound effect on the instrument performance (for example, the spatial resolution is controlled by the extraction field). Furthermore, ions with differing parameters can be modelled. This is particularly useful as the axial velocity that results from the MALDI process,

where there is no consensus within the literature. SIMION can model all axial velocities, mitigating the problematic effect of not knowing the specific value. The final section of this chapter focuses on the methods for controlling SIMION and manipulating the output. Lua scripts that control geometry file, potential array files, workbench programs and rigorous optimisation processes that use minimisation algorithms have been described.

The next chapter will characterise a reflectron combined with a linear ion microscope, that simultaneously achieves high mass and spatial resolution ion images.

4

Characterisation of a reflectron ion microscope

4.1 Introduction

This chapter presents and characterises a microscope imaging mass spectrometer that incorporates a reflectron mass analyser capable of obtaining simultaneously high mass and spatial resolutions.

Spatially-mapped ion images can in principle be focused through non-linear trajectories with minimal time-of-flight distortion. Schueler demonstrated a secondary ion microscope that employed three 90° hemispherical electrostatic analysers to resolve images to approximately 1 μm without first-order chromatic aberrations [93], and similar MALDI-based designs have provided comparable results. Hazama and co-workers have also characterised a multi-turn ion microscope, the MULTUM-IMG, that uses four electrostatic analysers to cycle ions a set number of turns before detection, significantly separating their times-of-flight. A mass resolution of 130,000 $m/\Delta m$ over a window of 8 Da was reported after 500 cycles for the angiotensin II ion [95, 96]. However, images were shown to be sensitive to any misalignment of the ion optics, and degraded after one cycle, contrary to simulations that accounted for third-order aberrations and suggested no image distortion.

Reflectrons offer the potential to record well-resolved spatial images over wide mass ranges with high mass resolution [22]. They act as ion mirrors that extend ion flight times and correct for the initial kinetic energy spread. Reflectrons routinely achieve mass resolutions in the 10^4 - 10^5 range depending on whether they are in single-stage, dual-stage, or multi-reflecting configurations [148–151]. Suits and co-workers recorded velocity-mapped images through a reflectron, suggesting that the initial spatial distribution of ions may be similarly imaged by adjusting the ion optical voltages to focus the image plane that follows the velocity focus [152]. Reflectrons are also compatible with post extraction differential acceleration (PEDA) techniques, which immediately extract ions from a surface following ionisation and correct for their initial velocity distribution, allowing well-resolved spatial images to be obtained without compromising the mass resolution.

The ion microscope combined with a reflectron presented in this chapter comprises four distinct regions: ion optics, deflector plates, a reflectron, and a detector assembly. Within the ion optics there is a five plate lens system containing a repeller, extractor (which is pulsed) and an einzel lens. The deflector plate steers the ion packet into the reflectron. The reflectron comprises 65 individual electrodes and reverses the ion direction. Finally, an MCP/scintillator assembly converts ions into photons which are recorded by external cameras. A schematic of the instrument is shown in Fig. 4.3, and will be discussed in more detail throughout the chapter.

4.2 Principles of a reflectron

The gridless reflectron used in this thesis is a cylindrically symmetric hollow tube containing concentric electrodes with a linear voltage (positive polarity) gradient. A large positive voltage applied to the last electrode of the reflectron causes the positive ions to decelerate, stop, and accelerate back out of the reflectron.

When ions are created using a pulsed laser they receive a distribution of initial kinetic energies [153]. The temporal spread is reduced when the kinetic energy

distribution of an ion cluster is minimised. The following equations will describe how the temporal spread is reduced by combing PEDA and a reflectron [22, 97]. In Fig. 4.1 and 4.2 the red circle symbolises the ion as it travels through the electrodes (shown in blue), the separation, velocity and time at different positions are detailed as L, v and t respectively. In Fig. 4.1 the red dotted line indicates the increased potential after the extractor plate has been pulsed. The variables used are shown in Fig. 4.1 and 4.2.

The total ion energy U_{L1}, in the extraction region is the sum of the initial velocity v_0, and the potential difference between the repeller plate and extractor plate $(V_R - V_E)$. The velocity, v_1, of an ion at the exit of the extraction region is:

$$v_1 = \sqrt{\frac{2}{m}\left(q(V_R - V_E) + \frac{mv_0^2}{2}\right)}\,, \tag{4.1}$$

where m is the mass of the ion and q is the ion's charge.

The ToF of an ion that has travelled through a PEDA optics, shown in Fig. 4.1, can be determined with the following equation [97]:

$$t_2 = \frac{mv_x L_2}{q(V_E + \Delta V)} \times \left[\sqrt{\left(1 + \frac{2q(V_E+\Delta V)(L_2-\Delta x)}{L_2 m {v_x}^2}\right)} - 1\right] + t_{\Delta x}\,, \tag{4.2}$$

where L_2 is the distance between extractor plate and the entrance to the einzel lens, $t_{\Delta x}$ is the switch time, Δx is the distance of the ion from the extractor when the pulse is applied and ΔV is the increase in electrode potential after the pulse has been applied. PEDA increases the velocity of ions as they travel through the acceleration region (L_2). Ions that are travelling slower before the pulse is applied (ions with small initial velocities), have travelled a shorter distance through

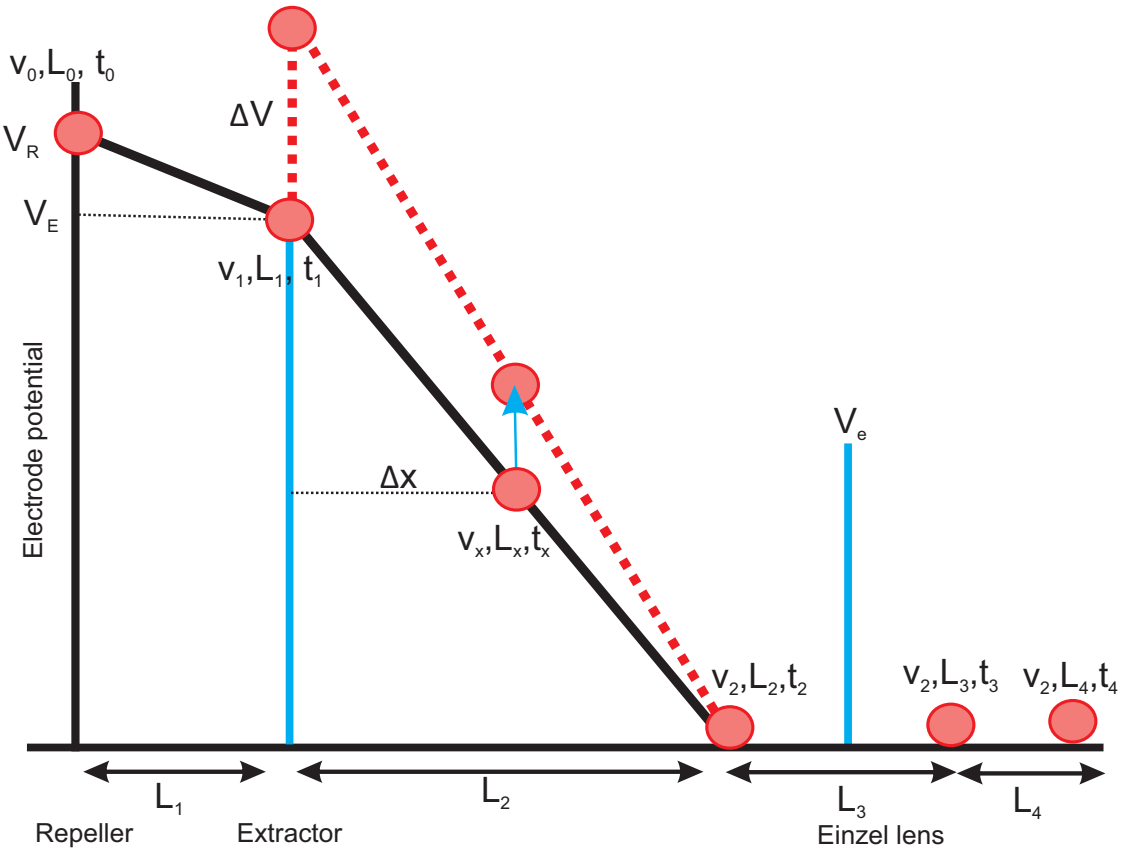


Figure 4.1: A cartoon representing an ion trajectory through the reflectron which terminates at the detector. The variables illustrated in the cartoon are used to determine the ion flight time in the equations below.

the acceleration region and therefore gain the largest increases in velocity, and vice versa for ions with large initial energy. If the potential is increased to an appropriate magnitude, and a suitable switch time is chosen, the velocity spread is reduced and ions form a temporal focus.

Ions then enter an einzel lens. The velocity of an ion entering this region is the same as its velocity as it exits the extraction region, v_2. The time, t_3, of the ion at the exit of the einzel lens is defined as:

$$t_3 = t_2 + \frac{v_2 m L_3}{q V_i}\left(\sqrt{1-\left(\frac{2qV_i}{m{v_2}^2}\right)}+1\right), \tag{4.3}$$

where V_i is the electrode potential of middle plate in the einzel lens. There are two

grounded plates equidistant (before and after) from V_i. After the last grounded plate there is a field-free region. At this stage it is important to split the drift region between the einzel lens and reflectron into two distinct parts: before the temporal focus (L_4) and after the temporal focus (L_5), as shown in Fig. 4.1 and 4.2. The temporal focus can be thought of as a pseudo-origin for ions entering the reflectron. The velocity in this section is constant, and the time that an ion spends in the drift region is given by:

$$t_4 = \frac{L_4}{v_2} \,, \tag{4.4}$$

$$t_5 = \frac{L_5}{v_2} \,, \tag{4.5}$$

where L_x is the length of the respective drift regions. Next, the ions enter a reflectron. Ions have a symmetrical parabola shaped path within the reflectron, and enter and exit with the same velocity, v_2, as shown in Fig. 4.2.

The variables used in the following equations are illustrated in Fig. 4.2. The total flight time of an ion in the reflectron can be expanded as a Taylor series:

$$t(U) = t(U_0) + \left.\frac{dt}{dU}\right|_{U=U_0} (U - U_0) \; + \ldots \; \left.\frac{d^n t}{dU^n}\right|_{U=U_0} \frac{(U - U_0)^n}{n!} \tag{4.6}$$

In equation (4.6), U_0 is the average kinetic energy of ions of a particular m/z. To reduce the temporal spread, the total flight time $t(U)$, of each ion needs to be close to the average flight time for that m/z ion, $t(U_0)$. This is achieved by reducing as many terms in the Taylor series after $t(U_0)$ as possible. As each subsequent term in the Taylor series has a smaller magnitude, the remainder of this section will focus on reducing the most significant term, the first differential, to zero, and achieving first-order time focusing.

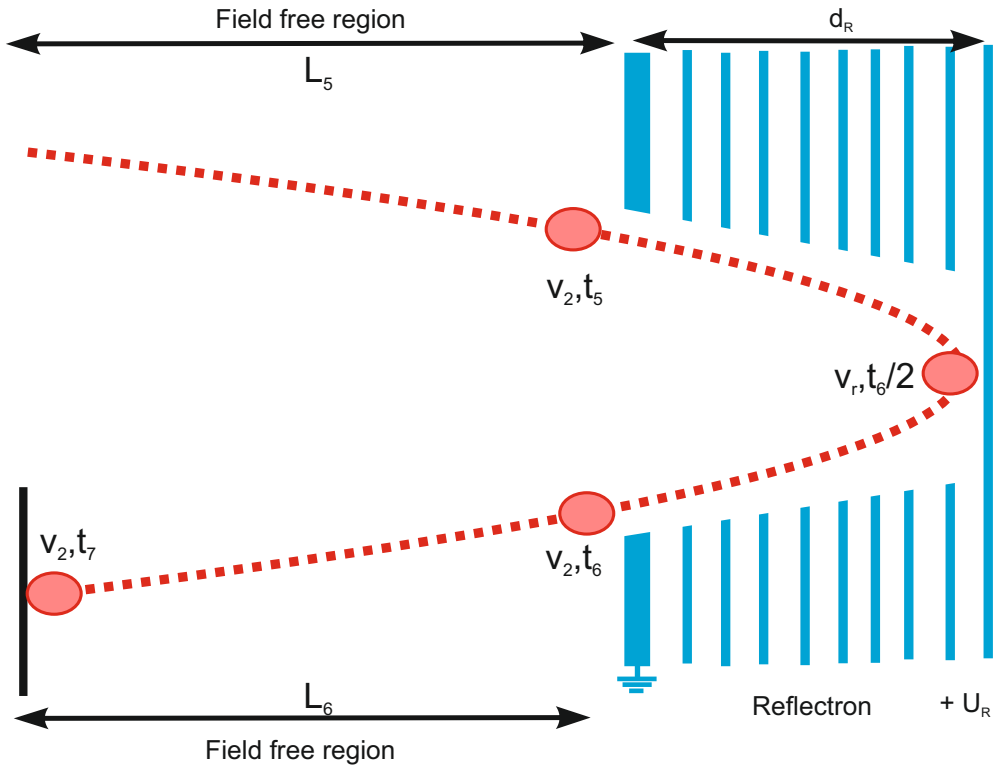


Figure 4.2: A cartoon representing an ion trajectory through the reflectron and terminating at the detector. The variables illustrated in the cartoon are used in the ion trajectory calculations.

The ions trajectories travelling through a reflectron are shown in Fig. 4.2. First, ions are in a drift region L_5, they then enter the reflectron with a length d_r. Within the reflectron there is a uniform reflecting field with potential $U_R = kx$, where U_R is the potential applied to the last plate in the reflectron stack, x is a specific electrode in the reflectron and k is a constant controlled by the resistor chain. Finally, ions enter another drift region L_6. These three regions are used to compensate for the differences in flight time of ions with different kinetic energies reducing dt/dU to zero.

The time that an ion spends in these regions, t_x, can be compartmentalised into:

$$t_x = t_5 + t_6 + t_7 \ , \tag{4.7}$$

where t_5 and t_7 are the time in the drift region before and after the ion enters

the reflectron, and t_6 is the total time that an ion spends in the reflectron. The time that an ion spends in the drift region before entering the reflectron can be determined by equating the potential energy of the ion with its kinetic energy:

$$t_5 = \frac{L_5}{\sqrt{2q\frac{U}{m}}} \, . \tag{4.8}$$

The final section of the ToF is a drift region L_6. The time spent in this region t_7 is analogous to the time-of-flight between the pseudo-source and entrance of the reflectron calculated in equation (4.8).

The reflectron has an increasing positive potential applied as a constant gradient throughout the reflectron stack, along the ToF axis. This causes a deceleration of the positive ion until it stops and is accelerated in the opposite direction, out of the reflectron. The ion enters and exits the reflectron with the same kinetic energy. The time taken for an ion to reach the turn around point is $t_6/2$. The flight time within the reflectron is determined from the momentum of the ion:

$$t_6 = \frac{2mv}{F_r} \, , \tag{4.9}$$

where F_r is the electric force within the reflectron. The velocity of the ion and the electric field in the reflectron can be substituted into equation (4.9) to give:

$$t_6 = \frac{2d_r}{U_r}\sqrt{\frac{2mU}{q}} \, , \tag{4.10}$$

where U_r is the potential of the reflectron. From equation (4.6), it follows that if the differential of the ions' flight time within the reflectron is reduced using first-order temporal focusing, the mass resolution is improved. Equation (4.7) can be simplified and written as a function of U:

$$t_x = \frac{A}{\sqrt{U}} + B\sqrt{U} \, , \tag{4.11}$$

with

$$A = \frac{L_5 + L_6}{\sqrt{2q/m}} \, , \tag{4.12}$$

and

$$B = \frac{2d_r}{U_r} \sqrt{\frac{2m}{q}} \, . \tag{4.13}$$

To minimise the kinetic energy distribution and the temporal spread, the second term in the Taylor series must be reduced to zero:

$$\frac{dt(U)}{dU} = \frac{B}{2\sqrt{U}} - \frac{A}{2U^{\frac{3}{2}}} = 0 \, . \tag{4.14}$$

Equation (4.14) is used to determine the conditions required for first-order time focusing:

$$d_r = \frac{(L_5 + L_6)U_r}{4U_0} \, . \tag{4.15}$$

Once first-order time focusing conditions are known, the total flight time for an ion travelling through the entire instrument can be determined:

$$t = \sum_{n=1}^{7} t_n \, . \tag{4.16}$$

To improve the mass resolution, the variation in total time $t - t_0$, where t_0 is the average ToF for a particular mass ion, must be minimised. Temporal spread

reduction occurs in two regions within the instrument: at the PEDA temporal focus and after the ions exit the reflectron. The conditions for these foci given in equation (4.3) and (4.15), must be chosen appropriately so that temporal spread of ions at each of these positions is minimised. Once an optimal temporal focus is obtained, the mass resolution of the instrument can be determined:

$$R = \frac{m}{\Delta m} = \frac{t}{2(t - t_0)} \ . \tag{4.17}$$

It is therefore essential that the optimal potential for the pulsed voltage and reflectron voltage is chosen to reduce the temporal spread of the ions. The following sections in this chapter investigate how these two parameters can be best optimised.

4.3 Simulation

SIMION was used to model the instrument *in silico* [132]. The reflectron was simulated, firstly to show that imaging mass spectrometery is possible with a reflectron ion microscope mass spectrometer, and secondly to provide optimal conditions for the instrument to achieve the best resolutions (mass and spatial resolution). SIMION models ion's starting positions, as a single point of a planar surface with a Gaussian distribution of kinetic energies. More information on the modelling programme can be found in Chapter 3.

The simulation finds the optimal voltage conditions to achieve the best mass and spatial resolution and provides an insight into the role of each instrument parameter. A genetic algorithm has been employed to efficiently search the topography of this multi-parametric problem, and to determine parameter values that correspond to optimal spatial and mass resolution. More information on the mechanism of the genetic algorithm is detailed in Chapter 3. To generate the first population, each variable was initially randomised and constrained to the maximum available

Parameter	Symbol	Optim. value
repeller	U_R	5.0 kV
extractor	U_E	4.713 kV
pulse (extractor)	U_P	5.258 kV
pulse time	τ	2.790 µs
einzel lens	U_i	1.713 kV
deflector	U_D	±0.111 kV
reflectron angle	θ_R	1.0°
reflectron	U_m	8.792 kV
detector angle	θ_D	1.55°

Table 4.1: Optimised parameter values predicted by the genetic algorithm for the reflectron MSI. Power supplies used to control the experiment have three decimal precision, however the voltage typically fluctuates by ± 3 V.

potential of each power supply. Ion trajectories were calculated based on the equations of motion and the resolution of each combination of variables was recorded. Combinations of variables that resulted in an improved resolution were more likely to be selected for breeding subsequent populations. This process was then repeated until a maximum number of generations was simulated. However, experimentally determined optimal voltage values were found to differ slightly from the simulated results. Experimental voltages were determined by a fine voltage scan [102]. Over the voltage range used it is possible to individually optimise parameters that have a significant effect on the spatial resolution (extractor potential and einzel lens voltage) and parameters that significantly affect mass resolution (reflectron voltage and PEDA step voltage). Table. 4.1 details each parameter, their symbol, and the values of the parameter determined by the genetic algorithm. The deflector plates U_D, are a pair of plates with opposite polarity parallel to the ToF axis. The reflectron angle θ_R, is defined as the angle relative to the ToF axis, and the reflectron voltage is the potential of the last plate of the reflectron stack (linear step function applies a sequentially decreasing voltage on the last 57 concentric ring electrodes within the reflectron). The location of each parameter is shown in Fig. 4.3.

In practice, a single-stage gridless reflectron was joined to a home-built imaging ToF-MS to increase the mass resolution beyond 3,000 $m/\Delta m$ that has previously

been achieved. Fig. 4.3 illustrates the resulting instrument focusing ions (red trace) generated from a sample surface, placed perpendicular to the time-of-flight axis, through the ion optics and drift space. The ions are then deflected into the reflectron and turned towards a detector at the end of a field-free region. Ions impacting on the detector are amplified using dual-stack microchannel plates and converted to photons by an Exalite 404 screen. Flashes of light corresponding to individual ion events are then recorded simultaneously using an imaging sensor and photo multiplier tube.

The previous sub-sections have shown that the resolutions of the reflectron are heavily dependent on a number of factors. The spatial resolution is dependent on the extraction potential, einzel lens voltage and reflectron angle. The mass resolution for a specific m/z value, is dependent on the magnitude of the PEDA pulse, switch time of PEDA, reflectron voltage and detector angle. The following sub-section will show how these simulations do not exactly match the optimal experimental conditions, but provide a good place to begin the experimental optimisation.

4.4 Spatial resolution

The optimal voltages for the instrument were determined by scanning a small voltage range, which is centred on the prediction from SIMION. The experimental voltages differ from those predicted by SIMION primarily because SIMION idealises ion trajectories. However, there are also errors introduced when the constituent parts of the instrument were machined which resulted in slight misalignment, and therefore breakages in symmetry of the electric fields which perturb ion trajectories.

The molecule used for the characterisation and optimisation of the mass spectrometer was Rhodamine B. The mass spectrum for Rhodamine B is well documented, and has four distinct peaks in the mass range 300 - 400 Da. This makes it an ideal candidate for the characterisation of mass and spatial resolution [154]. The Rhodamine mass spectrum allows the instrument to be calibrated, as described in Chapter 2. Moreover, Rhodamine B readily ionizes when subjected to 355 nm

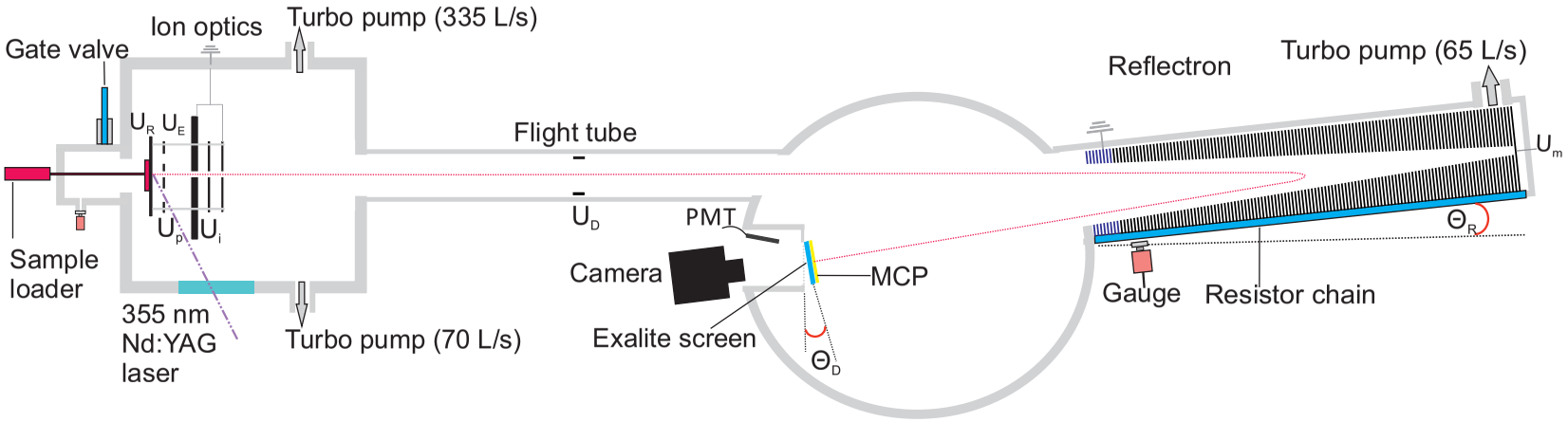


Figure 4.3: Schematic of the microscope imaging mass spectrometer. The red trace shows a typical ion trajectory, originating from the sample surface, as it travels through the instrument, terminating at the detector. The instrument parameters include: $U_R =$ repeller voltage, $U_E =$ extractor voltage, $U_P =$ pulse voltage, $U_i =$ einzel lens voltage, $U_D =$ Deflector voltage, $U_m =$ Reflectron voltage, $R_\Theta =$ reflectron angle and $D_\Theta =$ Detector angle.

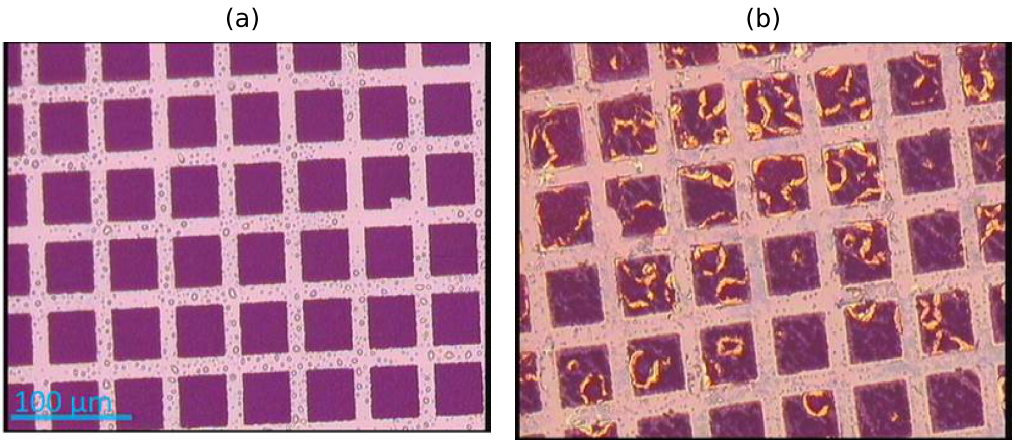


Figure 4.4: Optical images of Rhodamine B dye sample sprayed through nickel mesh that were used to calculate spatial resolution. (a) Pre-ionisation. (b) Post-ionisation.

radiation [46]. Six other molecules, spanning a 200 - 700 Da mass range are used to show the mass and spatial resolution dependence on mass. The molecules used are: Coumarin (202 Da), Rhodamine 560 Chloride (267 Da), Auromine O (288 Da), Rhodamine B (315 - 399 Da), Rhodamine 6G (443 Da), Rhodamine 640 Percholrate (472 - 491 Da) and Exalite 404 (587-658 Da).

In the following ion images the spatial resolution is optimised using a saturated solution of Rhodamine B which is sprayed through a Nickel mesh (Goodfellow) with a 63 µm pitch (wire diameter = 14 µm, grid = 49 µm). This creates an array of specifically defined dimensions containing the analyte on an ITO plate, as shown in Fig. 4.4. The ion images for the characterisation of the reflectron were acquired using a CCD camera that was gated over the most abundant mass peak in Rhodamine B (343 Da). Each image was acquired by approximately 10,000 laser shots.

4.4.1 Correcting distortions

An ion with low kinetic energy (purple) penetrates a smaller distance into the reflectron than ions with high kinetic energy (green). The difference in penetration depth causes ions to exit the reflectron at different heights. ΔS_2 shows the difference in exiting height for the two example trajectories. Ions then enter a field-free region

which does not act to re-converge the trajectories. Therefore, when ions with a velocity distribution arrive at the detector the spatial profile will be broadened (as denoted by $d' \neq 0$ in Fig. 4.5). This results in worsened spatial resolution, reducing the instrument's performance.

Deflector plates are commonly used as mass filters in mass spectrometry. The ions of interest can be directed into the mass spectrometer by pulsing the deflector voltage as ions pass through it. Instead, this thesis uses a deflector plate and the adjustment of the reflectron angle relative to the ToF axis to compensate for the spatial broadening caused by ions with different velocities, as shown in Fig. 4.5.

The deflector plate steers ions into the reflectron using a uniform electric field perpendicular to the ToF axis, shown in Fig. 4.6 (a). Ions with a high kinetic energy (green) are in the deflecting field for a shorter time than those of low kinetic energy (green), illustrated in Fig. 4.6 (b). The time that an ion is subject to the orthogonal field is proportional to the deflection angle, therefore high kinetic energy ions have a smaller deflection angle β, than low kinetic energy ions. After a field-free distance x_2 (distance between deflector and entrance to the reflectron), ions with a small β (those with higher kinetic energy) have a smaller deflection distance S_1 compared with low kinetic energy ions with larger β (the difference in S_1 for low and high kinetic energy ions).

The objective of the incorporation of the deflector and choosing an appropriate reflectron angle is to ensure that ions with the same m/z and starting position are electrostaticly projected onto the same position on the detector. Fig. 4.6 (c) shows that if the reflectron angle and deflector voltage are chosen appropriately, a reduction in the lateral broadening for different kinetic energy ions can be achieved.

The conditions to minimise the broadening (d') can be derived geometrically starting with S_1:

$$S_1 = (x_1 + x_2)\ \tan\beta = \frac{(x_1 + x_2)v_y}{v_x} = \frac{(x_1 + x_2)\, x_1\, q\, E_D}{m v_x^2}\ , \tag{4.18}$$

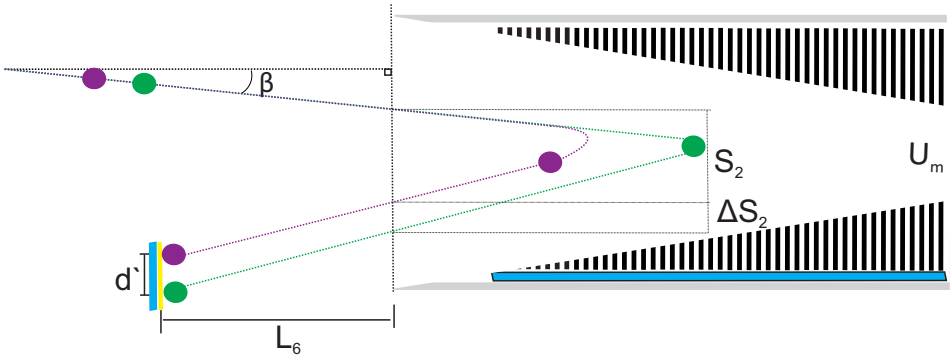


Figure 4.5: Diagram showing how two ions (purple - low kinetic energy, green - high kinetic energy) enter a reflectron at an angle from the ToF axis and have their spatial profile broadened. β is the angle between the ToF axis and ion trajectory as the ions enter the reflectron, S_2 is the difference between the entrance and exit height of the lower energy ion, ΔS_2 is the difference in exit positions for the two ions, and d' is the lateral broadening.

where E_D is the electric field of the deflector and v_x is the velocity of an ion along the ToF axis and v_y is the velocity perpendicular to the ToF axis.

The distance between the ToF axis and the orthogonal position that ions enter the reflectron, $S_1^{'}$, is determined using the reflectron angle, θ_R, and the orthogonal displacement S_1:

$$S_1^{'} = \frac{S_1}{\cos\theta_R} \, . \tag{4.19}$$

To determine S_2, the time an ion spends in the reflectron, t_r, is required:

$$t_r = \frac{2mv \, \sin\alpha}{qE_R} \, , \tag{4.20}$$

where v is the instantaneous velocity of an ion along the ToF axis ($v = \sqrt{v_x + v_y}$) and E_R is the electric field within the reflectron. Therefore, S_2 can be defined as:

$$S_2 = v = \cos\alpha \, t_R \, . \tag{4.21}$$

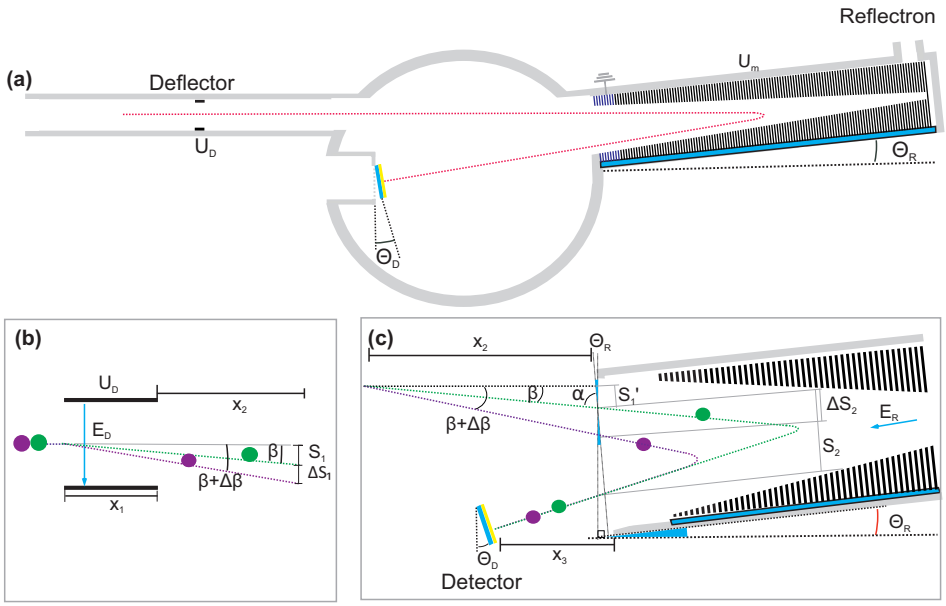


Figure 4.6: Ion trajectories showing how the combination of a deflector and reflectron can reduce spatial broadening of ions with the same m/z, but with different kinetic energies. (a) A section of the reflectron schematic taken from Fig. 4.3, showing the relative positions of the deflector, reflectron and detector. (b) Inset of the deflector showing two ion trajectories: purple (low kinetic energy) and green (high kinetic energy). β is the off-axis angle at which high kinetic energy ions enter the reflectron; $\beta + \Delta\beta$ is the angle entrance for low kinetic energy ions. S_1 and $S_1 + \Delta S_1$ define the respective displacement of the different energy ions as they enter the reflectron. S_2 is the difference in entrance and exit height of the ions in the reflectron, ΔS_2 is the difference in entrance height between the two ions with different kinetic energy. x_1 is the length (along the ToF axis) of the deflector plates, x_2 is the distance between the deflector plates and the entrance of the reflectron, and x_3 is the distance between the reflectron and detector. θ_R and θ_D are the reflectron and detector angles with respect to the normal of the ToF axis. The pale blue segments in (c) indicate angles with the same magnitude.

Combining equations (4.18), (4.19) and (4.21) allows the total distance S_T, between the initial ToF axis and the exit of the reflectron to be determined:

$$S_T = S_1' + S_2 = \frac{(x_1 + x_2)\, x_1\, q\, E_D}{m\ \cos\theta_R\ v_x^2} + \frac{2mv^2\ \sin\alpha\cos\alpha}{qE_R}\,, \tag{4.22}$$

with the substitutions: $U = \frac{m{v_x}^2}{2q}$ and $v = \sqrt{v_x + v_y}$, S_T is simplified:

$$S_T = \frac{(x_1 + x_2)\, x_1\, E_D}{2\cos\theta_R\, U} + \sin\alpha\cos\alpha\left(\frac{4U + E_D^2\, x_1^2}{E_R\, U}\right). \tag{4.23}$$

To correct the broadening of ion trajectories (to first-order) the change in orthogonal displacement of ions entering and exiting the reflectron with different kinetic energy needs to be minimised:

$$\frac{\mathrm{d}S_T}{\mathrm{d}U} = 0\,. \tag{4.24}$$

The minimisation of S_T can be simplified by discounting a number of variables that were forced to take specific values, including x_1, x_2 and x_3 when the instrument was machined. Furthermore E_R is fixed as it has a negligible effect on the spatial resolution (this will be discussed later). This leaves the following variables to simultaneously optimise: U, α, E_D and θ_R.

Using the angles at which ions enter the reflectron, the ToF axis and the deflection angle, the following relationship can be determined:

$$\alpha + \beta + \theta_R = \frac{\pi}{2}\,. \tag{4.25}$$

Therefore, $\sin\alpha = \cos(\beta + \theta_R)$ and $\cos\alpha = \sin(\beta + \theta_R)$. As the deflection angle depends on the kinetic energy of an ion, $\sin\alpha$ and $\cos\alpha$ are not constant. As this is a multi-parametric optimisation problem, a genetic algorithm was used to determine the global minimum. The following sub-sections present simulations and experimental data showing this optimisation process.

Using SIMION it is possible to determine the deflector voltage required to stigmatically focus ions originating on the ToF axis (centre of the sample) onto a position sensitive detector is 70 V, shown in Fig. 4.7. The simulations and the

experiment have a specific voltage range that the deflector must be operated within, otherwise ions collide with various parts of the instrument and an ion image is not acquired. The maximum and minimum voltage applied to the deflector, whilst still being able to generate an ion image, correspond to the maximum distance above and below the centre of the ToF axis where ions can originate. Once these distances are known, it is then possible to predict the maximum dynamic field of view of the instrument. Fig. 4.7 shows the voltage range that can be applied to the deflector whilst still producing an ion image. Fig. 4.7 (a) is the simulated minimum voltage corresponding to a distance of 1.8 mm above the ToF axis, and Fig. 4.7 (c) shows the maximum simulated voltage which can be applied whilst being able to record an ion image. This corresponds to a distance of 1.8 mm below the ToF axis. If the deflector voltage is outside of this range the ions do not reach the detector. Therefore, this instrument has a field of view of $\approx 10\,\mathrm{mm}^2$.

Additionally, Fig. 4.7 shows that the spatial resolution is not significantly affected by changing the deflector voltage over this range. However, equation (4.23) does indicate that the resolution depends on the deflector voltage. This absence of a significant effect on the spatial resolution in the experimental images can be attributed to two reasons. First, ions that are imaged at different deflector voltages originate from positions away from the ToF axis. A deflector voltage focuses a particular initial ion position. If this initial position changes, the deflector voltage required to focus this new position changes. Therefore, the spatial resolution which is approximately constant over the voltage range used in these experiments is as expected, as the sample surface is much greater than the field of view of the detector. Second, other variables in equation (4.23) have a greater effect on the spatial resolution over this deflector voltage range. This will be discussed in more detail next in the context of the reflectron angle variation.

The reflectron is attached to the main body of the instrument by flexible stainless steel bellows. This allows the reflectron to be moved in one dimension away from

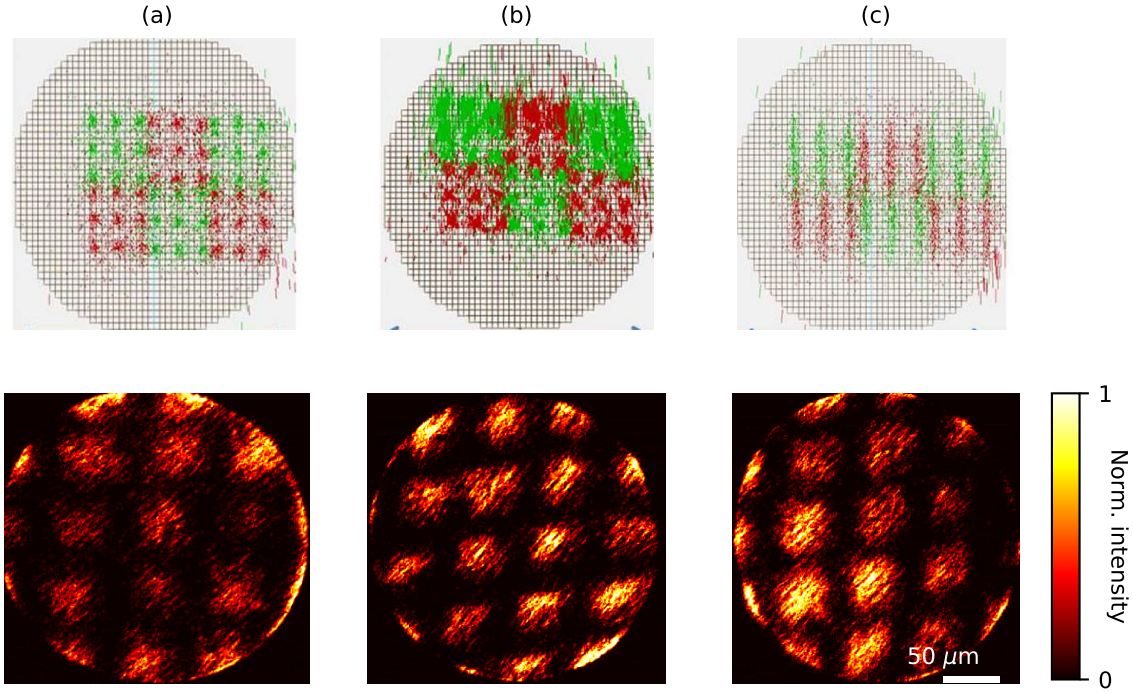


Figure 4.7: Simulated (top row) and experimental images (bottom row) for the reflectron MSI at different deflectors voltages: a) 30 V, b) 70 V and c) 130 V. The deflector voltages in a) and c) correspond to the minimum and maximum deflection angle achievable when using the reflectron.

the ToF axis, as shown in Fig. 4.3. The spatial focus plane of the reflectron is dependent on the angle of the reflectron relative to the ToF axis. To characterise the effect that the reflectron angle variation has on the spatial resolution, larger grid patterns (140 µm pitch) were used. This allows the effects of small angle changes, which correspond to significant changes in resolution to be easily observed. There are well defined limits within which the reflectron arm can be move to maintain ion imaging. The limits for the angle adjustment of the reflectron are ≈ 0.3 - 1.1°. If this angle is exceeded, ions are prevented from reaching the detector.

The reflectron angle is approximated by using $\theta = \tan^{-1}\left(z/y\right)$, where the length of the reflectron z, is 769 mm, the reflectron is then moved by a small amount x which is measured perpendicular to the reflectron chamber (despite it moving in an arc). Fig. 4.8 shows ion images taken with the reflectron angles -0.3 - 2.08°. The

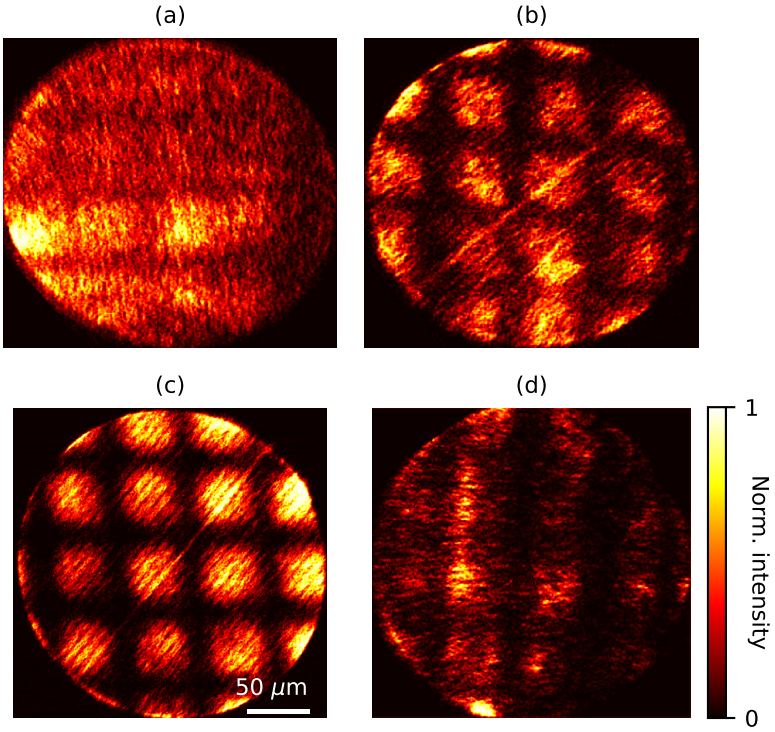


Figure 4.8: Sequential ion images showing the change in spatial resolution as the reflectron is moved away from the ToF axis. (a) Reflectron 4 mm (0.3°) in -y direction. (b) Reflectron moved 5 mm (0.37°) in the +y direction. (c) Optimal reflectron position, reflectron moved 9.7 mm (0.72°) in the +y direction. (d) Reflectron moved 18 mm (2.08°) +y direction.

optimal angle for the reflectron was found to be 0.72°, as shown in Fig. 4.8 (c). This value is similar to 1° which is the optimal reflectron angle predicted by SIMION.

As can be seen in Fig. 4.8, the reflectron angle significantly affects the distortion of the ion image. If the angle is not in an optimal position (Fig. 4.8 (a) (d)) lateral distortion becomes prevalent, reducing the resolution. This angular dependency is consistent with equation (4.23).

An additional benefit of the adjustable reflectron angle is that it allows the reflectron-mode MSI to be converted into a linear ToF; further details of the linear ToF experiment can be found in the following theses by Dr.Winter[102] and Dr.Guo[26]. In summary, the lateral broadening of the ion trajectories caused by the reflectron has been reduced. The parameter with the most significant effect

is the reflectron angle θ_R. The parameters E_D and α, have been shown to have a limited effect on the resolution.

4.4.2 Ion focusing

The variable with the most profound effect on the spatial resolution is the extraction potential, controlled by the voltage difference between the first two plates in the ion optics (repeller and extractor). Chapter 6 investigates the dependency of the spatial resolution on the variables in an MSI mass spectrometer and shows that the worsened spatial resolution is primarily a result of ions with a large velocity component orthogonal to the ToF axis. The most effective way to reduce the magnitude of the transverse velocity, and therefore improve the spatial resolution, is to apply the optimal extraction field between the first two plates in the ion optics. It can be seen from Fig. 4.9, that as the voltage is linearly increased, the ions are initially unfocused shown in Fig. 4.9 (a) (b). The images then become focused and the grid structure becomes well defined in Fig. 4.9 (c). Finally, as the voltage is increased beyond the optimal focusing conditions, the image becomes unresolved again in Fig. 4.9 (d). When the repeller is at 5 kV, the optimal value for the extractor voltage is 4.68 kV, closely matching SIMION which predicts a voltage on the extractor electrode of 4.71 kV.

An einzel lens is formed using the third, fourth and fifth electrode in the ion optics (see Fig. 4.3). The third and fifth are grounded, and the fourth plate has a positive potential applied to it. The einzel lens is used to adjust the position of the spatial focus plane, ensuring that the spatial focus and temporal foci overlap at the detector. In practice, when the voltage of the einzel lens is adjusted, the grid patterns become focused. Fig. 4.10 shows ion images as the voltage of the einzel lens is scanned through 1.6 - 1.72 kV, ion images with voltages above and below the optimal values (see Fig. 4.10) are out of focus.

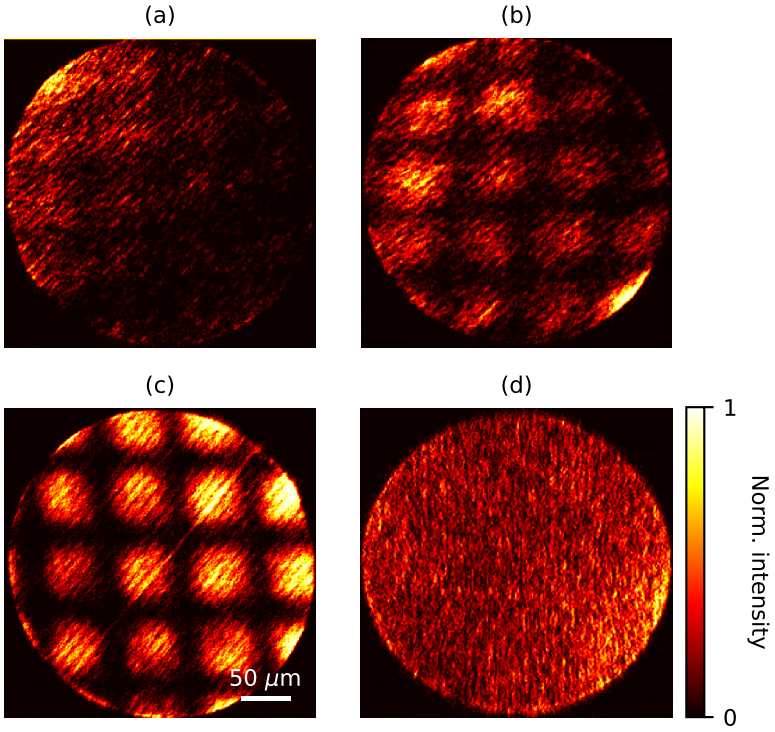


Figure 4.9: Sequential images showing the change in spatial resolution as the extractor is scanned through a voltage range, whilst the repeller is held at 5 kV. (a) $U_E = 4.64$ kV. (b) $U_E v = 4.66$ kV. (c) $U_E = 4.68$ kV. (d) $U_E = 4.70$ kV.

The spatial resolution is determined by measuring the distribution of ion impacts on the detector. When images are acquired with the CCD camera, a matrix is formed that specifies the intensity at each pixel. Before the spatial resolution is calculated, the pixel number needs to be converted into a distance.

$$P = \frac{d_s}{n} \,, \tag{4.26}$$

where P is the pixel size in mm, d_s is the diameter of the scintillator screen and n is the number of pixels across the the diameter. A 25 mm diameter scintillator screen was used for these experiments. More information on the detector setup can be found in Chapter 2.

Table. 4.2 details the optimal experimental values for each parameter charac-

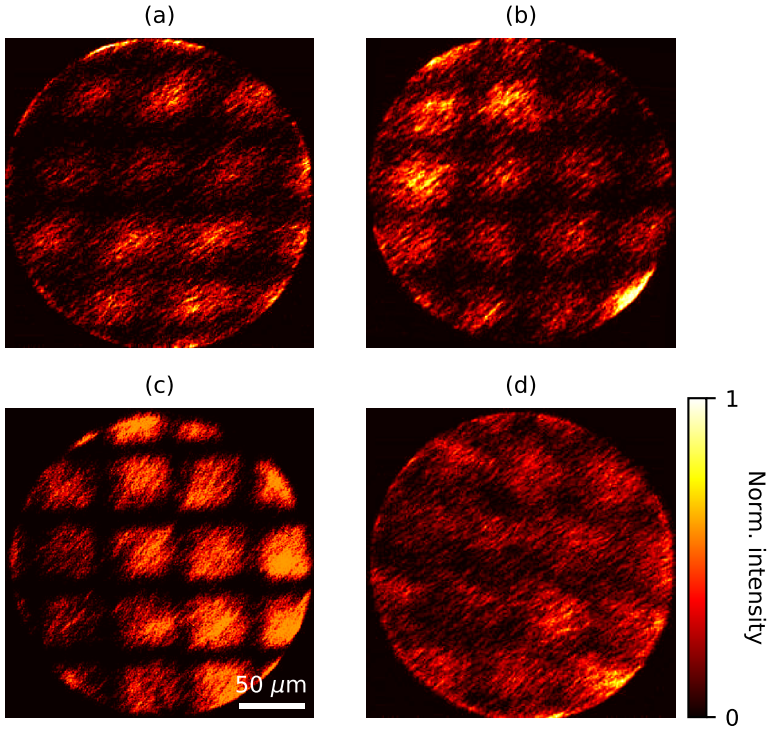


Figure 4.10: Grid pattern of Rhodamine B with changing potential applied to the einzel lens. (a) $U_i = 1.60\,\text{kV}$. (b) $U_i = 1.66\,\text{kV}$. (c) $U_i = 1.68\,\text{kV}$. (d) $U_i = 1.72\,\text{kV}$.

Variable	SIMION (kV)	Experiment (kV)
U_R	5	5
U_E	4.712	4.681
U_i	1.715	1.68
θ_R	1	0.72

Table 4.2: Optimal parameters for the variables that affect spatial resolution in the reflectron MSI.

terised in this sub-section. The following sub-section explains how the spatial resolution is quantified.

4.4.3 Image magnification

The magnification, M, is determined by measuring the distance from the centre of one feature, to the centre of the next, on the detector, D_d. This is divided by the pitch of the grid pattern and wire diameter ($\delta + \phi$) on the repeller plate shown in equation (4.27) [108, 139].

$$M = \frac{D_d}{\delta + \phi} \, . \tag{4.27}$$

The image used for the characterisation is a grid pattern with 49 µm pitch and 14 µm wire diameter. Finally, combining the magnification M, and the difference between the widths at 20% and 80% of the maximum of each feature, $D_{20-80\%}$, the spatial resolution R_s, can be determined using:

$$R_s = \frac{D_{20-80\%}}{M} \, . \tag{4.28}$$

4.4.4 Fourier transformation

Artefacts such as regular striped patterns which are apparent in Fig. 4.11 (a) and originate from the experiment, are convolved with ion events. These artefacts are likely due to the CCD camera as they are not present in the ion images taken with Tpx3Cam and PImMS camera (shown later in the Chapter). This reduces the quality of the ion images. These artefacts and the subsequent spatial resolution of ion images can be improved by using Fourier Transforms.

The Fourier Transform (FT) is a mathematical method which can decompose an image into its sine and cosine components. The data set in this thesis has finite dimensions so a Discrete Fourier Transform (DFT) is used. The two-dimensional spatial domain is FT to represent the image in the frequency domain. In the Fourier domain image each point represents a particular frequency corresponding to a data point in the spatial domain image. The term FT refers to both the frequency domain representation and the mathematical operation that converts it to a function of time. The inverse FT is used to convert frequencies back into a two-dimensional space.

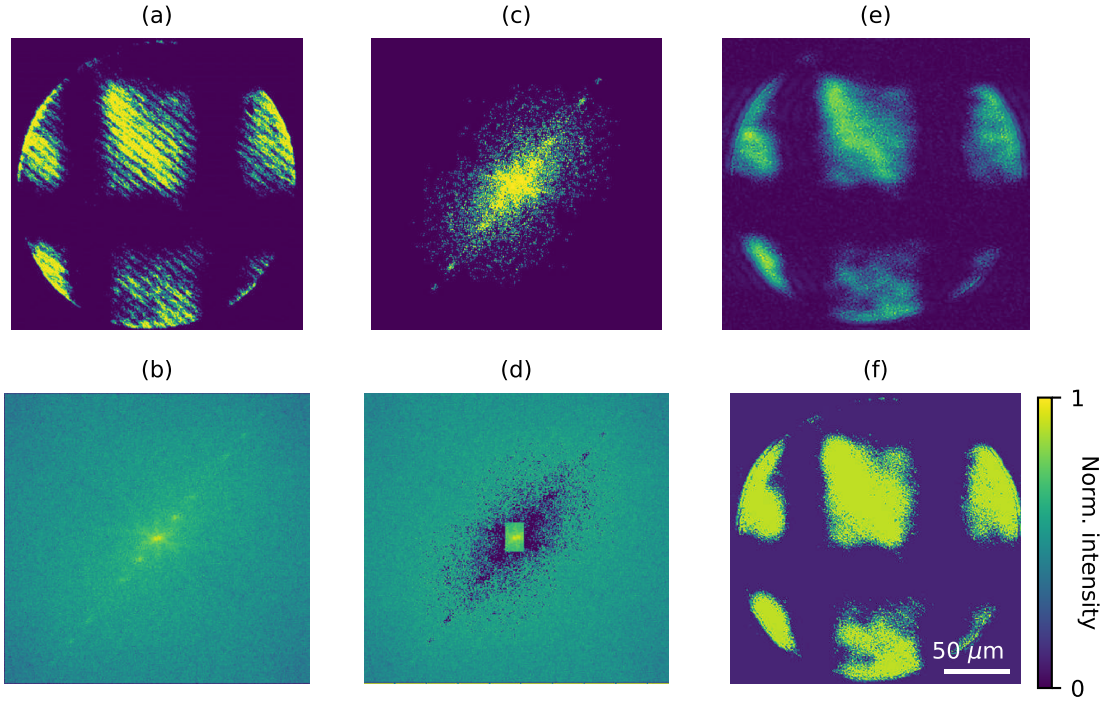


Figure 4.11: Fourier Transform filtration process: (a) Raw ion image from the reflectron MSI taken with a CCD camera, (b) Fourier Transform of the ion image, (c) non-zero frequencies that corresponds to geometrical structures in the ion image, (d) FT after filtration and (e) resultant ion image after Fourier filter has been applied, (f) contrast adjusted Fourier filtered ion image of 343 Da mass peak of Rhodamine B.

The FT ($x(k,l)$) and inverse FT ($x(m,n)$) for an image with $N \times M$ pixels are defined as:

$$X[k,l] = \sum_{m=0}^{M-1}\sum_{n=0}^{N-1} x(m,n)e^{-2\pi i(\frac{mk}{M}+\frac{nl}{N})} \qquad (4.29)$$
$$k = 0,1,M-1, \ ,l = 0,1,N-1\,,$$

$$x[m,n] = \frac{1}{MN}\sum_{k=0}^{M-1}\sum_{l=0}^{N-1} X(k,l)e^{2\pi i\left(\frac{mk}{M}+\frac{nl}{N}\right)} \qquad (4.30)$$
$$m = 0,1,...,K-1, \ ,n = 0,1,...,L-1\,,$$

where k and l are frequencies that correspond to different geometrical features (such as the repeating grid patterns on the sample surface) within the image, and (m,n) are the spatial coordinates. M,N and K,L are the size of the spatial and frequency arrays (which are equal).

Equation (4.29) and (4.30) can be separated using Euler's formula, into a real and imaginary component:

$$e^{i2\pi(\frac{mk}{M}+\frac{nl}{N}))} = \cos 2\pi\left(\frac{mk}{M}+\frac{nl}{N}\right) + i\sin 2\pi\left(\frac{mk}{M}+\frac{nl}{N}\right). \tag{4.31}$$

The FT produces a complex number valued output image which can display an image with magnitude and phase. In image processing, only the magnitude of the FT is normally displayed, as it contains most of the information about the geometric structure of the spatial domain image. However, the phase information of the Fourier image, in this instance, is also retained. This is because it is required to perform the inverse FT (equation (4.30)), after the image has been processed in the frequency domain.

An FT filtering algorithm has been used to remove artificial lines on the ion image of a grid pattern shown in Fig. 4.11 (a). The programme uses the MATLAB module FFT (fast Fourier transforms) [155–157]. The FFT reduces computational time (from weeks to seconds) by expressing the DFT of length N as the sum of two DFTs with length N/2 with the first half consisting of even samples and the second consisting of odd samples, further information can be found [158].

The ion image in Fig. 4.11 (a) is Fourier transformed to give the frequency spectrum shown in Fig. 4.11 (b). The frequency spectrum after the FT displays intense (bright) regions that correspond to geometrical structure (repeating grid pattern) in the spatial domain. In addition, the closer to the centre of the matrix that the intense region occurs, the larger the structure in the spatial domain. Using this information, the regular repeating square pattern can be identified as the central intense spot in Fig. 4.11 (b). The other spots can be attributed to artefacts by repeating this process and filtering different frequencies (which correspond to the other spots in Fig. 4.11 (b)). The artefacts can be removed with a low-pass filter by applying a threshold which if exceeded, results in that element within the matrix being set to zero. All of the elements that exceed the threshold chosen in

the current data set are shown in Fig. 4.11 (c). The location of the low-pass filter is shown in Fig. 4.11 (d). The box at the centre of the image can be adjusted to ensure useful information is retained during the filtering process. The resulting spatial image is shown in Fig. 4.11 (e) has all the stripes removed producing the expected image from the reflectron MSI.

A comparison of the intensity profiles from the ion images is shown in Fig. 4.11 (d). Qualitatively, it can be observed that the signal after the FT is much smoother, as a result of the absence of the stripes in the ion image. The FT does not affect the spatial resolution, which has been optimised for the 343 Da ion of Rhodamine B, and has a value of 11.7 μm in both cases. The convoluted step-wise linear and Gaussian function after the FT has been applied is the same as the function applied to the raw ion image.

Fig. 4.12 (a) shows an ion image of Rhodamine B after centroiding. An intensity profile is integrated across the ion image shown as the pink line in Fig. 4.12 (b). This intensity profile is used to determine the spatial resolution, which is defined as the distance along the profile over which the intensity increases from 20 to 80% of the maximum value (or 30 to 90% of the maximum in instances where the profile baseline is already higher than 20%). The intensity profile is then fitted with a Gaussian function that has been convoluted with a step function to account for the grid pattern, and a linear function to account for the laser incident angle, which is shown in Fig. 4.12 (d). To implement this convoluted function, a script using a SciPy optimise module from the python library has been developed. This script requires four initial inputs which allow the function to converge and determine the spatial resolution: the standard deviation of the convolved function, the pixel location of the two opposite sides of the feature, and the maximum intensity of the feature, as shown in Fig. 4.12.

The spatial resolution determined using equation (4.28) for the ion image in Fig. 4.12 is 11.7 µm ± 2.8 µm.

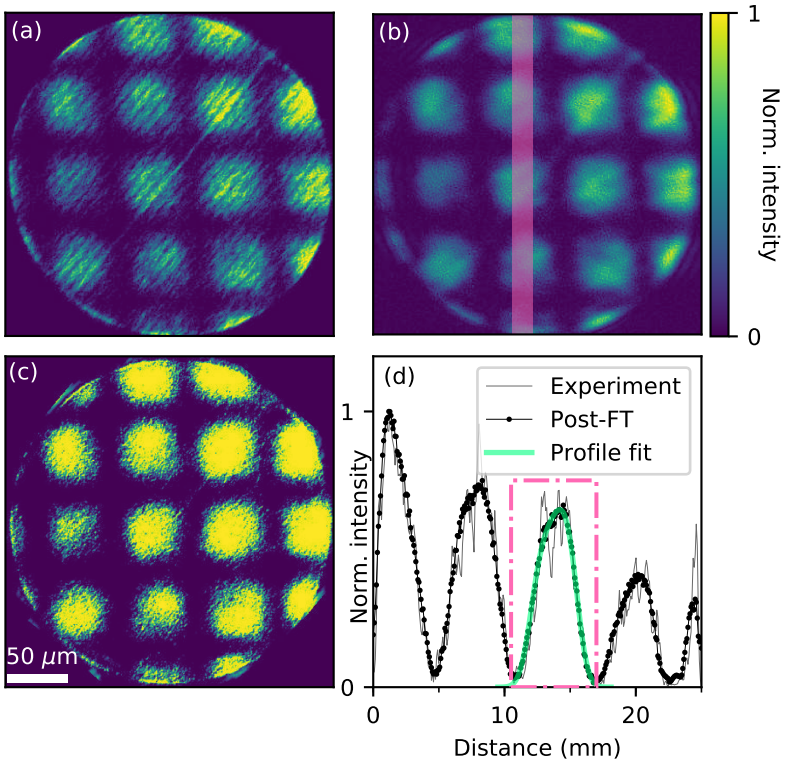


Figure 4.12: The centroided CCD image of Rhodamine B. (a) Ion image gated on the 343 Da mass peak is processed to determine the instrument's spatial resolution. Applying a Fourier transform to the image removes unwanted artefacts (b). Adjusting the image contrast demonstrates the clarity of the resulting grid pattern (c). The spatial resolution is determined from the 20-80% intensity rises observed along profiles running perpendicular to the wire silhouettes in (d). Each profile is fitted using a Gaussian function convolved with a step function representing the grid, and a linear function that accounts for the 20° incidence angle of the laser.

Fig. 4.13 shows how the spatial resolution changes for molecules over a 500 Da mass range. Error bars associated with each data point were determined by recording the spatial resolution of ion images in four identical experiments. The spatial resolution is better than 20 µm over the mass range between 300 - 600 Da. The spatial resolution outside of this range is reduced as the applied electric field is unable to correct the transverse velocities of the ions as they leave the repeller plate. The spatial resolution of Coumarin 450 and Rhodamine 560 Chloride were obtained using a nickel mesh with a 140 µm pitch; a grid pattern with a smaller pitch could not be resolved as the resolution was not sufficient. The instrument can be re-optimised for other mass ranges using velocity corrected ion extraction

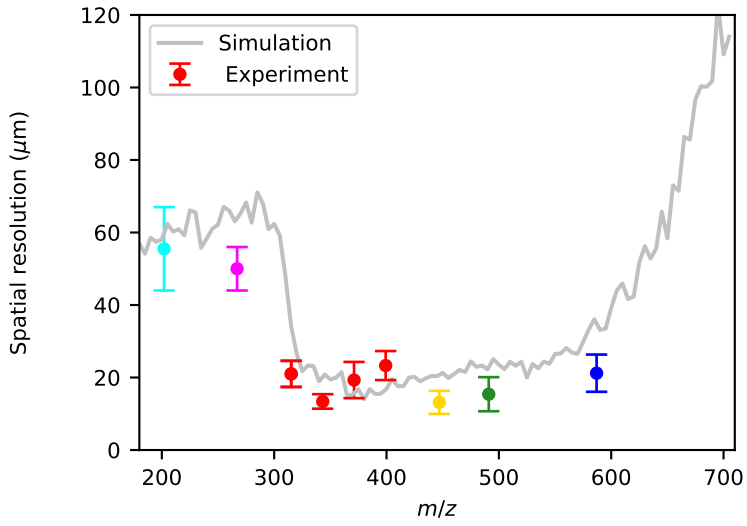


Figure 4.13: The spatial resolution dependence on m/z when the instrument is optimised for 343 Da, categorised using seven laser dyes (cyan = Coumarin 450, pink = Rhodamine 560 chloride, red = Rhodamine B, yellow = Rhodamine 640 perchlorate, green = Rhodamine 6G chloride, and blue = Exalite 404), and compared with simulated data from SIMION 8.1 (grey line). The spatial resolution is better than 20 μm between 300 - 600 Da. The spatially focused window can be shifted to lower or higher m/z ranges by applying a linear scaling parameter to each electrode in the ion microscope [102].

where lighter ions are resolved using smaller potentials, and heavier ions are resolved using larger potentials [26, 139].

4.5 Mass Resolution

The mass resolution R_M, is determined by the modal arrival time for a particular m/z and the FWHM (Δt) of the arrival time distribution of ions created by a laser pulse, $R_M = m/\Delta m = t/2\Delta t$. Δt is determined using the SciPy optimise module [1]. A Gaussian function is fitted to each peak in the ToF spectrum, shown as a black dashed line on the inset in Fig. 4.14 (a). To fit the function, four initial guessed inputs are made: x-coordinate of modal time of each peak, maximum intensity of the ToF peak, minimum height for a peak in the ToF spectra before a curve is fit, and the standard deviation of the intensity distribution. A minimum peak threshold prevents electrical noise from the photo multiplier tube being mistaken

[1] https://docs.scipy.org/doc/scipy/reference/optimize.html

for ion events. This is set depending on the individual spectrum: if a higher laser power is used, the signal-to-noise ratio is high and the minimum threshold is set at a low value, conversely if the laser power is low, the signal-to-noise ratio is low and the threshold has to be more carefully chosen. The initial standard deviation is set at 7 ns which gives the fitting program enough flexibility to calculate efficiently all experimental mass resolutions presented in this thesis. Once a curve has been fitted to the ToF peak the standard deviation σ is determined. This value is then used to approximate Δt:

$$\Delta t = 2\sigma\sqrt{2\ln 2}\,, \tag{4.32}$$

Figure. 4.14 (b) illustrates how the instrument's mass resolution changes with m/z when optimised for 343 Da. SIMION predicts the maximum resolution is 30,000 $m/\Delta m$ at 343 Da, and that it halves within $\pm$ 25 Da. However, convoluting the simulation with the 3.7 ns response time of the Exalite 404 screen (dashed grey line) indicates that the expected measurable resolution will be approximately 8,000 $m/\Delta m$, in agreement with the experimentally determined resolution. The effect of the finite response time of the detector also explains why three of the four m/z peaks observed in Fig. 4.14 (b) have comparable mass resolutions (red circles). By contrast, peaks observed under identical conditions for the remaining six laser dyes lie outside the effective mass range, and demonstrate better agreement with the predicted behaviour, as the FWHM of these dyes is larger that the response time of the detector. The mass spectra for each molecule used in the characterisation are shown in Fig. 4.15.

Consistent with spatial resolution, fixed ion optical potentials focus a particular m/z, and centre the effective mass range of the instrument around this point. The focused m/z can be changed by adjusting the potentials applied to each electrode, but keeping their ratio constant [139]. Higher potentials focus ions with larger

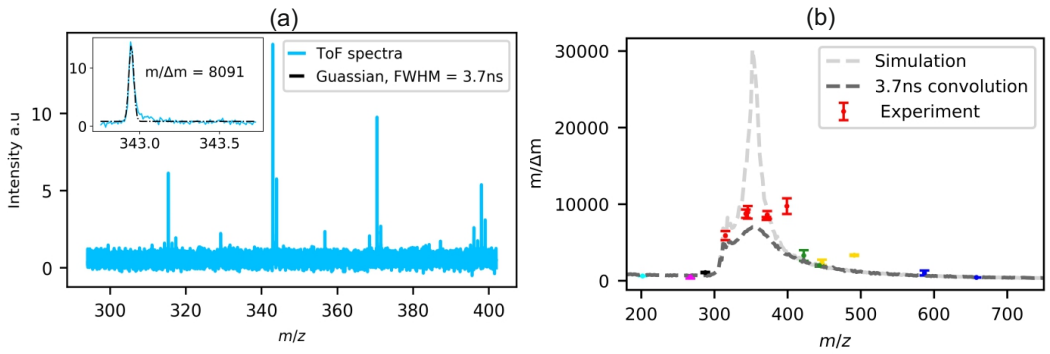


Figure 4.14: (a) The Rhodamine B mass spectrum fitted with a Gaussian function and acquired using optimal potentials shown in Fig. 4.16. (b) The mass resolution over a 500 Da mass range, compared with SIMION 8.1 simulations. The different dyes used to categorise the mass resolution are: Cyan = Coumarin 450, Pink = Rhodamine 560 Chloride O, Black = Auromine , Red = Rhodamine B, Green = Rhodamine 6G, Yellow = Rhodamine 640 Percholrate, Blue = Exalite 404.

Peak number (Da)	Mass resolution
316	6900
343	8091
372	7960
398	8062

Table 4.3: Mass resolution for the four peaks selected in Fig. 4.14 (a). The data points are also shown as red scatter points in Fig. 4.14 (b).

m/z and vice versa. Figure. 4.14(a) presents the laser desorption ionisation mass spectrum of Rhodamine B, optimised for its most intense peak at 343 Da and averaged over 2,000 laser shots. The figure inset demonstrates that the mass resolution of this peak which is determined from the full width at half maximum of a fitted Gaussian function (black dotted line), is 8091 $m/\Delta m$.

As mentioned previously, a genetic algorithm can determine optimal variables when applied to a broad search space. However, this optimisation method can still return local minima (although the chance of this can be reduced by increasing the algorithms search time). Furthermore, the experimentally determined optimal values for the spatial resolution differ slightly from those predicted. Therefore, a blunt force approach was used to search the parameter space around the optimal value. The results presented in Fig. 4.16 were acquired using reflectron and PEDA step potentials

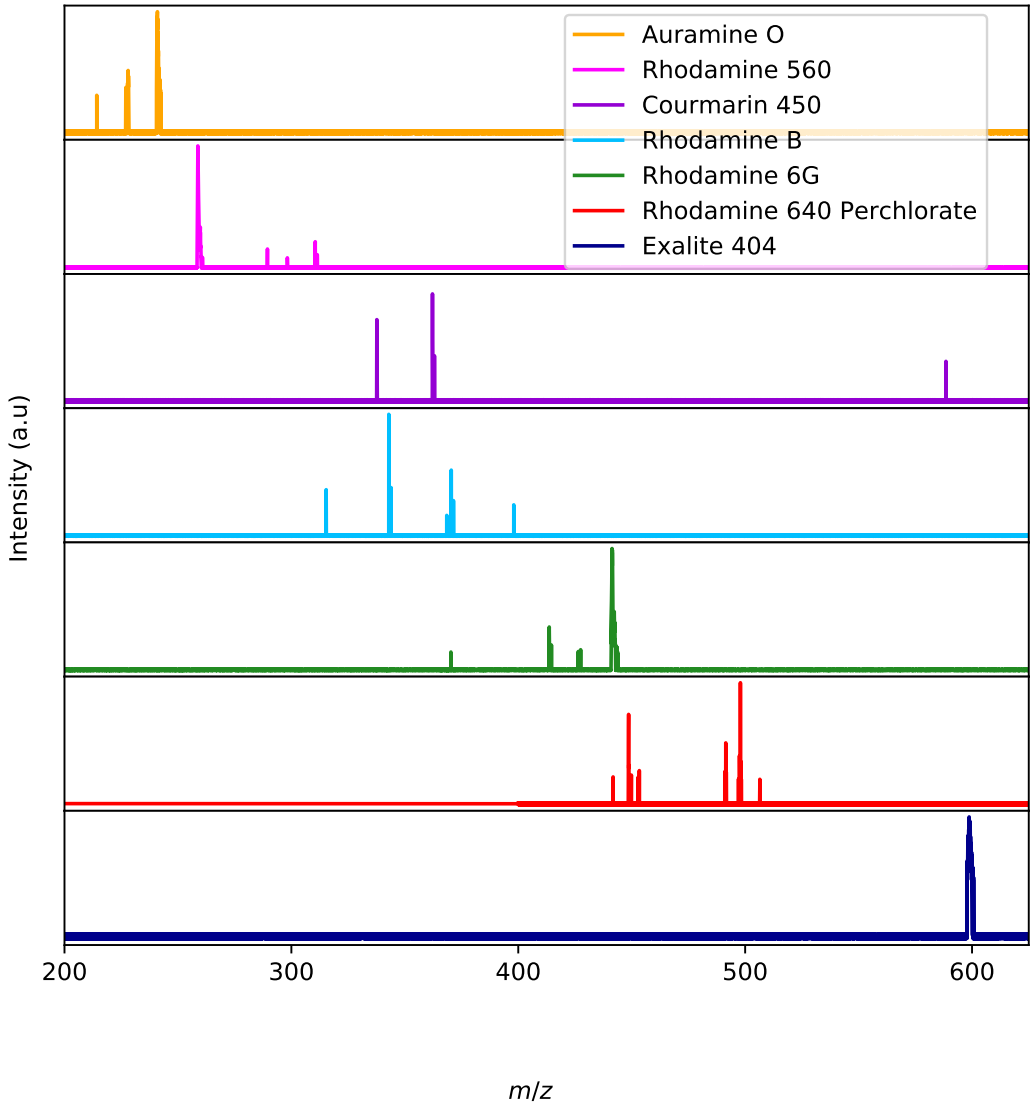


Figure 4.15: Mass spectra for all of the dyes used in the reflectron characterisation. A high laser power (100 mJ per pulse) was used to increase the signal-to-noise ratio in the spectra presented.

of $U_m = 8.75\,\text{kV}$ and $U_P = 0.59\,\text{kV}$. To confirm the optimal conditions, the attainable mass resolutions of 64 combinations of the reflectron and PEDA step potentials were simulated and recorded experimentally in 0.25 kV steps over $U_m = 8.00$ - $9.75\,\text{kV}$, and 0.05 kV steps over $U_P = 5.1$ - $5.45\,\text{kV}$. The results are illustrated in Figs. 4.16 (a) and (b) for the experiment and the simulation, respectively. Both data sets have a maximum resolution at $U_m = 8.75\,\text{kV}$, and only vary in U_P by one step. This peak represents the point at which the PEDA focal plane is successfully mapped onto the

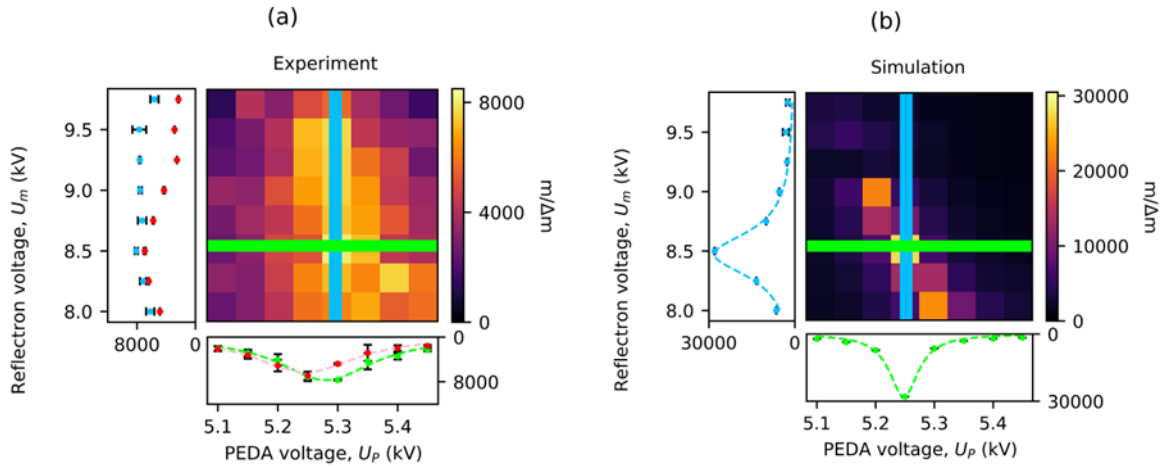


Figure 4.16: The measured (a) and simulated (b) mass resolutions as functions of the applied PEDA (U_P) and reflectron potentials (U_m), when focused for 343 Da. The global maxima represent the measured ($8100 \pm 700\, m/\Delta m$) and simulated ($30200 \pm 2900\, m/\Delta m$) points at which the PEDA pseudo-source plane is focused onto the detector by the reflectron. The blue and green traces crossing these maxima illustrate how the instrument depends on each parameter, as detailed in the text. Projections of each trace (blue and green circles) demonstrate the mass resolution dependence on U_m and U_P. The experimental results are comparable to the simulated data when the latter is convolved with the 3.7 ns response time of the detector shown as red circles in (a).

detector by the reflectron. A comparison of the experimental data in Fig. 4.16 (a) (blue and green circles) with the convoluted simulations (red circles) demonstrates agreement for the change in PEDA voltage, however, the reflectron potential exhibits a flatter profile, illustrating the resolution limit imposed by the scintillator.

4.5.1 Pseudo-source

Figures 4.16 (a) and 4.16 (b) also reveal an inverse relationship between the applied reflectron and PEDA step potentials. This can be understood in terms of the first-order energy-focusing condition (equation (4.14)) for a single-stage reflectron:

$$E_R = \frac{U_m}{d_r} = \frac{4U}{L(U)}\,, \tag{4.33}$$

where E_R is the electric field within the reflectron, d_r is the length of the reflectron, U_m is the voltage on the last plate in the reflectron stack, U is potential energy of

U_P (kV)	U_m (kV)	L (mm)	d (mm)	$m/\Delta m$
5.15	9.00	373	327	7100
5.20	8.75	541	336	18000
5.25	8.50	672	353	30200
5.30	8.25	759	365	17700
5.35	8.00	825	374	8900

Table 4.4: A table comprising simulated data where L is the distance between the first temporal focus and the entrance of the reflectron, d_r is the distance between the entrance of the reflectron and the maximum distance that an ion travels into the reflectron. The reflectron voltage listed in the table corresponds to the maximum mass resolution achieved for a given PEDA voltage in Fig. 4.16. There is an inverse linear relationship between the PEDA voltage (U_P) and the reflectron voltage (U_m). In addition, there is a linear dependency between L and d_r consistent with the conditions required for first-order temporal focusing.

the ion, and $L(U)$ is the combined length of the field-free region from the pseudo-source to the entrance of the reflectron and from the first charged plate of the reflectron to detector (previously L_5 and L_6).

Increasing the applied PEDA potential raises the average kinetic energy U of the focused m/z packet. This lengthens the field-free drift distance L between the PEDA temporal focal plane and the detector. This plane doubles as the pseudo-source for the reflectron. L can be thought of as a function of U, $L(U)$, so long as it remains fixed during a particular experiment. The PEDA time-of-flight equations can further be used to show that a small increase in U leads to a greater increase in $L(U)$, which decreases the required electric field E_R needed to satisfy the reflectron focusing condition. A screen-grab from SIMION, shown in Fig. 4.17, shows that the position of the pseudo-source moves towards the entrance of the reflectron when the PEDA voltage is decreased from 5.25 kV to 5.1 kV. The change in potential of the PEDA electrode increases the ions' potential (U), to satisfy the temporal focusing conditions in equation (4.33), the distance the ions travel into the reflectron d_r, must increase, which is achieved by lowering the potential U_m - resulting in an inverse relationship between PEDA voltage and reflectron voltage, consistent with Fig. 4.16. The inverse correlation observed between U_m and U therefore indicates that increasing the latter does not significantly affect the distance, d, that the

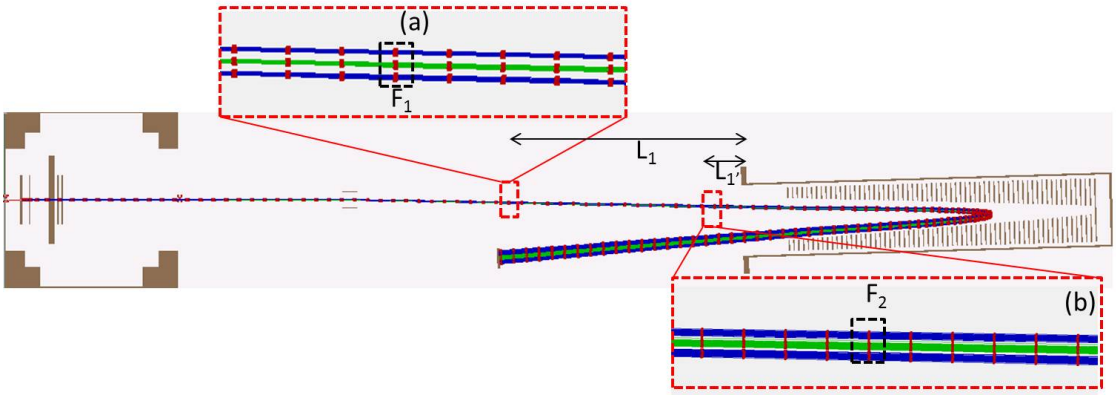


Figure 4.17: A screen-grab from SIMION showing the change in position of the pseudo-source (F_1 and F_2). Red dots indicate ion positions at 0.1 μs intervals. The position is dependent on the PEDA voltage U_P. (a) $U_P = 5.25$ kV, corresponding to L_1, results in optimal mass resolution. (b) For $U_p = 5.1$ kV, L_1 decreases (L_1'), resulting in a reduced mass resolution. L_1 can be increased moving the temporal focus closer to the entrance of the reflectron.

ions travel in the reflectron. This is shown in Table. 4.4. This trend appears in both the simulated and experimental data, although the latter is again obscured by the 3.7 ns emission lifetime of the scintillator.

The previous subsections have shown the optimisation process for each variable in the reflectron MSI mass spectrometer that affect the mass and spatial resolution. Combining these optimised variables provides the best achievable experimental resolution. Table. 4.5 details these optimised parameters, the corresponding ion image is shown in Fig. 4.11 (a).

For charged particles travelling through a uniform electric field formed from two parallel planar electrodes with voltages of V_1 and V_2, respectively, the motion of two particles with different masses (m_1 and m_2) can be overlapped by tuning the acceleration potential by a scaling factor of x whilst maintaining the ratio between V_1 and V_2:

$$\frac{V_1 - V_2}{m_1} = \frac{xV_1 - xV_2}{m_2} \,. \tag{4.34}$$

where x can be deduced from the ratio between m_1 and m_2 ($x = m_2/m_1$). Therefore,

Variable	SIMION (kV)	Experiment (kV)
U_R	5.00	5.00
U_E	4.712	4.681
U_P	5.25	5.300
U_i	1.715	1.680
U_D	0.070*	0.055*
U_m	8.500	8.500
θ_R	1.0	0.72

Table 4.5: Optimal parameters for each variable in the reflectron-microscope instrument. * These voltages do not affect the instrument's resolution for the reasons explained in the text.

the optimal PEDA window can be changed by adjusting the applied extraction field according to the m/z range of interest. This is achieved without changing the image magnification or the mass and spatial resolutions [102].

The optimised parameters predicted by SIMION are close to those found to be optimal in the laboratory, but they do differ slightly. The discrepancy is due to a number of factors. First, the applied voltage in the experiment is fed through a high voltage switch, which may reduce the output voltage to the electrode. Furthermore, the simulations assume cylindrical symmetry throughout the instrument, this is not the case in reality. For example, the simulations ignore the circuit board that houses the resistors used to apply the correct voltage to each electrode in the reflectron stack. However, this simplification *in silico* is difficult to avoid, otherwise the simulations would take significant amounts of time to complete.

4.6 Fast imaging sensors

Fast imaging sensors can simultaneously record mass spectra and ion images. Furthermore, they can record ion images for every event in a mass spectrum, if they are separated by at least two time bins can be recorded. This is a significant advantage as it increases the efficiency of data collection compared with a CCD camera. More information on the pixel architecture can be found in Chapter 2.

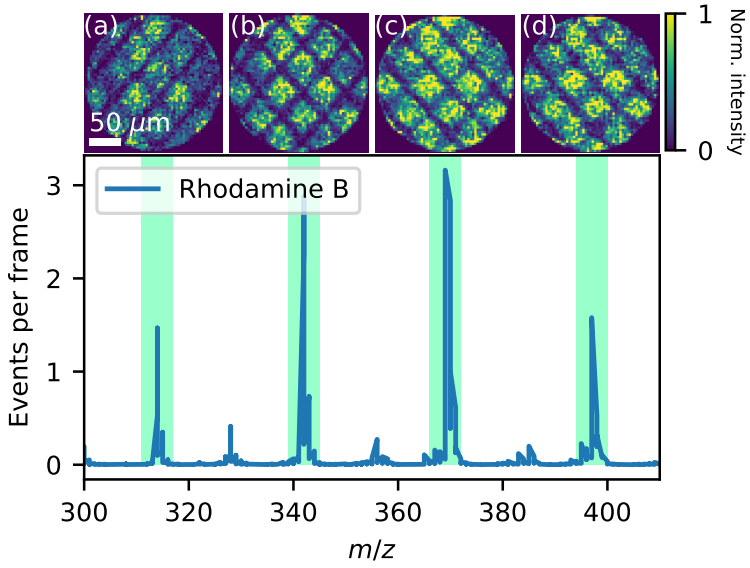


Figure 4.18: Multi-mass imaging data acquired using the PImMS1 sensor for Rhodamine B under the optimal conditions detailed in Chapter 4. Integrating over position (x, y) returns the mass spectrum, while integrating over the shaded time-of-flight peaks creates individual ion images for each m/z (a-d). The 12.5 ns precision of PImMS1 provides a mass resolution of 1600 $m\Delta m$ at 343 Da.

Fig.4.18 shows the mass spectrum of Rhodamine B recorded using a PImMS fast imaging camera installed with the 72 x 72 pixel PImMS1 sensor. The 12.5 ns timing precision of PImMS1 limits the achievable mass resolution in this case to 1600 $m/\Delta m$, but is more than sufficient to resolve ion images for each observed mass peak. Integrating the (x, y) data over the shaded time-of-flight ranges produces the ion images in Figs 4.18 (a-d). These are consistent with the dependency of spatial resolution on m/z shown in Fig. 4.13; Fig. 4.18 is centred on the focused m/z of 343 Da and is the best resolved. The data set is Fig. 4.18 was acquired with 9000 laser shots, and then spatially and temporally centroided [159].

Developments in fast imaging sensors have increased their achievable timing precision to 1.5 ns. This corresponds to a mass resolution of 24000 $m/\Delta m$ in vacuum over the mass range of Rhodamine B, and would allow the achievable mass resolution of the reflectron to be fully exploited, paving the way toward ion imaging of complex mass spectra.

Instrument	Mass resolution($m/\Delta m$)	Spatial resolution (µm)
Suits reflectron VMI	560	n/a
Linear ToF	≈3000	20 µm
Reflectron	≈1000	20 µm
Reflectron + PEDA	≈8000	14 µm

Table 4.6: Mass and spatial resolution for a linear ToF ion microscope and the reflectron ion microscope (with and without PEDA). Experiments performed with the Suits VMI used a P47 phosphor screen, and the Linear ToF and Reflectron used a exalite 404.

4.7 Conclusion

Incorporating a reflectron into an imaging microscope mass spectrometer allows the simultaneous achievement of a mass resolution of approximately 8100 $m/\Delta m$ and a spatial resolution approximately 12 µm. The experimental results shown above indicate that incorporating a reflectron into the PEDA MSI instrument will meet the goal of improving its mass resolving power without sacrificing its high spatial resolving power: mass resolution and spatial resolution are improved compared with the linear microscope ToF. Table. 4.6 compares the different variants of the instrument.

Development of the reflectron MSI provides a method for analysing biological samples with a high mass resolution requirement. For example, the mass peaks of the peptides Arg-Leu-Asp-Val-Leu-Gln (protonated molecular ion peak ($[MH]^+$) at 743.4 Da), which comprises ion peaks at 385.814 and 385.867 Da. These two ions commonly appear in the mass spectrum as two adjacent mass peaks which are only 0.053 Da apart. To distinguish these two peaks and obtain their respective spatial distributions, the microscope MSI instrument needs a mass resolution above 6750 $m/\Delta m$. The reflectron MSI instrument is able to perform this task, whilst the other instruments in Table. 4.6 cannot. Furthermore, this instrument can be re-tuned to operate in velocity map imaging conditions, paving the way for Coulombic explosion mechanisms of large molecules to be elucidated [152].

The mass range over which the mass resolution is optimised using the reflectron MSI instrument is approximately 25 Da. The spatial resolution is optimised over

a 300 Da mass range. The next chapter details a method to increase the mass range, of the reflectron MSI over a 300 Da mass range without comprising the spatial resolution.

5 Time-dependent velocity correction

5.1 Introduction

Ion optical focusing with fixed voltages optimises the mass and spatial resolutions for a specific mass-to-charge ratio, with the consequence that both resolutions decrease at higher or lower m/z. For this reason, post extraction differential acceleration (PEDA) techniques have been developed for microscope MSI to improve the mass resolution over wider mass ranges without compromising the spatial resolution.

As mentioned in previous chapters, the mass resolution in microscope ion imaging is defined by the temporal distribution of ions, for a given m/z arriving at the detector. This spread can be reduced with PEDA. In an experiment that uses the PEDA technique, an ion packet is extracted from the surface following ionisation and the potential of the extraction electrode is increased after the ions have passed through it. The pulse is applied after the ions have exited the extraction region and are located in the acceleration region, so their spatial information is retained in contrast to delayed extraction methods. Ions with slower initial velocities gain more kinetic energy from the voltage pulse compared with faster ions. This creates a temporal focus point that can be superimposed onto the detector using an einzel lens. This results in improved mass resolution by correcting the initial velocities along the

ToF axis. In the original PEDA technique, developed by Aoki *et al.*, a single m/z is focused [97]. Using this approach, the mass range, where the mass resolution is improved, corresponds to approximately 19% of the range that can simultaneously be spatially resolved with the reflectron MSI presented in the previous chapter.

To apply the benefits of PEDA over a wider mass range, multiple m/z must be focused during an experiment. The mass range over which the mass resolution is improved can be extended to cover approximately 39% of the spatially-resolved window using a double-field PEDA method [99]. With this method, the acceleration region is divided in half by placing an additional electrode between the extractor electrode and entrance to the einzel lens. The potential of this additional electrode is then increased at the same time as the extraction electrode - different mass ions are in different regions. The potentials of the two electrodes create two foci, resulting in two masses being focused. If the chosen masses are similar, the resolution between the masses is also improved. This results in heavier ions in the early region achieving temporal overlap at the same drift distance as lighter ions in the late region. This approach can, in principle, be extended by using multiple additional electrodes to focus a broader mass range. However, this is impractical as it would require many thin electrodes placed in close proximity to each other, each with a unique voltage.

This chapter presents a practical alternative that adjusts the potential of the extraction electrode by applying a time-dependent pulse voltage. This is in contrast to single- and double-field PEDA where the voltage increase is fixed. Applying a time-dependent voltage allows increasingly heavy ion species to be sequentially focused as they pass through the ion microscope. This broadens the mass range where the mass resolution is improved to cover more than 100% of the spatially-resolved mass range. This improvement allows every imaged compound to be acquired with high mass resolution.

5.2 Theory and simulation

The ToF spread observed when ions with the same m/z are emitted from a surface, with a distribution of initial velocities, can be reduced by using PEDA. In MALDI/LDI experiments, the initial velocities of the generated ions are independent of mass, and are approximately equal to the average velocity of the ejected ions [31, 160]. Therefore, heavier m/z ions will have larger ToF distributions compared to lighter ions. Note, this is still true when the initial velocities are mass-dependent, as their relative contributions to the final velocities will still be larger for heavier m/z. The PEDA pulse voltage must therefore be chosen to focus a particular m/z, with a higher potential on the extractor required to correct the velocity distribution of heavier ions.

Fig. 5.1 illustrates the electrodynamic PEDA method. The spatial resolution is retained as the pulse is applied after ions have left the extraction region (L_1). Heavier ions travel slower than lighter ions and therefore travel a shorter distance through the acceleration region (L_2) when the electrodynamic pulse is applied. These ions gain a larger increase in kinetic energy. Furthermore, within each ion packet, ions with slower initial velocities will be closer to the extraction electrode when the pulse is applied and will accelerate to overlap with faster ions, creating a temporal focus point. The six different coloured lines in Fig. 5.1 represent a continuum, not distinct steps, and show the change in potential for different mass ions. By raising the potential of the extraction electrode as a function of time, electrodynamic PEDA extends the benefits of single-field PEDA to a wider mass range.

The following sections present results for linear time-dependent PEDA and introduce a quadratic time-dependent PEDA. Quadratic PEDA has a potential function that can further improve the mass resolution over a larger mass range. The ion flight times for each variant are first determined using equations of motion to verify that the temporal spread can be reduced with this technique. The parameters that produce optimal mass resolution over a 600 Da mass range are estimated using

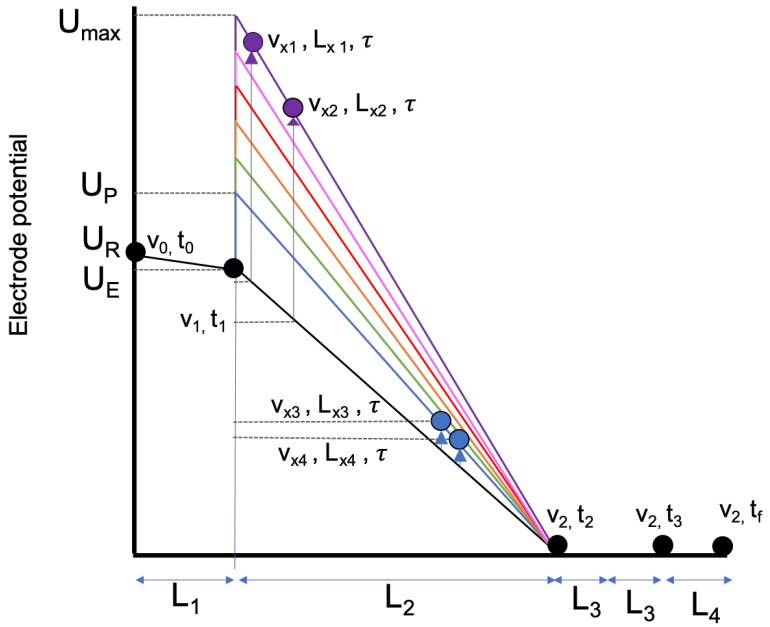


Figure 5.1: A cartoon showing the potential energy of an ion travelling through the electrodynamics ion optics. L_{1-4} are the separations between the electrodes (extraction region, acceleration region, length of the einzel lens, and field free region respectively). U_R is the repeller voltage, U_E is the extractor voltage, and U_p and $U_{\max}$ are the pulse voltage and maximum voltage applied to the extractor electrode, after a switch time τ - which is defined relative to t_0. The black circles represent ions with a distribution of mass and initial velocity. In the acceleration region four ions are shown: heavier ions - two purple circles with different velocities; lighter ions - two blue circles with different velocities. The different coloured lines show the different increases in the potential received by different mass ions, that are determined by the location in the acceleration region when the pulse is applied. v_{xn} and L_{xn} (for n = 1,2,3,4) are the velocities and positions in the acceleration region for the different mass ions when the pulse is applied. t_{1-3} is the ion flight time and the end of each region in the ion optics. t_f is the temporal focus for each mass ion.

the transfer matrix method (discussed in Chapter 6) and a Nelder-Mead simplex minimisation algorithm [161]. A SIMION simulation of the two PEDA variants combined with a reflectron, is then optimised using a genetic algorithm. This is followed by a comparison of the flight time differences for each pulsed technique, demonstrating the ability to improve the mass resolution over a wider mass range.

The experiments presented in this chapter use an exponential pulse shape which has an approximately linear increasing potential for ions between 300 - 600 Da, for which this mass spectrometer is optimised to record ion images. An exponential pulse shape is used because it is relatively simple to generate experimentally

compared with other pulse shapes.

5.2.1 Linear time-dependent PEDA

The ion optical system described in Fig. 5.1 creates separate ion extraction and differential acceleration regions. In the former, an ion is generated from the sample plate and then accelerated through a potential difference U_E towards the extraction electrode over a distance L_1. The velocity at the end of the extraction region, v_1 and flight time, t_1, are:

$$v_1 = \sqrt{\frac{2}{m}\left(q(V_R - U_E) + \frac{mv_0^2}{2}\right)}\,, \tag{5.1}$$

$$t_1 = \frac{mL_1v_0}{q(V_R - U_E)}\left(-1 + \sqrt{\frac{2q(V_R - U_E)}{mv_0^2} + 1}\right)\,. \tag{5.2}$$

The ion then enters the acceleration region and passes through a potential difference U_E, as it accelerates towards the grounded entrance of an einzel lens at $L_1 + L_2$. After a set time τ (switch time), the ion is located within this region at L_{xn} (where n represents ions with different m/z):

$$L_x = v_1(t_2 - \tau) + \frac{qU_E(t_2 - \tau)^2}{2mL_2}\,, \tag{5.3}$$

with a velocity v_x:

$$v_x = \sqrt{v_1^2 + \frac{2qU_EL_x}{mL_2}}\,. \tag{5.4}$$

At the switch time, τ, electrodynamic PEDA is initiated by applying a time-dependent potential $V_L(t,k)$ on the extractor, where k is the rate constant of the pulse defined by the resistance and capacitance. In the following experiments, the electrode is raised exponentially by a PEDA step potential, U_p, and continuously increases until it reaches a maximum potential $U_{\max}$. The step voltage, U_p, defines the first mass that is focused with this technique. The larger U_p the larger the

m/z of the first focused mass. If $t \geq \tau$ the voltage on the extractor at a particular time, in the experiment is defined by:

$$V_L(t,k) = U_p + (U_{\max} - U_p)\Big(1 - e^{-k(t-\tau)}\Big) \; . \tag{5.5}$$

The electrode potential is equal to U_E. When $t_2 - \tau$ is small i.e just after the pulse is applied, the function has an approximately linear increase. When $t_2 >> \tau$ the pulse shape is curved as it approaches $U_{\max}$, but by this time the ions of interest have left the acceleration region and are therefore unaffected. The voltages, U_p and $U_{\max}$, in addition to k, are appropriately chosen so that all ions of interest are subjected to the approximately linear voltage increase. Under these dynamic conditions an ion will exit the acceleration region with a velocity v_2 after a flight time t_2:

$$v_2 = v_x + \int_{\tau}^{t_2} a(t,k)\, \mathrm{d}t \; . \tag{5.6}$$

where a is the acceleration of the ion in the electric field:

$$a = \frac{qV(t,k)}{mL_2}. \tag{5.7}$$

Substituting equation (5.7) into equation (5.6) allows the velocity of the ion as it leaves the acceleration region to be determined:

$$v_2 = v_x + \frac{q}{mL_2}\Big(U_P(t_2 - \tau) + (U_{\max} - U_p)\Big((t_2 - \tau) + \frac{e^{-k(t-\tau)}}{k}\Big)\Big) \; . \tag{5.8}$$

Integrating v_2 with respect to time t_2, satisfies the following equation, which can be solved numerically or through a Taylor expansion to determine $t_2 - \tau$ and hence:

$$L_2 - L_x = v_x(t_2 - \tau) + \frac{q}{mL_2}\Big(\frac{U_P(t_2-\tau)^2}{2} + \frac{(U_{\max} - U_p)(t_2-\tau)^2}{2} - \frac{(U_{\max} - U_p)e^{-k(t_2-\tau)}}{k^2}\Big) \; . \tag{5.9}$$

After leaving the acceleration region, the ions travel through a conventional three-electrode einzel lens and field-free drift distance L_4 before they arrive at the detector.

The potential of the middle electrode in the einzel lens is U_i and each electrode is separated by a length L_3. The ions exit the einzel lens with a velocity v_2, which is the same velocity that the ions entered with, after a flight time t_3:

$$t_3 = t_2 + \frac{2mv_2L_3}{qU_i}\left(1 + \sqrt{\frac{1-2qU_i}{2mv_2^2}}\right) \tag{5.10}$$

The total ToF, t_f, for a particular ion is:

$$t_f = t_3 + \frac{L_4}{v_2} \tag{5.11}$$

The PEDA pulse corrects the velocity distribution for a given m/z; ions with slower initial velocities leave the einzel lens with a larger v_2 than ions with faster initial velocities. A particular m/z will therefore reach a temporal focus within the drift region. The position on the ToF axis where this temporal focus occurs is defined by the switch time and the magnitude of the pulse. These are appropriately chosen so that the temporal focus occurs at the position-sensitive detector. Electrodynamic PEDA allows additional (heavier) m/z to be consecutively focused onto the same point.

With a fixed resistor-capacitance combination $(1/k)$, the flight time t_f for ions travelling through the electrodynamic PEDA optics is a function of m/z, the initial velocity, the potentials applied to the ion optics (U_R, U_E, U_i, U_p, and $U_{\max}$), the reflectron potential (U_m), and the delay time τ. As shown in Chapter 6, the spatial resolution is determined by $U_R - U_E$. As this instrument is required to retain the spatial resolving capability, these potentials are fixed. Furthermore, as the detector position (or length L_4) is unchanged, the potential of the einzel lens is fixed. This leaves three parameters that can be changed when optimising the mass resolution over a specific mass range, U_p, $U_{\max}$, τ and U_m.

Chapter 4 showed the mass window where the spatial resolution is less than 20 μm is between 325 - 625 Da (this is discussed further in subsequent sections of this chapter). Therefore, an optimal PEDA pulse will increase the mass resolution for

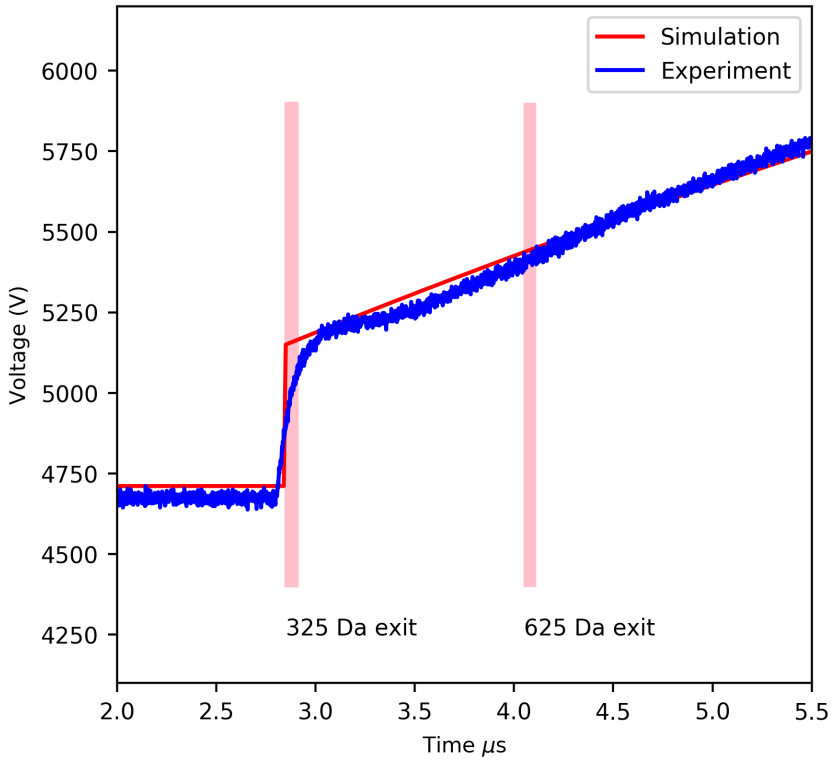


Figure 5.2: The time-dependent voltage applied, as a function of experiment time applied to the extractor electrode in simulation (red) and in the experiment (blue). The resistance and capacitance, which determine the rise time of the voltage pulse, were 200 kΩ and 60 pF, respectively. The step voltage was 5225 V and the maximum voltage was 8600 V. The pink lines indicate when the minimum and maximum mass ions in the optimised mass range exit the acceleration region. The voltage increases with an approximately constant gradient over this region.

ions over this range. First, the pulse time is chosen so that both 325 Da and 625 Da ions are located in the acceleration region when the potential on the extractor is increased. Experimentally, this was found to be when τ was set to 2.85 μs. The pulse shape over this region in shown in Fig. 5.2. The red line indicates the simulated pulse and the blue line indicates the experimental pulse. The shape of the exponential pulse is defined by the resistor-capacitor combination. To form a linear pulse over this region a 200 kΩ resistor was used and a capacitance of approximately 60 pF was inherent to the circuit. The pink lines show the time at which 325 and 625 Da ions exit the acceleration region, indicating the limits of the

mass range for time-variable PEDA. Ions outside of this range are not located in the acceleration region when the initial pulse is applied.

To determine the combination of U_p, $U_{\max}$ and U_m that results in the highest mass resolution over this range, SIMION simulations were completed in two parts. First, the mass resolution for 17,500 combinations of U_p, $U_{\max}$ and U_m for a 325 Da ion were simulated, as shown in Fig. 5.3. These simulations allow the effect on the mass resolution, for changing each variable, to be visualised. Fig. 5.3 (a) shows that the optimal U_p, U_m combination is around 5.150 kV and 8.250 kV respectively. The maximum mass resolution achieved with the electrodynamic optics for a 325 Da ion is approximately 27,000 $m/\Delta m$. It is clear from Fig. 5.3 (b) that the mass resolution for a 325 Da ion does not change significantly when the maximum voltage applied to the PEDA electrode is increased. Moreover, the optimal mass resolution at each U_m step is similar, therefore, U_m is fixed at 8.5 kV for the remainder of this chapter.

The second stage of simulation is to determine the optimal conditions for linear electrodynamic PEDA optic used a genetic algorithm (more detail of the algorithm is discussed in Chapter 3). The genetic algorithm was used to minimise the sum of the standard deviations of the arrival time, for ions between 325 Da - 625 Da. Fig. 5.4 shows the results from three genetic algorithm simulations where the mass range that was optimised is constrained to different ranges: red = 325 - 475 Da, blue = 325 - 550 Da and black = 325 - 625 Da. The mass resolution between the two maxima decreases as the mass range is increased. This can be attributed to the increase in the electrode potential becoming increasingly mismatched with the optimal conditions between the two maxima as mass range increases. This is addressed in the following sub-section with a quadratic electrodynamic pulse that can maintain the maximum resolution over an even broader mass range.

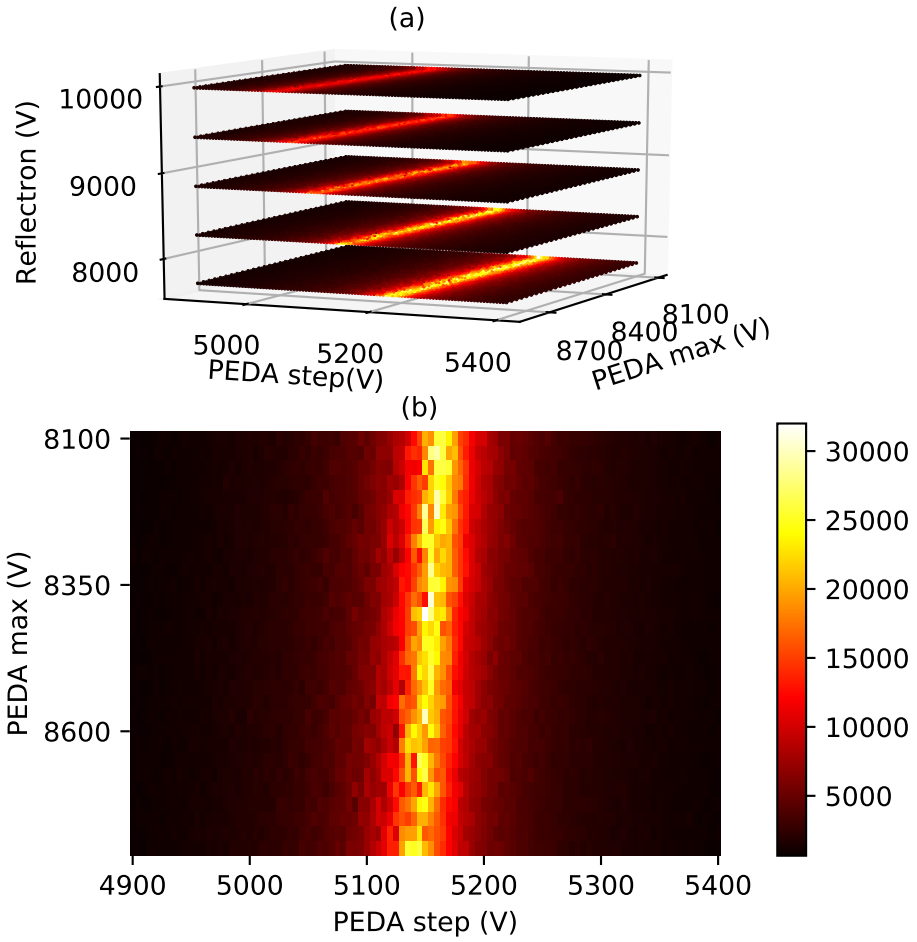


Figure 5.3: Simulated mass resolution for a 325 Da ion as a function of PEDA step voltage (U_p), PEDA maximum voltage ($U_{\max}$) and reflectron voltage (U_m). The colour scale indicates the mass resolution. (a) 17,500 individual simulation showing the dependency of mass resolution on each parameter. U_p was scanned over a voltage range 4900 - 5400 V with a 10 V step size, $U_{\max}$ was scanned from 8100-8800 V with a 10 V step size, and U_m was scanned from 8 - 10 kV in 500 V steps. A reflectron voltage above 8 kV is required to reserve the ion trajectories, and the power supply for the reflectron restricts the maximum voltage to 10 kV. (b) 2D slice from (a) with a reflectron voltage of 8500 V. The maximum mass resolution achieved is approximately 27,000 $m/\Delta m$, when the step voltage is 5150 V. The PEDA maximum voltage does not significantly affect the mass resolution of the 343 Da ion.

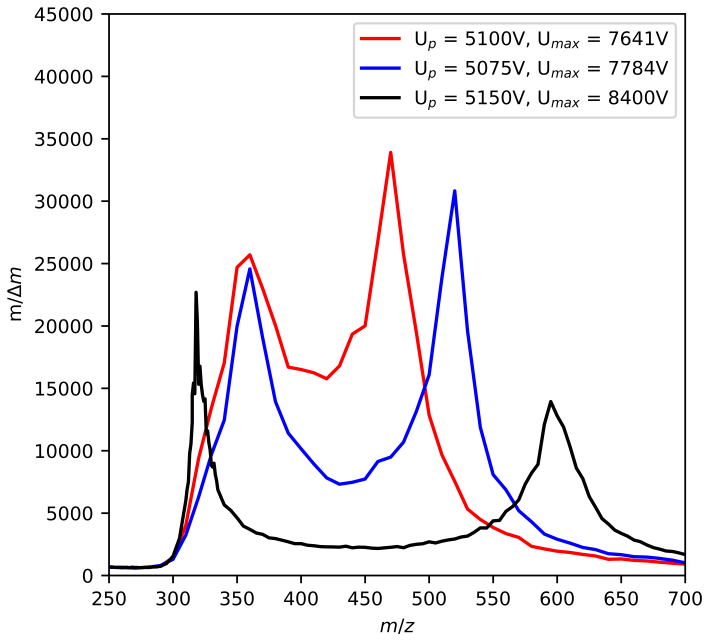


Figure 5.4: Mass resolutions for ions in the range 250 - 700 Da determined from SIMION simulations. U_p and $U_{\max}$ can be customised to change the mass range over which the resolving power is improved.

5.2.2 Quadratic time-dependent PEDA

In a Wiley-McLaren ion optics, the ToF (and therefore the mass resolution) is proportional to $\sqrt{m/z}$ [8]. The five plate ion optics presented in this chapter have a similar proportionality. This proportionality means that a quadratic pulse shape can more accurately provide the potential required to improve the mass resolution over a wider mass range, than a pulse that increases linearly with time.

The linear electrodynamic pulse can only match the quadratic behaviour at a maximum of two points. It is therefore expected that it will create two temporally focused maxima, with reduced performance in between. This effect can be seen in Fig. 5.4, where the two focused masses are separated by mass range with reduced resolving power. This occurs because after the initial focal point at 325 Da in Fig. 5.5, the linear case overcompensates for the kinetic energy required to create a temporal focus at the detector.

The velocity of an ion before the time-dependent pulse is the same for each

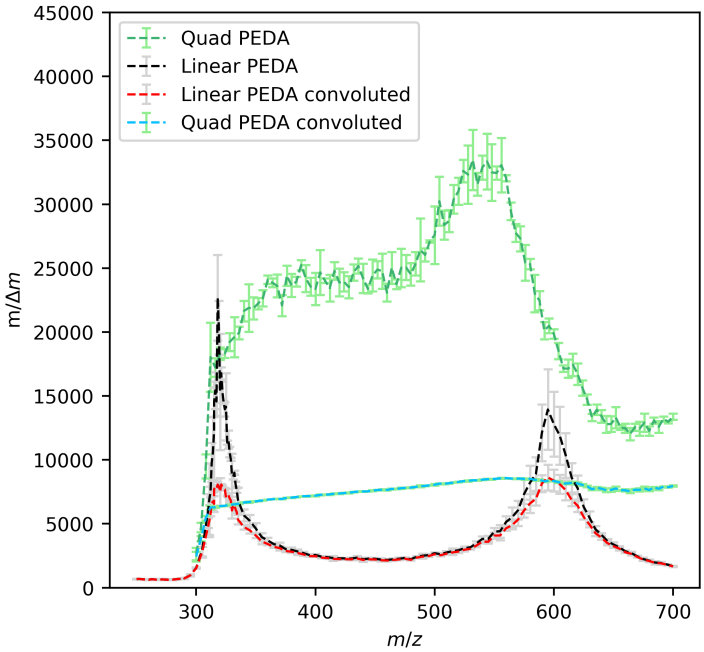


Figure 5.5: Simulated mass resolutions for 250 - 700 Da ions. The black line is resolution recorded when linear electrodynamic PEDA was used. The light green line indicates the mass resolution when a quadratic pulse shape was used. The red and dark green lines show the mass resolutions for linear and quadratic PEDA, respectively, when convoluted with 3.7 ns to account for the instrument response time. The standard deviation was determined by repeating each simulation three times.

PEDA variant and given by equation (5.4). The voltage applied to the extractor plate, V_Q, for the quadratic PEDA variant is defined as:

$$V_Q(t) = \begin{cases} U_p + r(t-\tau) + s(t-\tau)^2\,, & t \geq \tau \\ U_p & \text{otherwise} \end{cases} \tag{5.12}$$

where r and s are constants that determine the gradient of the function. As mentioned previously, the magnitude of U_p defines the m/z of the first focused mass. The velocity of an ion as it leaves the acceleration region, after it has been subjected to the quadratic potential is given by:

$$v_2 = v_x + \frac{q}{mL_2}\left(U_p(t-\tau) + \frac{r(t-\tau)^2}{2} + \frac{s(t-\tau)^3}{3}\right). \tag{5.13}$$

Integrating v_2 with respect to time yields:

$$L_2 - L_x = v_x(t-\tau) + \frac{q}{mL_2}\left(\frac{U_p(t-\tau)^2}{2} + \frac{r(t-\tau)^3}{6} + \frac{s(t-\tau)^4}{12}\right), \tag{5.14}$$

which can be solved numerically to determine $(t_2 - \tau)$ and therefore v_2 from equation (5.13).

Once v_2 is known for a given mass and initial velocity, the total flight time can be determined from equation (5.11). The mass resolution for different combinations of variables can be calculated and optimised. The values for U_p, r and s in the quadratic function, and the pulse time were allowed to vary, all other parameters were fixed. Following their optimisation by a genetic algorithm that minimised the sum of the standard deviations for ion flight times over the range of v_0 (0 - 1000 ms^{-1}) and m/z (300 - 600 Da). U_p and the constants r and s were set to 580 V, $4.990 \times 10^8\,\mathrm{Vs}^{-1}$ and $1.814 \times 10^{13}\,\mathrm{Vs}^{-2}$ respectively. The results are presented in Fig. 5.5.

With a quadratic pulse, the mass resolution is greater than 22,000 $m/\Delta m$ over all ions between 300 - 600 Da. The mass resolution is maximised at approximately 550 Da. This is because the voltage applied to the single-stage reflectron focuses one specific mass as a result of the temporal focusing conditions detailed in Chapter 4. The red and dark green traces in Fig. 5.5 show the mass resolutions for the linear and quadratic PEDA variants after convolution with 3.7 ns Gaussian function, which accounts for the instrument response time [102]. It can be seen from the dark green line that the mass resolution is kept constant over the entire mass range of interest when the quadratic pulse is applied.

If the instrument response time is reduced and mass resolutions greater than 8500 $m/\Delta m$ can be recorded experimentally, it is worthwhile pursuing further improvements to the resolution. Increases in mass resolution are possible if a higher-order polynomial function is used. This would allow the voltage applied to the PEDA optics to more accurately approximate the true relationship between ToF and m/z. This relationship differs from a quadratic as a result of using a five plate ion optic arrangement compared with the three plate configuration used by Wiley and McLaren.

5.2.3 Comparison of pulsed variants

To compare the performance of the four PEDA variant: single-field, double field, linear electrodynamic and quadratic (Fig. 5.6 (a-d) respectively), the time difference t_d, for different mass ions were determined. This was achieved by calculating the expected ToF for different m/z across a range of initial velocities ($v_0 = 0$ - $1000\,\mathrm{ms}^{-1}$) and masses ($m/z = 300$ - $600\,\mathrm{Da}$) and comparing them to flight times determined using an average initial velocity ($\overline{v}_0 = 500\,\mathrm{ms}^{-1}$) for each mass. The time-of-flight difference is defined as:

$$t_d = t_f(v_0, m/z) - t_f(\overline{v}_0, m/z)\ , \tag{5.15}$$

The time of flight difference determined from equation (5.15) is a metric for the expected ToF resolution at the detector. A smaller t_d corresponds to higher mass resolution and vice versa.

The instrument parameters used in the simulation are: $L_1 = 1.45\,\mathrm{cm}$, $L_2 = 3.95\,\mathrm{cm}$, $L_3 = 0.79\,\mathrm{cm}$, $L_4 = 91.02\,\mathrm{cm}$, $U_R - U_E = 450\,\mathrm{V}$, $U_E = 4550\,\mathrm{V}$, $U_i = 1728\,\mathrm{V}$, and $\tau = 2.59\,\mu\mathrm{s}$. Fig. 5.6 (a) and (b) were modelled using the calculations developed by Aoki [97] and Guo [99], respectively. Fig. 5.6 (c) and (d) were modelled by the equations presented earlier in this chapter. The extractor step potential was 930 V for single-field PEDA, and 920 V for the double-field PEDA. The second PEDA electrode of the latter was situated at the midpoint of the acceleration region and raised by 410 V. For the approximately linear electrodynamic PEDA in Fig. 5.6(c), τ was changed to $2.67\,\mu\mathrm{s}$ to optimise the PEDA pulse $V_Q(t, k)$ over the 300 - 600 Da window. The simulations for this variant used $U_p = 544\,\mathrm{V}$, $U_{\max} = 2590\,\mathrm{V}$, and $k = 2.3 \times 10^5\,\mathrm{ms}^{-1}$. The simulation for quadratic PEDA were optimised with $U_p = 580\,V$, $r = 4.990 \times 10^8\,\mathrm{Vs}^{-1}$, $s = 1.814 \times 10^{13}\,\mathrm{Vs}^{-2}$, and $\tau = 2.67\mu\mathrm{s}$.

The linear electrodynamic pulse in Fig. 5.6(c) which can be thought of as a many-field adaptation of the double-field method, improves this result, indicating that it will significantly broaden the overall mass range that can be experimentally

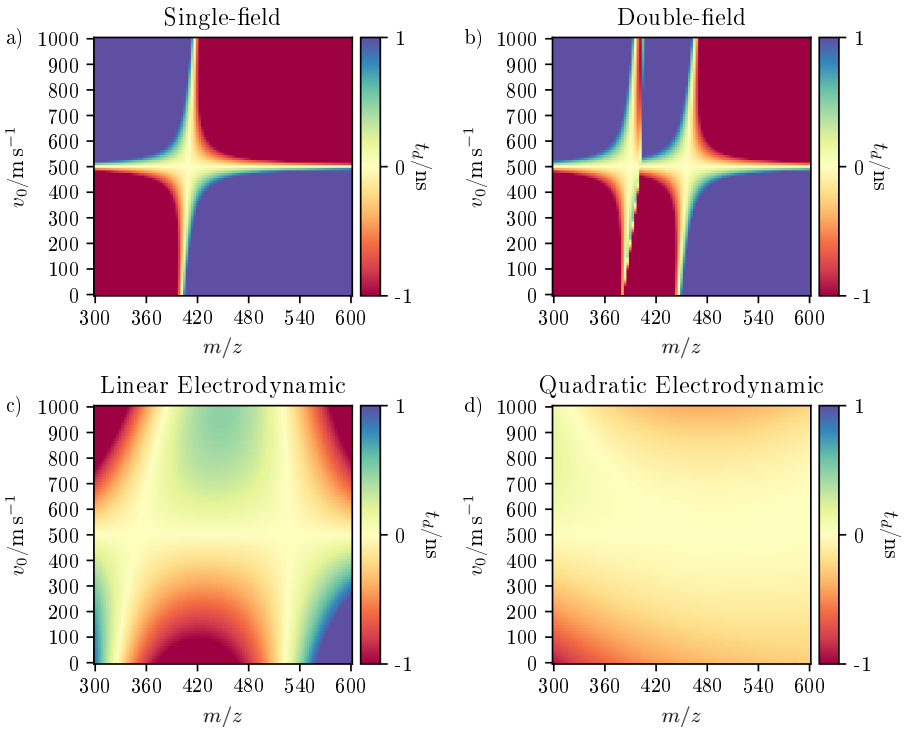


Figure 5.6: Time of flight difference for ions with a mass range 300 - 600 Da and initial velocities 0 - 1000 ms^{-1}. Ions are focused using (a) single-field PEDA, (b) double-field PEDA, (c) Linear electrodynamic PEDA and (d) Quadratic electrodynamic PEDA. The 300 - 600 Da window covers the range over which the ion microscope can experimentally record spatially-focused images, when optimised using the parameters listed in the text. Each map is scaled between ± 1 ns.

imaged, with high mass resolution. Moreover, the quadratic pulse modelled in Fig. 5.6(d) provides further improved performance, focusing the entire window to at least ± 1 ns. However, there are significant technical challenges of developing a quadratic pulse with a rise time less than 10 μs. For this reason, the following section presents the experimental results achieved using the only linear electrodynamic PEDA variant combined with a reflectron ion microscope.

5.3 Experimental methods

Electrodynamic PEDA was tested using a home-built ToF microscope imaging mass spectrometer detailed in Chapter 4. The instrument uses the temporal focus created by the PEDA ion optics as the pseudo-source for the reflectron. With this instrument, ion images have been recorded with mass resolutions as high

as $8100 \pm 700\, m/\Delta m$ under single-field PEDA conditions. Moreover, there is no degradation in spatial resolution caused by the reflectron or the single-field PEDA optics. When using a $22\,\mathrm{Vmm^{-1}}$ extraction field (the optimised spatial conditions determined in Chapter 4), ion images can be resolved to approximately $14\,\mu$m over 300 - 600 Da. This defines the mass range over which the experimental mass resolution will be improved. The mass and spatial resolutions established by electrodynamic PEDA were determined as functions of m/z by recording mass spectra and ion images for six dyes: Rhodamine 560 chloride, Rhodamine B, Rhodamine 6G chloride, Rhodamine 640 perchlorate, BBQ and 4-(2-Carboxyphenyl)-7-diethylamino-2-(7-diethylamino-2-oxochroman-3-yl)-chromylium perchlorate (which is referred to as p12 from here on in). Analagous to the samples imaged in other chapters, each sample was electrosprayed through a nickel mesh onto an ITO plate to produce grids with a $63\,\mu$m pitch.

5.3.1 Mass resolution

Fig. 5.7 illustrates the mass resolution dependence of the electrodynamic PEDA method on m/z. SIMION predicts two focused mass ranges centred at 325 Da and 600 Da when using a quasi-linear pulse shape (grey trace). These maxima reach 8100 and 8400 respectively, with decreased resolution in between, after convolution with 3.7 ns Gaussian function to account for instrument response. Table. 5.1 lists each parameter used in the simulation and the experiment to achieve these resolutions. A 8100 ± 700 $m/\Delta m$ mass resolution determined *in silico* under similar conditions as using a single-field PEDA pulse, shows that using a time-variable pulse to sequentially focus multiple m/z does not significantly reduce the attainable resolution of the instrument. The drop in performance between the two peaks can be attributed to the shape of the applied pulse. A linear function can only intersect a quadratic function at two points, which corresponds to the

Variable	SIMION	Experiment (kV)
U_R	5.0 kV	5.0 kV
U_E	4.712 kV	4.681 kV
U_p	5.150 kV	5.225 kV
$U_{\max}$	8.400 kV	8.600 kV
τ	2.85 μs	2.85μs
U_i	1.708 kV	1.715 kV
U_D	0.055 V	0.055 V
U_m	8.500 kV	8.500 kV
θ_R	1.0°	0.7°

Table 5.1: Optimal parameters for improved mass resolution using time-dependent PEDA between 300 - 600 Da in the reflectron-microscope instrument.

maximised resolutions. Outside of these regions the ideal potential required for temporal focusing is less well approximated, resulting in reduced performance.

The mass resolution determined experimentally is an average of three experiments, with the error bars shown in Fig. 5.7 corresponding to one standard deviation. As discussed in Chapter 4, the mass resolution is determined by fitting a Gaussian function to the ToF peak acquired with a PMT. An optimal mass resolution is attained when a low laser power is used, as surface charge is reduced. The mass resolutions presented in this chapter were acquired with typical laser powers between 20 - 100 mJ/pulse. The measured mass resolutions of six dyes, shown as different coloured scatter points in Fig. 5.7, matches the simulated trend, when the latter is convolved with the 3.7 ns response time of the instrument. The experimental results again tend towards two maxima, with the most resolved point matching the mass resolution of 8100 ± 700 $m/\Delta m$ reported for the single-field PEDA experiment.

The conditions required to achieve the highest mass resolution were determined by setting the voltages of the power supplies to those predicted by SIMION, and then scanning a small range above and below these values. This resulted in parameters that differ slightly from those predicted by SIMION, which are given in Table. 5.1. These inconsistencies are likely a result of differences in capacitance between the experiment and simulation. The simulation used a capacitance of 60 pF. However, it was difficult to measure an accurate experimental capacitance due to its small

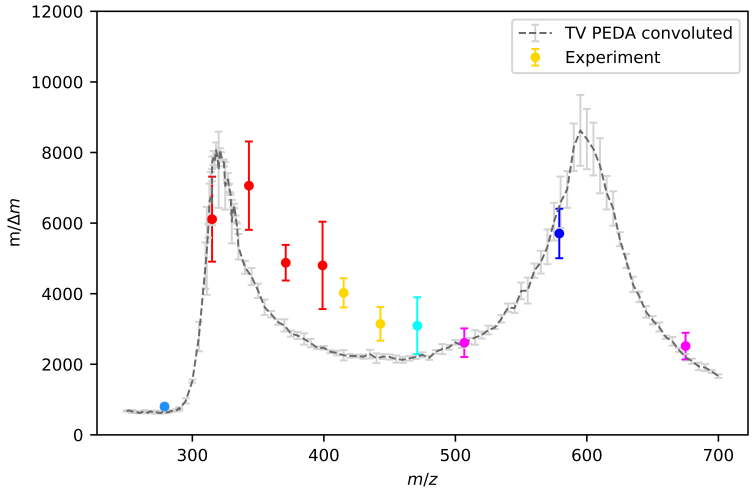


Figure 5.7: Experimental and simulated mass resolutions for 250 - 700 Da ions.The grey line represents the simulated resolution convoluted with a Gaussian instrument function with a 3.7 ns width. The experimentally determined mass resolutions are shown as scatter points: Light blue - Rhodamine 560 chloride, Red - Rhodamine B, Yellow - Rhodamine 6G chloride, Cyan - Rhodamine 640 perchrolate, Pink - BBQ and Navy Blue - p12 . The chosen range corresponds to the spatially-resolved mass range.

magnitude. An average capacitance of 60 pF recorded over three readings, in which the capacitance varied by approximately 20 pF, was used. Furthermore, geometry assumptions in the simulation such as cylindrical symmetry around the time-of-flight axis may not adequately describe the electric fields within the instrument, therefore causing the resolution to differ.

5.3.2 Spatial resolution

The experimental results in this chapter have focused on the linear electrodynamic PEDA variant that can improve the mass resolution over a wide mass range. However for this technique to be useful the spatial resolution must not be affected. This sub-section examines the spatial resolutions for ion images acquired using electrodynamic PEDA.

The ion images are acquired by gating the CCD camera over the mass peaks of interest. The ion images of nine different mass peaks are shown in Fig. 5.8. The image for a 288 Da ion is distorted as this mass is outside the optimal mass

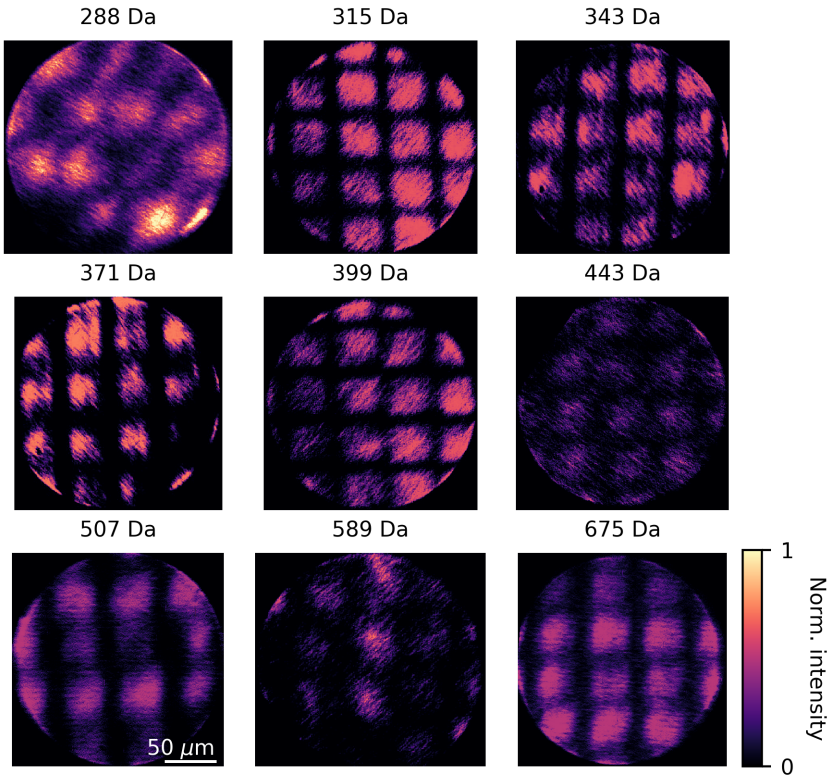


Figure 5.8: Ion images recorded with a CCD camera from the reflectron MSI, using electrodynamic ion optics in the region where the potential increases nearly linearly with time. The ions in the 315 - 625 Da region lie within the optimised mass window and show well-resolved grid patterns in their images, whereas the 288 Da ion lies outside that range and its image are unfocused.

window, therefore the used voltages are inadequate for focusing this particular mass. All other ion images are within the optimised mass range; the spatial resolution allows the grid patterns to be observed.

The electrodynamic variables (U_p, $U_{\max}$ and τ) can be adjusted to focus different mass ranges, and mass ranges of varying sizes. The mass range that has been optimised is 325 - 625 Da, as over this range the spatial resolution is better than 20 μm, shown in Fig. 5.9. The grey line shows the simulated resolution for integer m/z between 250 - 750 Da. The coloured scatter points indicate different dye molecules used to cover the mass range (blue = Rhodamine 560 Chloride, red = Rhodamine B, pink = BBQ, green = p12). The spatial resolution determined from simulations and the experiment show two locations where the spatial resolution

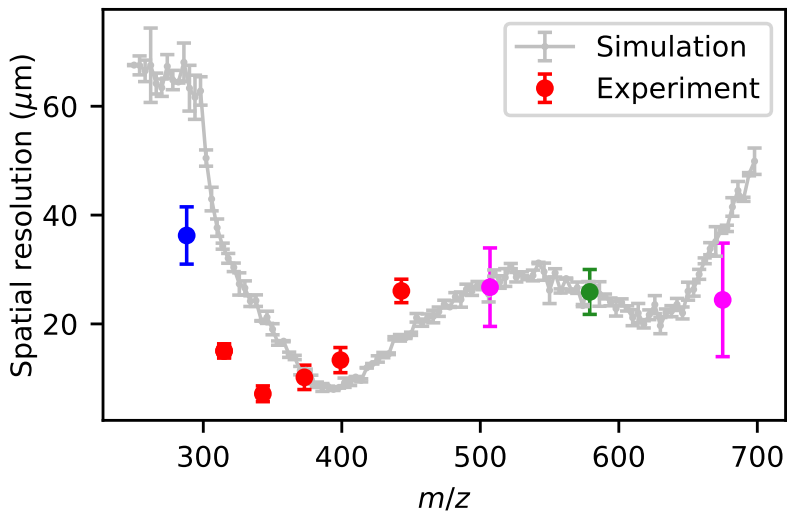


Figure 5.9: Experimental and simulated spatial resolutions for ion between 250 - 700 Da. The grey line shows the simulated spatial resolutions determined using SIMION. The coloured scatter points represent the experimentally determined spatial resolutions: Blue - Rhodamine 560 chloride, Red - Rhodamine B, Pink - BBQ and green - p12.

has a local maximum. As with the mass resolution, this can be attributed to using a linear time-dependent voltage pulse despite the approximately quadratic dependency of ion flight time on m/z.

Each ion image is fitted with a piece-wise boxcar function convolved with a Gaussian to approximate the FWHM of the ion distribution at the detector. This value is divided by the magnification factor to determine the spatial resolution (a detailed description of the spatial resolution calculation can be found in Chapter 4). The experimentally determined spatial resolution has very good agreement with the simulation.

5.4 Conclusion

PEDA improves the mass resolution in an ion microscope without adversely affecting the spatial resolving power of the instrument. This chapter has presented two additional PEDA variants: linear time-dependent PEDA and quadratic time-dependent PEDA, building on previous work by Aoki *et al.*[97] and Guo *et al.*[99].

Linear time-dependent PEDA increases the electric field strength of the extractor electrode on a microsecond time scale. This improves the mass resolution for a selected mass range. Furthermore, this variant of PEDA optimises the mass resolution for two m/z values. This is a result of the linear function intersecting a quadratic function at two locations. The mass resolution is improved between 325 - 625 Da, matching the mass range where the spatial resolution is optimised. The spatial resolution over this range is less than 20 μm and the mass resolution is above 2500 $m/\Delta m$. This chapter has also introduced simulations for a quadratic pulse variant, that is able to more accurately approximate the relationship between ion flight and m/z. As a consequence, this technique in theory achieves a maximum mass resolution greater than 8000 $m/\Delta m$ over the 300 Da mass range. Future experiments will develop electronics that are capable of applying a quadratic pulse to the extractor electrode.

The next chapter presents a high spatial resolution instrument designed in SIMION which can achieve 800 nm spatial resolution, and details the relationships that affect the instrument's resolution in a 4-plate ion microscope. The incorporation of electrostatic analysers is shown as a method to increase magnification, allowing the benefits of the high resolution instrument to be realised.

6 High resolution ion optics

6.1 Introduction

Improving the spatial resolution of an ion microscope allows the spatial position to be determined with increased precision within a complex environment. Furthermore, sub-micron spatial resolution allows the positional information within cells to be determined [162]. The ambition of this project is to develop an ion microscope that is capable of sub-micron spatial resolution, whilst retaining mass resolution. This mass spectrometer will be used to image biologically relevant molecules such as metabolites and lipids, over a mass range of 100 - 1200 Da, providing a route to high-throughput diagnostics.

Previous work has employed a five-plate ion optic design (repeller, extractor and an einzel lens) with a PEDA (applied to the extractor plate), adapted from a Wiley-McLaren mass spectrometer [118, 143]. With this setup spatial resolutions of 20 - 50 µm have been achieved [26].

To improve the spatial resolution two further developments in microscope imaging were considered. First, Duker and Illenberger developed an electron microscope comprised of four electrodes. This design, shown in Fig. 6.1, achieved 50 nm spatial resolution for electrons [163]. Although this resolution is very high, no

mass information can be attained. Second, Bruno Schueler developed the time-of-flight secondary ionisation mass spectrometry (TOF-SIMS) stigmatic imaging mass spectrometer, the TRIFT. This instrument was able to achieve a lateral resolution of 1 µm for a 70 µm active area [93]. Table. 6.1 shows the current achievements in microscope imaging. The resolutions achieved for micrscope ion imaging are for a small m/z range. To image other mass ranges the ion-optic voltages need to be re-tuned. In addition, the TRIFT can attain either high spatial resolution or high mass resolution. Each time a different mass is analysed the electrode potentials in the optics and ESA require adjustment. The five plate linear ToF has a large field of view and can simultaneously record spatial and mass resolution. However, resolutions are lower compared with the TRIFT.

This chapter will present an instrument that achieves high spatial and mass resolutions simultaneously, with a large field of view. The instrument presented in this chapter builds on strengths from all three instruments shown in Table. 6.1. The effects of chromatic aberrations on spatial resolution will be determined using equations of motion, for charged particles. With this information a combination of these three instruments has been designed *in silico* and then optimised using a genetic algorithm. The results from this genetic algorithm were validated, and then improved, using a downhill Nelder–Mead minimisation algorithm. An explanation of both routines is given in Chapter 3. Next, a systematic analysis of the mass resolution gained through the sequential addition of ESAs will be shown. Finally, incorporation of a PEDA ion optic after the ions have travelled through the ESAs further improves the optimal mass resolution achieved for the four-plate ion microscope mass spectrometer.

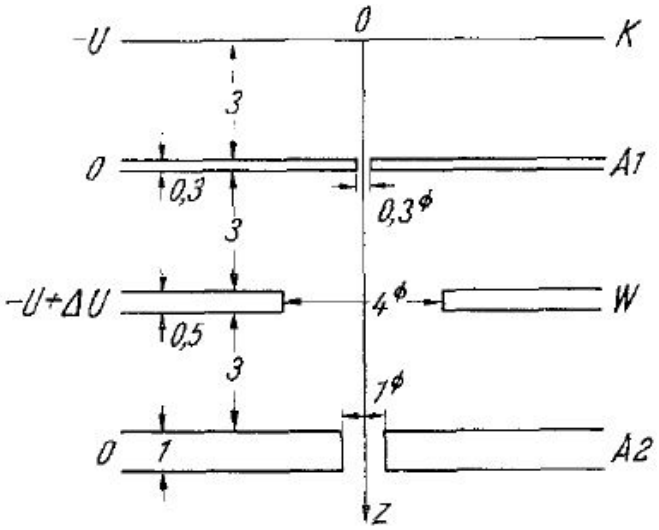


Figure 6.1: Optic design by Duker and Illenberger for an electron microscope with a spatial resolution of 50 nm. Dimensions are in mm. K - extraction surface cathode, A1, W and A2 are the three plates of the Einzel lens [163].

	$m/\Delta m$	Spatial resolution	Field of view
Electron Microscope	N/A	50 nm	50 nm
TRIFT	15,000	1-20 µm	25 - 400 µm
Linear ToF	2000	25 µm	0.5 cm

Table 6.1: Current ion microscope instrument resolutions.

6.2 Improving spatial resolution

In an optimal situation with no aberrations, a lens has a precisely defined focal point. When aberrations from a lens are introduced, ions are refracted differently depending on where they pass through the lens and the focal point becomes less well defined.

6.2.1 Spherical and Chromatic aberrations

Analogous to optical lens, ion optics can have aberrations. These aberrations cause the image formed by a lens to become blurred or distorted, with the nature of the distortion depending on the type of aberration. The blue box in Fig. 6.2 and Fig. 6.3 shows the effect of spherical and chromatic aberrations respectively.

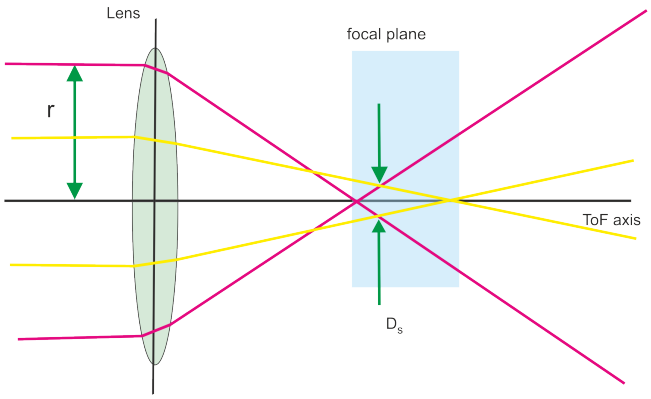


Figure 6.2: A graphic showing the blurring effect caused by spherical aberrations from ions with different initial starting positions in a cylindrically symmetric lens.

The following equations and figures explain the effect of spherical and chromatic aberrations on the focal point of a lens.

The extent of spherical aberrations can be determined by the circle of least confusion, as illustrated in Fig. 6.2. It is the narrowest cross section at the focal plane, formed by the ion trajectories entering a lens with radius, r. The diameter of the circle of confusion, D_s is given by:

$$D_s = \frac{C}{F} r^3 \ , \tag{6.1}$$

where C is a lens constant and F is the focal length. To minimise the spherical aberrations for a lens the focal length is increased, this is achieved using an enizel lens [164]. The einzel lens controls the position of the focus by changing the potential applied to the middle electrode. This allows the detector plane to be located further from the ion optics.

Chromatic aberrations are caused by ions travelling from the same source position, but with different energies as a result of surface ablation. This energy disparity results in different focal lengths for the respective ions, causing a blurring of the image, as illustrated in Fig. 6.3. The chromatic aberrations D_c can be quantified as:

$$D_c = Kr \frac{V_0}{\Delta V} \ , \tag{6.2}$$

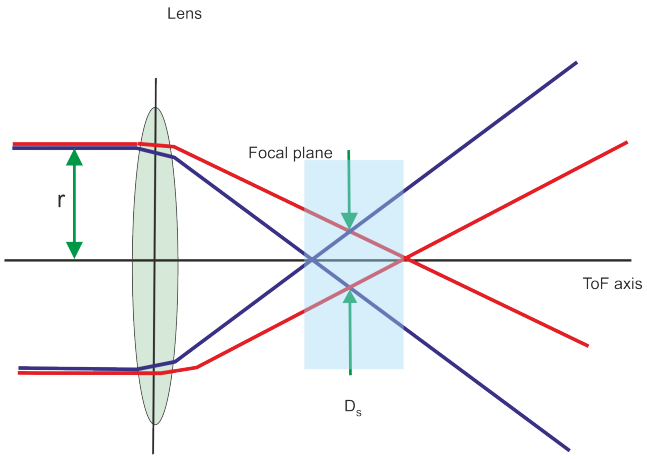


Figure 6.3: A graphic showing the blurring effect caused by chromatic aberrations from ions with different kinetic energies in a cylindrically symmetric lens. Lowest energy (blue) and highest energy (red).

where K is a lens constant, r is the lens radius, ΔV is the energy spread, and V_0 is the initial energy of the ions.

An increase in the potential of the lens reduces the chromatic aberrations and reduces the width of the focal plane. This improves the spatial resolution. Time dispersion caused by similar ions having different focal points is also reduced as the lens potential is increased.

This chapter investigates the factors that contribute to aberrations, and the extent to which they affect the spatial resolution of ions in a time of flight mass spectrometer.

6.2.2 Modelling ion trajectories with transfer matrices

Simulations will use ionisation parameters indicative of the MALDI process, as described in Chapter 3 [48]. In ion imaging, the chromatic aberrations introduced in the accelerating section are large and dominate over the spherical image aberrations introduced into the mass spectrometer [165]. Chromatic aberrations determine the ultimate achievable spatial resolution, calculated from the lateral spread of the ions [87, 93].

Fig. 6.4 shows an ion optic and ESA combination that was inspired by the electron microscope developed by Ducker *et al.* [163] and the TRIFT ion microscope [93]. This design was chosen to provide the greatest improvement in instrument resolution whilst maximising the field of view for a mass spectrometer operating as an ion microscope. From here on, this design will be referred to as a four-plate ion microscope.

A schematic of an ion (originating away from the ToF axis) as it travels from the sample plate, through the four-plate ion optics, into the electrostatic analyser, finally terminating at the detector, is shown as a red dotted line in Fig. 6.4. The extraction optics (V_1, V_2 and L_1) creates an acceleration region, formed from the sample surface and the einzel lens (V_2, V_3, V_4, L_2 and L_3). The ion optics project a magnified image of the ion emission profile into the first field-free region (L_4) of the mass spectrometer. The ions enter the ESA and undergo further magnification forming an image plane after they exit the ESA. This is imaged by an MCP/scintillator assembly.

The minimum spot size (best spatial resolution), with the absence of all deleterious effects, such as stray fields, is determined by the diameter of the resulting spot on the position sensitive detector and is defined as [93]:

$$x \approx \frac{2Z\Delta E_0}{V} \sin(\alpha)(1 - \cos(\alpha)) \ , \tag{6.3}$$

where Z, is the acceleration gap in the extraction region, ΔE_0 is the initial particle energy, V is the extraction voltage and, α is the emission angle from the sample surface.

The emission angle, α, is fixed for a particular analyte. In the case of MALDI imaging, the emission angle has a mean value of 0° and a FWHM of 60° [140]. The initial ion velocity, v_0, which determines the initial particle energy, is specific to an ablation process. For MALDI, the initial velocity is $500\,\mathrm{m\,s^{-1}} \pm 500\,\mathrm{m\,s^{-1}}$, this is discussed in Chapter 3. Two parameters remain, that can be optimised to improve spatial resolution, the extraction voltage, V, and the acceleration gap, Z.

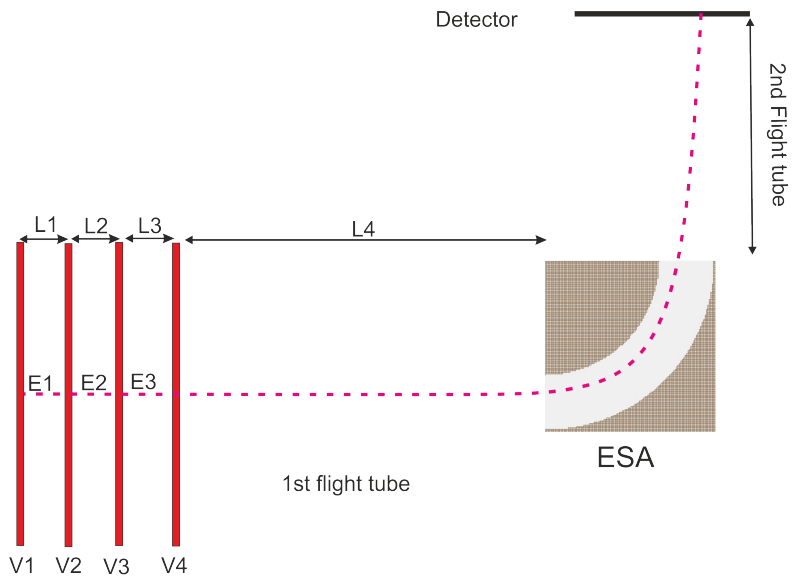


Figure 6.4: Schematic of ion optics and electrostatic analyser developed to improve spatial resolution. $L1$ is the acceleration region, $L2$ and $L3$ are the spacing of the Einzel lens. $E1-3$ are the electric fields in the ion optics. $V1-4$ are the potential at each electrode. ESA is a hemispherical electrostatic analyser.

Particle trajectories and flight times through the ion optics can be described by transfer matrices [166]. The transfer matrices are derived based on the work of Liebl [164]. The Newtonian equations for a charged particle moving in an electric field are used to define a matrix for each individual component within the instrument. In the four-plate ion optic spatial imaging instrument there are nine individual regions.

The transfer matrices for the four-plate ion optic setup and ESA ion microscope mass spectrometer are shown in equation (6.4). The final ion position is a product of these transfer matrices:

$$\begin{bmatrix} y \\ r' \end{bmatrix} = \mathbf{F_2\ E\ F_1\ A_3\ U_3\ A_2\ U_2\ A_1\ S} \tag{6.4}$$

where, y, is the orthogonal displacement from the time of flight axis, r' is the gradient of the ion trajectory with respect to its axial displacement and ToF. The matrices are defined as: F - flight tube, E - electrostatic analyser, A - aperture, U - uniform field and S - emission surface. The following sections will provide a detailed description of the derivation of the transfer matrices used in this chapter.

6.2.2.1 Derivation of transfer matrices

All equations will consider a positively charged ion with elementary charge, q. The transfer matrices will be derived in two dimensions, where x is the coordinate of the ion on the time of flight axis, y is the orthogonal displacement of an ion, and r' is the gradient of the ion trajectory with respect to the x and y axes, shown in Fig. 6.5. The electrodes are labelled identically to those in Fig. 6.4.

6.2.2.2 Uniform electric field

An electric field is defined as:

$$E_n = \frac{V_{n+1} - V_n}{L_n} \ . \tag{6.5}$$

Where n denotes the electrode number from Fig. 6.4. Within a uniform electric field the differential equations of motion can be integrated to produce the motion of the particle in the x,y-coordinate system as a function of time of flight, t. In a homogeneous electric field, a positive ion experiences a force in the direction of the electric field only, as illustrated in Fig. 6.5. The velocity of the ion in the electric field is:

$$v_1 = \sqrt{\frac{2qV_1}{m}} \ , \tag{6.6}$$

where v_1 is the velocity of a positively charged particle, and will accelerate in the direction of the electric field when a uniform homogeneous field is applied between two plates. The acceleration x'' and y'', and velocity x' and y' of the ion can be determined from the equations of motion:

$$x''m = qE \tag{6.7}$$

$$y''m = 0 \ . \tag{6.8}$$

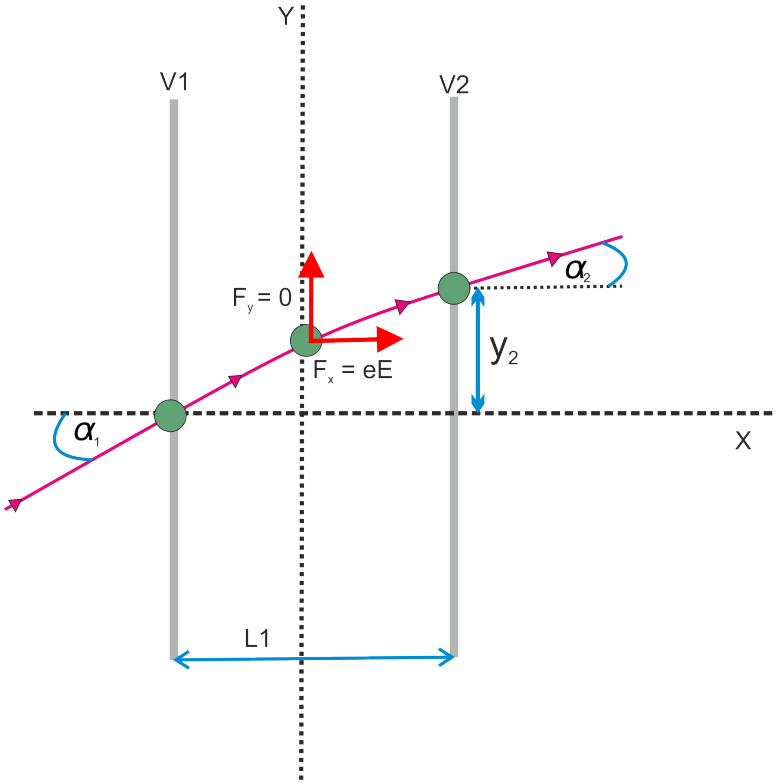


Figure 6.5: Ion trajectory through a cylindrically symmetric, uniform electric field. V_1 and V_2 are the potential applied to the electrodes.

$$x' = \frac{qEt}{m} + c_x \ , \tag{6.9}$$

$$y' = 0 + c_y \ , \tag{6.10}$$

where c is the constant of integration and equal to the velocity of the ion before it enters the uniform field in the x and y direction respectively. The velocity of the ions in the electric field in the x and y direction is therefore:

$$x' = \frac{qEt}{m} + v_1 \cos \alpha_1 \tag{6.11}$$

$$y' = 0 + v_1 \sin \alpha_1 \ . \tag{6.12}$$

The displacement is determined by integrating equation (6.11) and equation (6.12).

$$x = x_i + \frac{qEt^2}{2m} + v_1 t \cos\alpha_1 \tag{6.13}$$

$$y = y_i + v_1 t \sin\alpha_1 \ , \tag{6.14}$$

where x_i and y_i are the constant of integration and equal to the the initial x and y position of the ion. For the remainder of this derivation the ion will be assumed to enter the electric field at the origin. Eliminating t and solving the resulting equation, gives the orthogonal displacement of the ion as a function of time of flight position:

$$\frac{qEt^2}{2mv_1} + t\cos\alpha_1 - \frac{x}{v_1} = 0 \tag{6.15}$$

$$t = \frac{mv_1}{qE}\left(\sqrt{\cos^2\alpha_1 + \frac{2qEx}{m{v_1}^2}} - \cos\alpha_1\right) . \tag{6.16}$$

Substituting equation (6.6) and (6.16) into equation (6.14) yields:

$$y = \frac{2V_1 \sin\alpha_1}{E}\left(\sqrt{\frac{Ex}{V_1} + \cos^2\alpha_1} - \cos\alpha_1\right) . \tag{6.17}$$

This equation now enables the ion's orthogonal position to be determined at each point on the time of flight axis as it travels between the two electrodes, without knowing the corresponding time.

The next objective is to determine the position of the ion at the second electrode (when $x = L_1$). First equation (6.5) which defines an electric field, is rearranged:

$$\frac{E}{V_1} = \frac{1}{L_1}\left(\frac{V_2}{V_1} - 1\right) . \tag{6.18}$$

Inserting equation (6.18)) into equation (6.17),

$$y_2 = \frac{2L_1 \sin\alpha_1}{\frac{V_2}{V_1} - 1}\left(\sqrt{\frac{V_2}{V_1} - \sin^2\alpha_1} - \cos\alpha_1\right) . \tag{6.19}$$

To calculate the transfer matrix, the gradient of the ion trajectory with respect to the time-of-flight position in the electric field is calculated from equation (6.17):

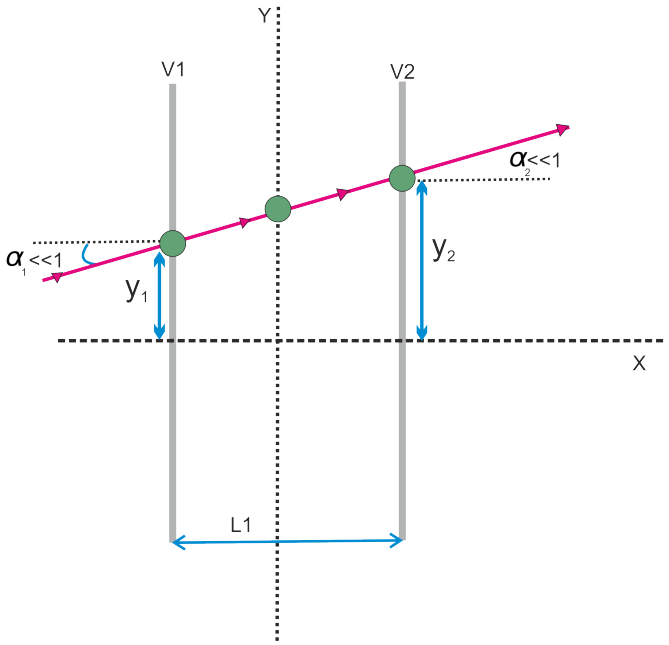


Figure 6.6: Paraxial approximation for ions travelling through a uniform electric field.

$$r' = \frac{dy}{dx} = \sin\alpha_1 \left(\frac{Ex}{V_1} + \cos^2\alpha_1 \right)^{-\frac{1}{2}} . \tag{6.20}$$

When $x = L_1$,

$$r' = \sin\alpha_1 \left(\frac{V_2}{V_1} - \sin^2\alpha_1 \right)^{-\frac{1}{2}} . \tag{6.21}$$

The derivations shown in equations (6.7) - (6.21) provide a precise description of an ion trajectory from entering, to exiting the electric field, as illustrated in Fig. 6.5.

The voltages applied to the four-plate ion optics design are very large, this allows significant simplification of the transfer matrix for a uniform field, by using the paraxial approximation [164]: $\alpha_1 \ll 1$, $\sin\alpha_1 \approx r_1'$, $\cos\alpha_1 \approx 1$ and $V_2/V_1 \gg r_1'$ for an ion at the first electrode. The adjusted ion trajectory, as shown in Fig. 6.6, follows a straight line from the first electrode V_1, to the second electrode V_2. Simplifying the equations of motion using the paraxial approximation, allows the orthogonal position and gradient of the ion as it arrives at the second electrode to be determined:

$$r_2 \approx r_1 + \frac{2L_1}{\sqrt{\frac{V_2}{V_1}} + 1} \tag{6.22}$$

$$r_2' \approx \sqrt{\frac{V_1}{V_2}} r_1', \tag{6.23}$$

or as a matrix for a uniform field U,

$$\begin{bmatrix} r_2 \\ r_2' \end{bmatrix}_U = \begin{bmatrix} 1 & \frac{2L_2}{\sqrt{V_2/V_1}+1} \\ 0 & \sqrt{V_1/V_2} \end{bmatrix} \begin{bmatrix} r_1 \\ r_1' \end{bmatrix}. \tag{6.24}$$

6.2.2.3 Emission surface

A special case of the matrix for a uniform field must be applied when an ion with energy qV_1, is emitted from a planar surface and accelerated across a uniform field with a potential V_a. In this case the initial ion energy is equal to the energy from the ablation process.

The ion will leave the acceleration region with kinetic energy equal to $q(V_1 + V_a)$. Substituting this into equation (6.19) and (6.21) gives the orthogonal displacement and the gradient of the trajectory when an ion is emitted from a planar surface in a uniform electric field:

$$y_a = \frac{2L_1 \sin\alpha_1 V_1}{V_a} \left(\sqrt{\frac{V_a}{V_1} + \cos^2\alpha_1} - \cos\alpha_1 \right) \tag{6.25}$$

$$r_a' = \sin\alpha_1 \left(\frac{V_a}{V_1} + \cos^2\alpha_1 \right)^{-\frac{1}{2}}. \tag{6.26}$$

When an ion is emitted from a planar surface, $V_1 \ll V_a$, equation (6.25) and (6.26) can be simplified to:

$$y_a \approx 2L_1 \sin\alpha_1 \sqrt{\frac{V_1}{V_a}} \tag{6.27}$$

$$r_a' \approx \sin\alpha_1 \sqrt{\frac{V_1}{V_a}}, \tag{6.28}$$

This can be represented as a matrix:

$$\begin{bmatrix} r \\ r' \end{bmatrix}_S \approx \begin{bmatrix} 2L_1 \sin\alpha_1 \sqrt{V_1/V_a} \\ \sin\alpha_1 \sqrt{V_1/V_a} \end{bmatrix} \begin{bmatrix} r_1 \\ r'_1 \end{bmatrix} . \tag{6.29}$$

6.2.2.4 Aperture

In ion optics, an aperture lens consists of a small circular hole in a metal plate that separates two regions of different longitudinal electric fields, as shown in Fig. 6.7. A charged particle passing through the aperture experiences a focusing effect due to the sudden change in the voltage gradient. Gauss's law can be used to determine the focal length of the ion and the ion trajectory through the aperture. Gauss's law can be expressed as:

$$\phi_E = \frac{Q}{\varepsilon_0} , \tag{6.30}$$

where ϕ_E is the electric flux, Q is the total charge enclosed within a volume V, and ε_0 is the electric permittivity constant. The electric flux ϕ_E is defined as a surface integral of the electric field:

$$\phi_E = \oiint E \, \mathrm{d}A . \tag{6.31}$$

In the case when there is no charged ions within the ion optics, equation (6.31) becomes:

$$\oiint E \, \mathrm{d}A = 0 . \tag{6.32}$$

The protrusion of the electric field from one region into another can be represented as a cylinder along the time of flight axis and through the aperture. Before the aperture, there is only one component to the electric field, which is along the x axis, E_a. However with the introduction of an aperture there is an additional component to the electric field along the y-axis, E_y, as illustrated in Fig. 6.7.

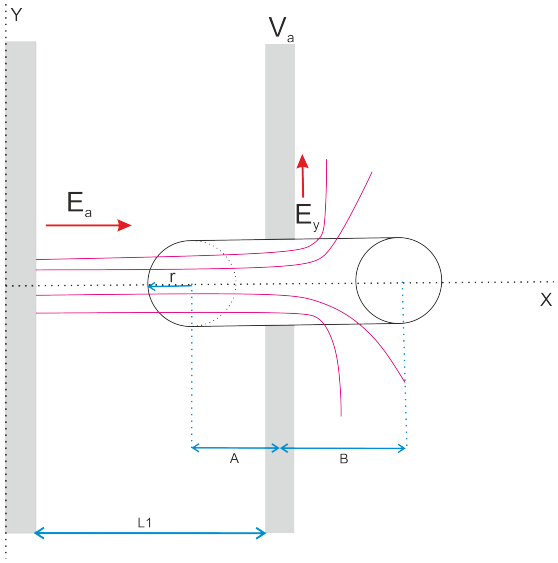


Figure 6.7: An ion trajectory through a round aperture. A and B define the protrusion of the electric field either side of the electrode. E_a and E_y are the component of the electric field in the x and y direction respectively.

The field line flux entering the the cylinder ϕ_i is:

$$\phi_i = E_a \int_0^{2\pi} \int_0^r r \, \mathrm{d}r \mathrm{d}\theta \, , \tag{6.33}$$

and the field lines within the cylinder $\phi_{A,B}$,

$$\phi_{A,B} = E_y \int_{-A}^{B} \int_0^{2\pi} \int_0^r r \, \mathrm{d}r \, \mathrm{d}\theta \, \mathrm{d}x \, . \tag{6.34}$$

The field line flux equals zero as a consequence of no space charge, allowing the simplification of equations (6.33) and (6.34),

$$0 = \pi r^2 E_a + 2\pi r \int_{-A}^{B} E_y \, \mathrm{d}x \, . \tag{6.35}$$

When a charged particle enters the cylinder it experiences an increase in radial momentum which can be quantified as:

$$\rho_y = m v_y \, , \tag{6.36}$$

This can be converted to:

$$F = -\frac{\Delta \rho_y}{\Delta t} \ , \tag{6.37}$$

where F is the force acting on the ion in the electric field. Substituting into equation (6.36) yields:

$$m v_y = -\int q E_y \, \mathrm{d}t \ . \tag{6.38}$$

This forms an integral which is a function of the time-of-flight axis and with the substitution:

$$v_x = \frac{\mathrm{d}x}{\mathrm{d}t} \ . \tag{6.39}$$

The radial momentum associated with the orthogonal electric field at the aperture can be determined by the substitution of equation (6.39) into equation (6.38):

$$m v_y = -\frac{q}{v_x} \int_{-A}^{B} E_y \, \mathrm{d}x \ . \tag{6.40}$$

Using the paraxial approximation, the horizontal component of velocity v_x is constant. Equation (6.35) can be incorporated into equation (6.40),

$$m v_y = \frac{q r E_a}{2 v_x} \ . \tag{6.41}$$

When the ion travels through the aperture, the trajectory is distorted by $\Delta r'$. The resultant trajectory can be separated into its x and y components of velocity, v_x and v_y respectively, as illustrated in Fig. 6.8.

$$\Delta r' = \frac{v_y}{v_x} \ . \tag{6.42}$$

Recognising that $qV = \frac{1}{2} m v_x^2$ and inserting into equation (6.41)

$$\Delta r' = \frac{E_a r}{4V} \ . \tag{6.43}$$

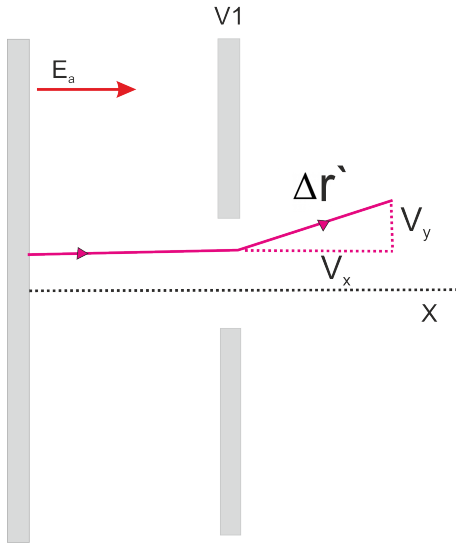


Figure 6.8: Distortion to the ion trajectory as it travels through a round aperture.

The focal length can be determined as:

$$-\frac{1}{f} = \frac{\Delta r'}{r} = \frac{E_a}{4V} \,. \tag{6.44}$$

The trajectory deflection $\Delta r'$, is proportional to the distance from the axis, r. The work done by the electric field energy qV_a, is large in comparison with the initial particle energy, so that qV can be replaced by qV_a,

$$-f = \frac{4V_a}{E_2 - E_1} \,, \tag{6.45}$$

where V_a is the voltage of the aperture measured against the particle source (zero particle energy), and E_1 and E_2 are the field strengths on either side of the aperture.

For the general case, when an aperture separates two regions with different, non-zero, electric fields, the focal length is given as:

$$-f = 4L \,. \tag{6.46}$$

Finally, the transfer matrix for the general case of an aperture can be written as:

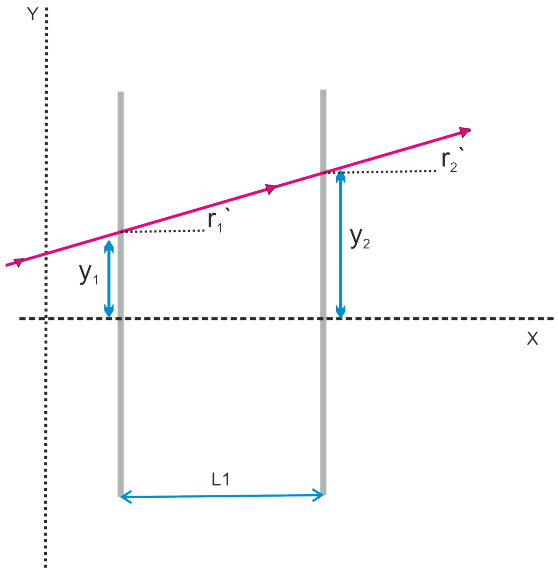


Figure 6.9: Ion travelling through a drift space, where there is no electric field.

$$\begin{bmatrix} r_2 \\ r_2' \end{bmatrix}_A = \begin{bmatrix} 1 & 0 \\ \frac{E_2 - E_1}{4V_a} & 1 \end{bmatrix} \begin{bmatrix} r_1 \\ r_1' \end{bmatrix} . \tag{6.47}$$

.

6.2.2.5 Field free region

A drift region will only change the orthogonal displacement, r, of a particle. The gradient, r', will remain constant, as shown in Fig. 6.9. The orthogonal displacement changes as a function of the length of the drift space, L, and the direction of the motion of the particle. This can be calculated using the equation for a linear function:

$$y_2 = r'L + y_1 \ . \tag{6.48}$$

The transfer matrix can be written as:

$$\begin{bmatrix} r_2 \\ r_2' \end{bmatrix}_F = \begin{bmatrix} 1 & L \\ 0 & 1 \end{bmatrix} \begin{bmatrix} r_1 \\ r_1' \end{bmatrix} . \tag{6.49}$$

Parameter	Value
L_1	10 mm
L_2	10 mm
L_3	9 mm
L_4	560 mm
V_1	5000 V
V_2	1500 V
V_3	2000 V
V_4	2000 V

Table 6.2: Parameters used to calculate ion trajectories for transfer matrices and SIMION simulations of the four-plate ion optic.

6.2.2.6 Trajectory calculation

The transfer matrices derived in the previous section are formulated to calculate the final ion positions after travelling through the ion optics:

$$\begin{bmatrix} r \\ r' \end{bmatrix} = \begin{bmatrix} L_4 & 0 \\ 0 & 1 \end{bmatrix} \begin{bmatrix} -1 & 0 \\ \frac{-1}{f} & -1 \end{bmatrix} \begin{bmatrix} L_3 & 0 \\ 0 & 1 \end{bmatrix} \begin{bmatrix} 1 & 0 \\ \frac{E_4-E_3}{4\,V_3} & 1 \end{bmatrix} \begin{bmatrix} 1 & \frac{2\,L_3}{\sqrt{V_3/V_2}+1} \\ 0 & \sqrt{V_2/V_3} \end{bmatrix} \tag{6.50}$$
$$\begin{bmatrix} 1 & 0 \\ \frac{E_3-E_2}{4\,V_2} & 1 \end{bmatrix} \begin{bmatrix} 1 & \frac{2\,L_2}{\sqrt{V_2/V_1}+1} \\ 0 & \sqrt{V_1/V_2} \end{bmatrix} \begin{bmatrix} r_i + 2\,L_1\sqrt{\frac{v_0}{V_1}}\sin(\alpha_i) \\ 2\,L_1\sqrt{\frac{v_0}{V_1}}\sin(\alpha_i) \end{bmatrix}.$$

Trajectories were calculated for three different initial orthogonal displacements ($r = 0$, 1 and 2 mm) and three different initial emission angles (α = -45° , 0° and 45°). The other parameters used in this calculation, such as the electrode potential and electrode separation, are shown in Table. 6.2. The position of the ions as they travel along the ToF axis for the four-plate ion microscope mass spectrometer are shown in Fig. 6.10. The ions are spatially focused onto a plane after 590 mm. In addition, the ions velocity focus occurs after 190 mm.

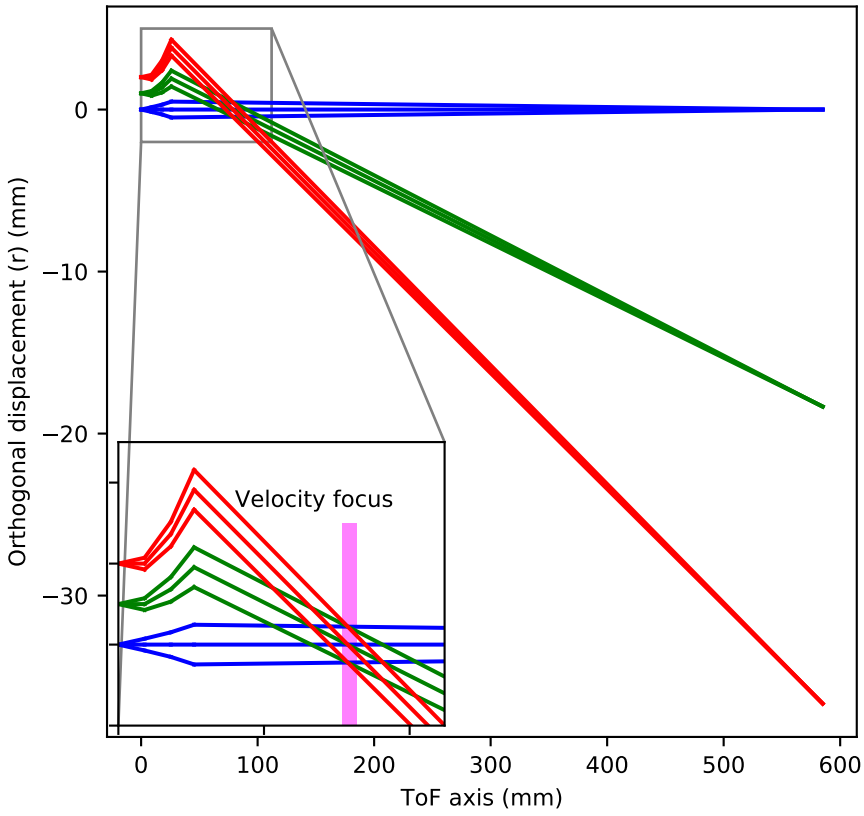


Figure 6.10: Ion trajectories, calculated as a function of position along the time of flight axis, using the transfer matrices in equation (6.50). The enlarged region in the window shows the ion trajectories as they travel through the ion optics.

6.2.3 Modelling ion optic trajectories with SIMION

SIMION simulations can, in principle, more accurately predict an ion's behaviour in an electric field compared with transfer matrices. SIMION does not use paraxial approximations and accurately models an electric field protruding through an aperture.

The high resolution instrument setup (ion optics and flight tube) was constructed in SIMION, the dimensions of the instrument were identical to those used in the transfer matrix calculation equation (6.50). Additionally, the ions' initial position ($r = 0, 1, 2\,\text{mm}$) and direction were equivalent to those used in equation (6.50). The resulting ion trajectories are shown in Fig. 6.11.

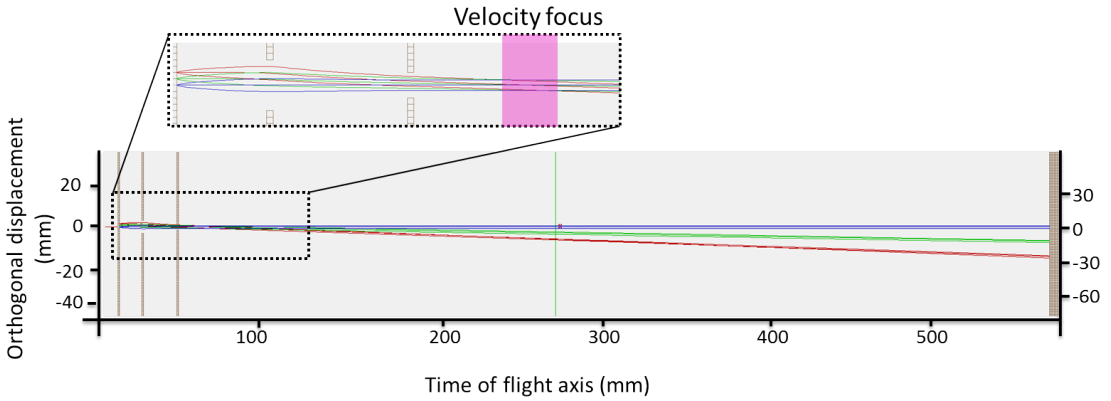


Figure 6.11: SIMION simulated flight paths of ions in the four-plate ion optics.

6.2.4 Comparison of ion trajectory calculation methods

The trajectories calculated broadly agree with the SIMION simulations illustrated in Fig. 6.10 and Fig. 6.11; the orthogonal displacement, spot spread and magnification have been used for comparison of the method. Table. 6.3 provides a comparison of these parameters. The distribution of impacts on the detector for the two different methods of trajectory calculation has the greatest degree of variation.

The trajectories originating from the same position ($y = 0{,}1{,}2$ mm), but travelling with different initial angles, separate to a greater extent (1.4 mm) in SIMION, than those calculated using transfer matrices (0.3 mm). This results in a less well defined focal point. The spot spread is used to determine the FWHM of ion impact, which is a measure of the spatial resolution. The difference between the two methods of trajectory calculation is the result of different precision levels. In SIMION, the electric field, and therefore the vectors of the ions, are calculated with sub-millimetre precision. This allows the simulation to more accurately predict the ion trajectory as it travels through the aperture when the field is no longer uniform. Simulations calculated using the transfer matrices assume a uniform field between electrodes, with a fixed adjustment to the trajectory to account for the lens effect, as the ion travels through the aperture of the electrode. Therefore, the transfer matrices calculated ion trajectories close to the aperture using inaccurate electric

	Transfer matrices			SIMION		
	$\bar{y}$	S	M	$\bar{y}$	S	M
Green	0	0.3	1.0	0	0.3	1.4
Blue	-18.2	0.3	18.2	-19.8	1.4	19.8
Red	-36.6	0.3	18.3	-28.7	1.4	14.5

Table 6.3: A comparison of ion trajectories (green, blue and red) calculated using the transfer matrices and SIMION for a four-plate linear ToF. $\bar{y}$ is the average displacement in millimetres at the detector, S is the average spot spread in millimetres at the detector and M is the average magnification.

fields. To prevent these inaccuracies in the description of the electric field, SIMION uses a 4^{th}order Runge Kutta method to determine electric fields (more details can be found in Chapter 3). Neglecting the correct electric field at the apertures results in sharp focal points and improved resolution (smaller spot spread) for ions calculated using the transfer matrices.

The transfer matrices validate that SIMION is modelling the ion trajectories with reasonable accuracy. In addition, the transfer matrices provide a greater understanding of ion behaviour in the electric fields within the four-plate ion optic design. Furthermore, the ion optic calculations are used in Chapter 5 to determine the time-of-flight differences for ions with different masses and different energies.

The following sections of this chapter will use SIMION to investigate and improve the spatial resolution of a simulated ion microscope imaging mass spectrometer.

6.2.5 Electrostatic analysers

Electrostatic analysers (ESA) are conventionally used as energy selectors as they provide simultaneous time focusing for different initial angles and initial energies as well as achromatic spatial focusing of charged particles; they permit the passage of ions with a particular energy, and can be tuned using specific electric fields [167, 168]. ESAs are grouped into two classifications: deflector analysers (1) and mirror analysers (2).

1. Deflector analysers: the energy of charged particles remains approximately constant along a circular optic axis. Deflector analysers are used for applications requiring large fields of view due to the relatively large acceptance angles of ion trajectories entering the ESA [169].

2. Mirror-type analysers: the design is based on electric fields in which particles are first decelerated and then re-accelerated. This results in higher order focusing, but a small dispersion to magnification ratio and limited field of view [170].

The simulations discussed below use an adapted deflector analyser. However, instead of the ESA selecting a specific particle energy, it is used to magnify off-axis ion trajectories. A specific voltage is applied to the ESA to ensure ions travelling along the ToF axis retain a constant radius, defined as the principal axis, as they travel through the ESA. It is derived in the following steps [171].

The potential energy of the ion as it travels along the principle axis of an ESA is zero. The ion follows a circular trajectory, therefore the centripetal force acting on the ion can be determined:

$$F = \frac{mv^2}{r_0} \,, \tag{6.51}$$

where r_0 is the radius of the trajectory that travels along the principal ray. This results in:

$$F = \frac{2U}{r_0} \,, \tag{6.52}$$

The Coulombic force resulting from the electrodes within the ESA is given by:

$$qE_R = \frac{Q_1 Q_2}{4\pi\epsilon_0 R_x^2} \,, \tag{6.53}$$

where qE_R is radial electric force on a charged particle, Q_1 and Q_2, are the charge applied to the inner and outer electrodes respectively. R_x is the radius

of the circular electrodes in the ESA, where x corresponds to either *in* or *out*, as illustrated in Fig. 6.12.

The gradient of the electric potential qE_R, over a distance R_x, between charged plates can be defined as:

$$qE_R = -\frac{\mathrm{d}V}{\mathrm{d}R_x} \,, \tag{6.54}$$

substituting in equation (6.53) yields:

$$-q\frac{\mathrm{d}V}{\mathrm{d}R_x} = \frac{Q_1 Q_2}{4\pi\epsilon_0 R_x^2} \,, \tag{6.55}$$

which is readily integrated:

$$-q\int \mathrm{d}V = \int \frac{Q_1 Q_2}{4\pi\epsilon_0 R_x^2}\,\mathrm{d}R_x \,. \tag{6.56}$$

This gives an equation that links the potential of the electrodes to their respective radii:

$$qV_{R_x} = 2\frac{Q_1 Q_2}{4\pi\epsilon_0 R_x} \,. \tag{6.57}$$

If ions travelling along the principal ray have zero potential, the voltage applied to the outer and inner electrode, V_{in} and V_{out}, respectively can be determined. This is achieved by equating the centripetal force of the ion travelling along the principal ray with the Coulombic force from the electrode.

$$\frac{Q_1 Q_2}{4\pi\epsilon_0} = qU_0 r_0 \,, \tag{6.58}$$

The electrode potential for each electrode in the ESA can then be defined as:

$$V_{R_x} = \frac{2U_0 r_0}{R_x} - 2U_0 = 2U_0\Big(\frac{r_0}{R_x} - 1\Big) \,. \tag{6.59}$$

The ion beam is focused according to Barber's rule [172] onto an image plane that lies on a straight line comprising, the object, the centre of deflection and the final image plane, as shown in Fig. 6.13. As the distance A decreases the distance B increases, thereby increasing the magnification.

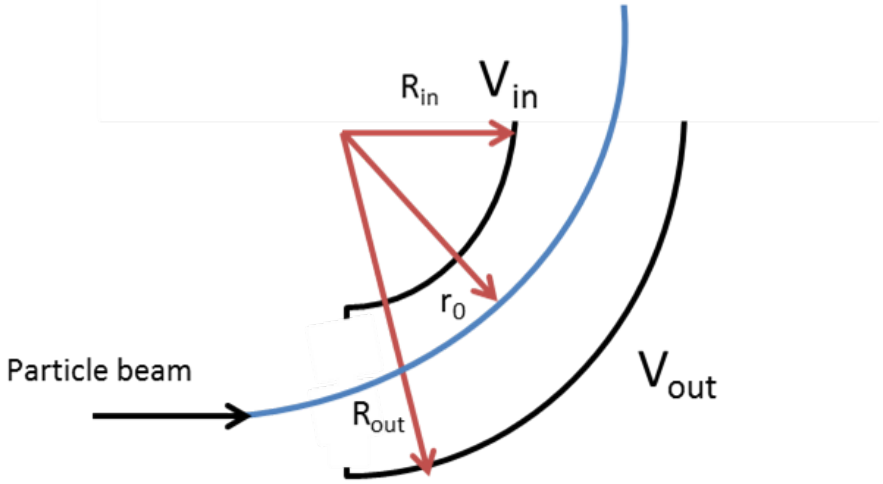


Figure 6.12: Schematic of ESA showing inner electrode V_{in}, at radius R_{in}, and outer electrode V_{out} at radius R_{out}, and the flight path of an ion along the principal radius, r_0.

If the object plane is located before the entrance slit of the ESA there will be an image plane after the ESA. The image plane comprises multiple starting locations of ions that are spaced on the axis that are orthogonal to the time of flight axis, shown in Fig. 6.13. If these ions are within a certain distance of the ToF axis they are able to travel, unhindered, around the ESA, albeit in a non-circular path. This non-circular path, caused by the ions entering the ESA off of the ToF axis, results in greater force imparted to the ions. Ions that deviate from r_0 experience a non-zero potential from the ESA. This in turn, means that their trajectories are pushed further from the initial axis on exiting the ESA, resulting in magnification of the ion trajectories.

6.2.6 Simulation

The four plate ion optic design with an electrostatic analyser contains a multitude of interdependent variables that need to be determined. This could be achieved using a brute force algorithm that attempts every possible combination of values to determine the best value that each variable can take to give optimal spatial resolution. However, due to the amount of variables that require simultaneous optimisation, a brute force algorithm would be computationally expensive. Instead, minimisation algorithms have been used.

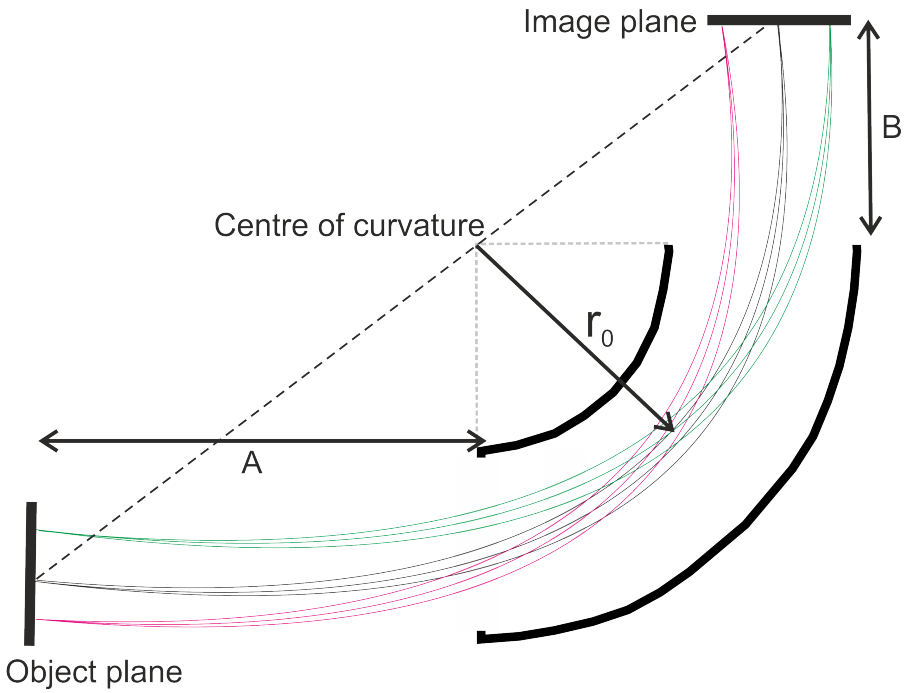


Figure 6.13: Cartoon depicting Barber's rules; the object plane, centre of curvature and image plane, all lie on a straight line.

The parameters to be simultaneously optimised using the minimisation algorithms include: the repeller voltage; the extractor position, aperture width and voltage; the third plate position, aperture width and voltage; the fourth plate position, aperture width and voltage.

Each variable requires predetermined parameter limits for the genetic algorithm. First, the available plate positions are defined. These values are stated as a range of positions on the x-axis for each plate e.g. the extractor can take positions between 42 mm – 49 mm, where 0 mm is the start of the ion optics chamber. Second, the aperture diameter, orthogonal to the time of flight axis are defined for each electrode (except the repeller plate), each plate can only take integer values between 1 - 5 mm. Finally, the maximum voltages are set for each plate based on the available power supplies.

The following section presents the results from applying two minimisation algorithms to optimise the spatial resolution for an ion microscope.

Parameter	Range of values input into the genetic algorithm
x_2	5 mm - 12 mm
x_3	5 mm - 12 mm
x_4	5 mm - 12 mm
V_1	5 kV; 30 kV
V_2	-5 kV − 5 kV; -30 kV − 30 kV
V_3	-5 kV − 5 kV; -30 kV − 30 kV
V_4	-5 kV − 5 kV; -30 kV − 30 kV

Table 6.4: List of parameters and parameter ranges used by the genetic algorithm for the optimisation of the four-plate ion optic design in SIMION 8.1.

6.2.7 Results from the minimisation algorithms

The four plate ion optic design shown in Fig. 6.4 was optimised for two different maximum voltage parameters: 5 kV and 30 kV. These maximum electrode voltages were chosen to be reflective of the applicable voltage range. 5 kV is currently used in the laboratory [102] and 30 kV was chosen as this is around the maximum voltage that can be applied easily between two plates with 10 mm separation in a 10^{-7} mbar vacuum, before electrical breakdown occurs [173]. The search space available for the genetic algorithm is shown in Table. 6.4.

Fig. 6.14 (a) shows the spatial resolution when the electrode potential was restricted to 5 kV for a 100 - 1200 Da range. The GA determines that the optimal spatial resolution for a 100 Da ion was 1 μm, increasing to 15.4 μm for a 1200 Da ion. When the Nelder-Mead algorithm was used the spatial resolution improves for every mass over this range. Fig. 6.14(b) shows the spatial resolution over the same mass range when the maximum electrode potential is 30 kV. For a 100 Da ion the spatial resolution was 0.8 µm, increasing to 1.5 µm for 1200 Da ion. Consistent with the 5 kV routine, the results from the Nelder-Mead method improves the resolutions for a 100 - 1200 Da ion to 0.6 μm and 0.9 μm respectively. The sequential application of minimisation algorithms can more accurately determine global minima [174]. Sequential algorithms have a reduced chance of becoming trapped in a local well compared with individual minimisation algorithms. This is a result of

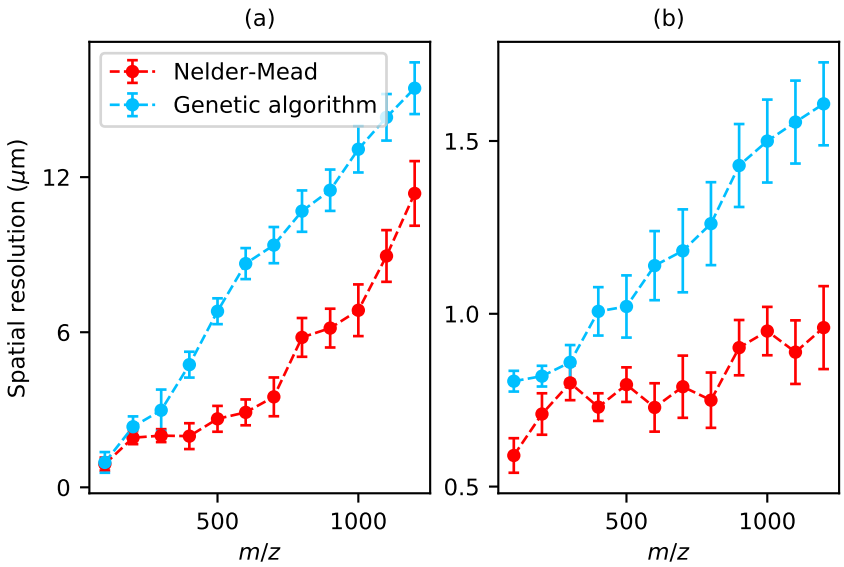


Figure 6.14: Simulation results from two minimisation algorithms: blue - genetic algorithm, red - Nelder Mead downhill simplex algorithm applied to the search space determined from the GA. The spatial resolution over a mass range of 100 - 1200 Da for a four-plate ion optic instrument including two ESAs is shown by circles for each algorithm. The standard deviations in each figure were determined by repeating each point three times. (a) The spatial resolution over the mass range when the maximum voltage applied to the electrodes was 5 kV. (b) The spatial resolution over the mass range when the maximum voltage applied to the electrodes was 30 kV.

the parameters in the second algorithm being confined to a region in which the global minimum is located, but without any bias from previous iterations of the minimisation procedure. It is worth noting that if the number of iterations of the GA are increased to a sufficiently large number, the global minimum could be determined by the algorithm exclusively. Tables that show the optimal values of each parameter and their corresponding resolutions determined by the GA and Nelder-Mead algorithms can be found in Appendix A.

In both routines, the larger the mass, the greater the improvement in spatial resolution after the Nelder-Mead algorithm. Furthermore, the optimal spatial resolution achieved in each search space degrades as the mass of the ion increases. This is a result of the increase in momentum and the subsequent increased penetration of the ion into the electric field in the extraction region and results in a less-defined image plane [87, 93].

Using the minimisation algorithms sequentially (genetic algorithm and then Nelder-Mead downhill simplex), significantly reduces the computational cost of finding values that improve the spatial resolution compared to a brute force approach. Moreover, in every case where the algorithms have been used sequentially, the optimal spatial resolution has been improved. However, by not checking every option for each variable it is impossible to state with complete certainty that the optimal values for each variable have been chosen. Furthermore, the standard deviation at each data point can in principle be reduced by increasing the number of iterations of the respective minimisation processes. Through the balance of minimisation and efficiency, the algorithms have been used sequentially to allow an adequate route to meet the objective of determining a combination of values that improve the spatial resolution from greater than 20 μm to sub-micron resolution, over a 1000 Da mass range.

6.3 Improving mass resolution

This chapter so far has focused on improving the spatial resolution for an ion microscope mass spectrometer.

Designing a mass spectrometer with high mass resolving power that will be applied to a sample comprised of more than one mass requires time focusing of the ions. This instrument has been developed for ions with a mass-to-charge ratio less than 1200 m/z so that it can be applied to lipid and metabolite analysis.

The instrument shown schematically in Fig. 6.4 can achieve a mass resolution of $m/\Delta m \approx 70$ *in silico*, when the potentials in the ion optics are restricted to a maximum value of 30 kV. The loss in mass resolution compared to previous ion microscope mass spectrometers [143] is a result of the difference in path length that the ions travel through the ESA as shown in Fig. 6.15. It can be seen that the ion packets have separated relative to each other, after exiting the ESA.

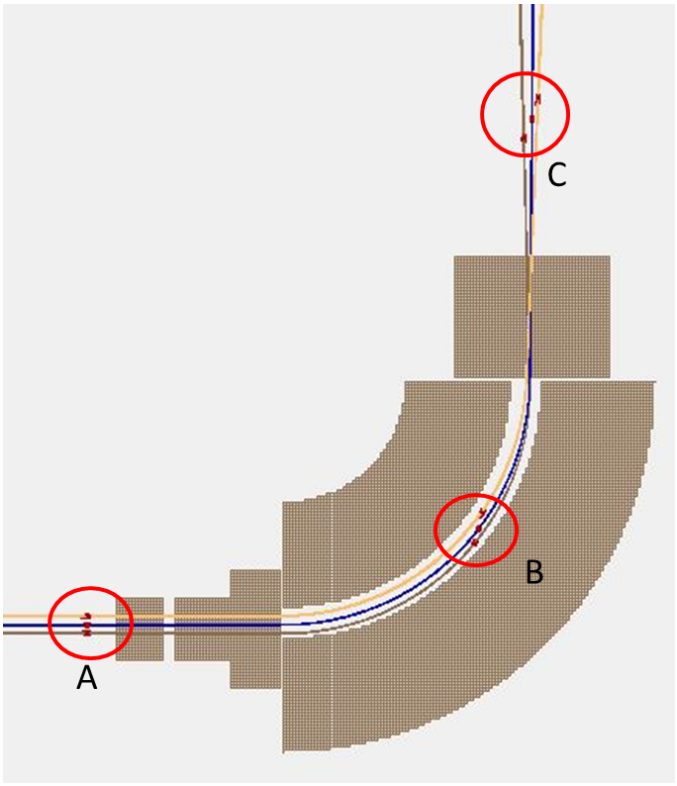


Figure 6.15: Ion position, for a 500 Da ion travelling through an ESA: before (A), during (B) +1 µs, and after (C), +2 µs.

Ions that travel in a circular path experience a centripetal force, therefore the velocities of the ions are inversely proportional to the radii of their trajectories, as shown in equation (6.51) and equation (6.52). If one ESA is used, ions with different radii have different velocities as they travel through the ESA, and therefore exit the ESA at different times, as shown in Fig. 6.15. This results in poor mass resolution. When two ESAs are used in combination, ions that have a smaller radius, and therefore a larger velocity, travelling through the first ESA (yellow in Fig. 6.16), have a larger radius and a smaller velocity in the second ESA and vice versa. This results in ions with different initial starting positions in the ESA, exiting the second ESA with a reduced temporal spread. However, the ions do not have symmetric trajectories, as a result of small differences in their energies of the ions, as they enter the ESA. Hence, the second ESA does not completely compensate for the temporal spread caused by the first ESA. This is shown in Fig. 6.16 by the yellow

trajectory: the ions have travelled a smaller distance after the three time intervals (A, B and C), compared to the blue and brown trajectories. Imhof *et al.*, provides a rigorous derivation and quantification of this effect [175].

The spot spread of the ions at the point labelled C in the field-free region, after travelling through two ESAs (Fig. 6.16) have a reduced time dispersion, in comparison to ions that have travelled through one ESA (Fig. 6.15). The dispersion between ion trajectories at C is less than at B, and continues to reduce as the ions travel away from the detector. It is eventually minimised at the temporal focus, located on the detector plane. The second ESA improves the mass resolution for 500 Da ions by 400%, achieving $m/\Delta m \approx 280$.

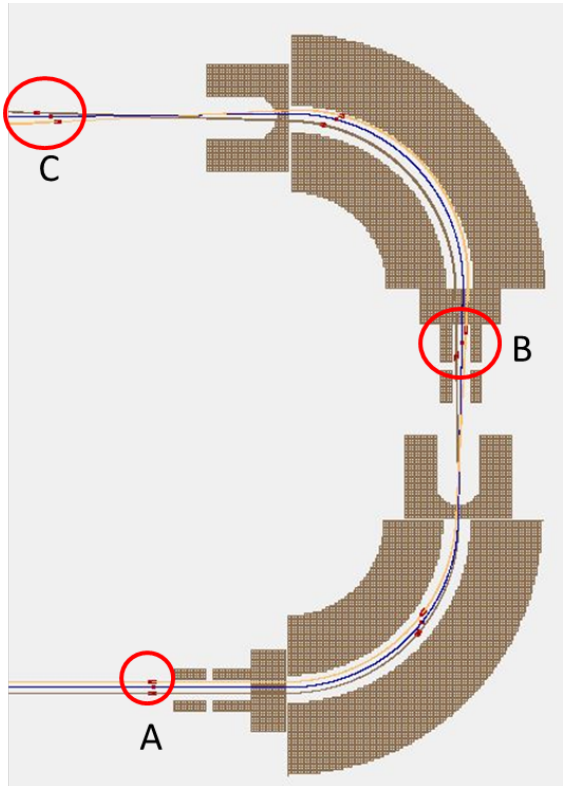


Figure 6.16: Ion position, for a 500 Da ion travelling through two ESA: before (A); during (B), +3 µs; and after (C), +5 µs.

6.3.1 Post Extraction Differential Acceleration

Post Extraction Differential Acceleration (PEDA) can significantly increase the mass resolution of an ion microscope imaging mass spectrometry [97, 99]. Ions are generated on a source plate (repeller) with an initial velocity. They are accelerated after ionisation by the electric field in the extraction region between the repeller and extractor. When the ion passes through the aperture of the extractor there is a distribution of ion velocities for a given mass which is preserved throughout the remainder of the instrument. An additional ion optic can be employed to increase the potential of the ion packet. This results in a reduced temporal spread and an improvement in the mass resolution of the ions that reach the detector. Increasing the electrode potential during the experimental cycle (after the ions have pasted the electrode), results in ions gaining additional kinetic energy based on their position along the time of flight axis. As the axial position of the ion depends on its initial velocity, an ion with a high initial velocity (located at the front of the ion packet) will gain less energy than an ion with a low initial velocity (located at the back of the ion packet). After acceleration, the ion enters a field-free region, with a reduced velocity spread, terminating at the detector. A smaller velocity spread results in a more highly resolved mass spectrum [26].

The increase in the distribution of ion velocities occurs after the ions travel through the ESAs. This is shown in Fig. 6.16 where the spot spread of the yellow, blue and brown ions have an increased temporal spread relative to each other after the ion exit the ESA, compared to when they enter. Therefore, for a PEDA optic to improve the mass resolution, it must be employed after the ESAs. To maximise the benefits of PEDA, two variables have to be optimised: the PEDA optic position and its pulse voltage. Due to the simplicity of the optimisation of these variables, a minimisation algorithm was not used. The PEDA pulse time was chosen so that the ions were located at the PEDA plate when the voltage was increased. The pulse time was 20.55 μs. The mass resolution was recorded as the

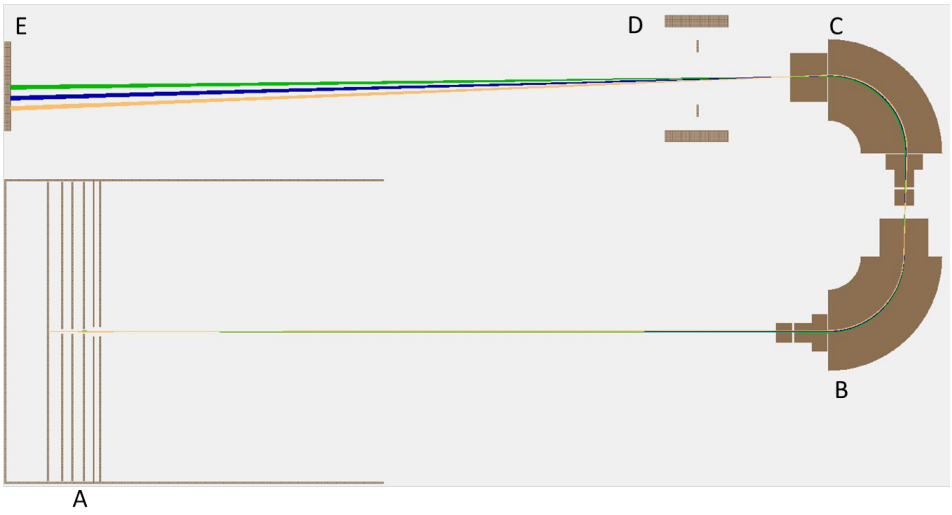


Figure 6.17: High spatial resolution ion microscope mass spectrometer design *in silico*. A: ion optics, B: 1st ESA, C: 2nd ESA, D: PEDA optic and E: detector.

PEDA optic position was incrementally moved along the time of flight axis. The position that corresponded to the best mass resolution was 65 mm from the exit from the second ESA along the ToF axis. The optimised ion microscope mass spectrometer design *in silico* is shown in Fig. 6.17.

Once the optimal position was identified, the pulse voltage was chosen by incrementing the voltage in 100 V steps over a range 0 - 30 kV until a maximum mass resolution was achieved, shown in Fig. 6.18 (a). The PEDA voltage used was 15.1 kV which is optimised for a 500 Da ion. This mass can be changed by re-tuning the ion optics. The PEDA plate placed after the second ESA does not affect the spatial resolution, 1 μm was retained over the entire voltage range scanned. As mentioned previously, an ion microscope is very dependent on the mass for which it is optimised. Fig. 6.18 (b) shows the mass resolution over a 1200 Da mass range. The inset shows the rapid decrease in mass resolution over a 40 Da range. The mass resolution decreased by approximately 50% after 2 Da, as shown in Fig. 6.18 (c). This is significantly worse compared with the five-plate optic design from which this instrument was developed. The rapid decrease in mass resolution can be explained by considering the magnitude of the ion's velocity. Ions generated in the four plate

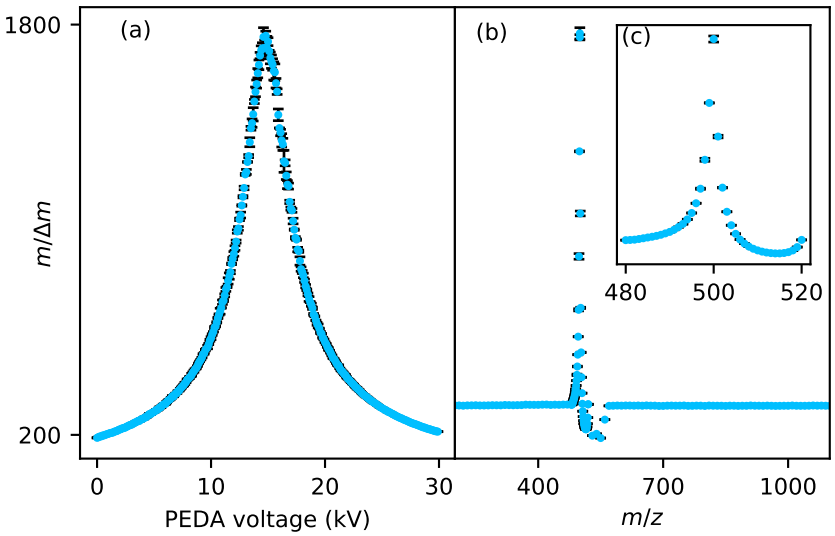


Figure 6.18: (a) Mass resolution achieved when the PEDA plate is scanned over a 30 kV voltage range. (b) Mass resolution recorded for 100-1200 Da ions. (c) Zoomed inset of the region where the mass resolution undergoes a rapid increase to the optimal value of approximately 1800 $m/\Delta m$. The resolution decreases by 50% over a two Dalton mass range - see text for explanation. The standard deviations are calculated from repeat run of the simulation.

design are exposed to a large acceleration compared with previous iterations of this instrument. A 500 Da ion in the original instrument has a velocity at the detector of approximately 43 900 m s^{-1}, compared with a 500 Da ion in the four plate ion optic which has an approximate velocity of 121 000 m s^{-1}. A larger velocity results in a shorter time in the PEDA region. Ions with a mass slightly larger than 500 Da are exposed to the PEDA pulse for a reduced time compared with the previous design, and therefore they do not benefit from the velocity correction.

When using PEDA optics in combination with a four-plate ion optic arrangement and two ESAs, an optimal mass resolution of 1800 $m/\Delta m$ was achieved, while retaining a spatial resolution of approximately 1.5 µm, for a 500 Da mass ion when the potentials applied to the ion optics are restricted to 30 kV.

	$m/\Delta m$	Spatial resolution	Field of view	Mass range
Linear ToF	2000	30 μm	0.5 cm	60 Da
Reflectron MSI	8100	14 µm	300 µm	60 Da
Reflectron + TV PEDA	8100	14 µm	300 µm	300 Da
four-plate ion optic + ESAs	1800	800 nm	400 µm	10 Da

Table 6.5: Instrument resolutions for ion microscope variant presented in this thesis.

6.4 Summary

This chapter has presented an *in silico* project to improve the spatial resolution and mass resolution of an ion microscope mass spectrometer. The chapter was compartmentalised into two sections, optimising spatial resolution and optimising mass resolution.

To improve the spatial resolution of the ion microscope mass spectrometer a number of steps were taken. First, previous work that provided inspiration for this project were amalgamated into one instrument: the four-plate ion optic imaging mass spectrometer. Second, an investigation into the chromatic aberrations of the lens system; the main factor that governs spatial resolution, was carried out. To understand the ion trajectories through the four-plate ion optics, the transfer matrices for ions at along ToF were calculated. This allowed the determination of the velocity and spatial focus, and manipulation of the ion optics to maximise the spatial resolution. This technique provides a close approximation for the ion trajectories but a higher level of precision was required. Next, a precise model of the ion optic design in SIMION provided a quantitative analysis of the obtainable spatial resolution. This model highlighted the need for an increased magnification of the ions. The required magnification was achieved by the incorporation of an ESA. Two different minimisation algorithms: a genetic algorithm and Nelder–Mead

downhill simplex, were then applied to the ion optic design including the ESA, to find the best spatial resolution.

The latter section of this chapter presented modifications to the four-plate ion optic design that improved mass resolution. The first modification was the addition of a second ESA. The additional ESA helps correct the difference in path length that ions starting from different positions on the repeller plate travel. This correction improved the mass resolution by a factor of four. A further improvement in mass resolution was made with the incorporation of a PEDA optic, a method to reduce the temporal spread of ions with different initial velocities. This pulse, when applied at the correct time and with the correct magnitude, gives a further six fold increase in mass resolution.

The optimal spatial and mass resolution for 500 Da ion was 800 nm and 1800 $m/\Delta m$, respectively. The four-plate ion optic instrument *in silico* provides an improvement on the previously best known spatial resolution in ion microscope mass spectrometry (achieved using TRIFT) of 1 µm, and a larger field of view diameter, 200 µm compared with 70 µm [93]. A comparison of the performance of ion microscope variants developed throughout this thesis is presented in Table. 6.5.

The next chapter will present multi-mass ion images from a Tpx3Cam combined with a reflectron ion microscope. A novel method that allows the Timepix3 sensor to be operated in continuous mode will be presented. Furthermore, by achieving high resolution with a CMOS sensor, the high-throughput nature of an ion microscope combined with an ultra-fast imaging sensor will be underscored.

7 Ion imaging with a Tpx3Cam

This chapter will present the development of a novel experimental procedure using a Tpx3Cam combined with a reflectron ion microscope to record time resolved ion images. A fast scintillator screen (exalite 404) allows ion events to be recorded with increased time resolution compared with a conventional P47 phosphor screen.

7.1 Introduction

The reflectron MSI presented in Chapter 4 and 5 demonstrates the high mass and spatial resolution capability of an ion microscope. The major appeal of this technique is its high-throughput capacity. The combination of CMOS sensors with an ion microscope improves the inherent benefits of this technique by allowing multiple mass peaks to be imaged in each experimental cycle [118, 176, 177].

Chapter 4 presents the data that was acquired with a PImMS sensor which was able to record an ion image for each peak in the mass spectrum concurrently. This CMOS sensor can record a ToF peak with a 25 ns timing precision corresponding to approximately 1600 $m/\Delta m$. In the current instrument configuration, a PMT can measure an ion event with a resolution of 4 ns (8100 $m/\Delta m$). To realise this mass resolution, a Timepix3 sensor with 1.5625 ns time resolution was used.

The Timepix chip is an evolution of the Medipix chip which can measure the time of arrival (ToA), time-over-threshold (ToT) or event counting, independently in each pixel [178]. The CMOS architecture of the Timepix sensor allows individual pixel information to be recorded with 20 ns timing precision. The sensor has been used in a number of high energy physics applications including X-ray radiography, neutron imaging and ion telescopes [128, 129, 179].

Molecular processes that occur on a sub-microsecond timescale can be studied using VMI. A Timepix sensor can be combined with an MCP stack in vacuum to record mass specific ion images [180–182]. VMI and spatial map imaging (SMI) can also be performed using an MCP/scintillator detector assembly that emits photons with a 400 - 1000 nm wavelength. The photons are recorded outside of the vacuum with an optical camera [112, 113], which is decoupled from the experimental setup, making upgrades and maintenance significantly easier.

Nomerotski *et al.*, developed a fast optical imaging device using a Timepix chip that can record visible photons for such applications [115]. This device was called the Tpx3Cam. This camera comprises a Timepix sensor bump-bonded to a silicon pixel array that has greater than 90% quantum efficiency [183]. Transistors in each pixel amplify the charge which is then transported to the digital readout by applying a biased electric field to silicon substrate. This allows photons produced from ion events at the detector to be recorded [184].

The latest version of this family of sensors is the Timepix3 chip which extends the functionality of Timepix by allowing simultaneous ToA and ToT measurements [185]. The ability to record ToT allows the time-walk effects that can reduce resolving power, to be corrected, this is discussed later in the chapter. Moreover, this chip is able to record events with 1.5625 ns time precision. This timing precision has been used in particle tracking experiments and to measure the electron distributions from the ionisation of high energy particles at the Large Hadron Collider [186].

Like its predecessor, this chip can be bump-bonded with a silicon pixel array (with the Timepix3 chip this device is called Tpx3Cam[1]) [187]. The new camera is capable of registering multiple hits with a time resolution of nanoseconds at a megahertz rate, presenting a ten-fold improvement in timing resolution and a one hundred-fold increase in throughput, compared with the TimepixCam. Weinacht *et al.* performed coincidence velocity map imaging with the Tpx3Cam [187]. These experiments studied fragments of a CH_2IBr molecule upon exposure to strong field ionisation. Coincidences between the resultant ions and electrons were recorded. This experiment achieved a 23.5 ns FWHM timing resolution before ToT correction and 13.9 ns FWHM after [187]. A limiting factor when recording the timing resolution was the rise time of the P47 phosphor screen which added a 7 ns convolution to the ToF spectrum. The experiments presented in this thesis use an exalite 404 screen which has a rise time of 3.5 ns, and should therefore be able to improve on this resolution [102].

Improving the timing resolution increases the quantity of data recorded by the device in a given time. The Tpx3Cam data is able to output 80 Mhits per chip per second. To handle this data rate, the Tpx3Cam employs an expensive Speedy PIxel Detector Readout (SPIDR) system [188]. SPIDR can also accept and timestamp an external trigger pulse, independent of the Timepix3 connection. Typically, the trigger is synchronised with the firing of the laser, providing a time reference for each recorded event. The SPIDR system costs £80,000 [189].

This chapter presents an alternative readout system that does not require an external trigger. Instead, the Tpx3Cam is operated in continuous readout mode and a fibre optic directs part of the laser beam onto the sensor to define a t_0 for each acquisition. As a result, a readout device that costs £3,000 can be used.

[1]This can also be referred to as a TimePix3Cam and a Timepix3 based camera in the literature.

7.2 Experimental setup

The specifications of the Timepix3 chip are outlined in the following section. This is followed by a description of the experimental configuration that allows a triggerless readout to be used with the Tpx3Cam, and the necessary data processing procedures.

7.2.1 Timepix3 chip

The Timepix3 chip comprises 256×256 pixel array measuring $14.08\,\text{mm} \times 14.08\,\text{mm}$. Each pixel is $55\,\mu\text{m} \times 55\,\mu\text{m}$. The pixels are collimated to allow circuitry such as transistors, to be shared. The sensor is made up of 8192 superpixels which are defined as 4×2 pixels with shared circuitry. 64 superpixels form a column and there are 128 columns in the pixel array, as shown in Fig. 7.1. Each pixel is identified by a unique 16 bit address. A 16 bit address can take 65536 (256×256) individual values. This address specifies the double column number (7 bit), superpixel number (6 bit) and the pixel number (3 bit).

The light sensitive area within a CMOS sensor pixel is low, as each pixel contains circuitry connected to the photo diode (work is currently ongoing to fully characterise the detection efficiency of the Tpx3Cam). This results in a greater number of required incident photons to activate the pixel in comparison with a CCD camera. This problem can be mitigated by using a microlens [110]. However, the Tpx3Cam used for experiments in this thesis does not currently have a microlens array bonded to its pixels. To increase the number of photons and reduce this problem, the detector assembly was operated at a higher potential. The voltage across the MCPs was increased to 2.0 kV and the exalite screen was increased to 5.0 kV from the voltages used in Chapter 4. The maximum voltage can then be applied safely to the MCP stack is 2.2kV. Furthermore, the pixel threshold, which defines the minimum number of photons required to activate a pixel on the Tpx3Cam was set to 1.39 keV. This is the minimum value required to prevent ambient radiation from activating pixels. The minimum number of photons required

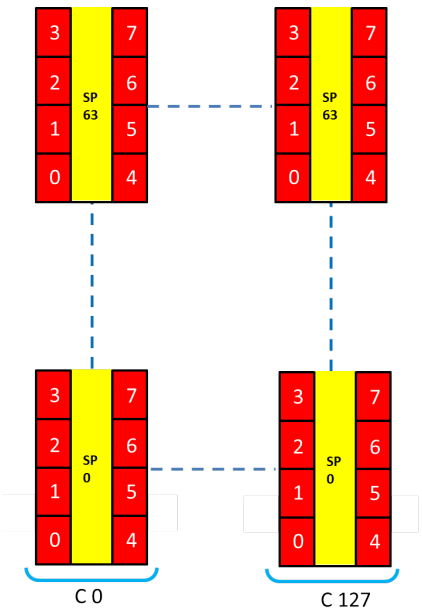


Figure 7.1: A schematic of the Timepix3 pixel array. Individual pixels are shown in red. Superpixels (SP) are shown in yellow. C0 and C127 indicates the first and last pixel column respectively.

to exceed this threshold voltage is approximately 500 at 430 nm wavelength. This is determined by considering the energy of a photon at this wavelength and the total energy required to activate a pixel.

As mentioned previously, the Timepix3 chip has a timing resolution of 1.5625 ns, this is achieved using two timestamps: the time of arrival (ToA) and the fine time of arrival (fToA). The ToA is a global clock which is used as an external reference clock for each pixel. The ToA register operates at 40 MHz (25 ns) using a 12 bit register which is equivalent to a clock cycle of 409.6 µs. The fToA is a local (pixel specific) clock operating at 640 MHz (1.5625 ns) with a 4 bit register, counting from 0-31. The camera can run continuously if the hit rate is below 40 Mhits $s^{-1}\,m^{-2}$, in the experiments presented in this chapter the average hit rate is 2.7 Mhits $s^{-1}\,m^{-2}$. In addition, successive events at a given pixel can only be recorded if they are separated by more than the ToT + 475 ns (dead time of the pixel).

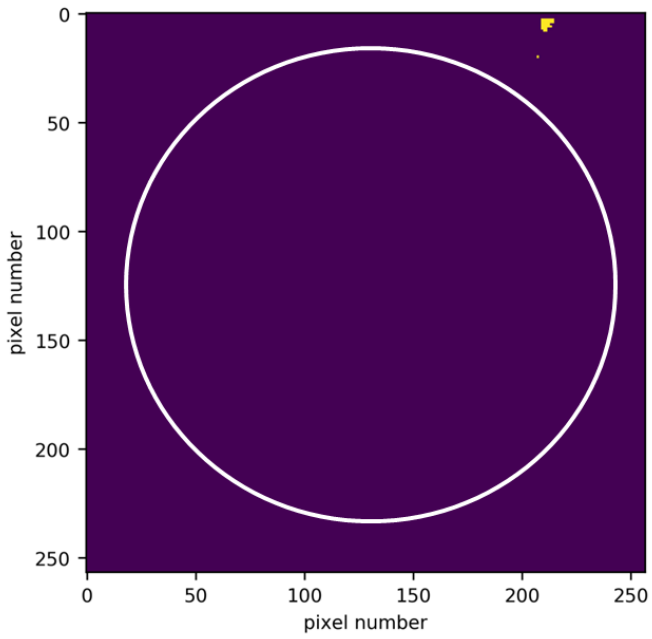


Figure 7.2: Tpx3Cam pixel array. The white circle indicates where the scintillator screen is focused onto the sensor. The yellow illuminate pixels are the laser spot from the fibre optic. The laser spot cluster is comprised of 27 pixels, of which 5 are responsible for t_0 in more than 99% of the experimental cycles.

7.2.2 Methods

The data that is presented in this chapter was collected using the ion microscope combined with a reflectron. Further details can be found in Chapter 4.

The timing precision available from the Timepix3 chip requires a high performance readout, typically a SPIDR system is used, but the work presented here uses a significantly less expensive USB 3.0 AdvaDAQ based readout. The readout system is able to process the maximum 40 Mhits $s^{-1}\,m^{-2}$ that can be recorded by the Timepix3 chip [190]. However, this readout system does not have the ability to receive an external trigger and must therefore run continuously. To circumvent this problem, a fibre optic cable was used to direct laser light from the experiment onto the sensor. This is achieved by splitting the laser beam (Thor lab Pellicle beamsplitter) as the laser pulse exits the internal housing of the laser system.

Focusing the laser directly at the sensor fills the pixel buffer which can stop events from being recorded. To reduce the intensity of the incident photons reaching

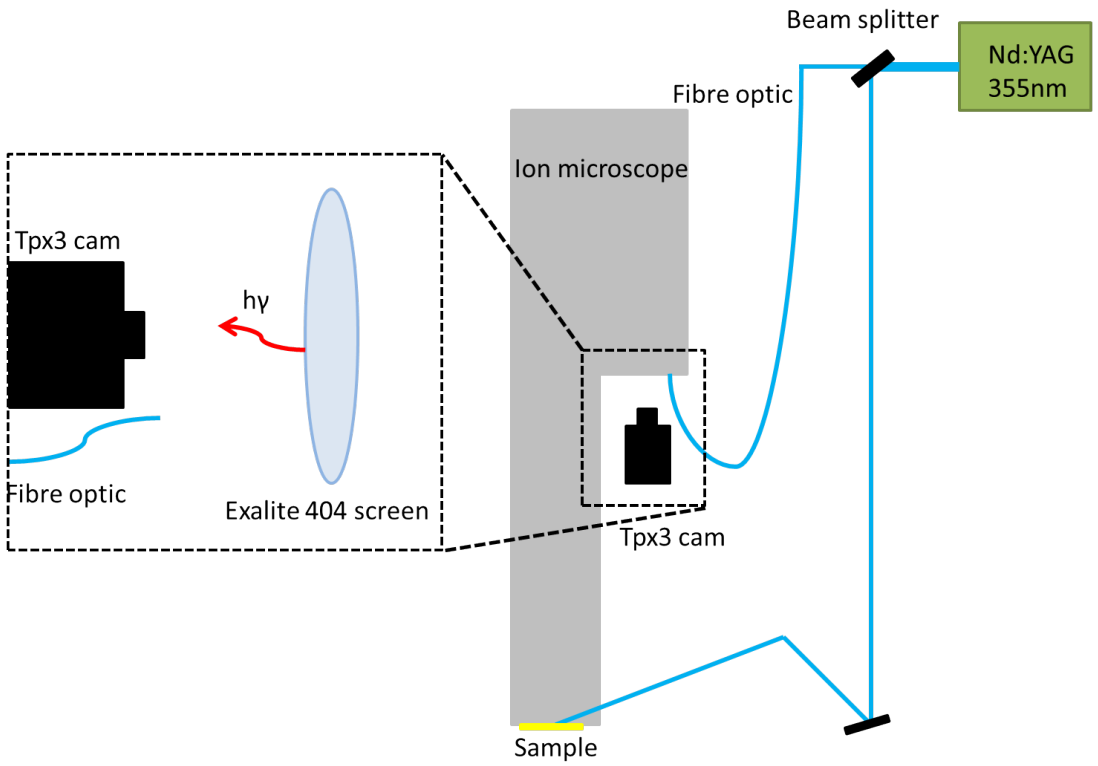


Figure 7.3: Cartoon showing the beam path of the laser through the fibre optic. Figure inset shows light exiting the fibre, reflecting from the outside of the exalite screen and returning to the Tpx3Cam to be used as a reference for the beginning of each laser shot.

the sensor, the laser is first directed at the scintillator screen. The reflected photons then only activate a small cluster of 27 pixels, this is shown as the yellow cluster in Fig. 7.2. This is achieved by attaching the fibre optic to the housing of the Tpx3Cam. In Fig. 7.2, the area within the white circle represents the pixels that are focused onto the scintillator screen, therefore the pixels illuminated by the flash do not record events from the screen. A cartoon of the experimental setup is illustrated in Fig. 7.3. The spatial position of the laser pulse that is used to define t_0 is now separated from the pixels that are used for experimental data. This assists data processing which is discussed in the next section. The number of pixels activated from the fibre was minimised to prevent the data files becoming excessively large. The use of this method to record part of the laser pulse by activating certain pixels creates a pseudo start time for each experiment within the data set.

The disadvantage of operating the Tpx3Cam in a continuous readout mode is that each data file must be separated into individual laser shots and the corresponding ToF spectrum in post processing. This issue is not encountered when the SPIDR readout is used. The following section presents the data processing protocols developed for the Tpx3Cam using a AdvaDAQ readout. Rhodamine B has been used to demonstrate multi-mass ion imaging with Tpx3Cam.

7.3 Data processing

The data presented in this chapter was recorded in five second intervals which corresponds to 50 laser shots, allowing efficient data handling. Moreover, this enables small data sets to be readily investigated, which is particularly useful for debugging. The data processing procedures presented in the following sections were developed using Python.

7.3.1 Data conversion

The Timepix3 chip readout mode is zero suppressed to reduce the file size and stores the data as an ASCII text file. The Timepix3 chip records the matrix index, the ToA, fToa and ToT whenever a pixel threshold is surpassed. The matrix index which is recorded by a 16 bit register contains the (x, y) coordinates for each event. The 16 bit number is converted into a binary form and separated into the column number which corresponds to the the last 7 digits, the super pixel number which is defined by the 3^{rd}- 8^{th} digits, and the pixel number which is determined from the 1^{st} - 2^{nd} and the 9^{th} digits, see Fig. 7.4 for a cartoon representation. The column number indicates the x coordinate, and the superpixel and pixel number indicate the y coordinate.

Once the x, y coordinates are known, the fToA and ToA clock can be used to categorise the specific arrival time of each event. The ToA is recorded by a 40 MHz clock, therefore to convert the number of clock cycles into nanoseconds, the ToA value is multiplied by 25. The fToA clock has a frequency of 640 MHz, the number

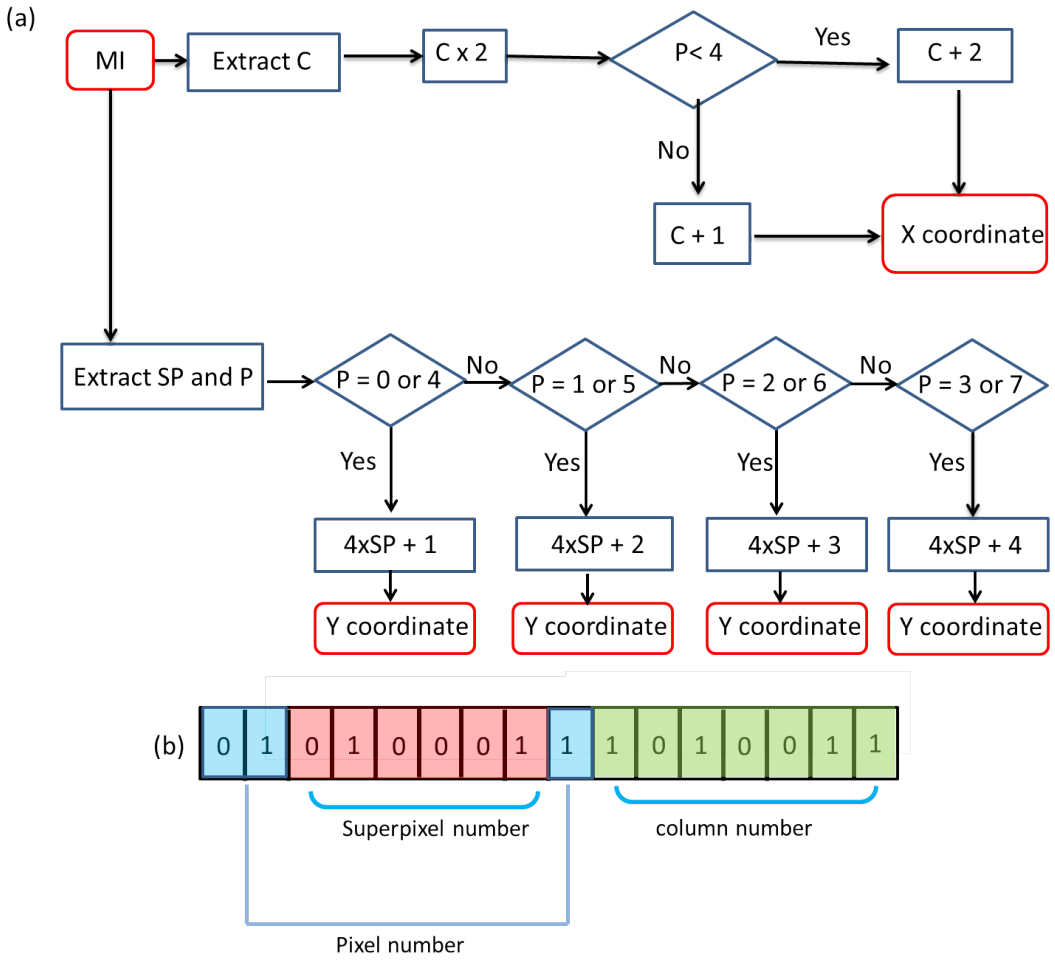


Figure 7.4: (a) Flow chart describing an algorithm that converts the matrix index (MI) of a pixel into an x, y coordinate. C = column, SP = super pixel and P = pixel. (b) An example of a 16 bit binary address and how it corresponds to the pixel, superpixel and column number. See text for details

of clock cycles is multiplied by 1.5625 to be converted into nanoseconds. The fToA is then subtracted from the ToA to give events in 1.5625 ns time bins. With this information, the data is now in the format (x, y, t, ToT), where t is the arrival time for an event with 1.5625 ns precision (ToA - fToa).

Fig. 7.5 demonstrates the benefits of using the fToA clock to determine the arrival time of an event. It is clear from the figure that using the fToA clock allows an additional peak from the mass spectrum of Rhodamine B to be observed. The reduction in the number of counts between the ToA and ToA - fToA is a result of the difference in bin widths of 25 ns versus 1.5625 ns respectively.

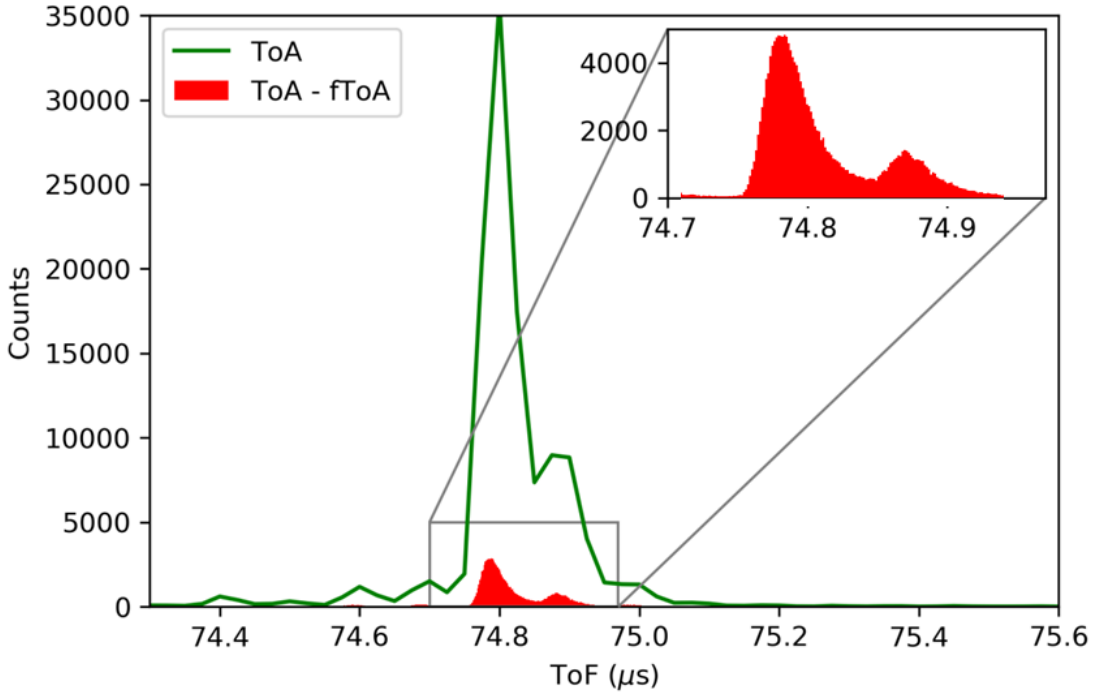


Figure 7.5: A 372 Da ion mass peak from a Rhodamine mass spectra recorded with the Tpx3Cam. The green line indicates the arrival time distribution if only the ToA (40 MHz clock) is used. The bin widths of the green trace are 25 ns. The red histogram shows the time of arrival when the fToA is subtracted. By doing this, an additional mass peak is observed. The bin widths of the red trace are 1.5625 ns.

7.3.2 Clustering

Operating the Tpx3Cam in continuous mode outputs non-sectioned data sets. To split this data into individual ToF spectra a machine learning protocol called clustering is used [191]. In Python, a clustering algorithm called Kmeans can be implemented with a machine learning module from the Scikit package [192].

The objective for this clustering algorithm is to partition n observations into k clusters, where n is the number of ion events and k is the number of laser shots. There are three steps to the clustering algorithm: initialisation, assignment and repetition. The initialisation generates k initial centroids, with the Timepix data set k equal to the number of lasers shots. The assignment stage involves associating each data point with the nearest mean which is determined by measuring the Euclidean distance between the centroid and the timestamp of each ion event.

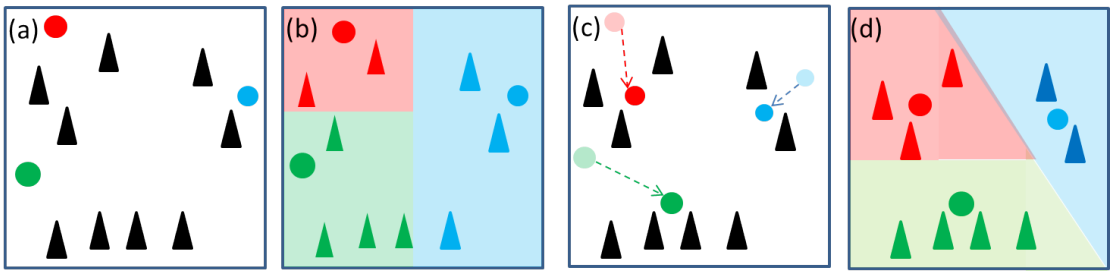


Figure 7.6: Clustering algorithm used to separate the continuous Tpx3Cam data file into individual laser shots. The circle represent the centroids. (a) Initialisation of centroids - the number of centroids is equal to the number of laser shots. (b) Assignment of each datum to the nearest centroided. (c) centroids move to average value in each cluster. (c) is then repeated until there are no further improvements. (d) clustered data set.

The centroid of each new cluster becomes the new centroid. This process is then repeated until the mean has converged. A pictorial representation is shown in Fig. 7.6. Clustering provides an efficient away to segment the data as most ion events occur in a period of 100 µs after the laser pulse, with a 100 ms separation between the next laser shot. In addition, the spatial position of the t_0 is constrained to the approximate region where the flash appears on the sensor. As a result of the non-complex nature of differentiating between these clusters, this process is highly accurate and computationally inexpensive.

Once clustered, data sets are aggregated by subtracting each ion event from the first event, which corresponds to the laser pulse, in each cluster. Ion events can then be grouped by time to form a ToF spectra, or by space to form an ion image.

7.4 Experiments with the Tpx3Cam

Using Nickel mesh with a 63 μm pitch, Rhodamine B dye samples were prepared with an electrosprayer as described in Chapter 2. The multi-mass imaging experiments that have been demonstrated in Chapter 4 and 5 were repeated, replacing the CCD camera and PMT with a Tpx3Cam. The camera does not need to be gated and the laser pulse was used to synchronise the Tpx3Cam acquisitions with the experimental cycles. The data sets were acquired for 15 minutes which corresponds to 9000 laser

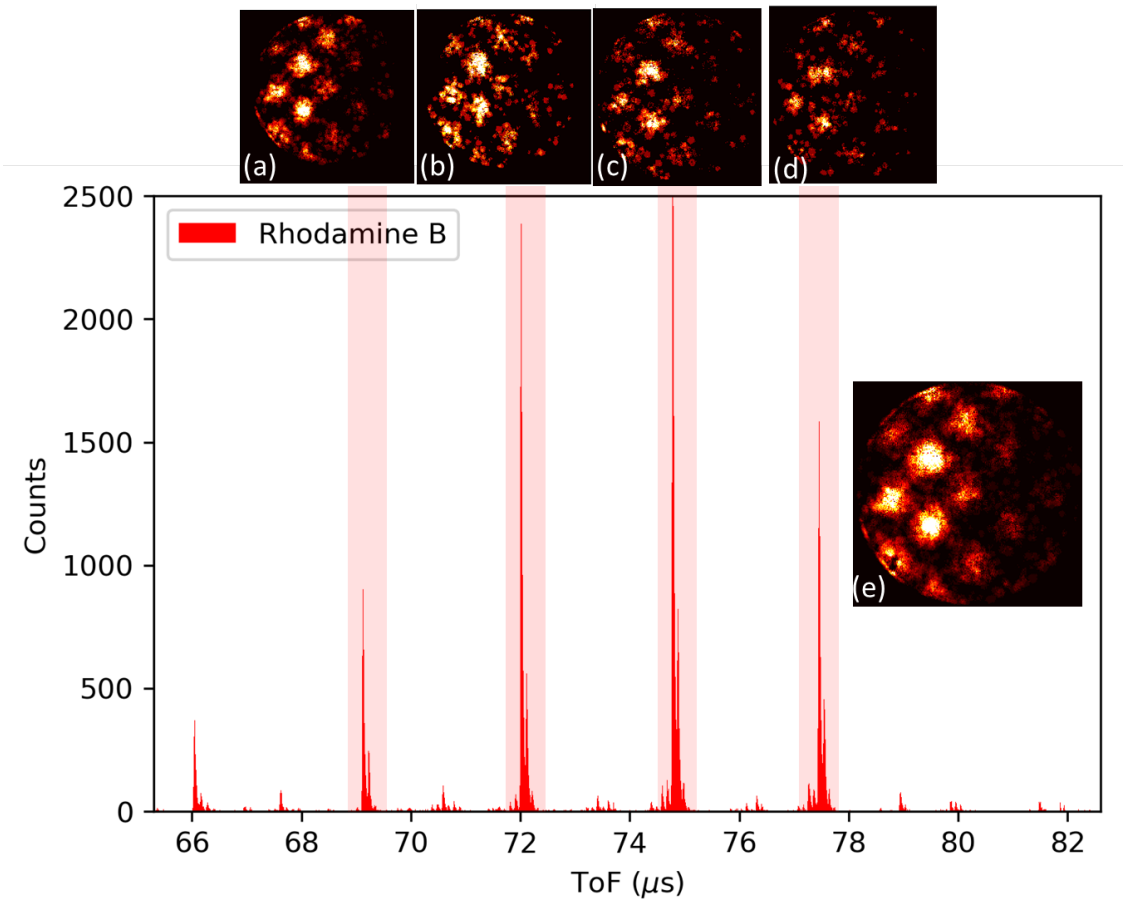


Figure 7.7: A ToF mass spectrum and the associated ion images for every major feature of Rhodamine B recorded with the Tpx3Cam. (a) Ion image of 315 Da ion. (b) Ion image of 343 Da ion. (c) Ion image of 372 Da ion. (d) Ion image of 399 Da ion. (e) Integrated ion image of all mass peak in Rhodamine B.

shots. Each five second file was on average 100 kB. To process this data using the methods described above took approximately 15 minutes.

7.4.1 Results

A mass spectrum and the associated ion images recorded with the Tpx3Cam are shown in Fig. 7.7. An ion image integrated for masses between 315 - 399 Da is shown in Fig 7.7(e). The spatial resolution of the ion image is calculated by using the method outlined in Chapter 4. The spatial resolution shown for the ion images in Fig.7.7, which covers a mass range of $315 < m/z < 399$, is less that 20μm.

When comparing the mass spectra and ion images collected with the Tpx3Cam

to those obtained with the CCD camera and PMT there are a few differences to note. Firstly, the intensity distribution for the ion image recorded with the CCD camera shown in Fig. 7.8(a) is more homogeneous compared with the ion image obtained using the Tpx3Cam shown in Fig. 7.8(b). This is likely as a result of different samples with a difference in sample surface depth being used when recording the data sets with the Tpx3Cam and the CCD/PMT. In addition, this difference may have occurred because the Tpx3Cam is slightly out of focus. Focusing the Tpx3Cam is particularly difficult because unlike the CCD camera there is no analogue image readout. Focusing must be fine tuned on an ion signal which is not consistent and therefore hard to focus on. Furthermore, the Tpx3Cam has a very sharp focal point which meant that placing the camera in the correct position required a high level of accuracy which was challenging. This will need to be addressed in the next generation of the experiment by mounting the camera onto a two-dimensional micrometer stage enabling fine adjustment. Another issue is that individual pixel thresholds across the sensor may not have exactly the same calibration, this is discussed later in the chapter. Individually or as a combination, these experimental limitations are likely to have reduced the homogeneity of intensity measured across the sensor.

Despite these differences, the overall form of both the mass spectrum and the ion image presented in Fig.7.8 is in close agreement with that obtained by the CCD and PMT. Both ion images exhibit the expected grid structure and the mass spectra show the same fragmentation pattern. However, the least intense peak corresponding to a Rhodamine B fragment at 74.658 μs is no longer observed above the baseline noise in the mass spectrum recorded with the Tpx3Cam. That being said, it is also worth noting that there is a reduced level of noise in the Tpx3Cam mass spectrum. This is because any noise that is observed on the detector assembly is not sufficient to surpass the pixel threshold voltage to trigger an event.

The major difference between the two acquisition methods is the temporal spread. With the PMT, the FWHM for a 372 Da Rhodamine ion is approximately 7 ns,

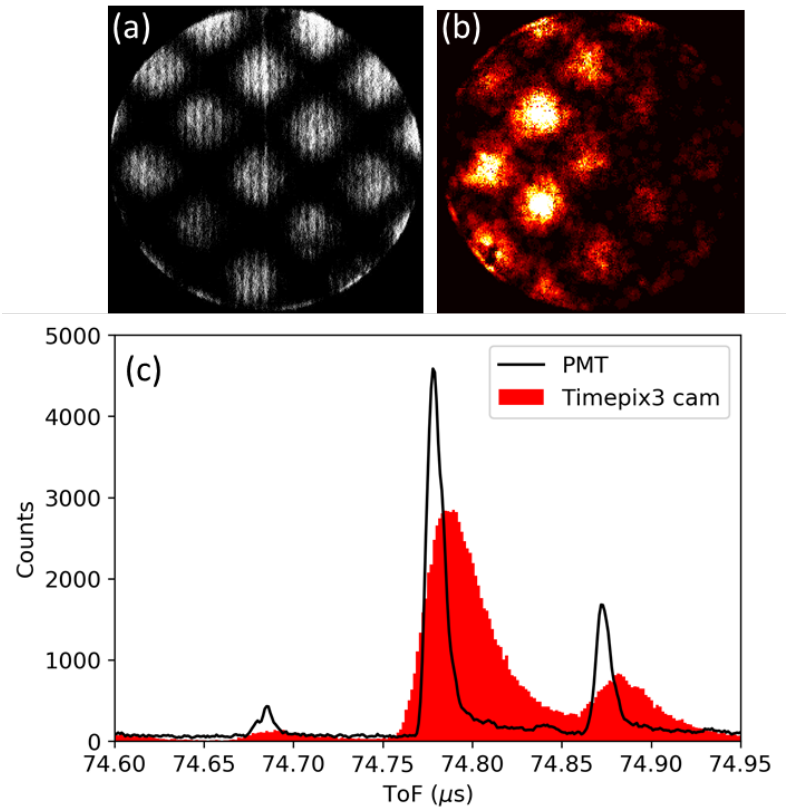


Figure 7.8: (a) Ion image of a Rhodamine B sample recorded with a CCD camera. (b) Ion image of a Rhodamine B sample recorded with the Tpx3Cam. (c) ToF mass spectra of Rhodamine B recorded with a PMT (black) and with the Tpx3Cam (red).

compared to a 40 ns FWHM record for the same m/z by the Tpx3Cam. This will be addressed in the remainder of this chapter. The next subsection will highlight an additional benefit of operating the Tpx3Cam in a continuous mode and using the laser to associate ion events with their experiment, as an alternative to an externally triggered readout system.

7.5 Exploring the time spread

The previous section concluded with multi-mass ion images that were recorded with a Tpx3Cam using a laser to determine the beginning of each experiment. The ion images recorded with this device achieved better than 20 μm spatial resolution. However, the temporal spread resulted in approximately FWHM = 40 ns, which is equivalent to 900 $m/\Delta m$ for the Rhodamine B mass peak. The following

section presents a number of methods that investigate the temporal spread of events recorded by the Tpx3Cam.

7.5.1 Laser shot variation

With the absence of an external trigger the data is read out in a continuous stream and clustered using the laser pulse. It is therefore essential that the correct t_0 is chosen for each experimental cycle when the data is clustered using the algorithm described earlier in the chapter. To verify that the assignment of t_0 is correct the time difference between the earliest event in each cluster in successive experiments is determined. The laser system used in these experiments is operated at a 10 Hz repetition rate, therefore the expected time difference between consecutive laser shots is 100 ms. The time difference between laser shots recorded over five seconds is shown in Fig 7.9 (a) - (e). It is clear from Fig. 7.9 (a) that certain t_0 are not separated by the repetition rate of the laser, instead there is a 409.6 μs offset. This is an issue with the AdvaDAQ readout software. The readout system records the number 12 bit clock cycles (4096 counts) which allows the ToA values for an event to be given large values. Without this, the readout system would be limited to record between 0 - 409.5 μs and therefore not able to record every time bin between consecutive laser shots as a unique number. Fig. 7.9 shows that periodically the number of clock cycles is incorrectly assigned. This will be addressed in future versions of the AdvaDAQ readout hardware.

The experiments with incorrectly assigned ToA values can be removed from the data set. Fig. 7.9 (b) shows the resultant variation in time difference between consecutive t_0, however there are still experiments where t_0 differs by approximately 60 μs, again these can be removed. Fig. 7.9(c) shows the time difference between constitutive laser shots after the removal of the 60 μs variations in Fig. 7.9 (b). The temporal resolution shows no discernible reduction when the time difference between laser shots (which determines t_0) is unconstrained, shown as a green histogram,

constrained to 0.1 s ± 300 μs shown red histogram, and constrained to 0.1 s ± 3 ns shown as a light blue histogram in Fig. 7.9 (d). This indicates that there is no dependency on the time spread of ion events and the time difference between different laser shots. The peak intensity does change, but this is expected as more events are removed from the analysis. A constant temporal spread demonstrates that this technique is not adversely affected by the issues with the readout system. This is because the ion events are clustered with the laser shot, and therefore if the laser shot moves the ion events also move by the same amount. Therefore, to correct these events 409.6 μs is subtracted from the ToA.

The pink boxes in Fig. 7.9 (e) show that the laser shot time difference occurs in time discrete time bins which correspond to the fToA clock count. This demonstrates that it is possible to identify experiments separated by a time difference between different t_0 of one time bin (1.5625 ns). An external trigger used to define a t_0 for a given experiment is limited to the inherent jitter that is associated with a laser system. The ability to define the experimental start time within one time bin is particularly advantageous for the high mass resolution ion microscope because the current laser system has a jitter of 6 - 10 ns which adds a convolution to the ToF spectrum. This convolution is of the order of the experimental resolution and is therefore significant. The Tpx3Cam operated in this configuration can reduce this convolution.

The following subsection addresses the temporal spread that has been recorded by the Tpx3Cam.

7.5.2 Centroiding

Each ion event causes a flash of light on the scintillator screen which is then detected by the Tpx3Cam. The flash typically illuminates several pixels resulting in a cluster of pixels being detected. The intensity profile of each flash on the phosphor screen is expected to be Gaussian [102], with the centre of the cluster being the most intense. For an event to be recorded, the charge build-up within the diodes of

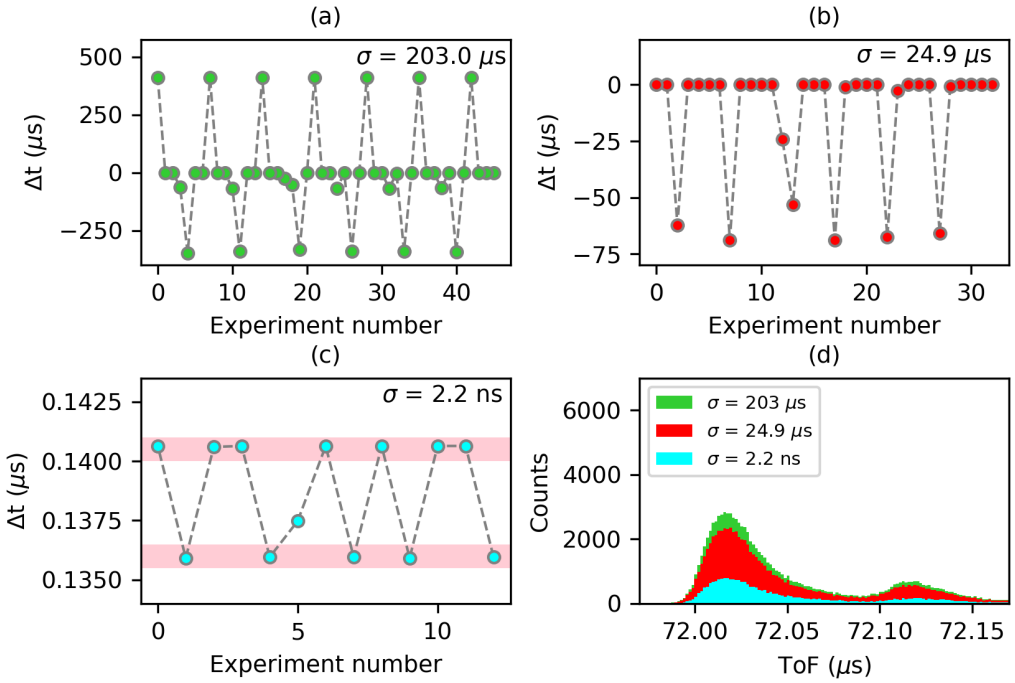


Figure 7.9: Time differences between sequential laser shots and the associated ToF spectra. Δt is the time difference between laser shots + $10^5 \mu$s. (a) The time difference between all laser shots recorded in a five second data file. (b) Sequential laser shots with a time difference of 0.1 s $\pm$ 300 μs. (c) Sequential laser shots separated by 0.1 s $\pm$ 3 ns. σ shows the standard deviation for the time difference between the laser shots. (d) The histogram plots of the entire experiment showing the ToF spectra when laser shots constraints from (a), (c) and (e) respectively. The pink boxes in (e) indicate the laser shots that have a time difference between the first recorded event in each experiment of 1.5625 ns. The resolution of the PMT shown in this spectrum is not optimised, the temporal spread has been shown to be as low as 4 ns in Chapter 4. This will further improve the resolution measured with the Tpx3cam.

an individual pixel must be sufficient to exceed an externally chosen threshold voltage. Pixels that lie towards the centre of a cluster will be subject to a higher photon flux, and should therefore be expected to exceed the threshold at an earlier time than those pixels towards the edge of a cluster. Since the earliest a pixel can detect an ion event is the actual time of the ion hit on the detector, the earliest time codes present within a cluster are typically the most accurate. This allows each cluster to be reduced to a single pixel and therefore a single time code. This process is discussed in more detail in Chapter 2.

A centroiding program was used to reduce the temporal spread of the ion events

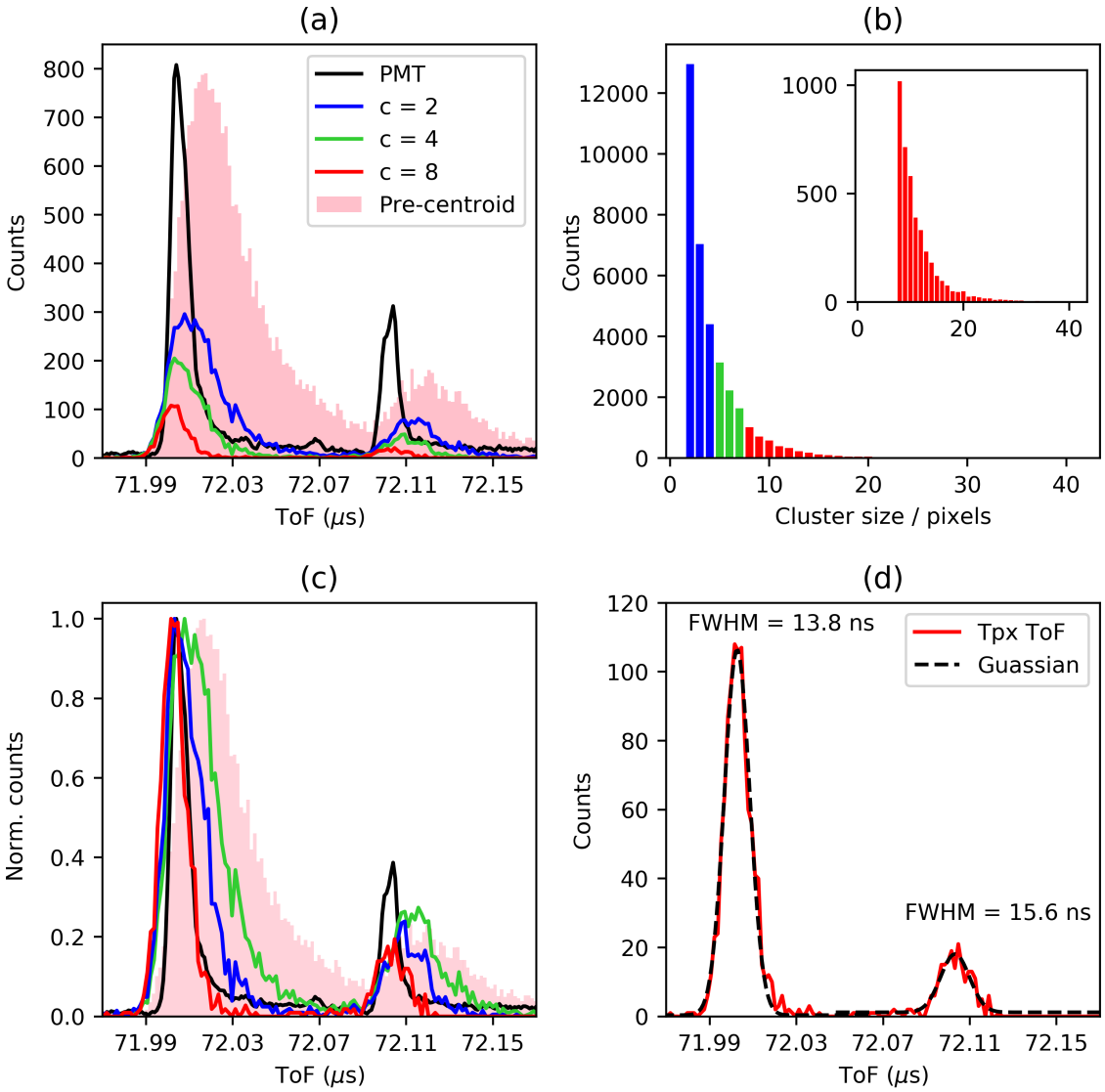


Figure 7.10: (a) ToF mass spectra of a 343 Da Rhodamine B ion. c indicates the minimum cluster size to be centroided. The PMT, shown as a solid black trace was normalised to the height of the pre-centroided data set, shown in pink. Sequential improvements in resolution are shown as c increases. (b) Shows the cluster distribution (number of pixels in a cluster) for the ToF spectra in (a). The different colours indicate the cluster distributions used for the ToF spectra with the corresponding colours in (a). (c) The normalised ToF spectra from (a). (d) The red trace from (a) has been fit Gaussian functions, the FWHM = 13.8 ns and FWHM = 15.6 ns which corresponds to approximately 3000 $m/\Delta m$. Further increases in the minimum cluster size are possible, but would require more statistics to accurately characterise the temporal resolution.

recorded with the Tpx3Cam [159]. To use this programme the data files need to be in the form x, y, number of time bins and the laser shot number. The x, y coordinates and the laser shot were already in the correct form, the arrival time of

each ion event was determined by dividing by the bin width (1.5625 ns) to convert into number of bins. This was followed by selecting a number of parameters for the centroiding programme. First, the maximum and minimum time code were fixed at 40,000 and 55,000 time bins respectively, this ensured that only clusters from the Rhodamine ions were processed. Second, the time window in which the algorithm searches for connected clusters was set to 64 bins, this corresponds to approximately 100 ns. This value was chosen to reflect the temporal spread shown in Fig. 7.8. Other time codes were tested, but resulted in insignificant changes to the temporal spread. The final parameters to be chosen were the minimum and maximum cluster size. The maximum cluster size was fixed at 40 pixels. The minimum cluster size was varied to characterise the effect that this has on the temporal resolution.

Fig. 7.10 (a) shows the improvement in resolution as the minimum cluster size is increased. Furthermore, the asymmetry in the ToF peak is reduced as the minimum cluster size increases. However, as the minimum cluster size increases, the signal intensity decreases. The red trace has a minimum cluster size set to 8 pixels, this shows the most improved temporal resolution, resolving the 372 Da mass peak to a FWHM approximately equal to 13.8 ns. This was decided as a sensible compromise between peak symmetry, signal intensity and improved resolution.

Increasing the minimum cluster size allows only larger clusters which correspond to larger, and therefore brighter, flashes on the scintillator screen to be centrioded. The higher the photon flux experienced by each pixel of the Tpx3Cam the earlier the pixel threshold is exceeded, resulting in a more accurate time code for the event. Conversely, smaller clusters are likely to be associated with less intense flashes, and will therefore have less accurate timing information. Fig. 7.10 (b) shows the distribution in pixels per cluster that were used to generate the red trace Fig. 7.10 (a). The smaller clusters are the most frequent which is a direct result of the MCP voltage. An increase in the frequency of larger clusters can be achieved by using a higher MCP voltage and hence higher detection efficiency.

Following on from the work presented, the effect that the MCP voltage has on cluster size distribution will be investigated. This should provide a pathway for a further reduction in temporal spread.

The next subsection will present the future work required to fully realise the full benefits of operating the Tpx3Cam in this configuration.

7.6 Future improvements to the time resolution

This section will outline how energy calibration to the Timepix3 sensor can in principle improve the temporal resolution.

7.6.1 Pixel calibration

The duration that a pixel exceeds its threshold voltage during an experimental acquisition is defined as the time over threshold (ToT) and is recorded for each event. The ToT is an estimate of the signal amplitude or in the case of the Tpx3Cam, the number of photons absorbed by the silicon sensor in front of the pixel. As the chip contains 65536 pixels that act as independent channels, their responses will not be identical. Therefore, it is necessary to perform an energy calibration across the detector. The SPIDR readout system has the ability to send different magnitude voltage pulses (test pulses) to the pixel array [193]. The external voltage generates a charge in each pixel. By changing the amplitude of the pulse the amount of charge in each pixel can be changed [194].

The test pulse calibration procedure measures the dependence of the ToT values on the injected voltage at each pixel. This allows the relationship between input charge and ToT value to be determined. Typically many different voltages over a range 0 - 600 mV are used to determine the calibration function. The ToT response to the voltage is very non-linear at low voltages (approximately 0 - 200 mV) and linear for higher voltages [195]. The experiments presented in this thesis are in the

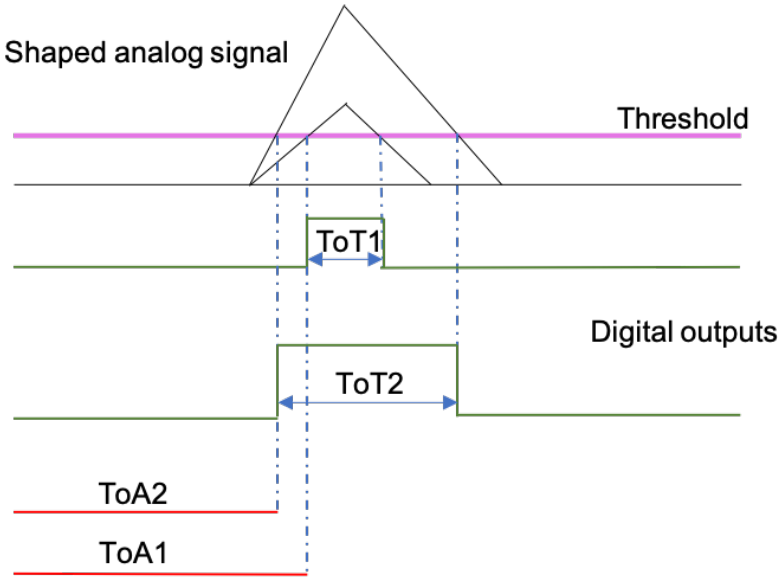


Figure 7.11: A cartoon illustrating the time-walk effect that can occur in a constant threshold discriminator located within a pixel. A typical event activates a number of pixels with a distribution of energies (ToA1 and ToA2). Pixels that are subject to larger energies surpass the threshold before pixels subjected to smaller energies. This broadens the signal for a given ion event, reducing the temporal resolution.

non-linear region of this curve. Once the calibration function is known, the change in ToT value across a cluster of pixels can reflect the change in energy [196, 197].

7.6.2 Time-walk correction

Once the detector is calibrated, a correction for the time-walk effect in the ToA is possible. The time-walk effect results in a distribution of ToA for a given event that depends on the number of photons (energy) recorded in a pixel. The time-walk effect in a constant threshold discriminator occurs because each event produces multiple photons that activate a cluster of pixels. The cluster size typically ranges from 4 - 25 pixels. A different number of photons arrives at each pixel within a cluster which causes the pixels to reach the threshold voltage at different times, as illustrated in Fig.7.11. Signals (photons) from the output of the Tpx3Cam electronics have a similar rise time, and as a result, larger signals cross the threshold earlier, producing a smaller ToA and larger ToT values compared with smaller signals. This effect causes the signal to broaden and therefore, reduces the temporal resolution.

A time-walk correction is achieved measuring the correlation between ToT and ΔToA from the interaction point which is usually taken as highest ToT. Weinacht *et al.* demonstrated a 40% reduction in the temporal spread after a time-walk correction [187]. This suggests that to achieve the full capabilities of the Timepix3 sensor a correction for the energy difference across a pixel is required. However, for the experiments presented in this chapter, the resulting improvement with this correction is expected to be nominal, as the ToF spectrum recorded with the PMT and the Tpx3Cam already match closely, as shown in Fig. 7.10 (c). Weinacht *et al.* used a P47 phosphor screen which allow a very high quantum efficiency (90%) of the Tpx3cam resulting in a large distribution of energies at over the pixel [115], and therefore a time-walk correction will be effective. Compared to exalite 404 which provides a quantum efficiency closer to 80% [102], the energy spread per pixel is smaller, and therefore a ToT correction will be less effective.

7.7 Summary

This chapter has presented a Tpx3Cam applied to an ion microscope mass spectrometer with a fast scintillator screen. The Tpx3Cam uses an inexpensive readout system that cannot be externally triggered. As a consequence, the camera is operated in a continuous mode using an optical fibre to direct the laser pulse at the sensor, which enables the data to be separated by individual experiments. Performing the experiment in this configuration reduces the cost of the readout system from £80,000 to £3,000.

The data analysis methods used to separate the continuous data into individual experiments has been presented. The spatial resolution recorded by the sensor was approximately 20 μm and compared well to the ion image recorded with the CCD camera. However, the temporal spread that was exhibited by the raw data was significantly larger than the corresponding spread recorded by a PMT. This was corrected using a centroiding algorithm which has improved the

time distribution to 13.8 ns FWHM, which corresponds to a mass resolution of approximately 3000 $m/\Delta m$. The temporal spread recorded with this Tpx3Cam is an comparable to the resolution achieved by Weinacht *et al.*, who recorded a 13.9 ns FWHM for the I^{2+} peak following strong field ionisation of CH_2IBr, although they do attribute a 7 ns convolution from the P47 screen used in their experiments. The resolution presented in this chapter has increased the recorded mass resolution by a factor of two compared with a PImMS camera which has previously been used in mass spectrometry. This chapter has also showed that operating the camera in a continuous mode can allow the start time of a particular experiment to be defined within a 1.5625 ns time window.

The next chapter will conclude the thesis and present the future direction of microscope ion imaging.

8 Conclusions and future work

This chapter summarises the main conclusions drawn from the simulation and experimental work reported in this thesis, and highlights a number of suggestions for future lines of investigation.

8.1 Conclusions

This thesis has presented developments in time-of-flight microscope ion imaging. This fully functional imaging mass spectrometer is now able to simultaneously acquire spatially resolved ion images with high resolution.

Chapter 1 provided a context for this thesis. The chapter begins with a brief history of mass spectrometry and an explanation of ionisation methods. The chapter then focused on two methods of ion imaging: microprobe and microscope. The former being the conventional technique that routinely achieves high mass and spatial resolution over a large mass range, and the latter being a high-throughput alternative. A comparison of the performance of these techniques then sets the objective of the thesis, which is to improve the resolutions of microscope ion imaging. Finally, this chapter gave an overview of the detector technology that can be coupled with an ion microscope to further improve throughput.

Chapter 2 describes the reflectron MSI used in chapters 4 and 5. This chapter also details two different sample preparation methods that can be used to improve ion yield in MALDI/LDI experiments. The simulation methods and a description of minimisation algorithms are detailed in Chapter 3.

The characterisation of a novel time-of-flight stigmatic ion microscope combined with a reflectron is detailed in Chapter 4. First, this instrument is optimised *in silico* with a genetic algorithm and a Nelder-Mead simplex minimisation routine. These simulations provided a starting point for experimental optimisation. This instrument can simultaneously achieve approximately $8100\,m/\Delta m$ and spatial resolution less than $14\,\mu$m over a 60 Da mass range. The mass resolution was found to be limited by the response time of the instrument. Fast imaging sensors have been augmented to the reflectron MSI and multi-mass ion imaging within one experimental cycle has been demonstrated. The data processing techniques developed for this instrument are also described.

The limited mass range over which the reflectron can achieve high mass resolution is addressed in Chapter 5 with the advent of electrodynamic PEDA, a variant of delayed extraction. This technique increases the voltage applied to the extractor plate as a function of time. This allows a broad mass range to have a reduced temporal spread. With this technique, a mass resolution greater than $3500\,m/\Delta m$ over a 300 Da mass range was achieved experimentally. This chapter also presents the simulations of the next generation of electrode pulsing - quadratic electrodynamic PEDA. Simulations show that if the voltage increase is modelled as a quadratic function, the maximum mass resolution achieved with single field PEDA ($30{,}000\,m/\Delta m$) can be achieved over 600 Da mass range.

Chapter 6 investigates the factors that contribute to the spatial resolving power in stigmatic ion imaging. This chapter then presents a simulated ion microscope that is capable of achieving 800 nm spatial resolution with a field of view diameter equal to $200\,\mu$m. This is achieved using large extraction fields to minimise transverse

velocities, and an ESA to magnify the ion image. The mass resolution is improved to approximately 1800 $m/\Delta m$ using a second ESA and pulsed PEDA optic.

The final experimental chapter presents the TimePix3 cam combined with the reflectron MSI. The Timepix3 cam, in principle, can acquire each peak in a mass spectra within one experimental cycle with a 1.5625 ns timing resolution. The motivation for this chapter was to develop a procedure with a reduced cost that would allow the Timepix3 cam to operate in continuous mode without using an external trigger. To achieve this, the data was associated with the correct experimental cycle by using an optical fibre connected to the laser system to activate a cluster of pixels creating a pseudo-t_0 for each experiment. This chapter presented progress towards this novel readout system. Firstly, the data processing methods used to construct the ion image and mass spectra recorded with the Timepix 3 cam were discussed. This was followed by a number of methods that aimed to reduce the temporal spread of ion events recorded by the sensor. This chapter concludes by outlining the future developments of this readout system.

The combination of these developments improves the performance of microscope ion imaging and makes this technique competitive with microprobe MSI. The resolution of the ion microscope combined with the high-throughput capability makes this an important technique for high resolution chemical analysis of complex surfaces.

8.2 The future

Microscope ion imaging with a reflectron still has a number of limitations that need to be addressed to make this technique preferential for spatial and chemical profiling. First, the spatial resolution achieved experimentally is an order of magnitude larger than the resolution that can be achieved by microprobe MSI. This has been addressed by simulations presented in Chapter 6. Future work will incorporate these ion optics into the reflectron MSI to achieve sub-micron spatial resolution.

The high-throughput capacity of the reflectron ion microscope can be improved by increasing the field-of-view. This can be achieved using an einzel lens placed at the entrance to the reflectron. The einzel lens reduces the magnification of the ion trajectories as they enter and exit the reflectron. Preliminary simulations have shown that the magnification can be reduced from $x80$ to $x40$.

Chapter 4 and 5 demonstrate significant improvements in the achievable mass resolution when a reflectron and pulsed ion optics are used. However, this resolution was limited experimentally as the instrument has an inherent response time. A new generation of CMOS sensors have sub-nano second timing resolution and can be placed in vacuum. Incorporation of these sensors into the reflectron MSI will allow the maximum resolution, which has been shown *in silico*, to be achieved experimentally.

Chapter 5 presents simulations for a novel pulsed variant that can increase the potential in the acceleration region using a quadratic function. The next stage will be to develop the electronics capable of generating this quadratic pulse on a microsecond time scale.

A Timepix3 cam was combined with the reflectron MSI in Chapter 7. Future work will optimise the cluster per pixel distribution which will be determined by varying the MCP voltage that will return the smallest temporal spread. The final section of Chapter 7 presented the method for a ToT calibration. After the pixels are calibrated the time-walk effect can be correct. These experiments require a readout system such as SPIDR that can issue test charge pulses to the pixel array. A SPIDR readout system will become available in the near future.

The exalite 404 screen used throughout this thesis can be further characterised using the Timepix3 sensors, verifying rise time and the decay constant to a high precision. Furthermore, the relationship between the quantum efficiency of the phosphor screen and the ToT can be determined. Future developments will incorporate microlenses with the Timepix3 pixel array, this will focus photons

onto the light sensitive area of the pixel and increase the number of events recorded in a given experiment.

Once these characterisation have been completed, electrodynamic PEDA will then be used to simultaneously reduce the temporal spread over a wide mass range, and the Timepix3 cam will then be used to record each of these events. The complexity of the mass spectra can then be increased to fully leverage the benefits of the 1.5625 ns timing precision of the Timepix3 cam.

After these improvements to the instrument have been made, the ion microscope will be a powerful analytic technique with high efficiency. The high speed and high resolution offered by this instrument makes it amenable to a analyse a wide range to biological samples such as diseased tissues. Furthermore, applications that use micro-arrays would benefit from microscope ion imaging. Micro-arrays are comprised of hundreds, if not thousands of individual wells that could be simultaneously imaged, providing a high-throughput method for screening analytes to determine the presence unknown species or bio-markers.

Further applications that would benefit from microscope ion imaging is SIMS analysis with water cluster ion beams [198]. Water cluster ion beams provide a pathway for intact high mass protein analysis. This technique currently has reduced spatial resolution compared with other cluster beam ion sources, as the water cluster cannot be focused without degradation. This application could be improved using an ion microscope, as the resolving power is decoupled from the ionisation area. Therefore, spatial resolutions that are significantly greater than the cluster size could be measured that would otherwise have been impossible.

References

(1) Ehl, R. G.; Ihde, A. J. *J. Chem. Educ.* (**1954**), **31**, 226.

(2) Hiebert, E. N., *Electric Discharge in Rarefied Gases: The Dominion of Experiment. Faraday. Plücker. Hittorf*, (1995).

(3) Hedenus, M. *Astronomische Nachrichten* (**2002**), **323**, 567–569.

(4) Thomson, J. J. *Longman, Green and Company* (**1921**), **1**,

(5) Aston, F. *Lond.Edinb.Dubl.Phil.Mag.J. of Sci.* (**1919**), **38**, 707–714.

(6) Conrad, R. *Trans. Faraday Soc.* (**1934**), **30**, 215–220.

(7) Cameron, A. E.; Eggers, D. F. *Rev. Sci. Instrum.* (**1948**), 605.

(8) Wiley, W. C.; McLaren, I. H. *Rev. Sci. Instrum.* (**1955**), **26**, 1150–1157.

(9) Newton, I., *Philosophiæ Naturalis Principia Mathematica*, (1687).

(10) Moniatte, M.; van der Goot, F.; Buckley, J.; Pattus, F.; van Dorsselaer, A. *FEBS Letters* (**1996**), **384**, 269–272.

(11) Beynon, J. H. *Microchim. Acta* (**1956**), **44**, 437–453.

(12) Finnigan, R. E. *Anal. Chem.* (**1994**), **66**, 969A–975A.

(13) Paul, W.; Steinwedel, H. Apparatus For Separating Charged Particles of Different Specific Charges., US2939952A, (1954).

(14) Mamyrin, B. A.; Karataev, V. I.; Shmikk, D. V.; Zagulin, V. A. *Am. Inst. of Phys.* (**1973**), **37**, 82–89.

(15) Kanu, A. B.; Dwivedi, P.; Tam, M.; Matz, L.; Hill Jr., H. H. *J. Mass Spectrom.* (**2008**), **43**, 1–22.

(16) Arpino, P.; Baldwin, M. A.; McLafferty, F. W. *Biomed. Mass Spectrom.* (**1974**), **1**, 80–82.

(17) Comisarow, M. B.; Marshall, A. G. *Chem. Phys. Lett.s* (**1974**), **25**, 282–283.

(18) Hu, Q.; Noll, R. J.; Li, H.; Makarov, A.; Hardman, M.; Graham Cooks, R. *J. Mass Spectrom.* (**2005**), **40**, 430–443.

(19) Shi, S. D.-H.; Hendrickson, C. L.; Marshall, A. G. *Proceedings of the National Academy of Sciences* (**1998**), **95**, 11532–11537.

(20) Dempster, A. J. *Phys. Rev.* (**1918**), **11**, 316–325.

(21) Aston, F. W. *Proceedings of the Royal Society of London. Series A - Mathematical and Physical Sciences* (**1937**), **163**, 391–404.

(22) Mamyrin, B., *Laser Assisted Reflectron Time-of-Flight Mass Spectrometry*; Elsevier: Amsterdam, (1994).

(23) Yeh, C.; Willey, K.; Robbins, D.; Duncan, M. *Int. J. Mass Spectrom. Ion Processes* (**1994**), **131**, 307–317.

(24) Tang, X.; Beavis, R.; Ens, W.; Lafortune, F.; Schueler, B.; Standing, K. G. *Int. J. Mass Spectrom. Ion Processes* (**1988**), **85**, 43–67.

(25) Verster, J. *Philips Research Reports* (**1963**), **18**, 465–605.

(26) Guo, A. *Improving the Performance of Microscope-Mode Imaging Mass Spectrometry*, DPhil Thesis, (2018).

(27) Yavor, M. I.; Plaß, W. R.; Dickel, T.; Geissel, H.; Scheidenberger, C. *Int. J. Mass spectrom.* (**2015**), **381-382**, 1–9.

(28) Shmikk, D.; Dubenskii, B. *Tech. Phys.* (**1988**), **58**, 1534–1537.

(29) Zhang, J.; Enke, C. G. *European J. Mass Spectrom.* (**2000**), **6**, 515–522.

(30) Zhang, J.; Gardner, B. D.; Enke, C. G. *J. Am. Soc. Mass Spectrom.* (**2000**), **11**, 765–769.

(31) Zhang, W.; Chait, B. T. *Int. J. Mass Spectrom. Ion Processes* (**1997**), **160**, 259–267.

(32) El-Aneed, A.; Cohen, A.; Banoub, J. *Appl. Spectrosc. Rev.* (**2009**), **44**, 210–230.

(33) Hoffman, E. d.; Stroobant, V., *Mass Spectrometry Principles and Applications*; John Wiley & Sons, Ltd: (2012).

(34) Creaser, C. S.; Ratcliffe, L. *Current Anal. Chem.* (**2006**), **2**, 9–15.

(35) Bleakney, W. *Phys. Rev.* (**1929**), **34**, 157–160.

(36) Harrison, A., *Chemical Ionization Mass Spectrometry*; Routledge: (1992).

(37) Beckey, H.; Hey, H.; Levsen, K.; Tenschert, G. *Int. J. Mass spectrom. and Ion Physics* (**1969**), **2**, 101–123.

(38) Mora, J. F. d. l.; Van Berkel, G. J.; Enke, C. G.; Cole, R. B.; Martinez-Sanchez, M.; Fenn, J. B. *J. Mass Spectrom.* (**2000**), **35**, 939–952.

(39) French, J. B.; Thomson, B. A.; Davidson, W. R.; Reid, N. M.; Buckley, J. A., *Atmospheric Pressure Chemical Ionization Mass Spectrometry*; Springer US: (1985).

(40) Robb, D. B.; Covey, T. R.; Bruins, A. P. *Anal. Chem.* (**2000**), **72**, 3653–3659.

(41) Beavis, R. C.; Chait, B. T.; Fales, H. M. *Rapid Commun. Mass Spectrom.* (**1989**), **3**, 432–435.

(42) Ninomiya, S.; Ichiki, K.; Yamada, H.; Nakata, Y.; Seki, T.; Aoki, T.; Matsuo, J. *Rapid Commun. Mass Spectrom.* (**2009**), **23**, 1601–1606.

(43) Van Vaeck, L.; Adriaens, A.; Gijbels, R. *Mass Spectrom. Rev.* (**1999**), **18**, 1–47.

(44) Morgan, R. P. *Org. Mass Spectrom.* (**1978**), **13**, 490–490.

(45) Macfarlane, R. D. *Trends in Anal. Chem.* (**1988**), **7**, 179–183.

(46) Shoji, O.; Motohiro, N.; Gen-etsu, M.; Ryuichi, A.; Yoshinao, W. *Rapid Commun. Mass Spectrom.* (**2004**), **18**, 2811–2817.

(47) Karas, M.; Hillenkamp, F. *Anal. Chem.* (**1988**), **1**, 2299–2301.

(48) Karas, M.; Bachmann, D.; Hillenkamp, F. *Anal. Chem.* (**1985**), **57**, 2935–2939.

(49) Moullintraffort, L.; Bruneaux, M.; Nazabal, A.; Allegro, D.; Giudice, E.; Zal, F.; Peyrot, V.; Barbier, P.; Thomas, D.; Garnier, C. *J. Biol. Chem.* (**2010**), **285**, 15100–15110.

(50) Karas, M.; Bahr, U.; Strupat, K.; Hillenkamp, F.; Tsarbopoulos, A.; Pramanik, B. N. *Anal. Chem.* (**1995**), **67**, 675–679.

(51) Zenobi, R.; Knochenmuss, R. *Mass Spectrom. Rev.* (**1998**), **17**, 337–366.

(52) Juhasz, P.; Costello, C. E.; Biemann, K. *J. Am. Soc. Mass Spectrom.* (**1993**), **4**, 399–409.

(53) Kaufmann, R. *J. Biotechnol.* (**1995**), **41**, 155–175.

(54) Berkenkamp, S.; Kirpekar, F.; Hillenkamp, F. *Science* (**1998**), **281**, 260–262.

(55) Nordhoff, E.; Ingendoh, A.; Cramer, R.; Overberg, A.; Stahl, B.; Karas, M.; Hillenkamp, F.; Crain, P. F.; Chait, B. *Rapid Commun. Mass Spectrom.* (**1992**), **6**, 771–776.

(56) Dai, Y.; Whittal, R. M.; Bridges, C. A.; Isogai, Y.; Hindsgaul, O.; Li, L. *Carbohydr. Res.* (**1997**), **304**, 1–9.

(57) Juhasz, P.; Costello, C. E. *Rapid Commun. Mass Spectrom.* (**1993**), **7**, 343–351.

(58) McCarley, T. D.; McCarley, R. L.; Limbach, P. A. *Anal. Chem.* (**1998**), **70**, 4376–4379.

(59) Chen, X.; Carroll, J. A.; Beavis, R. C. *J. Am. Soc. Mass Spectrom.* (**1998**), **9**, 885–891.

(60) Niu, S.; Zhang, W.; Chait, B. T. *J. Am. Soc. Mass Spectrom.* (**1998**), **9**, 1–7.

(61) Lu, I.-C.; Lee, C.; Lee, Y.-T.; Ni, C.-K. *Annual Review of Anal. Chem.* (**2015**), **8**, 21–39.

(62) Chu, K. Y.; Lee, S.; Tsai, M.-T.; Lu, I.-C.; Dyakov, Y. A.; Lai, Y. H.; Lee, Y.-T.; Ni, C.-K. *J. Am. Soc. Mass Spectrom.* (**2014**), **25**, 310–318.

(63) Knochenmuss, R. *Analyst* (**2006**), **131**, 966–986.

(64) Karas, M.; Bachmann, D.; Bahr, U.; Hillenkamp, F. *Int. J. Mass Spectrom. Ion Processes* (**1987**), **78**, 53–68.

(65) Ehring, H.; Karas, M.; Hillenkamp, F. *Org. Mass Spectrom.* (**1992**), **27**, 472–480.

(66) Karas, M.; Gluckmann, M.; Schafer, J. *J. Mass Spectrom.* (**2000**), **35**, 1–12.

(67) Karas, M.; Kruger, R. *Chem. Rev.* (**2003**), **103**, 427–440.

(68) Dreisewerd, K.; Schurenberg, M.; Karas, M. *Int. J. Mass Spectrom. Ion Processes* (**1995**), **141**, 127–148.

(69) Westmacott, G.; Ens, W.; Hillenkamp, F.; Dreisewerd, K.; Schurenberg, M. *Int. J. Mass spectrom.* (**2002**), **221**, 67–81.

(70) Ole Vorm, P. R.; Mann, M. *Anal. Chem.* (**1994**), **66**, 3281–3287.

(71) Mank, M.; Stahl, B.; Boehm, G. *Anal. Chem.* (**2004**), **76**, 2938–2950.

(72) Overberg, A.; Karas, M.; Hillenkamp, F.; Cotter, R. J. *Rapid Commun. Mass Spectrom.* (**1991**), **5**, 128–131.

(73) McDonnell, L. A.; Heeren, R. M. *Mass Spectrom. Rev.* (**2007**), **26**, 606–643.

(74) Honig, R. E.; Woolston, J. R. *Appl. Phys. Lett.* (**1963**), **2**, 138–139.

(75) Hillenkamp, F.; Unsöld, E.; Kaufmann, R.; Nitsche, R. *J. Appl. Phys.* (**1975**), **8**, 341–348.

(76) Van Vaeck, L.; Poels, K.; De Nollin, S.; Hachimi, A.; R, G. *Cell Biol. Int.* (**1997**), **21**, 635–648.

(77) Schober, Y.; Guenther, S.; Spengler, B.; Rompp, A. *Anal. Chem.* (**2012**), **84**, 6293–6297.

(78) Markus Stoeckli, T. B. F.; Caprioli, R. M. *Am. J. Mass Spectrom.* (**1999**), **10**, 67–71.

(79) Bednařík, A.; Machálková, M.; Moskovets, E.; Coufalíková, K.; Krásenský, P.; Houška, P.; Kroupa, J.; Navrátilová, J.; Šmarda, J.; Preisler, J. *J. Am. Soc. Mass Spectrom.* (**2019**), **30**, 289–298.

(80) Manicke, N.; Dill, A.; Ifa, D.; Cooks, R. *J. Mass Spectrom : JMS* (**2010**), **45**,

(81) Chandler, D. W.; Houston, P. L. *J. Phys. Chem.* (**1987**), **87**, 1445–1447.

(82) Eppink, A. T. J. B.; Parker, D. H. *Rev. Sci. Instrum.* (**1997**), **68**, 3477–3484.

(83) Amini, K.; Blake, S.; Brouard, M.; Burt, M. B.; Halford, E.; Lauer, A.; Slater, C. S.; Lee, J. W. L.; Vallance, C. *Rev. Sci. Instrum.* (**2015**), **86**, 103113.

(84) Kern, J. L. G.; Wu, T.-D.; Quintana, C.; Croisy, A. *BBA. Gen. Subjects.* (**2005**), **1724**, 228–238.

(85) Castaing, R.; Slodzian, G. *J. Microscopie* (**1962**), **1**, 395–410.

(86) R. Castaing and G. Slodzian, *Adv. Mass Spectrom.* (**1966**), **Vol 3**,

(87) Slodzian, G. *Secondry Ion Mass Spectrometry*, PhD thesis, (1975).

(88) Migeon, H. N.; Schuhmacher, M.; Slodzian, G. *Surf. Interface Anal.* (**1990**), **16**, 9–13.

(89) Bernius, M. T.; Chandra, S.; Morrison, G. H. *Rev. Sci. Instrum.* (**1985**), **56**, 1347–1351.

(90) De Chambost, E., *Chapter 1: A History of Cameca (1954–2009)*; Elsevier: (2011).

(91) Castaing, R.; Slodzian, G. *J.Phys E. Sci. Instrum.* (**1981**), **14**, 1119–1127.

(92) Schueler, B.; Sander, P.; Reed, D. *Vacuum* (**1990**), **41**, 1661–1664.

(93) Schueler, Bruno W. *Microsc. Microanal. Microstruct.* (**1992**), **3**, 119–139.

(94) Luxembourg, S. L.; Mize, T. H.; McDonnell, L. A.; Heeren, R. M. A. *Anal. Chem.* (**2004**), **76**, 5339–5344.

(95) Hazama, H.; Aoki, J.; Nagao, H.; Suzuki, R.; Tashima, T.; Fujii, K.-i.; Masuda, K.; Awazu, K.; Toyoda, M.; Naito, Y. *Appl. Surf. Sci.* (**2008**), **255**, 1257–1263.

(96) Hazama, H.; Yoshimura, K.; et.al, K. M. *J. Biomed. Opt.* (**2011**), **16**,

(97) Aoki, J.; Hazma, H.; Toyoda, M. *J. Mass Spectrom. Soc Jpn.* (**2011**), **59**, 57–61.

(98) Vestal, M. L.; Juhasz, P.; Martin, S. A. *Rapid Commun. Mass Spectrom.* (**1995**), **9**, 1044–1050.

(99) Guo, A.; Burt, M.; Brouard, M. *Int. J. Mass spectrom.* (**2017**), **429**, 121–126.

(100) Koppenaal, D. W.; Barinaga, C. J.; Denton, M. B.; Sperline, R. P.; Hieftje, G. M.; Schilling, G. D.; Andrade, F. J.; Barnes, J. H.; IV, I. *Anal. Chem.* (**2005**), **77**, 418–427.

(101) Brand, W. A. *J. Mass Spectrom.* (**1996**), **31**, 225–235.

(102) Winter, B. *Novel Method in Imaging Mass Spectrometry and Ion Time-of-Flight Detection*, DPhil Thesis, (2014).

(103) Wiza, J. L.; Henkel, P. R.; Roy, R. L. *Rev. Sci. Instrum.* (**1977**), **48**, 1217–1218.

(104) Stumpel, J. W.; Sanford, P. W.; Goddard, H. F. *J.Phys E. Sci. Instrum.* (**1973**), **6**, 397–400.

(105) Corr, J. J.; Kovarik, P.; Schneider, B. B.; Hendrikse, J.; Loboda, A.; Covey, T. R. *J. Am. Soc. Mass Spectrom.* (**2006**), **17**, 1129–1141.

(106) Yoshimura, H.; Hazama, H.; Aoki, J.; Toyoda, M.; Naito, Y.; Awazu, K. *Jpn. J. Appl. Phys.* (**2011**), **50**, 056701.

(107) Hicks, P. J.; Daviel, S.; Wallbank, B.; Comer, J. *J.Phys E. Sci. Instrum.* (**1980**), **13**, 713–715.

(108) Winter, B.; King, S. J.; Brouard, M.; Vallance, C. *Rev. Sci. Instrum.* (**2014**), **85**, 023306.

(109) Boyle, W. S.; Smith, G. E. *Bell Syst. Tech. J* (**1970**), **49**, 587–593.

(110) Vallance, C.; Brouard, M.; Lauer, A.; Slater, C. S.; Halford, E.; Winter, B.; King, S. J.; Lee, J. W. L.; Pooley, D. E.; Sedgwick, I.; Turchetta, R.; Nomerotski, A.; John, J. J.; Hill, L. *Phys. Chem. Chem. Phys.* (**2014**), **16**, 383–395.

(111) Amelio, G. F.; Tompsett, M. F.; Smith, G. E. *Bell Syst. Tech. J* (**1970**), **49**, 593–600.

(112) Matsumoto, K.; Nakamura, T.; Yusa, A.; Nagai, S. *Jpn. J. Appl. Phys.* (**1985**), **24**, 323–325.

(113) Mendis, S.; Kemeny, S. E.; Fossum, E. R. *IEEE Trans. Electron Devices* (**1994**), **41**, 452–453.

(114) Fossum, E. R. *Nucl. Instrum. Methods Phys. Res., Sect. A* (**1997**), **395**, 291–297.

(115) Fisher-Levine, M.; Nomerotski, A. *J. Instrum.* (**2016**), **11**, C03016–C03016.

(116) Amini, K.; Boll, R.; Lauer, A.; Burt, M.; Lee, J. W. L.; Christensen, L.; Brauthe, F.; Mullins, T.; Savelyev, E.; Ablikim, U.; Berrah, N.; Bomme, C.; Dusterer, S.; Erk, B.; Hoppner, H.; Johnsson, P.; Kierspel, T.; Krecinic, F.; Kupper, J.; Muller, M.; Muller, E.; Redlin, H.; Rouzée, A.; Schirmel, N.; Thogersen, J.; Techert, S.; Toleikis, S.; Treusch, R.; Trippel, S.; Ulmer, A.; Wiese, J.; Vallance, C.; Rudenko, A.; Stapelfeldt, H.; Brouard, M.; Rolles, D. *J. Phys. Chem.* (**2017**), **147**, 013933.

(117) Jungmann, J. H.; MacAleese, L.; Buijs, R.; Giskes, F.; de Snaijer, A.; Visser, J.; Visschers, J.; Vrakking, M. J. J.; Heeren, R. M. A. *J. Am. Soc. Mass Spectrom.* (**2010**), **21**, 2023–2030.

(118) Brouard, M.; Halford, E.; Lauer, A.; Slater, C. S.; Winter, B.; Yuen, W. H.; John, J. J.; Hill, L.; Nomerotski, A.; Clark, A.; Crooks, J.; Sedgwick, I.; Turchetta, R.; Lee, J. W. L.; Vallance, C.; Wilman, E. *Rev. Sci. Instrum.* (**2012**), **83**, 114101.

(119) Pooley, D. E.; Lee, J. W. L.; Brouard, M.; John, J. J.; Kockelmann, W.; Rhodes, N. J.; Schooneveld, E. M.; Sedgwick, I.; Turchetta, R.; Vallance, C. *IEEE Trans. Nucl. Sci* (**2017**), **64**, 2970–2981.

(120) Bass, M. J.; Brouard, M.; Clark, A. P.; Vallance, C. *J. Phys. Chem.* (**2002**), **117**, 8723–8735.

(121) Bouschen, W.; Schulz, O.; Eikel, D.; Spengler, B. *Rapid Commun. Mass Spectrom.* (**2010**), **24**, 355–364.

(122) Wang, L.; Browner, R. F. Oscillating Capillary Nebulizer., US5848751A, (1998).

(123) Stoian; Rosenfeld; Ashkenasi; Hertel; Bulgakova; Campbell *Phys. Rev. Lett.* (**2002**), **88**, 097603.

(124) Gluckmann, M.; Pfenninger, A.; Kruger, R.; Thierolf, M.; Karasa, M.; Horneffer, V.; Hillenkamp, F.; Strupat, K. *Int. J. Mass spectrom.* (**2001**), **210–211**, 121–132.

(125) Maštovská, K.; Lehotay, S. J.; Anastassiades, M. *Anal. Chem.* (**2005**), **77**, 8129–8137.

(126) Winter, B.; King, S. J.; Brouard, M.; Vallance, C. *Int. J. Mass spectrom.* (**2016**), **397–398**, 27–31.

(127) Wiza, J. L. *Nucl. Instrum. Meth. Phys. Res. A* (**1979**), **162**, 587–601.

(128) Niederlohner, D.; Bert, C.; Giersch, J.; Pfeiffer, K.-F.; Anton, G. *Nucl. Instrum. Methods Phys. Res., Sect. A* (**2003**), **509**, 138–145.

(129) Ballabriga, R.; Campbell, M.; Heijne, E. H. M.; Llopart, X.; Tlustos, L. *IEEE Trans. Nucl. Sci* (**2007**), **54**, 1824–1829.

(130) Zhao, A.; van Beuzekom, M.; Bouwens, B.; Byelov, D.; Chakaberia, I.; Cheng, C.; Maddox, E.; Nomerotski, A.; Svihra, P.; Visser, J.; Vrba, V.; Weinacht, T. *Rev. Sci. Instrum.* (**2017**), **88**, 113104.

(131) Turecek, D.; Holy, T.; Jakubek, J.; Pospisil, S.; Vykydal, Z. *J. Instrum.* (**2011**), **6**, C01046–C01046.

(132) Gahl, D., *SIMION 3D version 60*; ASMS: (1995).

(133) Sise, O.; Manura, D. J.; Dogan, M. *Eur. J. Phys.* (**2008**), **29**, 1165.

(134) Gil, S.; Saleta, M. E.; Tobia, D. *Am. J. Phys.* (**2002**), **70**, 1208–1213.

(135) Beavid, R. C.; Chait, B. T. *Chem. Phys. Lett.* (**1991**), **181**, 479–484.

(136) Karas, M.; Kruger, R. *Chem. Rev.* (**2003**), **103**, 427–440.

(137) Ens, W.; Mao, Y.; Mayer, F.; Standing, K. G. *Rapid Commun. Mass Spectrom.* (**1991**), **5**, 117–123.

(138) Knochenmuss, R.; Zhigilei, L. V. *J. Mass Spectrom.* (**2010**), **45**, 333–346.

(139) Winter, B.; Halford, E.; Brouard, M. *Int. J. Mass spectrom.* (**2013**), **356**, 14–23.

(140) Gluckmann, M.; Karas, M. *J. Mass Spectrom.* (**1999**), **34**, 467–477.

(141) Liang, C.-W.; Lee, C.-H.; Lee, Y.-T.; Ni, C.-K. *Chem. Asian. J.* (**2011**), **6**, 2986–2991.

(142) HTX-TM Sprayer., Accessed: 02.04.19, `www.htximaging.com`.

(143) Halford, E. *Microscope-Mode Imaging Mass Spectrometry with the PImMS Camera*, DPhil Thesis, (2015).

(144) Choi, K. S.; Lam, E. Y.; Wong, K. K. Y. *Opt. Express* (**2006**), **14**, 11551–11565.

(145) Muhlenbein, H.; Schomisch, M.; Born, J. *Parallel Comput.* (**1991**), **17**, 619–632.

(146) Wang, Q. J. *Water Resources Research* (**1991**), **27**, 2467–2471.

(147) Press, W. H.; Teukolsky, S. A.; Vetterling, W. T.; Flannery, B. P., *Numerical Recipes in Fortran 90 (2nd Ed.): The Art of Parallel Scientific Computing*; Cambridge University Press: (1996).

(148) Weickhardt, C.; Moritz, F.; Grotemeyer, J. *Mass Spectrom. Rev.* (**1996**), **15**, 139–162.

(149) Zhang, J.; Enke, C. G. *European J. Mass Spectrom.* (**2000**), **6**, 515–522.

(150) Zhang, J. *J. Am. Soc. Mass Spectrom.* (**2000**), **11**, 765–769.

(151) Yefchack, G.; Flory, C. *Int. J. Mass spectrom.* (**2002**), **214**, 89–94.

(152) Leskiw, B. D.; Kim, M. H.; Hall, G. E.; Suits, A. G. *Rev. Sci. Instrum.* (**2005**), **76**, 104101.

(153) Boesl, U.; Grotemeyer, J.; Walter, K.; Schlag, E. *Instrum. Sci. Technol.* (**1987**), **16**, 151–171.

(154) Johnson, L. V.; Walsh, M. L.; Bockus, B. J.; Chen, L. B. *J. Cell Biol.* (**1981**), **88**, 526–535.

(155) Johnson, S. G.; Frigo, M., *Implementing FFTs in Practice*; Connexions: (2008).

(156) Frigo, M. *Proc.ACM SIGPLAN Conf.on Programming Language Design and Implementation*, (1999); Vol. 34.

(157) Frigo, M.; Johnson, S. *Proc. 1998 IEEE Intl. Conf. Acoustics Speech and Signal Processing*, (1998); Vol. 3.

(158) Danielson, G.; Lanczos, C. *J. Franklin Inst.* (**1942**), **233**, 365–380.

(159) Slater, C. S., *Studies of Photoinduced Molecular Dynamics Using a Fast Imaging Sensor*; University of Oxford: (2013).

(160) Pan, Y.; Cotter, R. J. *Org. Mass Spectrom.* (**1992**), **27**, 3–8.

(161) Olsson, D. M.; Nelson, L. S. *Technometrics* (**1975**), **17**, 45–51.

(162) Zavalin, A.; Todd, E. M.; Rawhouser, P. D.; Yang, J.; Norris, J. L.; Caprioli, R. M. *J. Mass Spectrom.* (**2012**), **47**, 1473–1481.

(163) Möllenstedt, G.; Lenz, F., *Electron Emission Microscopy*; Academic Press: (1963).

(164) Liebl, H., *Applied Charged Particle Optics*; Springer: (2008).

(165) Ed, A. S., *Applied Charged Particle Optics*; Academic Press, New York: (1980).

(166) Nakabushi, H.; Sakurai, T.; Matsuda, H. *Int. J. Mass spectrom. and Ion Physics* (**1983**), **52**, 319–336.

(167) Poschenrieder, W. *Int. J. Mass spectrom. and Ion Physics* (**1972**), **9**, 357–373.

(168) Sakurai, T.; Matsuo, T.; Matsuda, H. *Int. J. Mass Spectrom. Ion Processes* (**1985**), **63**, 273–287.

(169) Zouros, T.; Benis, E. *J. Electron. Spectros. Relat. Phenomena* (**2002**), **125**, 221–248.

(170) Farnell, C.; Farnell, C.; Farnell, S.; Williams, J. *J. Propul. Power* (**2016**), **33**, 5638–658.

(171) Ilyin, A. *Nucl. Instrum. Methods Phys. Res., Sect. A* (**2003**), **500**, 62–67.

(172) Burgoyne, T. W.; Hieftje, G. M. *Mass Spectrom. Rev.* (**1996**), **15**, 241–259.

(173) Mulcahy, M.; Bolin, P., *High Voltage Breakdown Study*; National Technical Infomation Service: (1971).

(174) Byrne, C. *Inverse Problems* (**2008**), **24**, 015013.

(175) Imhof, R. E.; Adams, A.; King, G. C. *J.Phys E. Sci. Instrum.* (**1976**), **9**, 138.

(176) Jungmann, J. H.; MacAleese, L.; Visser, J.; Vrakking, M. J. J.; Heeren, R. M. A. *Anal. Chem.* (**2011**), **83**, 7888–7894.

(177) Jungmann, J. H.; Smith, D. F.; MacAleese, L.; Klinkert, I.; Visser, J.; Heeren, R. M. A. *J. Am. Soc. Mass Spectrom.* (**2012**), **23**, 1679–1688.

(178) Frojdh, C.; Graafsma, H.; Nilsson, H.-E.; Ponchut, C. *Nucl. Instrum. Meth. Phys. Res. A.* (**2006**), **563**, 128–132.

(179) Granja, C.; Polansky, S.; Vykydal, Z.; Pospisil, S.; Owens, A.; Kozacek, Z.; Mellab, K.; Simcak, M. *Planet. Space Sci.* (**2016**), **125**, 114–129.

(180) *Nucl. Instrum. Methods Phys. Res., Sect. A* (**2011**), **633**, S190–S193.

(181) Kiss, A.; Jungmann, J. H.; Smith, D. F.; Heeren, R. M. A. *Rev. Sci. Instrum.* (**2013**), **84**, 013704.

(182) Gademann, G.; Huismans, Y.; Gijsbertsen, A.; Jungmann, J.; Visschers, J.; Vrakking, M. J. J. *Rev. Sci. Instrum.* (**2009**), **80**, 103105.

(183) Nomerotski, A.; Chakaberia, I.; Fisher-Levine, M.; Janoska, Z.; Takacs, P.; Tsang, T. *J. Instrum.* (**2017**), **12**, C01017–C01017.

(184) Fisher-Levine, M.; Boll, R.; Ziaee, F.; Bomme, C.; Erk, B.; Rompotis, D.; Marchenko, T.; Nomerotski, A.; Rolles, D. *J. Synchrotron Radiat.* (**2018**), **25**, 336–345.

(185) Poikela, T.; Plosila, J.; Westerlund, T.; Campbell, M.; Gaspari, M. D.; Llopart, X.; Gromov, V.; Kluit, R.; van Beuzekom, M.; Zappon, F.; Zivkovic, V.; Brezina, C.; Desch, K.; Fu, Y.; Kruth, A. *J. Instrum.* (**2014**), **9**, C05013–C05013.

(186) Levasseur, S.; Dehning, B.; Gibson, S.; Sandberg, H.; Sapinski, M.; Sato, K.; Schneider, G.; Storey, J. *J. Instrum.* (**2017**), **12**, C02050–C02050.

(187) Zhao, A.; van Beuzekom, M.; Bouwens, B.; Byelov, D.; Chakaberia, I.; Cheng, C.; Maddox, E.; Nomerotski, A.; Svihra, P.; Visser, J.; Vrba, V.; Weinacht, T. *Rev. Sci. Instrum.* (**2017**), **88**, 113104.

(188) Visser, J.; van Beuzekom, M.; Boterenbrood, H.; van der Heijden, B.; Muñoz, J.; Kulis, S.; Munneke, B.; Schreuder, F. *J. Instrum.* (**2015**), **10**, C12028–C12028.

(189) Amsterdam Scientific Instruments., Accessed: 09.02.19, `www.amscins.com`.

(190) Turecek, D.; Jakubek, J.; Soukup, P. *J. Instrum.* (**2016**), **11**, C12065–C12065.

(191) De Hoon, M.; Imoto, S.; Nolan, J.; Miyano, S. *Bioinformatics* (**2004**), **20**, 1453–1454.

(192) Kmeans clustering., Accessed: 01.11.18, `www.scikit-learn.org/:sklearn.clustering`.

(193) Visser, J.; van Beuzekom, M.; Boterenbrood, H.; van der Heijden, B.; Muñoz, J.; Kulis, S.; Munneke, B.; Schreuder, F. *J. Instrum.* (**2015**), **10**, C12028–C12028.

(194) Turecek, D.; Jakubek, J.; Kroupa, M.; Soukup, P. *2011 IEEE Nuclear Science Symposium Conference Record*, (2011), 1722–1725.

(195) Turecek, D.; Jakubek, J.; Soukup, P. *J. Instrum.* (**2016**), **11**, C12065–C12065.

(196) Jakubek, J. *Nucl. Instrum. Methods Phys. Res., Sect. A* (**2011**), **633**, S262–S266.

(197) Akiba, K.; Artuso, M.; Badman, R.; Borgia, A.; Bates, R.; Bayer, F.; van Beuzekom, M.; Buytaert, J.; Cabruja, E.; Campbell, M.; Collins, P.; Crossley, M.; Dumps, R.; Eklund, L.; Esperante, D.; Fleta, C.; Gallas, A.; Gandelman, M.; Garofoli, J.; Gersabeck, M.; Gligorov, V. V.; Gordon, H.; Heijne, E. H.; Heijne, V.; Hynds, D.; John, M.; Leflat, A.; Llin, L. F.; Llopart, X.; Lozano, M.; Maneuski, D.; Michel, T.; Nicol, M.; Needham, M.; Parkes, C.; Pellegrini, G.; Plackett, R.; Poikela, T.; Rodrigues, E.; Stewart, G.; Wang, J.; Xing, Z. *Nucl. Instrum. Methods Phys. Res., Sect. A* (**2012**), **661**, 31–49.

(198) Sheraz (née Rabbani), S.; Barber, A.; Berrueta Razo, I.; Fletcher, J. S.; Lockyer, N.; Vickerman, J. C. *Surf. Interface Anal.* (**2014**), **46**, 51–53.

Appendices

A
Appendix 1

A Genetic algorithm parameter values

This appendix details the identity of each parameter determined by the genetic algorithm that resulted in optimal spatial resolution for a four plate ion optic arrangement. The initial ion conditions have been specified in Chapter.6. In the following tables, l_x is the spacing between the electrodes measured in (mm), A_x is the aperture width of each electrode measured in (mm), V_x is the voltage applied to the electrode and R is the resolution achieved using these parameter values. The two tables show the results from genetic algorithms where the voltage on the electrodes are restricted to 5 kV and 30 kV respectively.

Mass(Da)	L_1	A_1	L_2	A_2	L_3	A_3	V_1(V)	V_2(V)	V_3(V)	V_4(V)	R(µm)
100	10	4	8	4	9	4	2915	-3411	1528	-526	1.35
200	10	4	8	4	9	4	2047	-2924	223	-2986	3.20
300	10	4	8	4	9	4	3548	-4225	1970	1112	4.07
400	10	4	8	4	9	4	3484	-2953	2104	236	6.35
500	10	4	8	4	9	4	3359	-3052	1266	2087	7.11
600	10	4	8	4	9	4	4570	-2758	2014	-4078	9.10
700	10	4	8	4	9	4	3758	-1951	2440	1861	8.51
800	10	4	8	4	9	4	4894	-2390	2727	-2432	10.5
900	10	4	8	4	9	4	3046	-3515	1716	574	10.3
1000	10	4	8	4	9	4	3436	-2784	1843	-1316	12.4

Table A.1: List of parameters and their values determined by the genetic algorithm for the optimisation of the four-plate ion optic when the voltage applied to the plates is restricted to a maximum of 5 kV.

Mass(Da)	L_1	A_1	L_2	A_2	L_3	A_3	V_1(V)	V_2(V)	V_3(V)	V_4(V)	R(µm)
100	10	4	8	4	9	4	27176	-11738	18470	-5169	0.80
200	10	4	8	4	9	4	27168	-10261	18834	10929	0.82
300	10	4	8	4	9	4	26865	-20949	16886	8194	0.89
400	10	4	8	4	9	4	26651	-13729	17856	6547	1.04
500	10	4	8	4	9	4	25946	-23983	15349	10791	1.03
600	10	4	8	4	9	4	26377	-6682	18608	12616	1.11
700	10	4	8	4	9	4	27554	-10507	19066	9155	1.17
800	10	4	8	4	9	4	27005	-12181	18385	8187	1.18
900	10	4	8	4	9	4	26890	-21361	15868	13442	1.42
1000	10	4	8	4	9	4	28543	-16511	17998	14816	1.50

Table A.2: List of parameters and parameter values determined by the genetic algorithm for the optimisation of the four-plate ion optic design when the voltage applied to the plates is restricted to a maximum of 30 kV.